Microwave Electromechanics: Measuring and Manipulating the Quantum State of a Macroscopic Mechanical Oscillator

by

Jennifer Wightman Harlow

A.B., Harvard University, 2007

M.S., University of Colorado, 2010

A thesis submitted to the

Faculty of the Graduate School of the

University of Colorado in partial fulfillment

of the requirements for the degree of

Doctor of Philosophy

Department of Physics

2013

This thesis entitled:
Microwave Electromechanics: Measuring and Manipulating the Quantum State of a Macroscopic
Mechanical Oscillator
written by Jennifer Wightman Harlow
has been approved for the Department of Physics

_____
Prof. Konrad W. Lehnert

_____
Prof. Cindy A. Regal

Date _____

The final copy of this thesis has been examined by the signatories, and we find that both the
content and the form meet acceptable presentation standards of scholarly work in the above
mentioned discipline.

Harlow, Jennifer Wightman (Ph.D., Physics)

Microwave Electromechanics: Measuring and Manipulating the Quantum State of a Macroscopic

  Mechanical Oscillator

Thesis directed by Prof. Konrad W. Lehnert

In the past several years, the field of optomechanics has progressed from proof-of-principle experiments to the realization of mechanical oscillators and measurements in the quantum regime. Mechanical oscillators are of great interest because they can have small dissipation rates, can couple to many different systems of interest, and are the fundamental elements of ultrasensitive force detectors. Coupling these mechanical oscillators to microwave or optical fields provides a two-fold advantage. Firstly, information about mechanical position can be encoded in the interrogating field, enabling sensitive readout of the mechanical oscillator. Secondly, the radiation pressure force of that field can be used to control the state of the mechanical oscillator. Including a high-quality microwave or optical cavity enhances both of these effects, as the field strength is resonantly increased.

The major questions in the field of optomechanics in the last several years have dealt with using mechanical oscillators for ultrasensitive measurements and as tools for quantum information. Both of these goals have the prerequisite that we be able to read out the motion of the mechanical oscillator in a quantum efficient manner. To that end, we developed a nearly shot-noise limited microwave interferometer capable of measuring mechanical motion with an imprecision below that at the standard quantum limit. This achievement is not only a critical improvement for the electromechanical experiments we do, but is also an important tool for any experiment that encodes the information of interest in microwave fields. In order to use mechanical oscillators as tools for quantum information, the mechanical oscillator must also be cooled into the quantum regime and fully controllable by the interrogating fields. To this end, we used the radiation pressure of microwave fields to cool our macroscopic mechanical oscillator to less than one phonon. We also

demonstrated coherent transfer between itinerant microwave states and the mechanical oscillator, even for incident fields with less than one photon of energy.

These accomplishments have set the foundation for further experiments to extend the quantum information abilities of optomechanical systems, couple diverse quantum systems via a mechanical intermediary, and potentially explore the foundations of quantum mechanics at macroscopic scales.

Dedication

In memory of Ethan.

Acknowledgements

There are many people who deserve thanks for their contributions of one kind or another to my journey through graduate school.

I'd like to first thank Cindy Regal, James Thompson, Michael Hermele, Scott Bunch, and Jun Ye for agreeing to be on my PhD defense and/or my Comps III committee and providing valuable feedback on my work.

I want to thank all of the people who have worked on the Microwave Electromechanics experiment, either as a Lehnert Lab member or collaborator: Cindy Regal, John Teufel, Tobias Donner, Mike Demoret, Reed Andrews, Tauno Palomaki, Kat Cicak, and Ray Simmonds. All of these people have significantly contributed to the fabrication, data taking, analysis, understanding, and/or publications contained within this dissertation. In particular, I'd like to thank John for teaching me most of what I know about optomechanics, exhibiting endless patience with all of the stupid questions I have asked over the years, teaching me how to count to 10, and making me memorize $\hbar$.

I additionally want to thank everyone else who has been a member of the Lehnert Lab with me: Nathan Flowers-Jacobs, Manuel Castellanos-Beltran, Françios Mallet, Scott Hoch, Will Kindel, Hsiang-Sheng Ku, Adam Reed, Joe Kerckhoff, Michael Schroer, Brad Mitchell, Mehmet Anil, and Gerwin Koolstra. We may not share publications or work together directly, but they certainly contributed in countless ways to the day-to-day success of my individual work and the success of our experiments as a whole.

Many thanks also go out to the support staff and shops of JILA, without whom we could

not do what we do. In particular, I owe endless thanks to JR as well as everyone in the JILA instrument shop for always being friendly and helpful beyond my expectations.

I thank the many people have read and given their expert feedback on different sections of this document: Will Kindel, Brad Mitchell, Adam Reed, Bob Peterson, Joe Britton, Ryan Bowler, Tom Purdy, Tauno Palomaki, John Teufel, Manuel Castellanos-Beltran, and Justin Bohnet. I thank Mike Foss-Feig and Dominic Meiser for providing invaluable insights on some of the theory contained in this dissertation.

I also want to thank the people who have gone above and beyond to support me personally at some point in the last six years: Craig Hogle, Ethan Townsend, Chris Rosen, Phil Makotyn, Phoenix Dai, Tobias Donner, John Teufel, Danny Goodman, Rob Barton, Karen Lauffer, Mike Foss-Feig, Will Kindel, Alejandra Collopy, Teesa Christian, Steve Reaser, Cathy Klauss, Yomay Shyur, everyone at Wardenburg PHP, and the many other people who have been there for me.

Lastly, I would like to thank Konrad, who fits in every category listed above. Obviously, he has taught me many things about physics, helped me through many problems both scientific and technical, and guided my scientific path through graduate school. However, he has gone above and beyond the minimum responsibilities of an advisor many times and I would like to acknowledge some of those efforts. I very much appreciate Konrad's extensive involvement and investment toward production of high quality talks and publications. Not only has this resulted in many works that I am proud of, but it has taught me critical professional communication skills that will be relevant to anything I do in my life. Furthermore, Konrad has read and given feedback on every single part of this document, in many cases helping to make it more correct, complete, understandable, and helpful. But most of all, I am particularly thankful for Konrad's best quality: his willingness to listen, consider, and adapt to difficult situations and concerns. This quality has helped us to overcome many difficulties and made it possible for me to complete my PhD. Thank you!

Contents

Tables

Table

Figures

Figure

Chapter 1

Introduction to optomechanics

The field of optomechanics is currently a very popular and fast-progressing area of physics for a variety of reasons from ultrasensitive measurement applications to quantum information processing to tests of quantum theory at macroscopic scales. The field encompasses a wide range of experiments using electromagnetic fields at gigahertz to terahertz frequencies and mechanical oscillators[1] with attogram to kilogram masses. The wide extent of this interest stems from the very simple yet versatile basis for an optomechanical system; namely, a mechanical oscillator coupled to an electromagnetic field. This coupling provides two main functions. The first is that the electromagnetic field can be used to interrogate the mechanical oscillator, picking up information about the mechanical position. The second is that the radiation pressure force of that field on the mechanical oscillator can be used to control the mechanical oscillator. In this introductory chapter, I will focus on these two universal features of optomechanical systems and provide examples of experiments that utilize and explore them. Note that the term 'optomechanics' is usually used to describe experiments employing macroscopic mechanical oscillators (collective motional modes of many atoms). These experiments are close analogs of cold ion experiments that demonstrate control over the motion of a single trapped ion. Another resource for learning about optomechanical systems, the effects they exhibit, and all of the experimental groups investigating these effects is a recent review paper [1].

---

[1] Note that throughout this dissertation, I use the word 'oscillator' in the sense of a simple harmonic oscillator, not an electronic oscillator. This use allows more clarity in distinguishing the mechanical element from the electromagnetic cavity or 'resonator'. In the few instances where the mechanical element is able to generate its own oscillations, I call these 'self-oscillations'.

1.1   Optomechanical systems as ultrasensitive detectors of motion

Modern measurement tools frequently employ electromagnetic fields (at either optical or electrical frequencies), as those fields allow for fast, non-invasive, measurement of systems. Additionally, interferometric techniques enable very sensitive detection of small phase shifts in these fields due to a system of interest. However, electromagnetic fields are limited in their ability to sensitively read out certain quantities of interest because they cannot image with subwavelength resolution and they couple poorly to some systems of interest, such as sound waves or gravitational waves. In contrast, mechanical oscillators are capable of probing very small scales and can universally couple to all forces, and thus many different systems of interest. This makes them very good intermediaries for measurement, as the mechanical oscillator can interact with the system of interest and then be read-out very sensitively by its interactions with an electromagnetic field.

The basic optomechanical (or electromechanical) system consists of a mechanical oscillator coupled to an optical (or electrical) field. As an example, consider an optical field bouncing off of a mirror attached to a mechanical oscillator (Figure 1.1(a)). The phase of the reflected wave is very sensitive to the mechanical displacement; thus, a sensitive readout of the reflected phase allows sensitive inference of the mechanical position. This interaction, and thus the sensitivity of readout, can be enhanced by coupling the mechanical motion to a high-Q electromagnetic resonance, increasing the strength of the interacting field. This situation is shown in Figure 1.1(b), where a fixed, partially transparent mirror is placed a distance l away from the mechanically compliant, reflective mirror. These mirrors form a resonant cavity such that interrogating optical fields at frequencies near the cavity resonance cause both a more intense field within the cavity as well as an enhanced phase shift of the outgoing field. We often break this down into two steps: the mechanical displacement changes the length, and therefore the resonant frequency of the cavity, and then the resonant frequency change imparts a phase shift onto the outgoing field. This allows us to extend the ideas from this basic model of cavity optomechanics to any system where the resonant frequency of a resonant structure is coupled to the motion of a mechanical oscillator. In
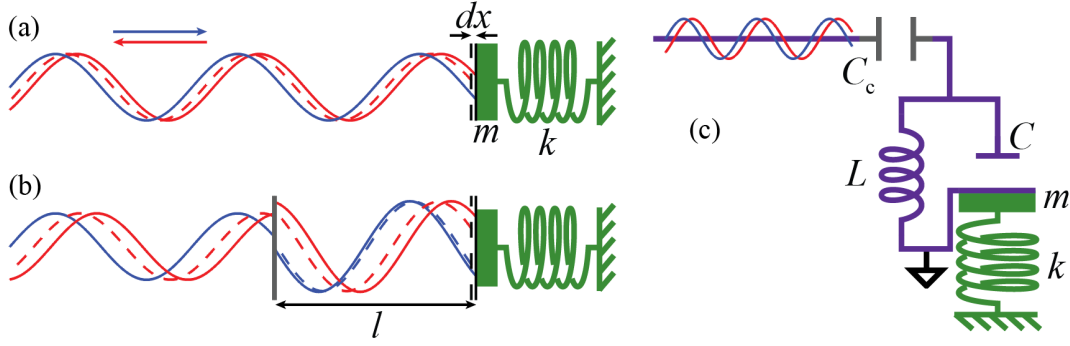
Figure 1.1: Mechanical motion can be inferred from the phase shift of interrogating electromagnetic fields. (a) An incoming light field (rightgoing, blue) reflects off of a perfect mirror (black), attached to a mechanical oscillator with mass m and spring constant k (green). The phase of the outgoing light field (leftgoing, red) depends on the position of the mechanical oscillator. Shown are the outgoing field reflected from the mirror for two displacements separated by dx (shown as solid or dashed mirrors and fields). (b) Adding a partially reflective mirror (gray) creates a resonant cavity of length l. Again, the steady-state rightgoing (blue) and leftgoing (red) fields are shown for the two positions of the mechanical oscillator. For interrogating fields near resonance, the field inside the cavity is intensified and the phase shift from displacement dx is enhanced. (c) An analogous system can be made in the microwave frequency regime by replacing the partially reflective mirror by a coupling capacitor C_c, the perfectly reflecting mirror by a boundary condition (short or open), and the freely propagating optical fields by transmission lines or more generally any resonant LC circuit with a resonant frequency that is modulated by mechanical motion.

particular, our research focuses on an electromechanical system where mechanical motion changes the capacitance, and therefore resonant frequency, of an LC resonant circuit, once again imparting a phase shift on the outgoing electrical fields (Figure 1.1(c)).

Many optomechanical experiments rely on either the canonical optical setup of a Fabry-Perot resonator with a movable mirror [2, 3, 4, 5, 6] or the canonical electrical setup of a mechanically variable capacitance [7, 8, 9, 10, 11, 12, 13, 14, 15, 16]. However, these are not the only ways to realize coupling of mechanical motion to the resonant frequency of an electromagnetic resonant structure. A few examples of optomechanical systems that employ novel coupling mechanisms are shown in Figure 1.2. Figure 1.2(a) depicts a microtoroid resonator that supports whispering gallery optical modes around its circumference. Mechanical motion of the toroid can change this circumference, thereby changing the resonant frequency for the circular modes [17, 18]. Figure
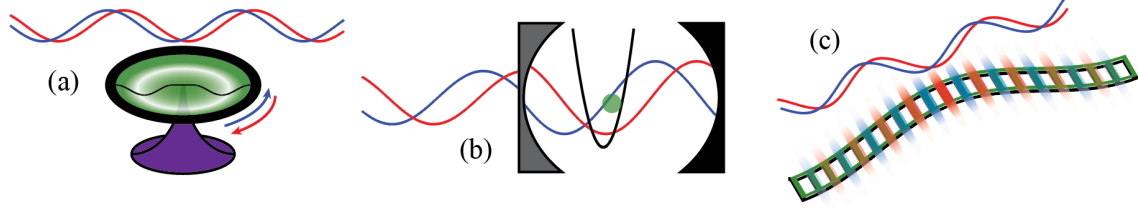
Figure 1.2: Novel optomechanical coupling schemes. Shown for each example are the mechanical element (green) and right and left traveling optical modes (red and blue). (a) A microtoroid's mechanical motion modifies the circumference for whispering-gallery optical modes. (b) A dielectric harmonic oscillator dispersively couples to an optical cavity mode. (c) A photonic crystal patterned mechanical beam supports both mechanical and optical modes.

1.2(b) shows a dielectric material confined to a harmonic well and placed in the middle of a rigid optical cavity. This dielectric material couples to the cavity resonance frequency in analogy to dispersive coupling in atomic systems. The dielectric object can be made out of a thin membrane [19, 20, 21], a nanoparticle [22], or even the center of mass motion of an atomic cloud [23, 24, 25]. Figure 1.2(c) shows a mechanical beam that has been patterned with a photonic crystal structure, allowing photonic and phononic modes to exist and couple in a single structure [26].

1.1.1   Examples of optomechanical systems as ultrasensitive detectors

While the field of optomechanics has recently exploded with many different schemes to optimize sensitive detection and control, the central idea of coupling electromagnetic fields to a mechanical oscillator for ultrasensitive measurement is not new. In fact, Henry Cavendish's experiment in 1798 to detect the density of the earth could be argued to be optomechanical in nature (see Figure 1.3 and reference [27]). Cavendish's experiment measured the angular displacements of two small masses hung from a torsional pendulum due to the presence of two larger, fixed masses. As the entire experiment was enclosed in a thick wooden box to isolate it from wind and temperature gradients, Cavendish read out the displacement of the masses by illuminating the masses with a lamp and then observing the result with a telescope. In this way, he used mechanical oscillators to convert gravitational forces to optically detectable information.
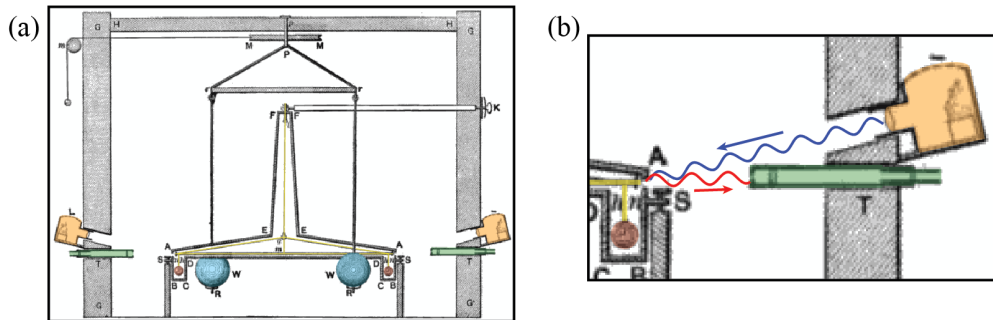
Figure 1.3: Schematic of Cavendish's experiment to determine the density of the earth, adapted from [27]. (a) Two small masses (which I have false colored red) are free to rotate on a torsional pendulum (yellow). Angular displacements due to their gravitational interaction with two heavier, fixed masses (blue) are read out via light from a lamp (orange) and detected by a telescope (green). The density of the earth was determined by comparing these measurements with measurements of the weights of the masses and the torsional force of the pendulum wire. (b) Closer view of the optomechanical readout mechanism. I have included an illustration of the incident (blue) and reflected (red) light.
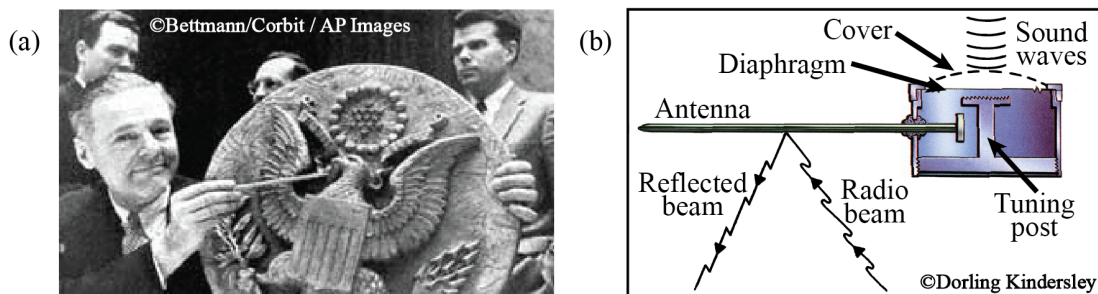
Figure 1.4: Soviet surveillance using optomechanics. (a) Henry Cabot Lodge, Jr., US ambassador to the United Nations, reveals the Great Seal bug to the UN. Image from [28]. (b) Illustration of the surveillance device contained within the Great Seal. Image adapted from [29] and included with permission from Dorling Kindersley.

Another early optomechanical device was cleverly employed as a surveillance bug by the USSR during the cold war. In 1946, the United States ambassador in Moscow received a two-foot wooden replica of the Great Seal of the United States as a gift from the Soviets (see Figure 1.4 and a much more complete historical description at reference [30]). What the US ambassador did not know was that the seal was outfitted with a bug designed to allow eavesdropping by Soviets located outside of the building. The bug (illustrated in Figure 1.4(b)) consisted of a diaphragm attached to a resonant cavity. When sound waves hit the diaphragm, they changed the resonant frequency of the cavity and also the charge on an attached antenna. Radio waves were reflected off the antenna from a van parked outside the embassy building. Demodulation of these waves allowed access to information about sounds in the ambassador's office. This device was particularly clever because it was passive and therefore could be entirely contained in the Great Seal with far less chance of discovery than an active bug. In fact, it took the US six years to eventually find the device.

The Cavendish experiment and the Great Seal bug are surely some of the first uses of optomechanical devices for ultrasensitive measurement. However, neither of these examples really required sensitivities approaching the fundamental limits of detection. It was instead the search for gravitational waves that brought cavity optomechanics and ultrasensitive interferometric detection together with the goal of understanding and approaching the ultimate sensitivity. The goal of gravitational wave detection is to observe a propagating curvature of spacetime by determining very small changes in lengths. Two main schemes, one electromechanical and one optomechanical, for detecting such small changes are described and analyzed in detail in a 1978 paper by Braginsky [31]. The first, which had already been experimentally attempted at the time, involved using a Weber antenna or bar. This device was a long cylinder that would support vibrations upon interaction with a gravitational wave. These vibrations could then be amplified and read out via an electric circuit (see Figure 1.5(a)). Since the initial proposals, Weber antenna experiments for gravitational wave detection have made vast improvements [7] and are still being carried out by multiple groups [9, 11]. The second scheme proposed by Braginsky, which at the time was still in the early stages experimentally, involved using a Michaelson optical interferometer to detect differences in the
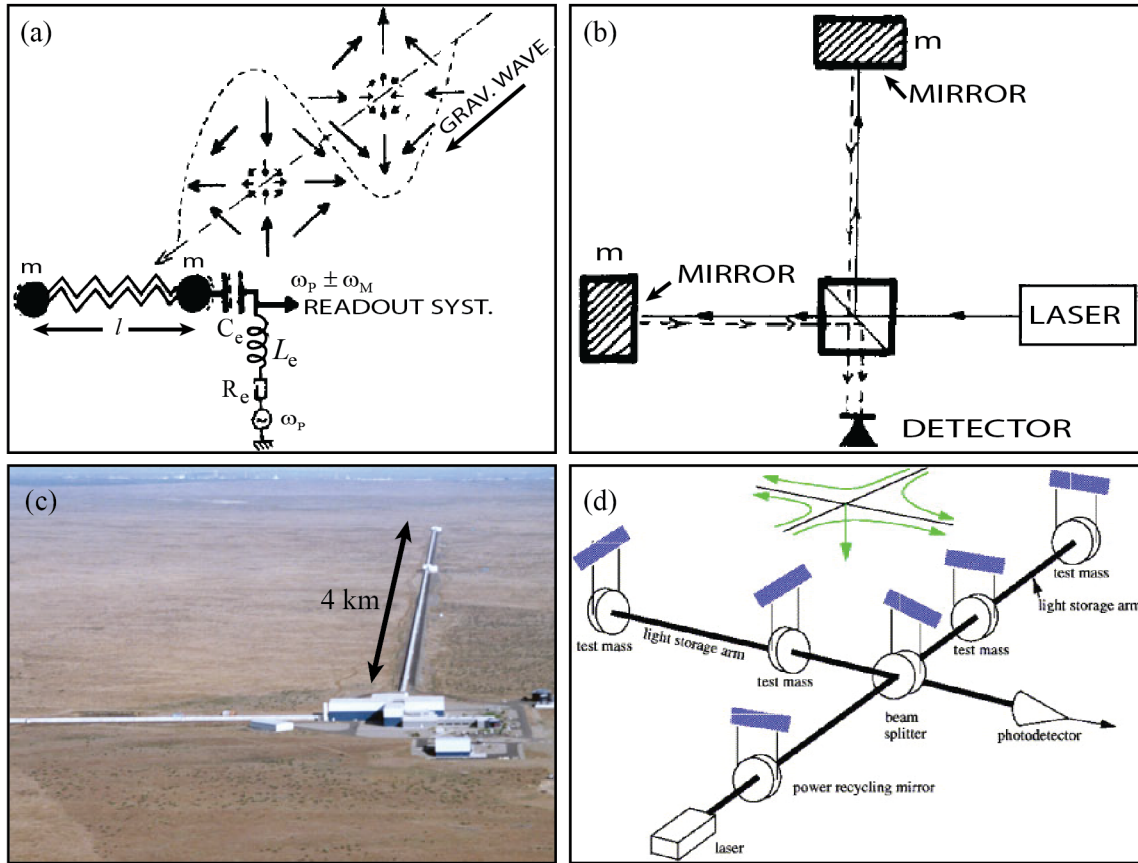
Figure 1.5: Optomechanical systems as ultrasensitive gravitational wave detectors. (a) Electromagnetic readout scheme for measuring vibrations of a Weber bar due to interaction with a gravitational wave. The Weber bar is modeled as two masses m on a spring, separated by a distance l and is coupled to a driven LC circuit. Image from [31]. (b) Interferometric scheme proposed for measuring differential perpendicular displacements of two masses m. Also from [31]. (c-d) Photograph (from [32]) and schematic (from [2]) of LIGO, demonstrating the realization of large-scale optomechanical experiments for detecting gravitational waves. Images included with permission from LIGO and Elsevier.

lengths of two perpendicular arms (see Figure 1.5(b)). This idea of an ultrasensitive interferometric detection of mechanical motion has evolved from its primarily theoretical foundation in 1978 to a very large experimental collaboration, the Laser Interferometer Gravitational Wave Observatory (shown in Figures 1.5(c-d)). Additionally, the long-term interest in optomechanical detection by the gravitational wave community is responsible for much of the foundational theoretic work upon which the field of optomechanics is built.

There are also two, more recently conceived, experiments that use optomechanical coupling for applications requiring extremely sensitive measurement at small length scales. The first, atomic force microscopy (AFM) is a widely-used technique for imaging surfaces with nanoscale resolution (Figure 1.6(a)). AFM employs a very sharp tip attached to the end of a cantilever (essentially a diving board mechanical oscillator) that can interact with a very small surface area of the sample of interest. Surface forces on the tip are translated into deflections of the cantilever, which can then be read out by an optical field reflected off of the cantilever. The use of the mechanical oscillator as an intermediary allows spatial measurement resolution on scales far smaller than what could be achieved by interrogating the sample directly with an optical field. The second ultrasensitive-measurement application aided by the use of an optomechanical system is magnetic resonance force microscopy (MRFM). MRFM is similar to AFM, except that the force of interest is not the normal force between the cantilever tip and the sample, but rather the magnetic dipole force between nuclear spins in the sample and a nearby magnetic particle (Figure 1.6(b)). MRFM is also different
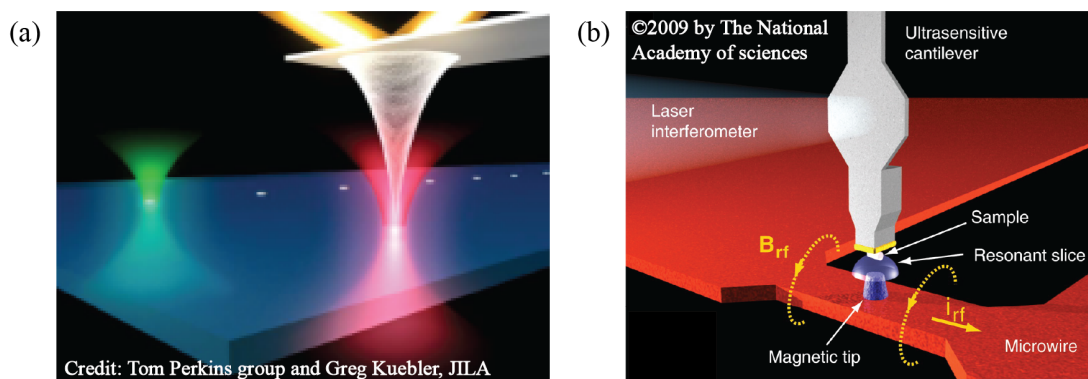
Figure 1.6: Applications of optomechanical systems for ultrasensitive detection on small length scales. (a) Artistic rendering of an AFM. A sharp tip attached to a cantilever (both white) interacts with the sample surface (blue). The force imparted on the tip causes displacements of the cantilever, which can be read-out by a reflected optical field. Image from [33], and included with permission from JILA. (b) Artistic rendering of an MRFM experiment. Forces between a magnetic tip and the nuclear spins in the sample cause displacements of a cantilever, which can again be read-out with a reflected optical field. MRFM allows a three dimensional image of the sample by using an external magnetic field to control the position of a resonantly sensitive slice of space (in a similar scheme to NMR). Image from [5] and included with permission from D. Rugar.

from AFM in that the obtainable information is not limited to the surface of the sample. It uses the techniques of nuclear magnetic resonance (NMR) imaging to obtain a three dimensional image of the sample. So far, the best force sensitivity achieved by an optomechanical system used for MRFM was $S_{FF}^{1/2} = 0.82$ aN/Hz$^{1/2}$, as was demonstrated with a 5 kHz mechanical cantilever [34]. The ultimate goal of MRFM is to reach sensitivities good enough to detect single nuclear dipoles with forces on order 10 fN. This realization would be particularly exciting, as groundbreaking applications for three dimensional images of nanostructures such as molecules and proteins are abundant. Cold ion systems have also produced exceptionally good force sensitivities, reaching $S_{FF}^{1/2} = 390$ yN/Hz$^{1/2}$ [35] and are proposed as ultrasensitive detectors of electric and magnetic fields [36]; however, it may be more difficult to integrate these systems with samples of interest for applications like MRFM.

1.2 Mechanical control by dynamical radiation pressure forces

At the beginning of this chapter, I emphasized that there were two functions that an optomechanical coupling provides. The first, which was introduced in the first section of this chapter, was ultrasensitive measurement of the mechanical position through a phase shift in the interrogating electromagnetic field. The second function is the ability to control the mechanical oscillator using the radiation pressure force from the electromagnetic field. The basic idea behind radiation pressure forces is simple to understand. If a continuous electromagnetic wave with power P is perfectly reflected from a surface (I assume the surface is moving at speed much less than c), then the force on that surface will be $F = dp/dt = (2/c)dE/dt = 2P/c$. The idea that we can use this radiation pressure force of photons to control a mechanical oscillator is also easy to understand if you have ever pushed someone on a swing. If you apply a force to the person on the swing once per oscillation as they are moving away from you, as you typically do when pushing a swing, you amplify their motion. If you instead decide to apply a force to the person on the swing once per oscillation as they are moving toward you, you deamplify their motion. Thus, the phase with which the radiation pressure force acts can cause either damping or amplification of harmonic motion.

Ideas about and observations of radiation pressure forces have a long history. Initial theoretic understanding of radiation pressure and observations of its effect on comets go back to Kepler and Maxwell. The tails of comets (as seen in Figure 1.7(a)), which are made of gas and dust debris from the comet nucleus, are observed to always point away from the sun due to forces from solar radiation pressure and solar wind [39]. Along with these observations came the idea of using radiation pressure forces to propel a spacecraft, known as a solar sail. Until recently, such solar sails were limited to theory and science fiction; however, in 2010 the Japan Aerospace Exploration Agency (JAXA) launched and successfully demonstrated solar sailing with the Interplanetary Kite-craft Accelerated by Radiation of the Sun (IKAROS). In 2011, NASA also launched and demonstrated a solar sail called NanoSail-D [40]. To give some sense of the scale of forces involved, the solar radiation pressure force on IKAROS (which is predominantly reflecting and has surface area $200\ \mathrm{m}^2$) when it was near Venus (0.73 AU from the sun) is approximately $F_{\mathrm{rp}} = 3$ mN. By contrast, the solar radiation pressure force on Halley's comet (which is predominantly absorbing and has diameter 10 km) at its closest distance to the sun (0.6 AU) is approximately $F_{\mathrm{rp}} = 1$ kN. However, if we instead look at the accelerations (to account for the different scales of mass), we would find $a = 10\ \mu\mathrm{m/s}^2$ for IKAROS and $a = 5\ \mathrm{pm/s}^2$ for Halley's Comet. Forces due to solar wind also effect these objects,
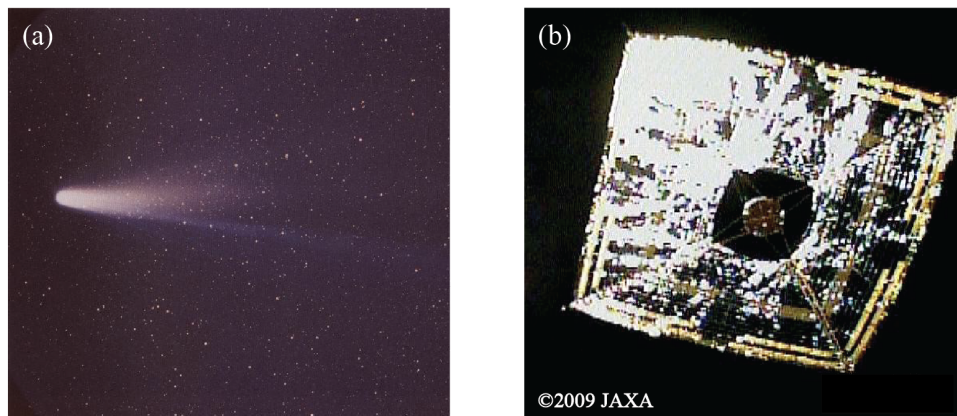
Figure 1.7: Images of radiation pressure in space. (a) Image of Halley's comet displaying a long tail, from [37]. (b) Image of the IKAROS solar sail from [38].

sometimes in much more complicated ways [41]. However, the absolute magnitude of the solar wind force on IKAROS, for example, is $F_{sw} = 1 \; \mu N$, a quantity negligible compared with the radiation pressure force.

The first quantitative measurement of the radiation pressure force was done in 1901 by E. F. Nichols and G. F. Hull, using a so-called Nichols radiometer [42]. This experiment was similar to Cavendish's experiment described earlier in that it used a torsional pendulum to measure the force and the rotation was read out from outside an enclosure using telescopes aimed at the pendulum. The apparatus is shown in Figure 1.8 and consists of a hanging wire with two surfaces, one reflecting and one absorbing. By shining light on these surfaces, the angle of rotation of the pendulum provides a measure of the differential radiation pressure force on the two surfaces.

More recently, radiation pressure forces have been used to manipulate systems of interest. Most notably, radiation pressure damping is the mechanism behind atomic cooling, which was
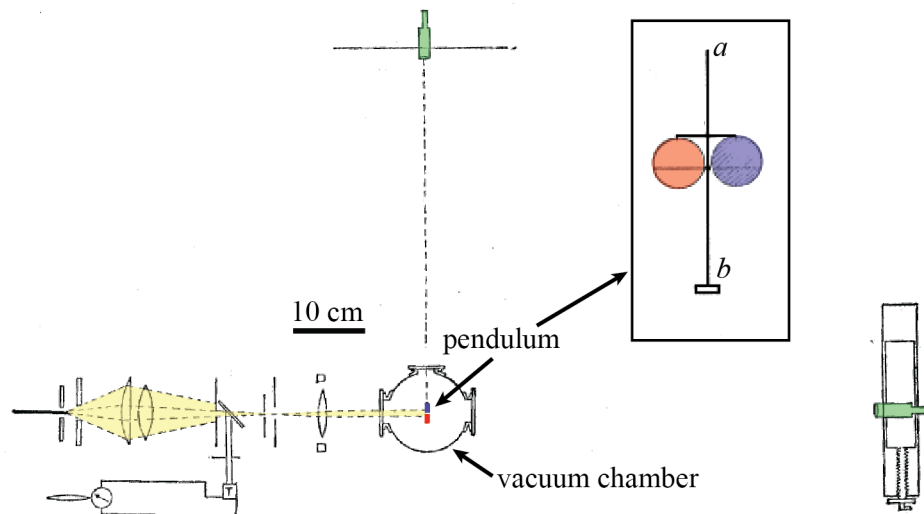
Figure 1.8: Nichols radiometer, adapted from [42]. The inset shows the torsional pendulum that rotates about the axis defined by a and b, from which hangs one reflecting surface (I false colored this red) and one absorbing surface (colored purple). The main figure shows the entire experimental apparatus viewed from above. The pendulum hangs from the center of a vacuum enclosure. Light (yellow) shines onto the pendulum, exerting a force on both surfaces. The light is aligned and the rotation of the pendulum is read out using telescopes (green).

first demonstrated in 1978 [43] and is a frequently-used tool of atomic physics. This same radiation pressure force applied to optomechanical experiments leads to all of the same effects and is described extensively throughout this dissertation.

In order to think about radiation pressure forces in a cavity optomechanical context, we return to the system model in Figure 1.1(b). The optical resonator is a Fabry-Perot cavity made of one partially reflecting mirror and one fully reflecting mirror, separated by distance l. This structure resonates at frequency $\omega_c = \pi c / l$ and has a total loss rate κ associated with internal losses as well as coupling to the itinerant optical modes through the partially reflecting mirror. The amount of energy stored in the cavity can be quantified in terms of number of photons $n_c = E/(\hbar \omega_c)$. The fully reflecting mirror is mechanically compliant, with mass m and spring constant k. The resonance frequency of this mechanical oscillator is $\Omega_m = \sqrt{k/m}$ and the loss rate is Γ_m. The energy of the mechanical mode can be quantified in terms of number of phonons $n_m = E/(\hbar \Omega_m)$. The combined optical cavity and mechanical oscillator can be understood by looking at an energy level representation of their state (Figure 1.9). The number of mechanical phonons increases from left to right, and the number of photons increases by one from the lower to upper row of states. Any state is separated in energy from the neighboring photon states by $\hbar \omega_c$ and the neighboring phonon states by $\hbar \Omega_m$. The linewidth κ of the cavity appears by broadening the levels, determining the bandwidth for resonant processes. Assuming that Γ_m is much smaller than all of the other rates in the problem, it does not play a role in the qualitative understanding of cooling presented here.

Figures 1.9(a,c,e) show a representation of the different frequencies involved in each of three different cavity drive schemes. Each of these images shows the cavity lineshape with the resonant frequency ω_c and linewidth κ, as well as the cavity drive (shown as a tall arrow). The resulting output fields (called sidebands on the drive) are shown as short arrows, with line thickness indicating intensity. Figures 1.9(b,d,f) show the accompanying energy level diagrams. The straight arrows show the cavity drives, while the wavy arrows show photons being emitted from the cavity. Only processes where a mechanical phonon is added or destroyed are shown. In Figures 1.9(a,b), the cavity drive is applied at the cavity resonance frequency. Two processes are present that add or
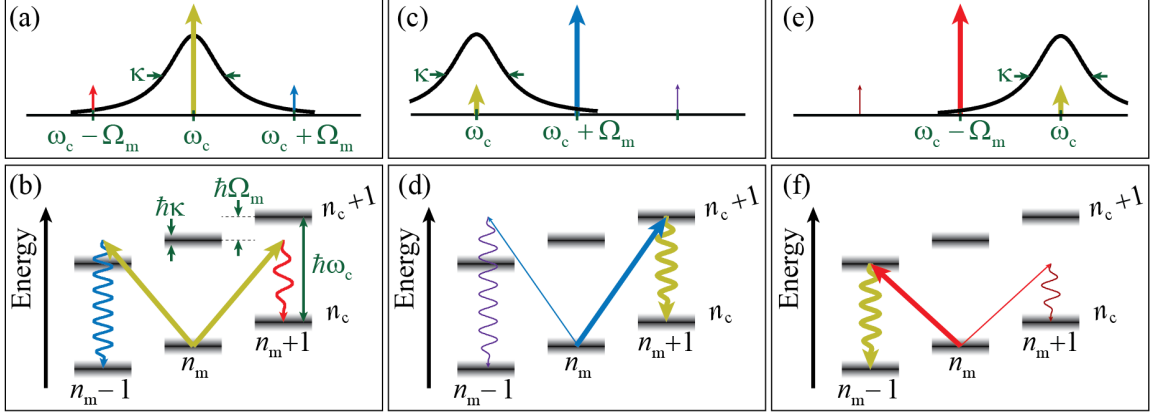
Figure 1.9: Energy level diagrams for different cavity drive choices. For each drive choice, a frequency diagram and energy level diagram are shown. Field intensities are indicated by arrow thickness. The three drive choices are (a,b) on-resonant, (c,d) blue-detuned, and (e,f) red-detuned.

destroy phonons. First, an on-resonant photon can be converted to a higher frequency photon by extracting a phonon of energy from the mechanical oscillator: $\hbar\omega_{\mathrm{c}}n_{\mathrm{c}} + \hbar\Omega_{\mathrm{m}}n_{\mathrm{m}} + \hbar\omega_{\mathrm{c}} \rightarrow \hbar\omega_{\mathrm{c}}n_{\mathrm{c}} + \hbar\Omega_{\mathrm{m}}(n_{\mathrm{m}} - 1) + \hbar(\omega_{\mathrm{c}} + \Omega_{\mathrm{m}})$. Alternatively, the on-resonant photon can be converted to a lower frequency, giving up a phonon to the mechanical oscillator: $\hbar\omega_{\mathrm{c}}n_{\mathrm{c}} + \hbar\Omega_{\mathrm{m}}n_{\mathrm{m}} + \hbar\omega_{\mathrm{c}} \rightarrow \hbar\omega_{\mathrm{c}}n_{\mathrm{c}} + \hbar\Omega_{\mathrm{m}}(n_{\mathrm{m}} + 1) + \hbar(\omega_{\mathrm{c}} - \Omega_{\mathrm{m}})$. These processes are both equally off-resonant and the sidebands they produce will therefore be equally filtered by the cavity. The result is that, for a large mechanical occupation Fock state, no net energy will be added or removed from the mechanical oscillator. Note that for even a large occupation mechanical state, there will be a significant contribution from the ground state and the asymmetry of these processes in that case (discussed later in this introduction) will exert quantum fluctuations that drive the mechanical oscillator. Figures 1.9(c,d) show the case of a drive detuned above the cavity resonance frequency (blue-detuned) by the mechanical frequency. This drive is now resonant with the process that down-converts the photon by giving a phonon to the mechanical oscillator. The other process is highly suppressed by the cavity response. Therefore, the blue-detuned drive preferentially gives up energy to the mechanical oscillator, amplifying its motion. Figures 1.9(e,f) show the case of a drive detuned below the cavity frequency (red-detuned). In this case, the resonant process is the one that up-converts photons by

extracting energy from the mechanical oscillator. The net effect of this process is thus to cool the oscillator. The cavity linewidth κ and relative positions of the sidebands determine the balance of the up and down-conversion processes. The preference for processes with sidebands near the cavity frequency can be attributed to resonant vs. off-resonant energy level transitions, a higher density of available states near the cavity frequency, or simply suppression of sidebands far off resonance by the cavity response, but these are all different ways of saying the same thing. For optomechanical systems in the resolved sideband regime ($\Omega_m \gg \kappa$, also sometimes called the 'good cavity limit' in our field), the imbalance between sidebands due to a drive detuned from the cavity frequency by $\pm\Omega_m$ is large and the off-resonant sidebands can be ignored. However, for optomechanical systems not in the resolved sideband regime ($\Omega_m \ll \kappa$, also sometimes called the 'bad cavity limit' in our field), the imbalance is smaller and the off-resonant process can limit the potential cooling or amplification.

Cooling the mechanical oscillator into its quantum ground state was a long-standing goal of the optomechanics field, inspired by ground-state cooling of trapped atomic ions [44], as it is a prerequisite to many interesting experiments involving quantum information and studies of fundamental quantum theory. Therefore, nearly every recent cavity optomechanical experiment has demonstrated radiation pressure damping and cooling to some degree or another [7, 8, 45, 19, 46, 12, 47, 21]. References [48, 49] have used radiation pressure cooling to achieve ground state mechanical occupation, and will be discussed more fully later in this introduction.

1.3   Quantum measurement and backaction

As measurements of mechanical position using optomechanical systems become more and more accurate, we might wonder what sets the fundamental physical limits on how sensitive a measurement is possible. The answer is that the quantum properties of light enforce a Heisenberg principle between the measurement uncertainty of the mechanical position and the perturbation of the mechanical momentum. I first describe this uncertainty closely following reference [50], which I find to be a very good introductory reference on quantum measurement. I then take a look at a few

of the optomechanics experiments that have been able to see the enforcement of the uncertainty principle on quantum measurement.

1.3.1 Quantum measurement and the associated Heisenberg uncertainty relations

I consider an example measurement of the position of a free mass m where a wave packet with a single photon of energy $(E = \hbar\omega)$ is reflected off of the mass (illustrated in Figure 1.10). The position of the mass can be inferred by measuring the time t it takes for the photon to leave from and return to $x = 0$, such that $x_{\mathrm{m,meas}} = ct/2$. To understand the uncertainty in this measurement, we need to consider the both the wave-like and particle-like properties of the photon wavepacket. If the wave packet has duration τ, then the uncertainty in its frequency is $\Delta\omega = 1/\tau$ and the uncertainty in its position (relative to its mean position x_{p}) is $\Delta x_{\mathrm{p}} = c\tau/2$. These relationships combine to put a Heisenberg limit on the simultaneous knowledge of the displacement x_{p} and momentum $p_{\mathrm{p}} = \hbar\omega/c$ of the photon: $\Delta p_{\mathrm{p}}\Delta x_{\mathrm{p}} \geq \hbar/2$. This Heisenberg uncertainty between the simultaneous photon position and momentum knowledge will then lead to an uncertainty in the mass' position $\Delta x_{\mathrm{m,meas}} = c\Delta t/2 = \Delta x_{\mathrm{p}}/2 = c\tau/4$. We could therefore imagine simply making the photon wave packet shorter and shorter in duration to get a more and more accurate measurement. However, this increase in sensitivity is accompanied by an increasingly strong disturbance back on the mass. Conservation of momentum $p_{\mathrm{p,i}} + p_{\mathrm{m,i}} = p_{\mathrm{p,f}} + p_{\mathrm{m,f}}$ reveals the change in momentum of the mass due
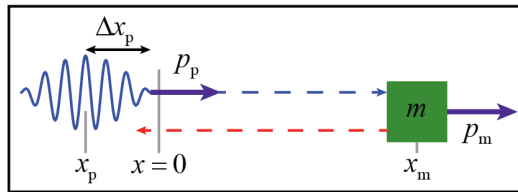
Figure 1.10: Simple scheme for position measurement. A single-photon wavepacket with instantaneous position x_{p}, position uncertainty Δx_{p}, and momentum $p_{\mathrm{p}} = \hbar\omega/c$ can be reflected off of a mass m with displacement x_{m} and momentum p_{m}. The mechanical position can be inferred by measuring the round trip time for the photon to travel from $x = 0$, reflect off the mass, and return to $x = 0$.

to the measurement: $p_{\mathrm{m,f}} - p_{\mathrm{m,i}} = (E_{\mathrm{p,i}} + E_{\mathrm{p,f}})/c \approx 2\hbar\omega/c$. Here I have assumed that the speed of the mass is much smaller than c. This momentum change of $2\hbar\omega/c$ is due to the predictable radiation pressure described in the previous section. However, an extra unknown momentum perturbation arises from the uncertainty in ω, such that $\Delta p_{\mathrm{m,perturb}} = 2\hbar/(c\tau)$. This perturbation will grow for large τ, enforcing a Heisenberg principle on measurement between the measured uncertainty in the mass's position and the backaction perturbation on momentum: $\Delta x_{\mathrm{m,meas}} \Delta p_{\mathrm{m,perturb}} \geq \hbar/2$. Note that this uncertainty principle is not the same thing as the uncertainty principle that would limit simultaneous knowledge of a mechanical oscillator's canonically conjugate quantum variables (the mass considered here was described as having a definite displacement x_{m} and position p_{m}, a completely classical description!) Instead, it is an uncertainty put on quantum measurement as a consequence of the Heisenberg uncertainty of the photon. Sometimes the backaction is attributed to the 'shot noise' of the photon, but this shot noise is also just the consequence of the photon's Heisenberg uncertainty principle. Another thing to note about this interaction is that after the measurement, the photon frequency uncertainty and the perturbation to the mass' momentum will be correlated. Therefore, measurements to demonstrate the presence of a quantum backaction force on the mass can either focus on directly observing the mass' extra momentum perturbations or on measuring correlations between perturbations of the mass' momentum and the measured light field.

I will now consider the case where the mass of interest is confined to a harmonic potential, as is the case for our optomechanics experiments. Now, perturbations of the momentum of the mass will evolve into perturbations of its position a quarter of an oscillation later. Therefore, many individual measurements averaged over many oscillations will no longer know about position and momentum separately, but rather refer to the total motion of the oscillator, which can be quantified by its energy in terms of phonon number $n_{\mathrm{m}} = E/(\hbar\Omega_{\mathrm{m}}) = kx^2/(2\hbar\Omega_{\mathrm{m}}) + p^2/(2m\hbar\Omega_{\mathrm{m}}))$. There will be a random contribution to the inference of mechanical motion due to the uncertainty in the measurements, which we call the imprecision $n_{\mathrm{m}}^{\mathrm{imp}} = \Delta n_{\mathrm{m,meas}}$ and an uncertainty in the motion due to the extra backaction fluctuations $n_{\mathrm{m}}^{\mathrm{ba}} = \Delta n_{\mathrm{m,perturb}}$. The quantities $x_{\mathrm{m,meas}}$ and $p_{\mathrm{m,perturb}}$ can be re-written

in terms of phonon number as $n_\mathrm{m}^\mathrm{imp} = k(\Delta x_\mathrm{meas})^2/(2\hbar\Omega_\mathrm{m})$ and $n_\mathrm{m}^\mathrm{ba} = (\Delta p_\mathrm{perturb})^2/(2m\hbar\Omega_\mathrm{m})$. The Heisenberg uncertainty product in terms of phonon number is then $n_\mathrm{m}^\mathrm{imp} n_\mathrm{m}^\mathrm{ba} \geq 1/16$. The minimum total uncertainty will occur when the contributions from imprecision and backaction are each equal to $1/4$, a point called the standard quantum limit, which will be discussed in more detail in the theory sections of this dissertation. Reaching this point requires a perfectly quantum efficient measurement. For a measurement employing a resonant microwave cavity, it makes sense to express the imprecision and backaction in terms of a cooperativity $\mathcal{C}$ (essentially measurement strength, proportional to the number of interrogating photons per time) rather than the variable τ above for a single photon. This gives $n_\mathrm{m}^\mathrm{imp} = 1/(16\mathcal{C})$ and $n_\mathrm{m}^\mathrm{ba} = \mathcal{C}$.

There are ways to avoid the total uncertainty limit on measurements of both quadratures of mechanical motion by using clever schemes to access only one quadrature of the motion. Most of these schemes will not be investigated in this dissertation, but I will address the concept of a backaction evasion measurement, where the mechanical motion is effectively probed at $2\Omega_\mathrm{m}$. This could be viewed as a train of many wave packets like the one above, spaced in time by $(2\Omega_\mathrm{m})^{-1}$. Then the backaction perturbations to momentum will always have returned to the momentum quadrature before the next measurement, enabling a measurement of position better than that at the standard quantum limit which introduces no extra position fluctuations due to the backaction force. Quantum backaction evasion has been investigated theoretically in references [51, 52, 53].

1.3.2   Optomechanics experiments exploring quantum backaction

The backaction motion n_m^ba imparted on a mechanical oscillator due to the interrogating electromagnetic field will be observable when that motion is comparable to the thermal motion of the oscillator n_m^th. Therefore, the important parameter for observing backaction motion in an experiment is $n_\mathrm{m}^\mathrm{ba}/n_\mathrm{m}^\mathrm{th} = \mathcal{C}/n_\mathrm{m}^\mathrm{th}$. There are currently three optomechanics experiments that have been able to observe quantum backaction by maximizing this quantity [54, 55, 56].

The first optomechanical experiment able to observe quantum backaction was reference [54], which used the collective motion of an ensemble of trapped atoms as the mechanical oscillator

coupled to the optical fields within a Fabry-Perot cavity. This experiment relied on minimizing the thermal motion of the atomic mode by employing simultaneous evaporative cooling of the atomic cloud, effectively coupling the cloud to a very cold thermal bath. The figure of merit for observing quantum backaction, $\mathcal{C}/n_{\mathrm{m}}^{\mathrm{th}} \sim 1$ was then achievable even for relatively small $\mathcal{C}$. More recently, this group also showed vacuum noise squeezing, another signature of quantum backaction [57].

The second optomechanical experiment to observe quantum backaction [55] employed a thin, megahertz frequency, dielectric membrane as the mechanical oscillator in the center of an optical Fabry-Perot resonant cavity. Unlike the cold-atom experiment, the difficulty in experiments with low-frequency mechanical oscillators is that the thermal mechanical motion is very large. In this case, it started out at $n_{\mathrm{m}}^{\mathrm{th}} = k_{\mathrm{B}}T/(\hbar\Omega_{\mathrm{m}}) = 7 \times 10^4$. Therefore, in order to observe quantum backaction, this experiment had to achieve very high cooperativity $\mathcal{C}$.

The third optomechanical experiment that observed quantum backaction [56] used a mechanically compliant photonic crystal as the optomechanical system. Rather than looking for excess mechanical motion due to radiation pressure forces, this experiment showed the presence of quantum radiation pressure by observing squeezing of vacuum noise due to correlations between the optical field fluctuations (shot noise) and the additional motional fluctuations of the mechanical oscillator.

In addition to the academic quantum measurement interests behind observing quantum backaction, the quantum limits on measurement may soon become relevant in applications of ultrasensitive measurement. The LIGO collaboration expects for their next generation experiment, advanced LIGO, to have sensitivity limited by quantum noise fluctuations over most of the frequencies of interest [58].

1.4 Macroscopic mechanical oscillators near the ground state

Preparing a macroscopic mechanical oscillator in its quantum ground state is a prerequisite for many interesting experiments for applications in quantum information as well as tests of quantum mechanics at larger and larger scales. These experiments in optomechanical systems follow in

the steps of the cold atom/ion community, which initially cooled clouds of atoms in 1978 [59, 43] and reached the ground state of motion in 1995 [44]. Since then, cold ions have been studied extensively for use in quantum information applications. Optomechanical systems have similar potential as tools for quantum information but are also capable of coupling to a more diverse set of quantum systems. Additionally, macroscopic mechanical oscillators in the quantum regime are interesting for studies of the intersection between quantum mechanics and gravity.

1.4.1   Achievements of ground state occupancy of macroscopic mechanical oscillators

The first, and widely attempted, step for optomechanical experiments employing macroscopic mechanical oscillators was to prepare the mechanical oscillator in its quantum ground state and have read-out sensitive enough to verify this ground state occupancy. There are now three experiments that have demonstrated macroscopic mechanical oscillators with occupancy less than one.

The first experiment [13] to demonstrate ground state cooling of a macroscopic mechanical oscillator uses a piezoelectric material to form the mechanical oscillator such that mechanical motion is converted to electrical signals of a microwave circuit (Figure 1.11(a)). This experiment is very
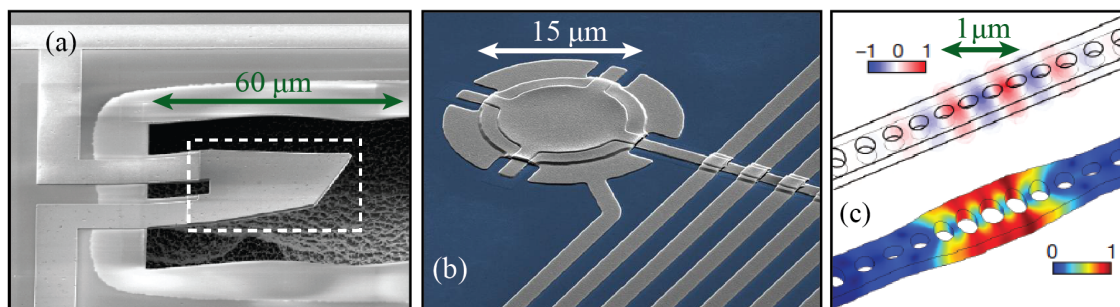
Figure 1.11: Macroscopic mechanical oscillators in the ground state. (a) Piezoelectric mechanical oscillator coupled to a superconducting microwave circuit. Image from [13], included with permission from Nature and A. N. Cleland. (b) Suspended mechanical membrane also coupled to a superconducting microwave circuit [48]. (c) Simulated optical (above) and mechanical (below) modes designed to be co-localized in a photonic-phononic crystal structure. Image from [49], included with permission from Nature and O. Painter.

different from the two that follow in that it employs a gigahertz frequency mechanical oscillator which, at the 25 mK temperature of this experiment, began with an occupation of less than 0.07 phonons. Therefore, no radiation pressure cooling needed to be used and the main advance over other systems employing high-frequency mechanical oscillators was the introduction of a coupled qubit that could sensitively read-out the state of the mechanical oscillator.

The second experiment to achieve ground state cooling [48] was also electromechanical in nature and used a suspended mechanical membrane as the upper plate of a resonant LC circuit's capacitance (Figure 1.11(b)). This mechanical oscillator has a resonant frequency of 10 MHz and therefore has an occupancy of 40 phonons even at 20 mK. Radiation pressure cooling was used to reduce the number of phonons from 40 to 0.34. The advantages over other systems of this type that allowed cooling to the ground state were the realization of superior electromechanical coupling and the use of a quantum efficient microwave interferometric readout. This details of this device and the interferometric scheme will be discussed in detail in the experimental sections of this dissertation.

The third experiment to verify mechanical occupancy less than one [49] used a nanobeam patterned with a periodic structure designed to support localized optical and mechanical modes that can couple via radiation pressure forces (Figure 1.11(c)). Optical input and output fields were coupled to this structure via evanescent coupling to a fiber taper. The mechanical resonance employed in this experiment was also in the gigahertz frequency range, but as this was an optical experiment, it was only cooled to 20 K, where the mechanical occupancy was about 100. This experiment used radiation pressure to cool the mechanical mode to 0.85 phonons. These three experiments represent an exciting first step toward the big goals of optomechanics in both the microwave and optical regimes.

1.4.2   Quantum effects in macroscopic mechanical oscillators

Cooling a mechanical oscillator to an occupancy less than one hints at the idea that it could behave quantum mechanically, but does not in itself constitute a measurement of quantum behavior. In fact, even if the mechanical oscillator behaved completely classically down to zero temperature,

a measurement of average occupation less than one would be possible. Therefore, measurements of the intrinsically quantum behavior of such an oscillator are of interest.

Perhaps the simplest indication of quantum behavior is an asymmetry of the measured mechanical sidebands. This effect can be understood by returning to the energy level diagrams used earlier in this chapter (Figure 1.12). If the optomechanical cavity is driven on resonance and the mechanical oscillator is not in its ground state (Figure 1.12(a)), the processes for adding and removing energy from the mechanical oscillator will be equally probable and the measured sidebands for these two processes will be equal in amplitude. However, if the mechanical oscillator is in its ground state (Figure 1.12(b)), extracting energy from the mechanical oscillator is forbidden. This therefore leads to an asymmetry in the sideband amplitudes which is a direct effect of the existence of a lowest energy state. It turns out (as derived in detail later in this dissertation) that the upper sideband (associated with removing energy from the mechanical oscillator) will be proportional to the mechanical occupancy n_{m}, while the lower sideband (associated with adding energy to the mechanical oscillator) will be proportional to $n_{\mathrm{m}}+1$. Derived from the quantum theory, this asymmetry of exactly one comes from the commutation relations of the mechanical field operators. It is, however, important to note that this is still a semiclassical result. If the world behaved completely classically down to zero temperature but the light field exhibited classical fluctuations with half
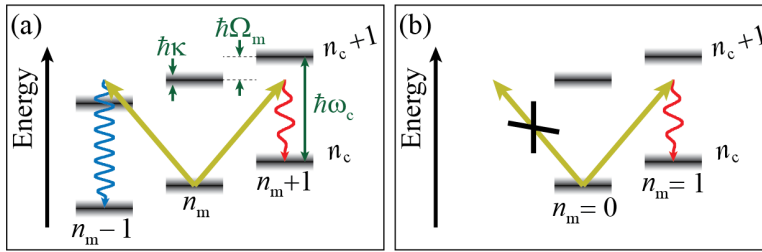
Figure 1.12: Energy level diagram of sideband asymmetry. (a) For most phonon levels, an on resonant cavity drive will excite two equally dominant processes, one each for increasing and decreasing the phonon occupation. (b) If the mechanical oscillator resides in the ground state of motion, the process for removing phonons is not allowed. This creates an imbalance in the two processes and an asymmetry in the associated sidebands.

a quantum worth of energy, the same result would arise. Nonetheless, seeing the asymmetry of exactly one suggests quantum behavior and provides a check on inferences of phonon number near the ground state. This asymmetry was first predicted [60] and demonstrated [61] in the 1980s in cold ion systems, and was used as proof that the ground state had been reached.

The first experiment with a macroscopic mechanical oscillator to observe the sideband asymmetry [62] was an extension of the third experiment highlighted for reaching the ground state above. As the mechanical oscillator in this experiment begins with an occupancy of 100 phonons, which would only present a 1% sideband asymmetry, it was cooled via radiation pressure to 2.8 quanta by applying a red-detuned cooling drive to one optical mode. They then used a much weaker readout drive applied either red or blue-detuned to a second optical mode in order to measure each sideband individually. The readout drive was made weak enough so as not to change the total radiation pressure forces present. This experiment demonstrated clear agreement with the quantum expectations for the assymmetry.

Perhaps even more impressively, the first experiment to reach ground state cooling [13], which was introduced above, was able to go far past simply observing occupancy or asymmetry suggestive of quantum behavior to being able to control that quantum behavior. This achievement was enabled by the very low thermal occupancy of the mechanical oscillator as well as its coupling to a superconducting qubit, a quantum system capable of very good quantum state preparation and manipulation. They were able to prepare the qubit with a single excitation and transfer that excitation into the mechanical oscillator, realizing a single-phonon mechanical state. This experiment demonstrated quantum control of a macroscopic mechanical oscillator unparalleled by other optomechanics experiments to date. However, the mechanical oscillator lifetime was only 6.1 ns, only slightly longer than the state transfer time and much less than typical qubit coherence times. That the mechanical oscillator is not long-lived compared to these other timescales limits the future prospects for more complicated quantum manipulation and makes investigation of other types of macroscopic mechanical oscillators with longer lifetimes still critical to the longer term goals of the field.

1.5   Quantum information applications of optomechanics

Once a macroscopic mechanical oscillator is in the quantum regime, it has the potential to be a very interesting tool for storage of quantum states as well as an intermediary between otherwise incompatible quantum systems. The history of using mechanical oscillators to store quantum states again goes back to cold ions. Quantum control over the states of these systems was realized in the 1990s [63] and this control has progressed from then to achieve quantum memories with coherence times on the order of minutes and coherent state manipulation capable of performing qubit logic gates, reviewed recently in reference [64].

Most of the optomechanics experiments presented so far (with the exception of the Cleland experiment just discussed) have employed steady-state fields to make continuous measurements of mechanical position and cool the mechanical motion to its ground state. However, as optomechanical systems move to explore quantum information applications, such as quantum state storage and coupling between different quantum systems, fast dynamical control of the optomechanical coupling will be required. In addition to the Cleland experiment, there are a few other demonstrations of dynamical control of states in optomechanical systems. Reference [18] demonstrated the ability to transfer an itinerant optical state into the mechanical oscillator, store it there, and recover the state, albeit all in the classical regime. Reference [65] swapped a signal pulse with an amplitude of a single quanta back and forth between an optical microtoroid cavity and the mechanical mode. Lastly, reference [66] demonstrates coherent state transfer between itinerant microwave fields and the mechanical oscillator at amplitudes of a single photon. This last experiment is discussed in the last experimental chapter of this dissertation.

In addition to state transfer and storage of quantum electromagnetic signals in a single optomechanical system, coherent quantum control over mechanical oscillators will open up the possibility of coupling otherwise incompatible quantum systems. For instance, proposals have been made for coupling optical and microwave systems via a mechanical oscillator [67, 68] (see Figure 1.13).
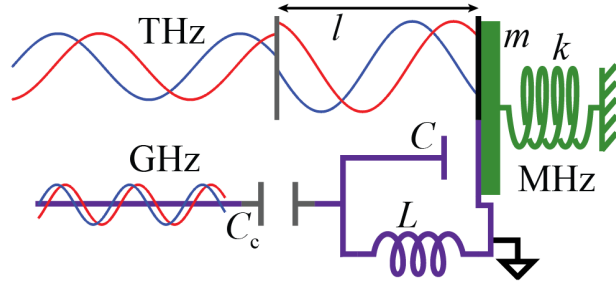
Figure 1.13: Proposed opto-electromechanical system. By coupling the motion of a mechanical oscillator to both an electrical resonator and an optical resonator, quantum information could be transferred between the GHz and THz frequency regimes.

1.6   Tests of quantum theory

As quantum mechanical effects are observed in increasingly large systems, tests of fundamental quantum theory are becoming possible. Some of these tests involve investigating increasingly complicated quantum states [69]. However, the tests that macroscopic mechanical oscillators in the quantum regime are particularly suited for are those of the interaction between quantum mechanics and gravity. As quantum objects approach larger and larger mass scales, the incompatibility between quantum mechanics and gravitational theory will eventually have to be reconciled. Various proposals about what measurements might lead to advanced understanding of the intersection between quantum mechanics and gravity have been made (see [70, 71, 72, 73] and references therein).

1.7   My contributions to the field of optomechanics

There are several important ways that my PhD work contributes to the field of optomechanics, some theoretical and some experimental.

My theoretical contributions were to extend the currently available theory to include effects that are not treated in other works. The first of these extensions, presented in Chapter 2, was to include reactive measurement port components in the model for a microwave circuit in order to correctly extract the microwave resonance parameters. This idea had previously been investigated in reference [74], but the model presented there produces different results, as discussed in Appendix

C. The second of these extensions, presented near the end of Chapter 2, was to extend the model and analysis of an optomechanical system, such as the one presented in [75], to allow excess photon noise due to the internal environment of the cavity as well as the measurement ports. This noise is often assumed to be only zero point fluctuations, as the thermal occupancy for a room temperature optical field or a dilution refrigerator microwave field is in theory zero. However, in Chapters 8.2 and 9 we observe excess cavity photons, which we model as a 'hot' internal cavity bath. The inclusion of excess cavity noise from the measurement ports in the model also makes it possible to understand the effects of excess generator or laser noise. Including both the Fano and excess cavity noise effects, I derived, the dressed cavity response and output spectral density for both a single cavity drive (Chapter 3.1, similar to [75]) and two cavity drives, one optimally red-detuned and one optimally blue-detuned (Chapter 3.1, to my knowledge this has not been done). Lastly, I worked through the problem of how to optimally shape the transfer field (which controls the coupling between the cavity and the mechanical oscillator) in order to achieve maximal transfer, storage, and retrieval efficiency of an arbitrary itinerant microwave field (Chapter 3.3).

I also contributed to the field of optomechanics through many experiments involving electromechanical systems. The first of these ([45], Chapter 8.1) showed our initial attempts at using the radiation pressure of the microwave field to cool the mechanical oscillator. For this experiment, I fabricated the device (see Chapter 5), contributed to data taking and analysis, and provided feedback on the manuscript. The second experiment ([76], Chapter 7), demonstrated our development of a quantum efficient microwave interferometer. For this experiment, I worked on the device design, fabricated the device (again see Chapter 5), contributed to data taking and analysis, and helped substantially with the manuscript. In the next experiment ([48], Chapter 8.2), we demonstrated achievement of cooling the mechanical oscillator to its quantum ground state. For this experiment, I mainly contributed to the theoretical framework necessary for analysis, as discussed above. A substantial part of my experimental time and understanding was devoted to looking for sideband asymmetry, which is detailed in Chapter 9. For this experiment, I developed the full theoretical understanding for two drive measurements and meticulously examined the complicated nature of

the calibrations required to achieve this result. The last experiment ([66], Chapter 11) showed our achievement of state transfer of coherent itinerant microwave fields to the mechanical oscillator. For this experiment, I provided experimental support and helped with the manuscript.

Chapter 2

Theory I: General mathematical formalism

The first step toward understanding the behavior of any system of interest is to find a set of equations (namely the equations of motion) that fully describe its evolution. Therefore, I devote this chapter to a very careful derivation of these equations, starting from a basic resonant circuit model of an electromechanical system. In Section 2.1, I analyze the microwave circuit used in our experiment, and then show how coupling a mechanical oscillator to the capacitive degree of freedom leads to an electromechanical coupling. In Section 2.2, I will then re-express the problem using operator formalism, which will be generally applicable to all optomechanical systems, regardless of their physical implementation in the microwave or optical regime.

2.1   Resonant circuit analysis

Our optomechanical system is formed by a mechanical oscillator in a microwave resonant circuit in such a way that mechanical motion modulates the capacitance, and therefore the resonant frequency, of the circuit. There are generally many ways to realize resonant circuits in the microwave regime: they can be made as quarter or half wave coplanar waveguides or as more lumped element series or parallel RLC circuits. They can also be coupled either inductively or capacitively to a measurement circuit. The goal of this section will be to show that it is generally possible to transform any such complex circuit network, possibly with many resonances, into a simple series RLC resonator about one of the resonances of the complex network. I will show that this is true for one specific example, the parallel RLC resonant circuit in series with a coupling capacitor.

2.1.1   Simple series RLC circuit

First, I will solve the simple RLC circuit with the foresight that the parallel RLC will be able to be simplified to a similar form. Here I find expressions for the resonant frequency and impedance looking into the series RLC circuit (Figure 2.1(a)). I have added 2's as subscripts to the circuit elements to distinguish them from similar elements in the parallel RLC circuit in Section 2.1.2.

The complex impedance of the series RLC resonant circuit is

$$Z_{\text{res}} = j\omega L_2 + \frac{1}{j\omega C_2} + R_2, \tag{2.1}$$

where $j = -\sqrt{-1} = -i$ (see Appendix B.1). At the resonant frequency of a resonant circuit, there will be equal amounts of energy stored in the electric and magnetic components. Thus, the impedance on resonance must be due only to the resistive part, which is real. Therefore, the resonance frequency is the frequency where the imaginary part of the impedance goes to 0:

$$\text{Im}[Z_{\text{res}}] = \omega L_2 - \frac{1}{\omega C_2} = 0 \quad \text{when} \quad \omega = \omega_0 = \frac{1}{\sqrt{L_2 C_2}}. \tag{2.2}$$
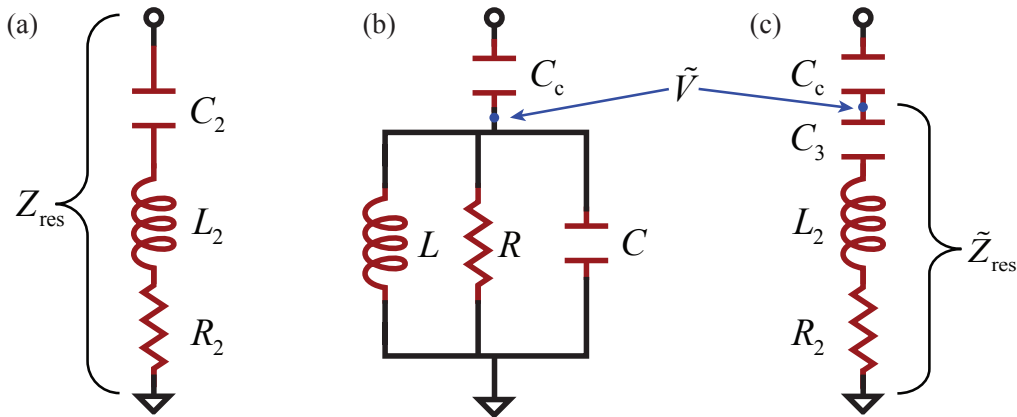
Figure 2.1: RLC models of a resonant microwave circuit. (a) Series RLC circuit. (b) Parallel RLC circuit with coupling capacitor. This is the model we generally used for our early devices. (c) Series RLC circuit with coupling capacitor taken out of C_2. For appropriate relations between the circuit elements in the parallel and the series cases, the total impedance looking into each of these circuits from their input node is Z_{res}. The impedance looking into the circuit from the node at voltage $\tilde{V}$ is $\tilde{Z}_{\text{res}}$.

I can expand the impedance to linear order about ω_0: $\omega = \omega_0 + \Delta\omega$

$$Z_{\text{res}} \approx R_2 + j\omega_0 L_2 + j\Delta\omega L_2 + \frac{1}{j\omega_0 C_2} - \frac{\Delta\omega}{j\omega_0^2 C_2} = \boxed{R_2 + 2j\Delta\omega L_2}. \tag{2.3}$$

2.1.2 Analogy of parallel RLC circuit to series RLC circuit

Finding the response of the parallel RLC circuit in series with a coupling capacitor C_{c} (Figure 2.1(b)) is more analytically complicated than the above series case, so it is helpful to simplify it by making an analogy to the series case. The resonator impedance for this circuit is

$$Z_{\text{res}} = \frac{-j}{\omega C_{\text{c}}} + \left(j\omega C + \frac{-j}{\omega L} + \frac{1}{R} \right)^{-1} \tag{2.4}$$

$$= \frac{-j}{\omega C_{\text{c}}} + \frac{j\omega L R^2(1 - \omega^2 LC)}{R^2(1 - \omega^2 LC)^2 + \omega^2 L^2} + \frac{\omega^2 L^2 R}{R^2(1 - \omega^2 LC)^2 + \omega^2 L^2} \tag{2.5}$$

$$\approx \frac{-j}{\omega C_{\text{c}}} + \frac{j\omega L}{(1 - \omega^2 LC)} + \frac{\omega^2 L^2}{R(1 - \omega^2 LC)^2}. \tag{2.6}$$

In the last step I have taken the limit of large $R \gg \omega L$ (small internal loss). For $\omega > (LC)^{-1/2}$, the second term of the impedance is negative imaginary and therefore acts like a capacitance. This capacitance adds in parallel with C_{c} and nothing special happens. However, when $\omega < (LC)^{-1/2}$, this term is positive imaginary and therefore acts like an inductance. This inductance can resonate with C_{c} at $\omega = \omega_0$:

$$\text{Im}[Z_{\text{res}}] = -\frac{1}{\omega C_c} + \frac{\omega L}{1 - \omega^2 LC} = 0 \quad \text{when} \quad \omega = \omega_0 = \frac{1}{\sqrt{L(C + C_c)}}. \tag{2.7}$$

Taylor expanding the impedance about ω_0 and keeping only terms to lowest order gives[1]:

$$Z_{\text{res}} = \frac{j\Delta\omega}{\omega_0^2 C_{\text{c}}} + \frac{j\Delta\omega L(1 + \omega_0^2 LC)}{(1 - \omega_0^2 LC)^2} + \frac{\omega_0^2 L^2}{R(1 - \omega_0^2 LC)^2} \tag{2.8}$$

$$= \frac{j\Delta\omega L(C + C_{\text{c}})}{C_{\text{c}}} + \frac{j\Delta\omega L(2C + C_{\text{c}})(C + C_{\text{c}})}{C_{\text{c}}^2} + \frac{L(C + C_{\text{c}})}{RC_{\text{c}}^2} \tag{2.9}$$

$$= \boxed{2j\Delta\omega L \frac{(C + C_{\text{c}})^2}{C_{\text{c}}^2} + \frac{L(C + C_{\text{c}})}{RC_{\text{c}}^2}}. \tag{2.10}$$

---

[1] Below, I will find that adding extra reactive components to the measurement circuit results in a Fano resonance and modifies the resonant frequency by a small amount. Therefore, I really should have expanded about the new resonant frequency, ω_{c}, instead of ω_0 here. This would make extremely minor corrections to the expressions for L_2, C_2, and R_2 depending on the Fano parameters below. However, the important part about this section was that there was a correspondence between the complex parallel circuit and the simple series RLC circuit. This will allow me to use the series RLC model to find expressions for the scattering matrix and allows extraction of the resonant frequency and damping rate. It is not important at all that I be able to exactly relate R, L, C, and C_{c} to these quantities because in practice R, L, C, and C_{c} are not known, and we would only ever care to know their approximate values.

Comparing this impedance to Equation 2.3 and the resonance frequency to Equation 2.2, I can find equivalent series components:

$$L_2 = L\left(\frac{C + C_{\mathrm{c}}}{C_{\mathrm{c}}}\right)^2, \qquad R_2 = \frac{L(C + C_{\mathrm{c}})}{RC_{\mathrm{c}}^2}, \qquad C_2 = \frac{C_{\mathrm{c}}^2}{C + C_{\mathrm{c}}}. \qquad (2.11)$$

Using reasonable values from one of our devices, $L \sim 10^{-9}$H, $C \sim 10^{-12}$F, $C_c \sim 10^{-15}$F, and $R \sim 10^6\Omega$, I find the following values for the equivalent series components: $L_2 \sim 10^{-3}$H, $C_2 \sim 10^{-18}$F, $R_2 \sim 10^3\Omega$.

2.1.3 External coupling to measurement

In order to drive or read out a microwave resonant circuit, we must couple it to external measurement lines. Typically, this involves adding one port (in a reflection geometry) or two ports (in a transmission geometry), each with impedance Z_0. Adding only these ports will result in a purely Lorentzian response of the circuit. However, we sometimes see in experiments that the circuit has a Fano resonant response rather than a Lorentzian. One example of such a resonance can be found in Appendix C. A Fano resonance is generally due to the interference between a Lorentzian resonance and a background standing wave. I attribute this to the presence of reactive components between the measurement ports and the resonant circuit. These components can set up an interference between standing waves in the measurement lines and the circuit response, resulting in a non-Lorentzian resonance at the output of the experiment.

I attribute the extra reactance observed to different effects for the transmission and reflection geometries. In the transmission geometry, the extra reactance in likely from parasitic inductance of the wire bonds between our sample and the external microwave lines, as has also been assumed in [74]. I can model this as some frequency-independent reactance BZ_0 associated with each line (see Figure 2.2(a)). In the reflection geometry, wire bonds alone cannot account for the Fano resonance (they would just modify the resonance frequency). However, there can be a Fano shape if there is some power being coupled out of the resonator through a very small capacitor to another invisible 'port'. This has indeed been observed in some of our experiments where resonances on one side of
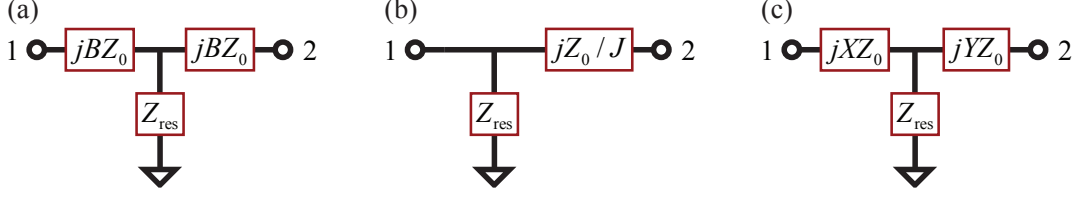
Figure 2.2: Resonant circuit coupled to measurement ports, including sources of Fano interference effects. (a) The transmission measurement model includes small reactive components coupling the resonator to each port. (b) The reflection measurement model includes a very large reactive component coupling the resonator to a second 'port'. (c) These two situations can be thought of as limiting cases of a more general model with reactive components XZ_0 and YZ_0.

a chip are visible from another, seemingly disconnected, port on the other side of the chip. I can model this power leakage by coupling the system to a second port through a very large frequency-independent reactance Z_0/J, where J is small (see Figure 2.2(b)). The two geometries can thus be treated as two limiting cases of the more general geometry in Figure 2.2(c):

Case 1: $X = Y = B$ Transmission geometry including wire bonds,

Case 2: $X = 0,\ Y = 1/J$ Reflection geometry with weakly coupled invisible 'port'.

Here, B and J are 0 in the absence of the above effects and can be positive or negative. In our experiments we typically measure $|B| < 1$.

2.1.4   Voltage response of circuit

In an electromechanical experiment, the quantity of interest is the motion of a mechanical oscillator which varies the capacitance C of a parallel RLC circuit. The only thing that this mechanical oscillator can truly care about is the voltage $\tilde{V}$ across that capacitor (Figure 2.1(b)) (this statement is verified in Appendix C). Therefore, the equivalent series circuit found above is not completely adequate as a model of the system because it does not have access to the necessary node. However, I can make a small modification to it by modeling the capacitor C_2 as two series capacitors: the real capacitor C_c and another capacitor $C_3 = C_\mathrm{c}C_2/(C_\mathrm{c} - C_2)$ (see Figure 2.1(c)).
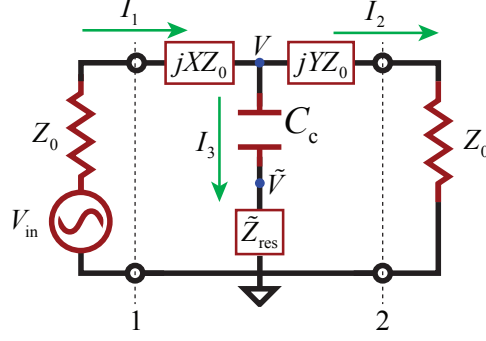
Figure 2.3: Full circuit model including measurement ports. An applied voltage V_{in} from port 1 of the circuit will result in a response of the voltage $\tilde{V}$ across the capacitor.

The impedance looking into the circuit from the point with voltage $\tilde{V}$ is then

$$\tilde{Z}_{\text{res}} \approx \frac{j\omega L}{(1 - \omega^2 LC)} + \frac{\omega^2 L^2}{R(1 - \omega^2 LC)^2}. \tag{2.12}$$

Expanding once again about ω_0 and keeping terms to leading order gives

$$\tilde{Z}_{\text{res}} \approx \frac{j\omega_0 L}{(1 - \omega_0^2 LC)} + \frac{\omega_0^2 L^2}{R(1 - \omega_0^2 LC)^2} = \frac{j}{\omega_0 C_{\text{c}}} + R_2. \tag{2.13}$$

Using the full model of the circuit and measurement in Figure 2.3, the voltage $\tilde{V}$ can be found in terms of the driving voltage V_{in} from port 1 by solving the following equations and doing basic circuit algebra:

$$I_1 = I_2 + I_3, \qquad \tilde{V} = I_3 \tilde{Z}_{\text{res}}, \qquad V = I_3 Z_{\text{res}} = I_2 Z_2 = V_{\text{in}} - I_1 Z_1, \tag{2.14}$$

where I define $Z_1 \equiv Z_0(1 + jX)$ and $Z_2 \equiv Z_0(1 + jY)$. Solving these equations to eliminate I_1, I_2, and I_3 gives

$$\frac{\tilde{V}}{V_{\text{in}}} = \frac{\tilde{Z}_{\text{res}} Z_2}{Z_{\text{res}}(Z_1 + Z_2) + Z_1 Z_2} = \frac{\tilde{Z}_{\text{res}} Z_2}{Z_1 + Z_2}\left(Z_{\text{res}} + \frac{Z_1 Z_2}{Z_1 + Z_2}\right)^{-1}, \tag{2.15}$$

$$Z_{\text{res}} + \frac{Z_1 Z_2}{Z_1 + Z_2} = R_2 + 2j\Delta\omega L_2 + \frac{Z_1 Z_2}{Z_1 + Z_2} = 2L_2\left(\frac{\kappa}{2} + j(\omega - \omega_{\text{c}})\right) = \frac{2L_2}{\chi_{\text{c}}[\omega]}, \tag{2.16}$$

$$\frac{\tilde{V}}{V_{\text{in}}} = \frac{\tilde{Z}_{\text{res}} Z_2}{2L_2(Z_1 + Z_2)}\chi_{\text{c}}[\omega]. \tag{2.17}$$

The cavity displays a Lorentzian response with resonant frequency $\omega_{\text{c}} = \omega_0 - \text{Im}[Z_1 Z_2/(Z_1 + Z_2)]/(2L_2)$, total loss rate $\kappa = (R_2 + \text{Re}[Z_1 Z_2/(Z_1 + Z_2)])/L_2$, internal loss rate $\kappa_0 = R_2/L_2$, and

external loss rate $\kappa_{\text{ext}} = \text{Re}[Z_1 Z_2/(Z_1 + Z_2)]/L_2 = Z_0(|Z_1|^2 + |Z_2|^2)/(L_2|Z_1 + Z_2|^2)$. I can divide up the external coupling into separate couplings for the left and right ports, $\kappa_l = Z_0|Z_2|^2/(L_2|Z_1 + Z_2|^2)$ and $\kappa_r = Z_0|Z_1|^2/(L_2|Z_1 + Z_2|^2)$. I have written the response in terms of the cavity susceptibility $\chi_c[\omega]$. The addition of reactive components to the feed line changes the frequency at which $\tilde{V}$ has the largest response. Therefore, effects of optomechanical coupling should be centered around ω_c rather than ω_0 (see Appendix C). Note that, while significant for optomechanical effects, this change in resonance frequency is not large enough to invalidate the previous assumption that a parallel RLC circuit can be modeled as a series RLC circuit near resonance (see previous footnote). I also define a quantity $c_{\text{in}} \equiv V_{\text{in}}\tilde{Z}_{\text{res}}Z_2/(2L_2(Z_1 + Z_2))$ for convenience, such that $\tilde{V}[\omega]/c_{\text{in}}[\omega] = \chi_c[\omega]$.

2.1.5 Energy stored in the circuit

Here I find the energy stored in the circuit in terms of the cavity parameters and the input power sent into port 1 of the network. I assume that the input voltage has the form

$$V_{\text{in}}[t] = \text{Re}\left[\check{V}_{\text{in}}[t]\right] = \text{Re}\left[V_0[t]e^{j\omega t}\right], \tag{2.18}$$

where V_0 is complex and I could generalize this to be a sum over many frequencies if there were multiple inputs. I assume that $V_0[t]$ changes slowly compared to the exponential component: $\dot{V}_0 \ll j\omega V_0$. This allows me to write the input power (or available power) as

$$P_{\text{in}} = \frac{V_{\text{in}}[t]^2}{4Z_0} = \frac{\text{Re}\left[\check{V}_{\text{in}}[t]\right]^2}{4Z_0} = \frac{V_0[t]^2 e^{2j\omega t} + V_0^*[t]^2 e^{-2j\omega t} + 2|V_0[t]|^2}{16Z_0} \approx \frac{|V_0[t]|^2}{8Z_0} = \frac{|\check{V}_{\text{in}}[t]|^2}{8Z_0}, \tag{2.19}$$

where I have eliminated the quickly oscillating terms. The assumption that $\dot{V}_0 \ll j\omega V_0$ also allows me to use impedances to go between the scooped voltages and currents, even though I am working in the time domain. This is illustrated by a calculation of the current through a capacitor with voltage V_{in} across it:

$$I[t] = \text{Re}\left[\check{I}[t]\right] = \text{Re}\left[C\dot{V}_0[t]e^{j\omega t} + j\omega C V_0[t]e^{j\omega t}\right] \approx \text{Re}\left[j\omega C V_0[t]e^{j\omega t}\right] = \text{Re}\left[j\omega C \check{V}_{\text{in}}[t]\right]. \tag{2.20}$$

The energy stored in the circuit near resonance is then

$$E[t] \;=\; 2\left(\frac{1}{2}L_2 I_3[t]^2\right) \approx \frac{L_2}{2}\left|\breve{I}_3[t]\right|^2 = \frac{L_2}{2}\left|\frac{\breve{V}[t]}{\tilde{Z}_{\mathrm{res}}}\right|^2 \tag{2.21}$$

$$=\; \frac{|\breve{V}_{\mathrm{in}}[t]|^2}{8L_2}\frac{|Z_2|^2}{|Z_1+Z_2|^2}\left|\frac{\breve{V}[t]}{\breve{c}_{\mathrm{in}}[t]}\right|^2 = P_{\mathrm{in}}\kappa_{\mathrm{l}}\left|\frac{\breve{V}[t]}{\breve{c}_{\mathrm{in}}[t]}\right|^2. \tag{2.22}$$

If the circuit is driven at only one frequency ω, the energy stored in the circuit will be $E[t] = P_{\mathrm{in}}\kappa_{\mathrm{l}}|\chi_{\mathrm{c}}[\omega]|^2$.

2.1.6   The scattering matrix

I have calculated how the voltage across the capacitor and the energy stored in the circuit depend on all of the circuit parameters. However, the quantity actually measured in an experiment is the output microwave field. This is related to the input microwave field through the scattering matrix (or S matrix)[77]:

$$[V_{\mathrm{out}}] = [S][V_{\mathrm{in}}], \qquad S_{ik} = \frac{V_{i,\mathrm{out}}}{V_{j,\mathrm{in}}} \quad (V_{k,\mathrm{in}} = 0 \text{ for } k \neq j). \tag{2.23}$$

I could just calculate the S-matrix by brute force. However, there is an equivalence trick that makes this simpler. This trick uses the impedance matrix:

$$[V] = [Z][I], \qquad Z_{ik} = \frac{V_i}{I_k} = \frac{V_{i,\mathrm{in}} + V_{i,\mathrm{out}}}{I_{k,\mathrm{in}} + I_{k,\mathrm{out}}} \quad (I_k = 0 \text{ for } k \neq j). \tag{2.24}$$

For a 2-port reciprocal network such as the one of interest here, the circuit can be compared to a T-equivalent circuit (Figure 2.4) to identify the elements of the impedance matrix. For our model,
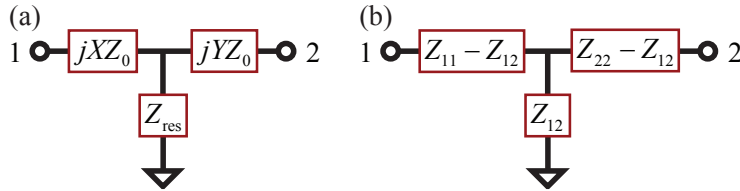
Figure 2.4: T-equivalent circuit representation. (a) Our circuit of interest. (b) The impedance matrix for our circuit can be easily found by comparing to the T-equivalent circuit.

this gives

$$Z_{12} = Z_{\text{res}}, \tag{2.25}$$

$$Z_{11} = jXZ_0 + Z_{\text{res}} = Z_{\text{res}} + Z_1 - Z_0, \tag{2.26}$$

$$Z_{22} = jYZ_0 + Z_{\text{res}} = Z_{\text{res}} + Z_2 - Z_0. \tag{2.27}$$

The S-matrix is then related to the impedance matrix by the expressions [77]

$$S_{21} = \frac{2Z_{21}Z_0}{\Delta Z}, \qquad S_{11} = \frac{(Z_{11} - Z_0)(Z_{22} + Z_0) - Z_{12}Z_{21}}{\Delta Z}, \tag{2.28}$$

$$\Delta Z \equiv (Z_{11} + Z_0)(Z_{22} + Z_0) - Z_{12}Z_{21}. \tag{2.29}$$

For our model, the scattering elements are then

$$
\begin{aligned}
S_{21}[\omega_{\text{p}}] &= \frac{2Z_{\text{res}}Z_0}{Z_{\text{res}}(Z_1 + Z_2) + Z_1 Z_2} & (2.30) \\
&= \frac{(Z_1^* + Z_2^*)\sqrt{Z_1 Z_2}}{(Z_1 + Z_2)\sqrt{Z_1^* Z_2^*}} \left(\frac{2Z_0}{Z_1^* + Z_2^*} \sqrt{\frac{Z_1^* Z_2^*}{Z_1 Z_2}} - \frac{Z_0|Z_1||Z_2|}{L_2|Z_1 + Z_2|^2} \frac{\tilde{V}[\omega_{\text{p}}]}{c_{\text{in}}[\omega_{\text{p}}]} \right) & (2.31) \\
&= \frac{(Z_1^* + Z_2^*)\sqrt{Z_1 Z_2}}{(Z_1 + Z_2)\sqrt{Z_1^* Z_2^*}} \left(N_2 - \sqrt{\kappa_{\text{l}}\kappa_{\text{r}}} \frac{\tilde{V}[\omega_{\text{p}}]}{c_{\text{in}}[\omega_{\text{p}}]} \right), & (2.32) \\
S_{11}[\omega_{\text{p}}] &= \frac{Z_{\text{res}}(Z_1 + Z_2 - 2Z_0) + Z_2(Z_1 - 2Z_0)}{Z_{\text{res}}(Z_1 + Z_2) + Z_1 Z_2} & (2.33) \\
&= \frac{Z_2(Z_1^* + Z_2^*)}{Z_2^*(Z_1 + Z_2)} \left(\frac{Z_2^*(Z_1 + Z_2 - 2Z_0)}{Z_2(Z_1^* + Z_2^*)} - \frac{Z_0|Z_2|^2}{L_2|Z_1 + Z_2|^2} \frac{\tilde{V}[\omega_{\text{p}}]}{c_{\text{in}}[\omega_{\text{p}}]} \right) & (2.34) \\
&= \frac{Z_2(Z_1^* + Z_2^*)}{Z_2^*(Z_1 + Z_2)} \left(N_1 - \kappa_{\text{l}} \frac{\tilde{V}[\omega_{\text{p}}]}{c_{\text{in}}[\omega_{\text{p}}]} \right). & (2.35)
\end{aligned}
$$

In both of these calculations, I have pulled out a factor of magnitude one in front of the expression. This factor will only add an overall phase offset to the scattering matrix, which we do not care about. Ignoring these prefactors, both terms of the scattering matrix can be written as one equation with index i:

$$\boxed{S_{i1}[\omega_{\text{p}}] = N_i - \sqrt{\kappa_{\text{l}}\kappa_{\text{i}}} \frac{V[\omega_{\text{p}}]}{c_{\text{in}}[\omega_{\text{p}}]}.} \tag{2.36}$$

In the past few expressions, N_i is a complex coefficient which stores information about any reactive components in the feed line and is also the value of the response far off-resonance. The values of

N_i for our two measurement models are

$$N_1 = \tfrac{jB}{1+jB}, \qquad N_2 = \frac{1}{1+jB}, \qquad \text{for the transmission geometry} \qquad (2.37)$$

$$N_1 = \tfrac{1+jJ}{1+jJ+2J^2}, \qquad N_2 = \frac{2J\sqrt{1+J^2}}{1+jJ+2J^2}, \qquad \text{for the reflection geometry.} \qquad (2.38)$$

If the circuit is driven at only one frequency, the response is that of a Fano resonance,

$$\boxed{S_{i1}[\omega_\mathrm{p}] = N_i - \sqrt{\kappa_\mathrm{l}\kappa_\mathrm{i}}\chi_\mathrm{c}[\omega]}. \qquad (2.39)$$

In the cases of $B = 0$ or $J = 0$, the response resumes a Lorentzian form.

2.1.7 Optomechanics introduced

I now consider the effect of the mechanical element, which modulates the capacitor C and thus the resonance frequency of the circuit. There is a force $F[t] = -\partial E[t]/\partial x$, sometimes referred to as the 'radiation pressure force' in analogy to the optical world, exerted on the mechanical element due to the voltage across the capacitor. When the mechanical oscillator moves infinitesimally, the charge on the capacitor plate stays constant, while the voltage changes. Therefore, I must find the derivative of energy with respect to C with the charge Q fixed:

$$F[t] \;=\; -\frac{\partial E}{\partial x} = -\frac{\partial}{\partial x}\left(\frac{Q^2}{2C}\right) = -\left(\frac{\partial \omega_\mathrm{c}}{\partial C}\right)^{-1}\frac{\partial \omega_\mathrm{c}}{\partial x}\frac{\partial}{\partial C}\left(\frac{Q^2}{2C}\right) \qquad (2.40)$$

$$\;=\; \left(\frac{-2(C+C_\mathrm{c})}{\omega_\mathrm{c}}\right) G\frac{Q^2}{2C^2} \approx \frac{-E[t]G}{\omega_\mathrm{c}} = \boxed{-\hbar G n_\mathrm{c}[t]}. \qquad (2.41)$$

Here, $G \equiv \partial \omega_\mathrm{c}/\partial x$ is the coupling constant between the cavity and mechanical oscillator and $n_\mathrm{c} = E/(\hbar\omega_\mathrm{c})$ is the number of photons in the cavity.

I can Fourier transform the force into the frequency domain (see Appendices B.1 and B.3 about Fourier transform definitions and convolutions):

$$F[t] \;=\; \frac{-GL_2}{\omega_\mathrm{c}}|\tilde{Z}_\mathrm{res}|^2|\tilde{V}[t]|^2 = -\hbar G\beta|\tilde{V}[t]|^2, \qquad (2.42)$$

$$F[\omega] \;=\; -\hbar G\beta \int_{-\infty}^{\infty} \tilde{V}[t]\tilde{V}^*[t]e^{-j\omega t}dt = -\hbar G\beta\tilde{V}[\omega] * \tilde{V}^*[-\omega]. \qquad (2.43)$$

The constants out front are just absorbed into β. This force causes a displacement $x[\omega] = \chi[\omega]F[\omega]$ where, for an oscillator with mass m, resonant frequency Ω_m, and damping Γ_m, the susceptibility is

$\chi[\omega] = [m(\Omega_{\mathrm{m}}^2 - \omega^2 + j\omega\Gamma_{\mathrm{m}})]^{-1}$. Note that this susceptibility is related to the mechanical suscepti-bility $\chi_{\mathrm{m}}^{-1}[\omega] = \Gamma_{\mathrm{m}}/2 + j(\omega - \Omega_{\mathrm{m}})$, which I will use throughout the majority of this dissertation, by $\chi[\omega] \approx (\chi_{\mathrm{m}}[\omega] - \chi_{\mathrm{m}}^*[-\omega])/(2jm\Omega_{\mathrm{m}})$. The mechanical motion due to this force then couples to the microwave frequency such that $\omega_{\mathrm{c}} \to \omega_{\mathrm{c}} + Gx[\omega]$. This modifies how the voltage inside the cavity relates to the voltage drive by convolving $\tilde{V}$ with x:

$$
\begin{aligned}
c_{\mathrm{in}}[\omega] &= \left(\frac{\kappa}{2} + j(\omega - \omega_{\mathrm{c}})\right)\tilde{V}[\omega] - jGx[\omega] * \tilde{V}[\omega] && (2.44) \\
&= \frac{\tilde{V}[\omega]}{\chi_{\mathrm{c}}[\omega]} + j\hbar G^2\beta\left(\chi[\omega]\left(\tilde{V}[\omega] * \tilde{V}^*[-\omega]\right)\right) * \tilde{V}[\omega]. && (2.45)
\end{aligned}
$$

In theory, this equation should provide a solution for $\tilde{V}$, allowing me to find the cavity response at any frequency, given any arbitrary drive $c_{\mathrm{in}}[\omega]$. Indeed, I have used this equation to derive the response of the circuit optomechanical system in the presence of both one and two large drives. It is important to realize this ability because it stresses the fact that the cavity optomechanical response is a completely classical effect. I will not present this here as the derivation is rather complicated with all of the convolutions and is much simpler using the quantized operator formalism that follows. However, I do want to stress that although I use quantum formalism to derive the dressed response in the following chapters, this quantity is fully contained in the classical equations of motion describing an LC resonant circuit coupled to a mechanical oscillator.

2.2 Operator formalism and derivation of equations of motion

So far, I have worked completely in the circuit notation of voltages and currents. However, it is helpful going forward to change to the canonical quantization representation of these equations, in part for notational simplicity, and in part because I will eventually be interested in quantum effects. Also note that as soon as I describe the electromechanical system in terms of operators, it will be completely mathematically equivalent to any optomechanical system in the optical regime. I will therefore switch at that point from calling the microwave circuit a 'circuit' to calling it a 'cavity'.

2.2.1   Canonical quantization

The classical series RLC circuit energy can be written in terms of the voltage V_{C_2} across the capacitor C_2 and the current I_3 through the inductor L_2 (also the current through C_2) or in terms of the charge Q on the capacitor:

$$E_{\text{circuit}} = \frac{L_2}{2} I_3[t]^2 + \frac{C_2}{2} V_{C_2}[t]^2 = \frac{L_2 \dot{Q}[t]^2}{2} + \frac{Q[t]^2}{2C_2}. \tag{2.46}$$

The Lagrangian of this system is then the kinetic part of the energy minus the potential part:

$$\mathcal{L}_{\text{circuit}} = \frac{L_2 \dot{Q}[t]^2}{2} - \frac{Q[t]^2}{2C_2}, \qquad \frac{\partial \mathcal{L}_{\text{circuit}}}{\partial \dot{Q}[t]} = L_2 \dot{Q}[t] = \phi[t]. \tag{2.47}$$

The canonical momentum is ϕ, the magnetic flux through the inductor. The classical Hamiltonian is

$$\mathcal{H}_{\text{circuit}} = \frac{\phi[t]^2}{2L_2} + \frac{Q[t]^2}{2C_2}. \tag{2.48}$$

To find the quantum Hamiltonian, I can just write these canonically conjugate classical variables as quantum operators which obey the canonical commutation relation:

$$\hat{\mathcal{H}}_{\text{cavity}} = \frac{\hat{\phi}^2}{2L_2} + \frac{\hat{Q}^2}{2C_2}, \qquad \left[\hat{Q}, \hat{\phi}\right] = -j\hbar. \tag{2.49}$$

Going further, I define lowering and raising operators $\hat{a}$ and $\hat{a}^\dagger$:

$$\hat{a}, \hat{a}^\dagger = \sqrt{\frac{L_2 \omega_c}{2\hbar}} \hat{Q} \mp j \sqrt{\frac{1}{2L_2 \omega_c \hbar}} \hat{\phi}, \qquad \left[\hat{a}, \hat{a}^\dagger\right] = \frac{-j}{\hbar}\left[\hat{\phi}, \hat{Q}\right] = 1, \tag{2.50}$$

$$\hat{\mathcal{H}}_{\text{cavity}} = -\frac{\hbar \omega_c}{4}(\hat{a} - \hat{a}^\dagger)^2 + \frac{\hbar}{4L_2 C_2 \omega_c}(\hat{a} + \hat{a}^\dagger)^2 = \boxed{\hbar \omega_c \left(\hat{a}^\dagger \hat{a} + \frac{1}{2}\right)}. \tag{2.51}$$

These operators are normalized such that $\hat{a}^\dagger \hat{a} = \hat{n}_c$, the photon number operator. I also define input and output raising and lowering operators, such that $\hat{a}^\dagger_{\text{in(out)}} \hat{a}_{\text{in(out)}} = P_{\text{in(out)}}/(\hbar \omega_c)$. I can then write the cavity response in terms of the operators:

$$\frac{\hat{\tilde{V}}}{\hat{c}_{\text{in}}} = \left(\tilde{Z}_{\text{res}} \sqrt{\frac{\hbar \omega_c}{L_2}} \hat{a}\right) \Big/ \left(\tilde{Z}_{\text{res}} \frac{\sqrt{\hbar \omega_c Z_0}|Z_2|}{L_2|Z_1 + Z_2|} \hat{a}_{\text{in}}\right) = \frac{\sqrt{L_2}|Z_1 + Z_2|}{\sqrt{Z_0}|Z_2|} \frac{\hat{a}}{\hat{a}_{\text{in}}} = \frac{1}{\sqrt{\kappa_l}} \frac{\hat{a}}{\hat{a}_{\text{in}}}, \tag{2.52}$$

$$\boxed{S_{i1}[\omega_p] = N_i - \sqrt{\kappa_i} \frac{\hat{a}[\omega_p]}{\hat{a}_{\text{in}}[\omega_p]}}. \tag{2.53}$$

I can quantize the mechanical oscillator using raising and lowering operators in a very similar manner to the cavity:

$$\hat{b}, \hat{b}^\dagger = \sqrt{\frac{m\omega_{\mathrm{m}}}{2\hbar}}\hat{x} \mp j\sqrt{\frac{1}{2m\hbar\omega_{\mathrm{m}}}}\hat{p}, \qquad \left[\hat{b}, \hat{b}^\dagger\right] = \frac{-j}{\hbar}\left[\hat{x}, \hat{p}\right] = 1, \tag{2.54}$$

$$\hat{\mathcal{H}}_{\mathrm{mech}} = \frac{\hat{p}^2}{2m} + \frac{m\omega_{\mathrm{m}}^2 \hat{x}^2}{2} = \frac{-\hbar\omega_{\mathrm{m}}}{4}(\hat{b} - \hat{b}^\dagger)^2 + \frac{\hbar\omega_{\mathrm{m}}}{4}(\hat{b} + \hat{b}^\dagger)^2 \tag{2.55}$$

$$= \frac{1}{2}\hbar\omega_{\mathrm{m}}(\hat{b}\hat{b}^\dagger + \hat{b}^\dagger\hat{b}) = \boxed{\hbar\omega_{\mathrm{m}}\left(\hat{b}^\dagger\hat{b} + \frac{1}{2}\right)}. \tag{2.56}$$

An interaction term in the Hamiltonian comes from modifying the cavity resonance frequency in the cavity Hamiltonian:

$$\hbar\omega_{\mathrm{c}}\left(\hat{a}^\dagger\hat{a} + \frac{1}{2}\right) \rightarrow \hbar\left(\omega_{\mathrm{c}} + G\hat{x}\right)\left(\hat{a}^\dagger\hat{a} + \frac{1}{2}\right) \tag{2.57}$$

$$= \hbar\omega_{\mathrm{c}}\left(\hat{a}^\dagger\hat{a} + \frac{1}{2}\right) + \hbar g_0 \left(\hat{b} + \hat{b}^\dagger\right)\left(\hat{a}^\dagger\hat{a} + \frac{1}{2}\right) \tag{2.58}$$

$$= \hat{\mathcal{H}}_{\mathrm{cavity}} + \hat{\mathcal{H}}_{\mathrm{interaction}}. \tag{2.59}$$

Here, $G = d\omega_{\mathrm{c}}/dx$, the mechanical zero point motion is $x_{\mathrm{zp}} = \sqrt{\hbar/2m\omega_{\mathrm{m}}}$, and $g_0 = Gx_{\mathrm{zp}}$ is the single photon coupling rate. The full system Hamiltonian is then

$$\hat{\mathcal{H}}_{\mathrm{system}} = \hat{\mathcal{H}}_{\mathrm{cavity}} + \hat{\mathcal{H}}_{\mathrm{mech}} + \hat{\mathcal{H}}_{\mathrm{interaction}} \tag{2.60}$$

$$= \boxed{\hbar\omega_{\mathrm{c}}\left(\hat{a}^\dagger\hat{a} + \frac{1}{2}\right) + \hbar\omega_{\mathrm{m}}\left(\hat{b}^\dagger\hat{b} + \frac{1}{2}\right) + \hbar g_0 \left(\hat{b} + \hat{b}^\dagger\right)\left(\hat{a}^\dagger\hat{a} + \frac{1}{2}\right)}. \tag{2.61}$$

2.2.2 Operator model including noise and external cavity inputs

Both the cavity and mechanical oscillator dissipate energy to the external environment. The cavity can dissipate energy to three different ports: the left measurement port, the right measurement port, and the internal port (this is the energy dissipated in the resistor). The dissipation rates to each port are κ_{l}, κ_{r}, and κ_0. The total cavity loss rate is $\kappa = \kappa_{\mathrm{l}} + \kappa_{\mathrm{r}} + \kappa_0$. The mechanical oscillator's dissipation is characterized by rate Γ_{m}. The fluctuation dissipation theorem states that any port with dissipation necessarily has fluctuations associated with it. These fluctuations are minimally quantum noise but in general could be thermal states, so I will model them as such. I will therefore assign a thermal noise operator $\hat{\xi}_i$ to each of the ports, where $i \in \{\mathrm{l}, \mathrm{r}, 0, \mathrm{m}\}$ for the left
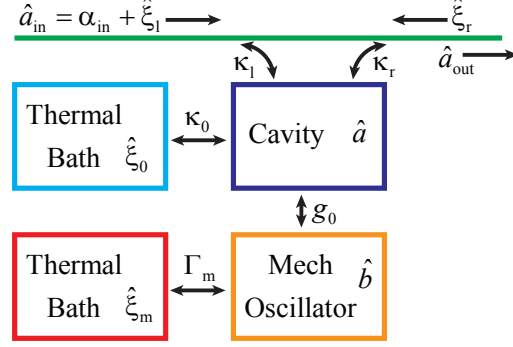
Figure 2.5: Operator model of an optomechanical system. The cavity, described by operator $\hat{a}$, is coupled to a mechanical oscillator, described by operator $\hat{b}$, via single photon coupling rate g_0. The cavity is coupled to two measurement ports and an internal 'port', or thermal reservoir, while the mechanical oscillator is only coupled to a thermal reservoir. Each of these ports is described by an operator $\hat{\xi}_i$ and has dissipation rate κ_i (or Γ_{m}). The input fields $\hat{a}_{\mathrm{in}}$ always enter from the left port. For the transmission geometry, the output field of interest $\hat{a}_{\mathrm{out}}$ is the one at the right port (as is shown).

feed line port, right feed line port, cavity thermal bath, and mechanical thermal bath, respectively (see Figure 2.5). The expectation values for the bath operators are

$$\left\langle \hat{\xi}_i^\dagger[t]\hat{\xi}_{i'}[t'] \right\rangle = n_i^{\mathrm{th}}\delta_{i,i'}\delta[t-t'] \qquad \text{and} \qquad \left\langle \hat{\xi}_i[t]\hat{\xi}_{i'}^\dagger[t'] \right\rangle = (n_i^{\mathrm{th}}+1)\delta_{i,i'}\delta[t-t'], \qquad (2.62)$$

where n_i^{th} is the thermal occupancy number of the bath. Note that if at any point in my calculations I set all of the bath temperatures to zero, I will recover the quantum results. The input field $\hat{a}_{\mathrm{in}}$ will be defined to be always incident from the left and include both a large classical driving field α_{in} and the noise operator $\hat{\xi}_{\mathrm{l}}$. The output field $\hat{a}_{\mathrm{out}}$ will be defined to always be to the right for the transmission geometry and always to the left in the reflection geometry. Similar models have been used to describe an optomechanical system elsewhere, such as in [75], but they often assume that the thermal occupation of the photon baths is zero ($n_{\mathrm{l}}^{\mathrm{th}} = n_{\mathrm{r}}^{\mathrm{th}} = n_0^{\mathrm{th}}$). This is not necessarily a bad choice, as the thermal occupancy for both optical fields at room temperature and microwave fields at dilution refrigerator temperatures are theoretically negligible. However, in our experiments we sometimes observe excess cavity noise that we choose to model as an elevated temperature of the cavity bath. Allowing all of the noise baths to generally be at nonzero temperature allows us to

include this effect and other possible ones (such as excess generator/laser noise). The extended analysis of what happens when these baths are not set to zero is one of the most important contributions I have made during my PhD.

2.2.3   Heisenberg-Langevin equations

I will now show how I can include the thermal baths into the Hamiltonian, resulting in a Langevin equation of motion (following [78, Chapter 7]). In order to include the thermal bath for the cavity directly in the Hamiltonian, I need to model it as a set of harmonic oscillators at all frequencies, represented by operators $\hat{d}[\omega, t]$ coupled to the cavity via coupling constant $\mu[\omega]$:

$$\hat{\mathcal{H}} = \hat{\mathcal{H}}_{\text{system}} + \hat{\mathcal{H}}_{\text{bath}} + \hat{\mathcal{H}}_{\text{sys}-\text{bath}}, \tag{2.63}$$

$$\hat{\mathcal{H}}_{\text{bath}}[t] = \hbar \int_{-\infty}^{\infty} \hbar\omega \left(\hat{d}^{\dagger}[\omega, t]\hat{d}[\omega, t] + \frac{1}{2} \right) d\omega, \tag{2.64}$$

$$\hat{\mathcal{H}}_{\text{sys}-\text{bath}}[t] = -j\hbar \int_{-\infty}^{\infty} \mu[\omega] \left(\hat{d}[\omega, t]\hat{a}^{\dagger}[t] - \hat{a}[t]\hat{d}^{\dagger}[\omega, t] \right) d\omega, \tag{2.65}$$

$$\left[\hat{d}[\omega, t], \hat{d}^{\dagger}[\omega', t'] \right] = \delta[\omega - \omega']\delta[t - t']. \tag{2.66}$$

The Heisenberg equations for the $\hat{d}$'s and $\hat{a}$ are

$$\dot{\hat{d}}[\omega, t] = \frac{j}{\hbar} \left[\hat{d}[\omega, t], \hat{\mathcal{H}}[t] \right] = j\omega\hat{d}[\omega, t] - \mu[\omega]\hat{a}[t], \tag{2.67}$$

$$\dot{\hat{a}}[t] = \frac{j}{\hbar} \left[\hat{a}[t], \hat{\mathcal{H}}[t] \right] = \frac{j}{\hbar} \left[\hat{a}[t], \hat{\mathcal{H}}_{\text{system}}[t] \right] + \int_{-\infty}^{\infty} \mu[\omega]\hat{d}[\omega, t]d\omega. \tag{2.68}$$

Solving for the $\hat{d}$ equations and substituting back in to the $\hat{a}$ equation, I get

$$\hat{d}[\omega, t] = e^{j\omega(t-t_0)}\hat{d}[\omega, t_0] - \mu[\omega] \int_{t_0}^{t} e^{j\omega(t-t')}\hat{a}[t']dt', \tag{2.69}$$

$$\dot{\hat{a}}[t] = \frac{j}{\hbar} \left[\hat{a}[t], \hat{\mathcal{H}}_{\text{system}}[t] \right] + \int_{-\infty}^{\infty} \mu[\omega]e^{j\omega(t-t_0)}\hat{d}[\omega, t_0]d\omega \tag{2.70}$$

$$- \int_{-\infty}^{\infty} \int_{t_0}^{t} \mu^2[\omega]e^{j\omega(t-t')}\hat{a}[t']dt'd\omega.$$

At this point, there are a few approximations to make. The first is that $\mu[\omega]$ is essentially frequency-independent over the frequency range of interest and that we can identify the dissipation rate $\kappa = 2\pi\mu^2[\omega]$. The second is that $\hat{a}$ goes smoothly to zero at $\pm\infty$ and thus

$$\int_{t_0}^{t} \hat{a}[t']\delta[t - t']dt' = \hat{a}[t]/2. \tag{2.71}$$

The equation for $\hat{a}$ then becomes

$$
\dot{\hat{a}}[t] = \frac{j}{\hbar}\left[\hat{a}[t], \hat{\mathcal{H}}_{\text{system}}[t]\right] + \sqrt{\frac{\kappa}{2\pi}}\int_{-\infty}^{\infty} e^{j\omega(t-t_0)}\hat{d}[\omega, t_0]d\omega - \kappa \int_{t_0}^{t} \hat{a}[t']\delta[t-t']dt' \tag{2.72}
$$

$$
= \frac{j}{\hbar}\left[\hat{a}[t], \hat{\mathcal{H}}_{\text{system}}[t]\right] + \sqrt{\kappa}\hat{a}_{\text{in}}[t] - \frac{\kappa}{2}\hat{a}[t], \tag{2.73}
$$

where I define

$$
\hat{a}_{\text{in}}[t] = \frac{1}{\sqrt{2\pi}}\int_{-\infty}^{\infty} e^{j\omega(t-t_0)}\hat{d}[\omega, t_0]d\omega. \tag{2.74}
$$

Here, $\hat{a}_{\text{in}}$ has the following commutator and expectation value:

$$
\left[\hat{a}_{\text{in}}[t], \hat{a}_{\text{in}}^{\dagger}[t']\right] = \frac{1}{2\pi}\int_{-\infty}^{\infty}\int_{-\infty}^{\infty} e^{j\omega(t-t_0)}e^{-j\omega'(t'-t_0)}\left[\hat{d}[\omega', t_0], \hat{d}^{\dagger}[\omega, t_0]\right]d\omega d\omega' \tag{2.75}
$$

$$
= \frac{1}{2\pi}\int_{-\infty}^{\infty}\int_{-\infty}^{\infty} e^{j\omega(t-t_0)}e^{-j\omega'(t'-t_0)}\delta[\omega-\omega']d\omega d\omega' \tag{2.76}
$$

$$
= \frac{1}{2\pi}\int_{-\infty}^{\infty} e^{j\omega(t-t')}d\omega, \tag{2.77}
$$

$$
= \delta[t-t'] \tag{2.78}
$$

$$
\left\langle \hat{a}_{\text{in}}^{\dagger}[t]\hat{a}_{\text{in}}[t']\right\rangle = \frac{1}{2\pi}\int_{-\infty}^{\infty}\int_{-\infty}^{\infty} e^{-j\omega(t-t_0)}e^{j\omega'(t'-t_0)}\left\langle \hat{d}^{\dagger}[\omega, t_0]\hat{d}[\omega', t_0]\right\rangle d\omega d\omega' \tag{2.79}
$$

$$
= \frac{1}{2\pi}\int_{-\infty}^{\infty}\int_{-\infty}^{\infty} e^{-j\omega(t-t_0)}e^{j\omega'(t'-t_0)}n_{\text{th}}[\omega]\delta[\omega-\omega']d\omega d\omega' \tag{2.80}
$$

$$
= n_{\text{th}}\frac{1}{2\pi}\int_{-\infty}^{\infty} e^{-j\omega(t-t')}d\omega \tag{2.81}
$$

$$
= n_{\text{th}}\delta[t-t']. \tag{2.82}
$$

I assumed that the noise was white in allowing n_{th} to be frequency-independent, as we would assume for a thermal bath. These are exactly the commutation relation and expectation value that were stated above for the different noise bath operators $\hat{\xi}_i$. It is also the way to incorporate any driving field input. The final equation for $\dot{\hat{a}}$ (the cavity operator) is called a Langevin equation of motion. There is a very similar equation for $\dot{\hat{b}}$ (the mechanical operator). I can therefore write down the Heisenberg-Langevin equations that correspond to my model:

$$
\dot{\hat{a}}[t] = \frac{j}{\hbar}\left[\hat{a}, \hat{\mathcal{H}}_{\text{system}}\right] - \frac{\kappa}{2}\hat{a}[t] + \sqrt{\kappa_l}\alpha_{\text{in}}[t] + \sum_{i=\{l,r,0\}}\sqrt{\kappa_i}\hat{\xi}_i[t], \tag{2.83}
$$

$$
\dot{\hat{b}}[t] = \frac{j}{\hbar}\left[\hat{b}, \hat{\mathcal{H}}_{\text{system}}\right] - \frac{\Gamma_{\text{m}}}{2}\hat{b}[t] + \sqrt{\Gamma_{\text{m}}}\hat{\xi}_{\text{m}}[t]. \tag{2.84}
$$

The first term of each expression is just the simple Heisenberg equation of motion for that operator. The second term of each expression accounts for the total damping of the cavity or mechanical field. The third term of the $\hat{a}$ equation accounts for the large classical drive through the left port. The final terms account for the coupling to all of the different thermal baths. These equations, along with the relation between input and output fields (from the bare cavity response found above) are all that is needed to completely describe the cavity optomechanical system and calculate any quantity of interest:

$$\dot{\hat{a}}[t] = -\left(\frac{\kappa}{2} - j\omega_{\rm c}\right)\hat{a}[t] + jg_0\left(\hat{b}[t] + \hat{b}^\dagger[t]\right)\hat{a}[t] + \sqrt{\kappa_{\rm l}}\alpha_{\rm in}[t] + \sum_{i=\{{\rm l,r,0}\}}\sqrt{\kappa_i}\hat{\xi}_i[t], \quad (2.85)$$

$$\dot{\hat{b}}[t] = -\left(\frac{\Gamma_{\rm m}}{2} - j\Omega_{\rm m}\right)\hat{b}[t] + jg_0\left(\hat{a}[t]\hat{a}^\dagger[t] + \frac{1}{2}\right) + \sqrt{\Gamma_{\rm m}}\hat{\xi}_{\rm m}[t], \quad (2.86)$$

$$\hat{a}_{\rm out,trans}[t] = N_2\hat{a}_{\rm in}[t] + N_1\hat{\xi}_{\rm r}[t] - \sqrt{\kappa_{\rm r}}\hat{a}[t] = N_2\hat{a}_{\rm in}[t] + N_1\hat{\xi}_{\rm r}[t] - \sqrt{\kappa_{\rm l}}\hat{a}[t], \quad (2.87)$$

$$\hat{a}_{\rm out,refl}[t] = N_1\hat{a}_{\rm in}[t] + N_2\hat{\xi}_{\rm r}[t] - \sqrt{\kappa_{\rm l}}\hat{a}[t]. \quad (2.88)$$

I have replaced the $\kappa_{\rm r}$ with a $\kappa_{\rm l}$ in the expression for $\hat{a}_{\rm out,trans}[t]$, as $\kappa_{\rm r} = \kappa_{\rm l}$ in the transmission geometry. This results in the nice consequence that the expressions for $\hat{a}_{\rm out,trans}[t]$ and $\hat{a}_{\rm out,refl}[t]$ are exactly the same with $N_1 \leftrightarrow N_2$. In the following chapters, I will do all calculations in the transmission geometry. However, it is easy to recover the reflection geometry result just by switching the N_i's.

2.3 Measurable quantities

In the previous section, I derived coupled equations of motion for the cavity and mechanical oscillator, as well as a relation of the cavity state and input to the output field. Thus, given any classical and noise inputs, I should be able to solve for the microwave output in terms of all of those inputs. However, the goal is to infer the state of the mechanical oscillator from the output microwave field. So, I will need to solve these equations for the state of the mechanical oscillator and then write the output field in terms of that state. In the following chapter I will make assumptions about the classical input field (be it at a single frequency or multiple frequencies), use the assumption

that that classical field is much larger than any fluctuations in the system to linearize about it, and then solve the above equations for $\hat{b}$, $\hat{a}$, and $\hat{a}_{\text{out}}$. What follows in this section are the quantities I will need to calculate from those fields in order to understand certain measurements of the output field.

2.3.1   Coherent dressed response of cavity

I have already introduced the scattering matrix (Equation 2.23); however, I have so far only looked at the response when the excitation is only at one frequency:

$$S_{i1}[\omega_{\text{p}}] = \frac{\hat{a}_{\text{out,i}}[\omega_{\text{p}}]}{\hat{a}_{\text{in}}[\omega_{\text{p}}]} = N_i - \sqrt{\kappa_{\text{l}}}\frac{\hat{a}[\omega_{\text{p}}]}{\hat{a}_{\text{in}}[\omega_{\text{p}}]} = N_i - \kappa_{\text{l}}\chi_{\text{c}}[\omega]. \tag{2.89}$$

However, I can imagine making the same measurement with a probe tone at ω_{p}, but also drive the cavity with another tone at ω_{d}. Measuring the response at ω_{p} now tells me about how the drive tone effects the cavity and mechanical parameters and their coupling. This is known as the dressed response (and is once again completely contained withing the classical equations of motion!).

2.3.2   Mechanical oscillator spectral density and occupancy

I can characterize the state of the mechanical oscillator through its spectral density (see Appendix B.2.2):

$$S_{bb}[\omega] = \left\langle \hat{b}^{\dagger}[-\omega]\hat{b}[\omega] \right\rangle. \tag{2.90}$$

This reveals the spectral content of the mechanical oscillator. Integrating over this function gives the mechanical oscillator's final phonon occupancy n_{m}^{f}:

$$n_{\text{m}}^{\text{f}} = \frac{1}{2\pi} \int_{-\infty}^{\infty} S_{bb}[\omega]d\omega. \tag{2.91}$$

2.3.3   Output field and voltage spectral densities

In order to infer the state of the mechanical oscillator from a measurement, I must also be able to relate the measurement to the input fields. This comes in two parts. I first relate the state

of the mechanical oscillator to the fields $\hat{a}_{\text{out}}$ immediately at the output of the cavity:

$$S_{a_{\text{out}} a_{\text{out}}}[\omega] = \left\langle \hat{a}_{\text{out}}^{\dagger}[-\omega] \hat{a}_{\text{out}}[\omega] \right\rangle. \tag{2.92}$$

In the end, I will want to express this output spectral density in terms of n_{m}^{f} in order to infer the mechanical state from my measurement. Chapter 3 focuses on finding $S_{a_{\text{out}} a_{\text{out}}}[\omega]$ in terms of n_{m}^{f} for several different input drive scenarios.

The second piece of the inference from a measurement is to relate $S_{a_{\text{out}} a_{\text{out}}}[\omega]$ to the voltage spectral density $S_{VV}[\omega]$ measured at the output of a homodyne or heterodyne detection. Chapter 4 focuses on relating $S_{a_{\text{out}} a_{\text{out}}}[\omega]$ to $S_{VV}[\omega]$.

Chapter 3

Theory II: Specific solutions to the equations of motion

Armed with the equations of motion for an optomechanical system derived in the previous chapter (Equations 2.85-2.88), I now turn to solving these equations for different choices of the input drive field. In Section 3.1, I assume a single large microwave drive as the input. In Section 3.2, I assume two large microwave drives, one near optimal red-detuning ($\omega_d - \omega_c \approx -\Omega_m$) and one near optimal blue-detuning ($\omega_d - \omega_c \approx \Omega_m$). For both the one and two-drive cases, I calculate the steady-state solutions for the mechanical field, cavity field, and output spectral density and response. In Section 3.3, I investigate the equations of motion in the time-domain with pulsed input tones, rather than in the steady-state regime.

3.1   Single cavity drive

In a majority of the optomechanics experiments done so far, and three out of six of those presented in this dissertation, a single input drive has been continuously applied and the ensuing steady state conditions of the system have been measured. This section focuses on the theoretical expectations for this case of a single input drive, and discusses the many different limiting cases and effects that are found.

3.1.1 Input assumptions

In this section, I will solve Equations 2.85-2.88, given that the input is a single drive at frequency ω_d:

$$\alpha_{in}[t] = \alpha_{in,0} e^{j\omega_d t}. \tag{3.1}$$

I can assume that the cavity field $\hat{a}$ and the output field $\hat{a}_{out}$ each have a large component at ω_d and smaller components at other frequencies and that the mechanical field operator $\hat{b}$ also has a steady state value and smaller fluctuating piece:

$$\hat{a}[t] = \alpha_0 e^{j\phi_d} e^{j\omega_d t} + \hat{a}_1[t], \qquad \hat{b}[t] = b_0 + \hat{b}_1[t], \tag{3.2}$$

$$\hat{a}^\dagger[t] = \alpha_0 e^{-j\phi_d} e^{-j\omega_d t} + \hat{a}_1^\dagger[t], \qquad \hat{b}^\dagger[t] = b_0^* + \hat{b}_1^\dagger[t],$$

$$\hat{a}_{out}[t] = \alpha_{out,0} e^{j\omega_d t} + \hat{a}_{out,1}[t]. \tag{3.3}$$

Here, $\alpha_{in,0}$ and $\alpha_{out,0}$ are generally complex, but α_0 is defined to be real with ϕ_d accounting for the phase of the cavity field. The classical drive photon number in the cavity is $n_d = \alpha_0^2$.

3.1.2 Steady state and classical solutions

To zeroth order (*i.e.* when $\hat{a}_1$, $\hat{b}_1$, and the $\hat{\xi}_i$'s are zero), solving the equations of motion gives solutions for each field:

$$b_0 = \frac{jg_0(1 + 2\alpha_0^2)}{\Gamma_m - 2j\Omega_m}, \qquad \alpha_{in,0} = \frac{\alpha_0 e^{j\phi_d}}{\sqrt{\kappa_l}\chi_c[\omega_d]}, \tag{3.4}$$

$$\alpha_{out,0} = N_2 \alpha_{in,0} - \sqrt{\kappa_l}\alpha_0 e^{j\phi_d} = (N_2 - \kappa_l \chi_c[\omega_d])\alpha_{in,0}. \tag{3.5}$$

where $\overline{\omega}_c = \omega_c + g_0(b_0 + b_0^*)$ is the new, shifted, cavity resonance frequency. The coherent cavity photon number and powers are related by

$$n_d = \alpha_0^2 = \kappa_l |\chi_c[\omega_d]|^2 |\alpha_{in,0}|^2 = \frac{\kappa_l P_{in}}{\hbar\omega_d} |\chi_c[\omega_d]|^2, \tag{3.6}$$

$$\frac{P_{out}}{\hbar\omega_d} = |\alpha_{out}|^2 = \frac{n_d}{\kappa_l}\left|\frac{N_2}{\chi_c[\omega_d]} - \kappa_l\right|^2, \tag{3.7}$$

$$P_{out} = P_{in}|N_i - \kappa_l\chi_c[\omega_d]|^2. \tag{3.8}$$

Although the expressions relating the photon number and powers seem simple, there is a hidden complexity in the fact that $\overline{\omega}_c$ depends on n_d:

$$\overline{\omega}_c = \omega_c + g_0(b_0 + b_0^*) = \omega_c - \frac{4\Omega_m g_0^2(1 + 2n_d)}{\Gamma_m^2 + 4\Omega_m^2} \approx \omega_c - \frac{2g_0^2 n_d}{\Omega_m}, \tag{3.9}$$

$$n_d = \frac{4\kappa_l P_{in}}{\hbar\omega_d\left(\kappa^2 + 4\left(\omega_d - \omega_c + 2g_0^2 n_d/\Omega_m\right)^2\right)}. \tag{3.10}$$

Here, I have assumed a drive of many photons ($n_d \gg 1$) and a high-Q mechanical oscillator ($\Omega_m \gg \Gamma_m$). This results in a cubic equation for n_d:

$$\frac{\Omega_m^{1/2}}{2^{3/2}\kappa^{3/2}g_0^3}\left(\frac{16g_0^6}{\Omega_m^2}n_d^3 + \frac{16g_0^4\kappa z}{\Omega_m}n_d^2 + g_0^2\kappa^2(4z^2 + 1)n_d - 2\kappa^3\Omega_m y\right) = 0. \tag{3.11}$$

Here, $z \equiv (\omega_d - \omega_c)/\kappa$ is the dimensionless drive detuning from the bare cavity resonance frequency, normalized to the cavity linewidth and $y \equiv (2P_{in}g_0^2\kappa_l)/(\hbar\omega_d\Omega_m\kappa^3)$ is a dimensionless parameter proportional to the input power. I have added a prefactor to the cubic equation, which does not change its solutions, in order to simplify the discriminant below. For some values of detuning and incident power (or z and y), there is only one real solution to this equation and the cavity resonant frequency will be stable and single-valued. For other values, there are three real solutions, resulting in a bifurcation. In these regions, the cavity frequency and number of photons will be hysteretic as power and detuning are changed. The discriminant of the cubic equation for n_d is

$$\mathcal{D} = -\left((4z^2 + 1)^2 + 16zy(4z^2 + 9) + 432y^2\right). \tag{3.12}$$

The cubic equation has three real roots when $\mathcal{D} > 0$ and only one real root when $\mathcal{D} < 0$. Thus, the boundaries between regions with three roots and one root occur when $\mathcal{D} = 0$ at

$$y^\pm = \frac{1}{108}\left(-2z(4z^2 + 9) \pm (4z^2 - 3)^{3/2}\right). \tag{3.13}$$

In order for these boundaries to be meaningful, they must be real and positive (since all the parameters that make up y are real and positive). The boundaries $y^\pm$ are real as long as $|z| \geq \sqrt{3}/2$ and positive only if z is negative. Therefore, there can be no boundary for $z > -\sqrt{3}/2$. Since $\mathcal{D} < 0$ at $z = 0$, this region must have only one root. Looking at the derivatives of the discriminant at the
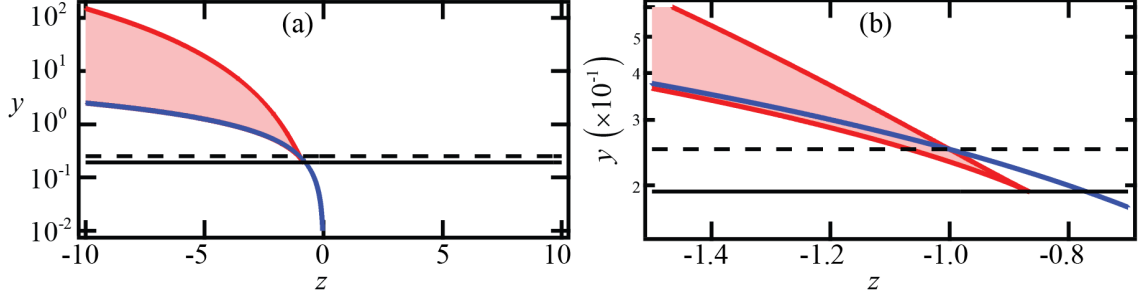
Figure 3.1: Regions of cavity nonlinearity as a function of dimensionless drive detuning $z = (\omega_\mathrm{d} - \omega_\mathrm{c})/\kappa$ and dimensionless input power $y = (2P_\mathrm{in}g_0^2\kappa_\mathrm{l})/(\hbar\omega_\mathrm{d}\Omega_\mathrm{m}\kappa^3)$. The red lines are the boundaries $y^\pm$ between three-solution and one-solution regions. The red shaded area between these lines shows where there are three solutions. The blue line shows the points where the drive is centered at the cavity frequency. The black line shows the maximum power for which there is only one solution at all detunings. The black dashed line shows the maximum power for which there is only one solution for the drive at the cavity frequency. (b) Zoom-in of (a) near the point of interest.

two boundaries reveals the discriminant's behavior everywhere:

$$\partial_y \mathcal{D}\Big|_{y^\pm} = \mp 8 \left(4z^2 - 3\right)^{3/2} . \tag{3.14}$$

Therefore, there will be three roots if $z \leq -\sqrt{3}/2$ and $y^- < y < y^+$ (see Figure 3.1 to see the different regions). The highest power for which the cavity is stable for all detunings is $y = 3^{-3/2}$.

There are some scenarios (such as the quantum backaction measurement with one drive discussed later) where I might want the drive to be exactly on resonance ($\omega_\mathrm{d} = \overline{\omega}_\mathrm{c}$). To achieve this, the power and detuning must be related:

$$n_\mathrm{d} = \frac{2\kappa\Omega_\mathrm{m}y}{g_0^2}, \qquad z = -\frac{2g_0^2 n_\mathrm{d}}{\kappa\Omega_\mathrm{m}}, \qquad y = -\frac{z}{4}. \tag{3.15}$$

The highest power for which this point is stable is $y = 1/4$, which occurs at $z = -1$, meaning that the power applied on resonance is limited: $n_\mathrm{d} \leq \kappa\Omega_\mathrm{m}/(2g_0^2)$. In the remainder of this thesis, I will assume that the power and detuning we apply is such that there is always only one solution for the cavity frequency and number of photons.

3.1.3 Linearized equations of motion

Substituting the derived steady-state values into the equations of motion gives the linearized equations of motion:

$$\dot{\hat{a}}_1[t] = -\left(\frac{\kappa}{2} - j\overline{\omega}_c\right)\hat{a}_1[t] + jge^{j(\omega_d t+\phi_d)}\left(\hat{b}_1[t] + \hat{b}_1^\dagger[t]\right) + \sum_{i=l,r,0}\sqrt{\kappa_i}\hat{\xi}_i[t], \tag{3.16}$$

$$\dot{\hat{b}}_1[t] = -\left(\frac{\Gamma_m}{2} - j\Omega_m\right)\hat{b}_1[t] + jg\left(e^{-j(\omega_d t+\phi_d)}\hat{a}_1[t] + e^{j(\omega_d t+\phi_d)}\hat{a}_1^\dagger[t]\right) + \sqrt{\Gamma_m}\hat{\xi}_m[t], \tag{3.17}$$

$$\hat{a}_{\text{out},1}[t] = N_2\hat{\xi}_l[t] + N_1\hat{\xi}_r[t] - \sqrt{\kappa_l}\hat{a}_1[t], \tag{3.18}$$

where $g \equiv g_0\sqrt{n_d}$ is the photon enhanced coupling rate. Multiplying the $\hat{a}_1$ and $\hat{b}_1$ equations by $e^{-j\omega t}$ and integrating gives the linearized equations of motion and their conjugates in the frequency domain:

$$\frac{\hat{a}_1[\omega]}{\chi_c[\omega]} = jge^{j\phi_d}(\hat{b}_1[\omega - \omega_d] + \hat{b}_1^\dagger[\omega - \omega_d]) + \sum_{i=l,r,0}\sqrt{\kappa_i}\hat{\xi}_i[\omega], \tag{3.19}$$

$$\frac{\hat{a}_1^\dagger[-\omega]}{\chi_c^*[\omega]} = -jge^{-j\phi_d}(\hat{b}_1^\dagger[-\omega + \omega_d] + \hat{b}_1[-\omega + \omega_d]) + \sum_{i=l,r,0}\sqrt{\kappa_i}\hat{\xi}_i^\dagger[-\omega], \tag{3.20}$$

$$\frac{\hat{b}_1[w]}{\chi_m[\omega]} = jg\left(e^{j\phi_d}\hat{a}_1^\dagger[\omega - \omega_d] + e^{-j\phi_d}\hat{a}_1[\omega + \omega_d]\right) + \sqrt{\Gamma_m}\hat{\xi}_m[\omega], \tag{3.21}$$

$$\frac{\hat{b}_1^\dagger[-w]}{\chi_m^*[\omega]} = -jg\left(e^{-j\phi_d}\hat{a}_1[-\omega + \omega_d] + e^{j\phi_d}\hat{a}_1^\dagger[-\omega - \omega_d]\right) + \sqrt{\Gamma_m}\hat{\xi}_m^\dagger[-\omega], \tag{3.22}$$

where $\chi_c[\omega] \equiv \left[\frac{\kappa}{2} + j(\omega - \overline{\omega}_c)\right]^{-1}$ and $\chi_m[\omega] \equiv \left[\frac{\Gamma_m}{2} + j(\omega - \Omega_m)\right]^{-1}$ are the cavity and mechanical susceptibilities, respectively.

These four equations can be written in terms of only four variables ($\hat{a}[\omega + \omega_d]$, $\hat{a}^\dagger[\omega - \omega_d]$, $\hat{b}[\omega]$, and $\hat{b}^\dagger[\omega]$) and can thus be solved exactly, resulting in the following solutions:

$$\hat{a}_1[\omega] = \frac{\chi_c[\omega]}{1 + g^2\left(\chi_c[\omega] - \chi_c^*[-\omega + 2\omega_d]\right)\left(\chi_m[\omega - \omega_d] - \chi_m^*[-\omega + \omega_d]\right)}$$
$$\times \left\{\left(1 - g^2\chi_c^*[-\omega + 2\omega_d]\left(\chi_m[\omega - \omega_d] - \chi_m^*[-\omega + \omega_d]\right)\right)\sum_{i=l,r,0}\sqrt{\kappa_i}\hat{\xi}_i[\omega]\right. \tag{3.23}$$
$$-g^2e^{2j\phi_d}\chi_c^*[-\omega + 2\omega_d]\left(\chi_m[\omega - \omega_d] - \chi_m^*[-\omega + \omega_d]\right)\sum_{i=l,r,0}\sqrt{\kappa_i}\hat{\xi}_i^\dagger[\omega - 2\omega_d]$$
$$\left.+jge^{j\phi_d}\sqrt{\Gamma_m}\left(\chi_m[\omega - \omega_d]\hat{\xi}_m[\omega - \omega_d] + \chi_m^*[-\omega + \omega_d]\hat{\xi}_m^\dagger[\omega - \omega_d]\right)\right\},$$

$$\hat{a}_1^\dagger[\omega] = \frac{\chi_c^*[-\omega]}{1 + g^2 \left(\chi_c[\omega + 2\omega_d] - \chi_c^*[-\omega]\right)\left(\chi_m[\omega + \omega_d] - \chi_m^*[-\omega - \omega_d]\right)}$$

$$\times \left\{ g^2 e^{-2j\phi_d} \chi_c[\omega + 2\omega_d]\left(\chi_m[\omega + \omega_d] - \chi_m^*[-\omega - \omega_d]\right) \sum_{i=l,r,0} \sqrt{\kappa_i}\hat{\xi}_i[\omega + 2\omega_d] \quad (3.24)\right.$$

$$+ \left(1 + g^2 \chi_c[\omega + 2\omega_d]\left(\chi_m[\omega + \omega_d] - \chi_m^*[-\omega - \omega_d]\right)\right) \sum_{i=l,r,0} \sqrt{\kappa_i}\hat{\xi}_i^\dagger[\omega]$$

$$\left. - jge^{-j\phi_d}\sqrt{\Gamma_m}\left(\chi_m[\omega + \omega_d]\hat{\xi}_m[\omega + \omega_d] + \chi_m^*[-\omega - \omega_d]\hat{\xi}_m^\dagger[\omega + \omega_d]\right) \right\},$$

$$\hat{b}_1[\omega] = \frac{\chi_m[\omega]}{1 + g^2 \left(\chi_c[\omega + \omega_d] - \chi_c^*[-\omega + \omega_d]\right)\left(\chi_m[\omega] - \chi_m^*[-\omega]\right)}$$

$$\times \left\{ \sqrt{\Gamma_m}\left(1 - g^2 \chi_m^*[-\omega]\left(\chi_c[\omega + \omega_d] - \chi_c^*[-\omega + \omega_d]\right)\right)\hat{\xi}_m[\omega] \quad (3.25)\right.$$

$$+ \sqrt{\Gamma_m}\left(-g^2 \chi_m^*[-\omega]\left(\chi_c[\omega + \omega_d] - \chi_c^*[-\omega + \omega_d]\right)\right)\hat{\xi}_m^\dagger[\omega]$$

$$+ jge^{-j\phi_d}\chi_c[\omega + \omega_d] \sum_{i=l,r,0} \sqrt{\kappa_i}\hat{\xi}_i[\omega + \omega_d]$$

$$\left. + jge^{j\phi_d}\chi_c^*[-\omega + \omega_d] \sum_{i=l,r,0} \sqrt{\kappa_i}\hat{\xi}_i^\dagger[\omega - \omega_d] \right\},$$

$$\hat{b}_1^\dagger[\omega] = \frac{\chi_m^*[-\omega]}{1 + g^2 \left(\chi_c[\omega + \omega_d] - \chi_c^*[-\omega + \omega_d]\right)\left(\chi_m[\omega] - \chi_m^*[-\omega]\right)}$$

$$\times \left\{ \sqrt{\Gamma_m}\left(g^2 \chi_m[\omega]\left(\chi_c[\omega + \omega_d] - \chi_c^*[-\omega + \omega_d]\right)\right)\hat{\xi}_m[\omega] \quad (3.26)\right.$$

$$+ \sqrt{\Gamma_m}\left(1 + g^2 \chi_m[\omega]\left(\chi_c[\omega + \omega_d] - \chi_c^*[-\omega + \omega_d]\right)\right)\hat{\xi}_m^\dagger[\omega]$$

$$- jge^{-j\phi_d}\chi_c[\omega + \omega_d] \sum_{i=l,r,0} \sqrt{\kappa_i}\hat{\xi}_i[\omega + \omega_d]$$

$$\left. - jge^{j\phi_d}\chi_c^*[-\omega + \omega_d] \sum_{i=l,r,0} \sqrt{\kappa_i}\hat{\xi}_i^\dagger[\omega - \omega_d] \right\}.$$

Here, the daggered equations contain the same information as the undaggered. However, I have included them here because it is helpful to see how to convert between the operators and their daggers (for any operator $(\hat{A}[\omega])^\dagger = \hat{A}^\dagger[-\omega]$). Later in this chapter I may omit daggered equations as they are easily found from the undaggered ones.

3.1.4   Effective mechanical susceptibility

In the absence of optomechanical coupling ($g = 0$), I can write the position of the mechanical oscillator coupled to it's thermal bath as

$$\hat{x}[\omega] = x_{\text{zp}}(\hat{b}[\omega] + \hat{b}^\dagger[\omega]) = x_{\text{zp}}\sqrt{\Gamma_{\text{m}}}(\chi_{\text{m}}[\omega]\hat{\xi}_{\text{m}}[\omega] + \chi_{\text{m}}^*[-\omega]\hat{\xi}_{\text{m}}^\dagger[\omega]). \tag{3.27}$$

When I re-introduce coupling to the cavity, but keep the cavity isolated from the cavity baths, the mechanical position is

$$\hat{x}[\omega] = \frac{x_{\text{zp}}\sqrt{\Gamma_{\text{m}}}(\chi_{\text{m}}[\omega]\hat{\xi}_{\text{m}}[\omega] + \chi_{\text{m}}^*[-\omega]\hat{\xi}_{\text{m}}^\dagger[\omega])}{1 + g^2\left(\chi_{\text{c}}[\omega + \omega_{\text{d}}] - \chi_{\text{c}}^*[-\omega + \omega_{\text{d}}]\right)\left(\chi_{\text{m}}[\omega] - \chi_{\text{m}}^*[-\omega]\right)}. \tag{3.28}$$

Here, mechanical fluctuations lead to a change in the cavity field, which exerts a force back on the mechanical oscillator. This built in feedback effect leads to a new, effective mechanical susceptibility for the mechanical oscillator, whose form is familiar from control theory[1][79, Chapter 11]:

$$\chi_{\text{m,eff}}[\omega] = \frac{\chi_{\text{m}}[\omega]}{1 + g^2\left(\chi_{\text{c}}[\omega + \omega_{\text{d}}] - \chi_{\text{c}}^*[-\omega + \omega_{\text{d}}]\right)\left(\chi_{\text{m}}[\omega] - \chi_{\text{m}}^*[-\omega]\right)}. \tag{3.29}$$

In the weak-coupling limit, $g \ll \kappa$, the effective mechanical susceptibility can be approximated as a Lorentzian by evaluating the χ_{c}'s at $\omega = \Omega_{\text{m}}$. This is a good approximation because the χ_{c}'s are fairly constant over the frequency range of interest (near the mechanical resonance frequency). I also make the approximation that $\chi_{\text{m}}^*[-\omega]$ near $\omega \approx \Omega_{\text{m}}$ is negligible (when $\Omega_{\text{m}} \gg \Gamma_{\text{m}}$). Writing the effective susceptibility as a function of an effective total frequency and total linewidth, I find

$$\frac{1}{\chi_{\text{m,eff}}[\omega]} \approx \frac{1}{\chi_{\text{m}}[\omega]} + g^2\left(\chi_{\text{c}}\left[\Omega_{\text{m}} + \omega_{\text{d}}\right] - \chi_{\text{c}}^*\left[-\Omega_{\text{m}} + \omega_{\text{d}}\right]\right) \equiv \frac{\Gamma_{\text{tot}}}{2} + j(\omega - \Omega_{\text{tot}}), \tag{3.31}$$

---

[1] Some authors like to emphasize the relationship to Dyson's equation rather than control theory and define a quantity called self-energy to relate the effective mechanical susceptibility to the bare susceptibility:

$$\Sigma[\omega] = j\left(\frac{1}{\chi_{\text{m,eff}}[\omega]} - \frac{1}{\chi_{\text{m}}[\omega]}\right) \approx jg^2\left(\chi_{\text{c}}[\omega + \omega_{\text{d}}] - \chi_{\text{c}}^*[-\omega + \omega_{\text{d}}]\right). \tag{3.30}$$

This expression is easily found from Equation 3.29 by making the approximation that $\chi_{\text{m}}^*[-\omega]$ is negligible near $\omega = \Omega_{\text{m}}$ (which is valid if $\Omega_{\text{m}} \gg \Gamma_{\text{m}}$).

where the effective total and optomechanically induced mechanical damping and resonance frequency are

$$\Gamma_{\text{tot}} = \Gamma_{\text{m}} + \Gamma_{\text{opt}}, \qquad \Omega_{\text{tot}} = \Omega_{\text{m}} + \Omega_{\text{opt}}, \qquad (3.32)$$

$$\Gamma_{\text{opt}} = 2g^2 \text{Re} \left[\chi_{\text{c}} \left[\Omega_{\text{m}} + \omega_{\text{d}} \right] - \chi_{\text{c}}^* \left[-\Omega_{\text{m}} + \omega_{\text{d}} \right] \right] \qquad (3.33)$$

$$= 4g^2 \left(\frac{\kappa}{\kappa^2 + 4(\Delta + \Omega_{\text{m}})^2} - \frac{\kappa}{\kappa^2 + 4(\Delta - \Omega_{\text{m}})^2} \right), \qquad (3.34)$$

$$\Omega_{\text{opt}} = -g^2 \text{Im} \left[\chi_{\text{c}} \left[\Omega_{\text{m}} + \omega_{\text{d}} \right] - \chi_{\text{c}}^* \left[-\Omega_{\text{m}} + \omega_{\text{d}} \right] \right] \qquad (3.35)$$

$$= 4g^2 \left(\frac{\Delta + \Omega_{\text{m}}}{\kappa^2 + 4(\Delta + \Omega_{\text{m}})^2} + \frac{\Delta - \Omega_{\text{m}}}{\kappa^2 + 4(\Delta - \Omega_{\text{m}})^2} \right). \qquad (3.36)$$

Here, Δ is the detuning of the drive away from the cavity resonance frequency: $\Delta = \omega_{\text{d}} - \overline{\omega}_{\text{c}}$. The χ_{c}'s above really should have been evaluated at Ω_{tot} rather than Ω_{m}. However, in the weak coupling limit, the change in resonance frequency is fractionally very small, so evaluating at Ω_{m} will not make much difference.

3.1.5 Phonon spectrum and mechanical occupancy

I can re-write Equations 3.25-3.26 for $\hat{b}$ and $\hat{b}^\dagger$ with coefficients to simplify the subsequent algebra:

$$\hat{b}_1[\omega] = s_1[\omega] \hat{\xi}_{\text{m}}^\dagger[\omega] + s_2[\omega] \hat{\xi}_{\text{m}}[\omega] \qquad (3.37)$$

$$+ s_3[\omega] \sum_i \sqrt{\frac{\kappa_i}{\kappa}} \hat{\xi}_i^\dagger[\omega - \omega_{\text{d}}] + s_4[\omega] \sum_i \sqrt{\frac{\kappa_i}{\kappa}} \hat{\xi}_i[\omega + \omega_{\text{d}}],$$

$$\hat{b}_1^\dagger[-\omega] = s_1^*[\omega] \hat{\xi}_{\text{m}}[-\omega] + s_2^*[\omega] \hat{\xi}_{\text{m}}^\dagger[-\omega] \qquad (3.38)$$

$$+ s_3^*[\omega] \sum_i \sqrt{\frac{\kappa_i}{\kappa}} \hat{\xi}_i[-\omega + \omega_{\text{d}}] + s_4^*[\omega] \sum_i \sqrt{\frac{\kappa_i}{\kappa}} \hat{\xi}_i^\dagger[-\omega - \omega_{\text{d}}].$$

As I explained in Section 2.3.2, the phonon spectrum is given by

$$S_{bb}[\omega] = \left\langle \hat{b}^\dagger[-\omega]\hat{b}[\omega] \right\rangle \tag{3.39}$$

$$= |s_1[\omega]|^2 \left\langle \hat{\xi}_{\rm m}[-\omega]\hat{\xi}_{\rm m}^\dagger[\omega] \right\rangle + |s_2[\omega]|^2 \left\langle \hat{\xi}_{\rm m}^\dagger[-\omega]\hat{\xi}_{\rm m}[\omega] \right\rangle \tag{3.40}$$

$$+ |s_3[\omega]|^2 \sum_{i,j} \frac{\sqrt{\kappa_i \kappa_j}}{\kappa} \left\langle \hat{\xi}_i[-\omega+\omega_{\rm d}]\hat{\xi}_j^\dagger[\omega-\omega_{\rm d}] \right\rangle$$

$$+ |s_4[\omega]|^2 \sum_{i,j} \frac{\sqrt{\kappa_i \kappa_j}}{\kappa} \left\langle \hat{\xi}_i^\dagger[-\omega-\omega_{\rm d}]\hat{\xi}_j[\omega+\omega_{\rm d}] \right\rangle$$

$$= |s_1[\omega]|^2 \left(n_{\rm m}^{\rm th} + 1 \right) + |s_2[\omega]|^2 n_{\rm m}^{\rm th} \tag{3.41}$$

$$+ |s_3[\omega]|^2 \sum_i \frac{\kappa_i}{\kappa} \left(n_i^{\rm th} + 1 \right) + |s_4[\omega]|^2 \sum_i \frac{\kappa_i}{\kappa} n_i^{\rm th}$$

$$= |s_1[\omega]|^2 \left(n_{\rm m}^{\rm th} + 1 \right) + |s_2[\omega]|^2 n_{\rm m}^{\rm th} + |s_3[\omega]|^2 \left(n_{\rm c}^{\rm th} + 1 \right) + |s_4[\omega]|^2 n_{\rm c}^{\rm th}, \tag{3.42}$$

where $n_{\rm m}^{\rm th}$ is the thermal mechanical occupancy and $n_{\rm c}^{\rm th} \equiv \kappa^{-1} \sum_{i={\rm l,r,0}} \kappa_i n_i^{\rm th}$ is the total cavity thermal occupancy. Substituting in the coefficients and simplifying, I find the mechanical spectrum:

$$S_{bb}[\omega] = \frac{\Gamma_{\rm m} |\chi_{\rm m}[\omega]|^2 |\chi_{\rm m,eff}[-\omega] - \chi_{\rm m}[-\omega]|^2}{|\chi_{\rm m}[\omega] - \chi_{\rm m}^*[-\omega]|^2} \left(n_{\rm m}^{\rm th} + 1 \right)$$

$$+ \frac{\Gamma_{\rm m} |\chi_{\rm m}[\omega]|^2 |\chi_{\rm m,eff}[\omega] - \chi_{\rm m}^*[-\omega]|^2}{|\chi_{\rm m}[\omega] - \chi_{\rm m}^*[-\omega]|^2} n_{\rm m}^{\rm th} \tag{3.43}$$

$$+ \frac{x_{\rm zp}^2}{\hbar^2} S_{FF}[-\omega] |\chi_{\rm m,eff}[\omega]|^2 \left(n_{\rm c}^{\rm th} + 1 \right) + \frac{x_{\rm zp}^2}{\hbar^2} S_{FF}[\omega] |\chi_{\rm m,eff}[\omega]|^2 n_{\rm c}^{\rm th}.$$

Here, S_{FF} is the the radiation pressure force spectrum,

$$S_{FF}[\omega] \equiv \frac{\hbar^2 g^2 \kappa}{x_{\rm zp}^2} |\chi_{\rm c}[\omega+\omega_{\rm d}]|^2. \tag{3.44}$$

This result is very similar to that in reference [75], except that they write the answer in terms of the self energy (see Footnote 1) and there are a several minor differences in notation between their work in mine. Perhaps the most important (and least obvious) difference is that they define the spectral density as $S_{cc}[\omega] = \int dt e^{i\omega t} \left\langle \hat{c}^\dagger[t]\hat{c}[0] \right\rangle = \left\langle \hat{c}^\dagger[\omega]\hat{c}[-\omega] \right\rangle$. This is my definition with $\omega \to -\omega$. This will not affect the final mechanical occupancy, because that involves integrating the spectral density over all negative and positive frequencies, but it does mean that their spectral density ends up being centered about $\omega = -\Omega_{\rm m}$ rather than $\omega = \Omega_{\rm m}$.

My expression for the spectrum is peaked near $\omega = \Omega_m$. Therefore, I can simplify by making the very good approximation that $\chi_m[-\omega] = \chi_{m,\text{eff}}[-\omega] = 0$ near $\omega \approx \Omega_m$ (valid in the limit $\Omega_m \gg \Gamma_m$):

$$S_{bb}[\omega] = \left(n_m^{\text{th}} \Gamma_m + \frac{x_{\text{zp}}^2}{\hbar^2} \left(S_{FF}[-\omega](n_c^{\text{th}} + 1) + S_{FF}[\omega] n_c^{\text{th}} \right) \right) |\chi_{m,\text{eff}}[\omega]|^2 . \tag{3.45}$$

This result is fully general for any coupling regime. I can specialize to the weak-coupling regime by substituting in the effective mechanical susceptibility and making the approximation that $S_{FF}[\omega]$ is relatively constant over the frequency range of interest (near the mechanical resonance frequency). If this is true, then I can simply evaluate it at Ω_m (not Ω_{tot}). This is reasonable because $S_{FF}[\omega]$ is a function of only the χ_c's, which change on frequencies of order $\kappa \gg \Gamma_m$. Making this approximation,

$$S_{FF}[\omega] \quad \approx \quad S_{FF}[\Omega_m] = \frac{\hbar^2(1 + n_m^0)\Gamma_{\text{opt}}}{x_{\text{zp}}^2}, \tag{3.46}$$

$$S_{FF}[-\omega] \quad \approx \quad S_{FF}[-\Omega_m] = \frac{\hbar^2 n_m^0 \Gamma_{\text{opt}}}{x_{\text{zp}}^2}, \tag{3.47}$$

$$n_m^0 \quad \equiv \quad \frac{S_{FF}[-\Omega_m]}{S_{FF}[\Omega_m] - S_{FF}[-\Omega_m]} = -\frac{\kappa^2 + 4(\Delta + \Omega_m)^2}{16\Delta\Omega_m}. \tag{3.48}$$

Here, n_m^0 is the mechanical occupancy in the absence of both mechanical damping and cavity thermal photons ($\Gamma_m = 0$, $n_c^{\text{th}} = 0$). For a red-detuned drive at frequency $\omega_d \approx \omega_c - \Omega_m$, this factor is $n_m^0 = \kappa^2/(16\Omega_m^2)$. It therefore depends on how far in the resolved sideband regime the system is and is zero in the far resolved sideband limit ($\Omega_m \gg \kappa$). Conversely, for a blue-detuned drive at frequency $\omega_d \approx \omega_c + \Omega_m$, this factor is $n_m^0 = -1 - \kappa^2/(16\Omega_m^2)$, which is nonzero even in the far resolved sideband regime.

The mechanical spectrum in the weak-coupling regime is

$$S_{bb}[\omega] = \left(n_m^{\text{th}} \Gamma_m + \left(n_c^{\text{th}} + n_m^0 + 2 n_c^{\text{th}} n_m^0 \right) \Gamma_{\text{opt}} \right) |\chi_{m,\text{eff}}[\omega]|^2 , \tag{3.49}$$

which has a Lorentzian profile of width Γ_{tot}, centered about Ω_{tot}. The final mechanical occupancy

in the weak coupling regime is

$$
\begin{aligned}
n_{\mathrm{m}}^{\mathrm{f}} &= \frac{1}{2\pi} \int_{-\infty}^{\infty} S_{bb}[\omega] d\omega && (3.50) \\
&= \left(n_{\mathrm{m}}^{\mathrm{th}} \Gamma_{\mathrm{m}} + \left(n_{\mathrm{c}}^{\mathrm{th}} + n_{\mathrm{m}}^{0} + 2 n_{\mathrm{c}}^{\mathrm{th}} n_{\mathrm{m}}^{0} \right) \Gamma_{\mathrm{opt}} \right) \frac{1}{2\pi} \int_{-\infty}^{\infty} \frac{1}{(\Gamma_{\mathrm{tot}}/2)^2 + (\omega - \Omega_{\mathrm{m}})^2} d\omega && (3.51) \\
&= \boxed{\frac{n_{\mathrm{m}}^{\mathrm{th}} \Gamma_{\mathrm{m}} + \left(n_{\mathrm{c}}^{\mathrm{th}} + n_{\mathrm{m}}^{0} + 2 n_{\mathrm{c}}^{\mathrm{th}} n_{\mathrm{m}}^{0} \right) \Gamma_{\mathrm{opt}}}{\Gamma_{\mathrm{m}} + \Gamma_{\mathrm{opt}}}}. && (3.52)
\end{aligned}
$$

The total motion of the oscillator (including zero point motion) can be divided up into a component originating from the thermal phonon bath and a component originating from the various cavity baths:

$$
n_{\mathrm{m}}^{\mathrm{f}} + 1/2 = \frac{\Gamma_{\mathrm{m}}(n_{\mathrm{m}}^{\mathrm{th}} + 1/2)}{\Gamma_{\mathrm{m}} + \Gamma_{\mathrm{opt}}} + \frac{\Gamma_{\mathrm{opt}}(1 + 2 n_{\mathrm{m}}^{0})(n_{\mathrm{c}}^{\mathrm{th}} + 1/2)}{\Gamma_{\mathrm{m}} + \Gamma_{\mathrm{opt}}} = \frac{\Gamma_{\mathrm{m}}(n_{\mathrm{m}}^{\mathrm{th}} + 1/2)}{\Gamma_{\mathrm{m}} + \Gamma_{\mathrm{opt}}} + n_{\mathrm{m}}^{\mathrm{ba}}. \tag{3.53}
$$

The first of these components is a weighted mechanical bath occupancy. By modifying Γ_{opt}, the coupling of the mechanical oscillator to the mechanical bath can be either diluted or strengthened. The second component is called the backaction occupation $n_{\mathrm{m}}^{\mathrm{ba}}$, as it is the motion of the mechanical oscillator caused by the radiation pressure of the photon field. This expression, converted to a force spectral density, gives the same result (up to a factor of two due to the definition of spectral densities) at that found for $S_{\mathrm{FF}}^{\mathrm{qba}}[\Omega]$ in reference [80].

3.1.6   Important limits of the mechanical occupancy

Here, I will look at various interesting limits of Equation 3.52, the final mechanical occupancy in the weak coupling regime. For an off-resonant drive ($\Delta = \omega_{\mathrm{d}} - \overline{\omega}_{\mathrm{c}} \neq 0$), Γ_{opt} will be nonzero and there will be a net dynamical radiation pressure on the mechanical oscillator. Turning the drive power up sufficiently such that $|\Gamma_{\mathrm{opt}}| \gg \Gamma_{\mathrm{m}} n_{\mathrm{m}}^{\mathrm{th}}$, the final occupancy will be

$$
n_{\mathrm{m}}^{\mathrm{f}} = n_{\mathrm{c}}^{\mathrm{th}} + n_{\mathrm{m}}^{0} + 2 n_{\mathrm{c}}^{\mathrm{th}} n_{\mathrm{m}}^{0} = n_{\mathrm{c}}^{\mathrm{th}} - \left(1 + 2 n_{\mathrm{c}}^{\mathrm{th}} \right) \frac{4(\Omega_{\mathrm{m}} + \Delta)^2 + \kappa^2}{16 \Omega_{\mathrm{m}} \Delta}. \tag{3.54}
$$

The detunings that minimize and maximize the final mechanical occupancies are

$$
\Delta_{\mathrm{optimal,min}} = -\Omega_{\mathrm{m}} \sqrt{1 + \frac{\kappa^2}{4\Omega_{\mathrm{m}}^2}} \qquad \text{and} \qquad \Delta_{\mathrm{optimal,max}} = \Omega_{\mathrm{m}} \sqrt{1 + \frac{\kappa^2}{4\Omega_{\mathrm{m}}^2}}. \tag{3.55}
$$

In the far resolved sideband limit ($\Omega_m \gg \kappa$), these detunings are just $\pm\Omega_m$, while in the far unresolved sideband limit ($\Omega_m \ll \kappa$), they are $\pm\kappa/2$. Using these detunings, I will now go back to the original expression for n_m^f, as (even ignoring technical experimental reasons) there are limits on the largest drive powers that can be applied usefully. In the amplifying case ($\Delta > 0$), increasing the drive power will decrease the total mechanical linewidth. The mechanical oscillator can no longer be stable once its linewidth becomes negative. Thus, the largest $|\Gamma_{opt}|$ can be is Γ_m. As $|\Gamma_{opt}|$ goes to Γ_m, the total linewidth goes to zero and the occupancy is amplified until it diverges. In the cooling case ($\Delta < 0$), Γ_{opt} is positive and the total mechanical linewidth grows with power. The mechanical oscillator will only remain an underdamped oscillator while $Q_{tot} = \Omega_{tot}/\Gamma_{tot} > 1/2$. Thus, the largest Γ_{tot} can be is $2\Omega_{tot}$ and the minimum possible final occupancy (assuming an initially high Q oscillator, $Q_m = \Omega_m/\Gamma_m \gg 1$) is

$$n_{m,min}^f = \frac{n_m^{th}}{2Q_m} + \frac{1}{2}\left(\left(1 + 2n_c^{th}\right)\sqrt{1 + \frac{\kappa^2}{4\Omega_m^2}} - 1\right). \tag{3.56}$$

In order for the mechanical occupancy to reach the ground state ($n_{m,min}^f < 1$), the system must have a sufficiently large initial mechanical quality factor such that $n_m^{th} < 2Q_m$, it must be in the resolved sideband limit ($4\sqrt{2}\Omega_m > \kappa$), and the cavity thermal occupancy must be less than one ($n_c^{th} < 1$). If the cavity and mechanical oscillator are coupled to baths at the same temperature, this last requirement can be written another way: $n_m^{th} < \omega_c/\Omega_m$. However, in experiments, we observe excess cavity occupancy that indicates that the thermal temperature of the cavity is higher than that of the mechanics. Thus, the requirement that $n_c^{th} < 1$ is the more fundamental one. The last requirement is technical rather than fundamental - that the incident power can be turned up sufficiently high that $\Gamma_{opt} \gg n_m^{th}\Gamma_m$.

In the far resolved sideband limit applicable to our most recent experiments on cooling and control of the mechanical oscillator, the final occupancies given an optimally red and optimally

blue-detuned drive are

$$n_{\mathrm{m}}^{\mathrm{f}} = \frac{n_{\mathrm{m}}^{\mathrm{th}}\Gamma_{\mathrm{m}} + n_{\mathrm{c}}^{\mathrm{th}}\Gamma_{\mathrm{opt}}}{\Gamma_{\mathrm{m}} + \Gamma_{\mathrm{opt}}} \qquad \text{for } \omega_{\mathrm{d}} = \omega_{\mathrm{c}} - \Omega_{\mathrm{m}}, \tag{3.57}$$

$$n_{\mathrm{m}}^{\mathrm{f}} = \frac{n_{\mathrm{m}}^{\mathrm{th}}\Gamma_{\mathrm{m}} - (n_{\mathrm{c}}^{\mathrm{th}} + 1)\Gamma_{\mathrm{opt}}}{\Gamma_{\mathrm{m}} + \Gamma_{\mathrm{opt}}} \qquad \text{for } \omega_{\mathrm{d}} = \omega_{\mathrm{c}} + \Omega_{\mathrm{m}}. \tag{3.58}$$

The case of an on-resonance drive is much simpler than the detuned drive cases because Γ_{opt} is zero (although n_{m}^{0} blows up so it is critical to use $n_{\mathrm{m}}^{0}\Gamma_{\mathrm{opt}} = 4g^2\kappa/(\kappa^2 + 4\Omega_{\mathrm{m}}^2)$). The final occupancy is

$$n_{\mathrm{m}}^{\mathrm{f}} = n_{\mathrm{m}}^{\mathrm{th}} + n_{\mathrm{m}}^{\mathrm{ba}} = n_{\mathrm{m}}^{\mathrm{th}} + \frac{4g^2\kappa(1 + 2n_{\mathrm{c}}^{\mathrm{th}})}{\Gamma_{\mathrm{m}}\left(\kappa^2 + 4\Omega_{\mathrm{m}}^2\right)}. \tag{3.59}$$

There is no net dynamic radiation pressure at this point, leaving the mechanical occupancy approximately at its initial value. However, there is an additional backaction heating term which corresponds to the extra motion induced in the mechanical oscillator by fluctuations of the input drive field (even when the cavity thermal occupancy is 0). Note that the quantum backaction seen with a single, on-resonance drive is maximized in the unresolved sideband regime (when $\Omega_{\mathrm{m}} \ll \kappa$).

One last interesting case is that of strong coupling for a red-detuned drive in the far resolved-sideband case. If I go back to Equation 3.42 and set the far-off resonance terms to zero ($\chi_{\mathrm{m}}[-\omega] = \chi_{\mathrm{c}}[-\omega + \omega_{\mathrm{d}}] = 0$), I find the following equation for the mechanical spectrum:

$$S_{bb}[\omega] = \frac{\left(n_{\mathrm{m}}^{\mathrm{th}}\Gamma_{\mathrm{m}} + g^2 n_{\mathrm{c}}^{\mathrm{th}}\kappa|\chi_{\mathrm{c}}[\omega + \omega_{\mathrm{d}}]|^2\right)|\chi_{\mathrm{m}}[\omega]|^2}{|1 + g^2\chi_{\mathrm{m}}[\omega]\chi_{\mathrm{c}}[\omega + \omega_{\mathrm{d}}]|^2}. \tag{3.60}$$

The denominator of this equation has roots at $\omega = \omega^{\pm} + j(\kappa + \Gamma_{\mathrm{m}})/4$ where $\omega^{\pm} = \Omega_{\mathrm{m}} \pm \sqrt{g^2 - (\kappa - \Gamma_{\mathrm{m}})^2/16}$. For large couplings, the spectrum looks like two peaks of width $(\Gamma_{\mathrm{m}} + \kappa)/2$ with splitting $2\sqrt{g^2 - (\kappa - \Gamma_{\mathrm{m}})^2/16} \approx 2g$. These are normal modes of the cavity and mechanical oscillator. The expression for the mechanical spectrum can then be re-written as

$$S_{bb}[\omega] = \frac{n_{\mathrm{m}}^{\mathrm{th}}\Gamma_{\mathrm{m}}\left(\kappa^2 + 4(\omega - \Omega_{\mathrm{m}})^2\right) + 4g^2 n_{\mathrm{c}}^{\mathrm{th}}\kappa}{\left((\frac{\Gamma_{\mathrm{m}}+\kappa}{2})^2 + 4(\omega - \omega^-)^2\right)\left((\frac{\Gamma_{\mathrm{m}}+\kappa}{2})^2 + 4(\omega - \omega^+)^2\right)}. \tag{3.61}$$

Integrating this equation, the final occupancy is

$$n_{\mathrm{m}}^{\mathrm{f}} = \frac{1}{2\pi}\int_{-\infty}^{\infty} S_{bb}[\omega]d\omega = \frac{(4g^2 + \kappa(\kappa + \Gamma_{\mathrm{m}}))\Gamma_{\mathrm{m}}n_{\mathrm{m}}^{\mathrm{th}} + 4g^2\kappa n_{\mathrm{c}}^{\mathrm{th}}}{(\kappa + \Gamma_{\mathrm{m}})(4g^2 + \kappa\Gamma_{\mathrm{m}})} \tag{3.62}$$

$$\approx \frac{(4g^2 + \kappa^2)\Gamma_{\mathrm{m}}n_{\mathrm{m}}^{\mathrm{th}} + 4g^2\kappa n_{\mathrm{c}}^{\mathrm{th}}}{\kappa(4g^2 + \kappa\Gamma_{\mathrm{m}})}. \tag{3.63}$$

3.1.7   Output field spectrum

I can substitute Equations 3.23-3.24 (re-written in terms of coefficients to simply the subsequent algebra) into Equation 2.88 for the output field to find $\hat{a}_{\text{out},1}$ and $\hat{a}_{\text{out},1}^{\dagger}$ (remember that this is for the transmission geometry; swap $N_1 \leftrightarrow N_2$ for the reflection geometry):

$$
\begin{aligned}
\hat{a}_{\text{out},1}[\omega] &= N_2\hat{\xi}_{\text{l}}[\omega] + N_1\hat{\xi}_{\text{r}}[\omega] + r_1[\omega]\hat{\xi}_{\text{m}}^{\dagger}[\omega - \omega_{\text{d}}] + r_2[\omega]\hat{\xi}_{\text{m}}[\omega - \omega_{\text{d}}] \quad\quad (3.64) \\
&\quad + r_3[\omega]\sum_i \sqrt{\frac{\kappa_i}{\kappa}}\hat{\xi}_i^{\dagger}[\omega - 2\omega_{\text{d}}] + r_4[\omega]\sum_i \sqrt{\frac{\kappa_i}{\kappa}}\hat{\xi}_i[\omega], \\
\hat{a}_{\text{out},1}^{\dagger}[-\omega] &= N_2^*\hat{\xi}_{\text{l}}^{\dagger}[-\omega] + N_1^*\hat{\xi}_{\text{r}}^{\dagger}[-\omega] + r_1^*[\omega]\hat{\xi}_{\text{m}}[-\omega + \omega_{\text{d}}] + r_2^*[\omega]\hat{\xi}_{\text{m}}^{\dagger}[-\omega + \omega_{\text{d}}] \quad\quad (3.65) \\
&\quad + r_3^*[\omega]\sum_i \sqrt{\frac{\kappa_i}{\kappa}}\hat{\xi}_i[-\omega + 2\omega_{\text{d}}] + r_4^*[\omega]\sum_i \sqrt{\frac{\kappa_i}{\kappa}}\hat{\xi}_i^{\dagger}[-\omega].
\end{aligned}
$$

The spectral density of the output field operators is

$$
\begin{aligned}
S_{a_{\text{out}}a_{\text{out}}}[\omega] &= \left\langle \hat{a}_{\text{out},1}^{\dagger}[-\omega]\hat{a}_{\text{out},1}[\omega]\right\rangle \quad\quad (3.66) \\
&= |r_1[\omega]|^2 \left\langle \hat{\xi}_{\text{m}}[-\omega + \omega_{\text{d}}]\hat{\xi}_{\text{m}}^{\dagger}[\omega - \omega_{\text{d}}]\right\rangle + |r_2[\omega]|^2 \left\langle \hat{\xi}_{\text{m}}^{\dagger}[-\omega + \omega_{\text{d}}]\hat{\xi}_{\text{m}}[\omega - \omega_{\text{d}}]\right\rangle \\
&\quad + |r_3[\omega]|^2 \sum_{i,j} \frac{\sqrt{\kappa_i\kappa_j}}{\kappa} \left\langle \hat{\xi}_i[-\omega + 2\omega_{\text{d}}]\hat{\xi}_j^{\dagger}[\omega - 2\omega_{\text{d}}]\right\rangle \\
&\quad + |r_4[\omega]|^2 \sum_{i,j} \frac{\sqrt{\kappa_i\kappa_j}}{\kappa} \left\langle \hat{\xi}_i^{\dagger}[-\omega]\hat{\xi}_j[\omega]\right\rangle \quad\quad (3.67) \\
&\quad + |N_2|^2 \left\langle \hat{\xi}_{\text{l}}^{\dagger}[-\omega]\hat{\xi}_{\text{l}}[\omega]\right\rangle + |N_1|^2 \left\langle \hat{\xi}_{\text{r}}^{\dagger}[-\omega]\hat{\xi}_{\text{r}}[\omega]\right\rangle \\
&\quad + N_2 r_4^*[\omega]\sum_i \sqrt{\frac{\kappa_i}{\kappa}} \left\langle \hat{\xi}_i^{\dagger}[-\omega]\hat{\xi}_{\text{l}}[\omega]\right\rangle + N_2^* r_4[\omega]\sum_i \sqrt{\frac{\kappa_i}{\kappa}} \left\langle \hat{\xi}_{\text{l}}^{\dagger}[-\omega]\hat{\xi}_i[\omega]\right\rangle \\
&\quad + N_1 r_4^*[\omega]\sum_i \sqrt{\frac{\kappa_i}{\kappa}} \left\langle \hat{\xi}_i^{\dagger}[-\omega]\hat{\xi}_{\text{r}}[\omega]\right\rangle + N_1^* r_4[\omega]\sum_i \sqrt{\frac{\kappa_i}{\kappa}} \left\langle \hat{\xi}_{\text{r}}^{\dagger}[-\omega]\hat{\xi}_i[\omega]\right\rangle \\
&= |r_1[\omega]|^2 \left(n_{\text{m}}^{\text{th}} + 1\right) + |r_2[\omega]|^2 n_{\text{m}}^{\text{th}} + |r_3[\omega]|^2 \left(n_{\text{c}}^{\text{th}} + 1\right) + |r_4[\omega]|^2 n_{\text{c}}^{\text{th}} \\
&\quad + \left(|N_2|^2 + N_2 r_4^*[\omega]\sqrt{\frac{\kappa_{\text{l}}}{\kappa}} + N_2^* r_4[\omega]\sqrt{\frac{\kappa_{\text{l}}}{\kappa}}\right) n_{\text{l}}^{\text{th}} \quad\quad (3.68) \\
&\quad + \left(|N_1|^2 + N_1 r_4^*[\omega]\sqrt{\frac{\kappa_{\text{l}}}{\kappa}} + N_1^* r_4[\omega]\sqrt{\frac{\kappa_{\text{l}}}{\kappa}}\right) n_{\text{r}}^{\text{th}}.
\end{aligned}
$$

Remember that $n_c^{th} = \kappa^{-1} \sum_i \kappa_i n_i^{th}$ for $i = \{l, r, 0\}$ and that if n_l^{th} or n_r^{th} is nonzero, n_c^{th} has a lower bound on its possible values. Re-written in terms of the final occupancy, the output spectrum is

$$
\begin{aligned}
S_{a_{out}a_{out}}[\omega] &= |r_1[\omega]|^2 \frac{\Gamma_{tot}}{\Gamma_m}(n_m^f + 1) + |r_2[\omega]|^2 \frac{\Gamma_{tot}}{\Gamma_m} n_m^f \\
&+ \left(|r_3[\omega]|^2 - |r_1[\omega]|^2 \frac{(1+n_m^0)\Gamma_{opt}}{\Gamma_m} - |r_2[\omega]|^2 \frac{n_m^0 \Gamma_{opt}}{\Gamma_m} \right)(n_c^{th} + 1) \\
&+ \left(|r_4[\omega]|^2 - |r_2[\omega]|^2 \frac{(1+n_m^0)\Gamma_{opt}}{\Gamma_m} - |r_1[\omega]|^2 \frac{n_m^0 \Gamma_{opt}}{\Gamma_m} \right) n_c^{th} \qquad (3.69) \\
&+ \left(|N_2|^2 + N_2 r_4^*[\omega] \sqrt{\frac{\kappa_l}{\kappa}} + N_2^* r_4[\omega] \sqrt{\frac{\kappa_l}{\kappa}} \right) n_l^{th} \\
&+ \left(|N_1|^2 + N_1 r_4^*[\omega] \sqrt{\frac{\kappa_l}{\kappa}} + N_1^* r_4[\omega] \sqrt{\frac{\kappa_l}{\kappa}} \right) n_r^{th}.
\end{aligned}
$$

Re-writing the different coefficients in terms of effective mechanical susceptibility gives

$$
|r_1[\omega]|^2 = g^2 \kappa_l \Gamma_m |\chi_c[\omega]|^2 |\chi_{m,eff}[-\omega + \omega_d]|^2, \qquad (3.70)
$$

$$
|r_2[\omega]|^2 = g^2 \kappa_l \Gamma_m |\chi_c[\omega]|^2 |\chi_{m,eff}[\omega - \omega_d]|^2, \qquad (3.71)
$$

$$
|r_3[\omega]|^2 = g^4 \kappa \kappa_l |\chi_c[\omega]|^2 |\chi_c[-\omega + 2\omega_d]|^2 |\chi_{m,eff}[\omega - \omega_d] - \chi_{m,eff}^*[-\omega + \omega_d]|^2, \qquad (3.72)
$$

$$
|r_4[\omega]|^2 = \kappa \kappa_l |\chi_c[\omega]|^2 |1 - g^2 \chi_c[\omega](\chi_{m,eff}[\omega - \omega_d] - \chi_{m,eff}^*[-\omega + \omega_d])|^2, \qquad (3.73)
$$

$$
\sqrt{\frac{\kappa_l}{\kappa}} (N_i r_4^*[\omega] + N_i^* r_4[\omega])
$$
$$
= -2\kappa_l \mathrm{Re}\left[N_i^* \chi_c[\omega] \left(1 - g^2 \chi_c[\omega] (\chi_{m,eff}[\omega - \omega_d] - \chi_{m,eff}^*[-\omega + \omega_d]) \right) \right]. \qquad (3.74)
$$

3.1.8 Limiting cases of the output spectrum

I assume from here on that the feed line has a purely real impedance: $N_2 = 1$, $N_1 = 0$. These results are now valid for either the transmission or reflection geometry. I also assume that measurements made with a detuned drive are done with a system in the far resolved sideband regime. Measurements with an on-resonance drive are still general for either sideband regime.

If the cavity is driven with a close to optimally red-detuned drive at $\omega_r \approx \bar{\omega}_c - \Omega_m$, the sideband enhanced by the cavity is the upper sideband, so I will set $\chi_{m,eff}[-\omega + \omega_r] = 0$ and $\chi_c[-\omega + 2\omega_r] = 0$. Not making the weak-coupling limit assumptions, the output spectrum is

$$
S_{a_{out}a_{out}}[\omega] = n_l^{th} + \frac{\kappa_l |\chi_c[\omega]|^2 \left(g^2 \Gamma_m (n_m^{th} - n_l^{th})|\chi_m[\omega - \omega_d]|^2 + \kappa(n_c^{th} - n_l^{th}) \right)}{|1 + g^2 \chi_c[\omega]\chi_m[\omega - \omega_d]|^2}. \qquad (3.75)
$$

To get this expression, I used the identities $\chi_m[\omega] + \chi_m^*[\omega] = \Gamma_m |\chi_m[\omega]|^2$ and $\chi_c[\omega] + \chi_c^*[\omega] = \kappa |\chi_c[\omega]|^2$. In the weak coupling limit, I can assume that $n_m^0 = 0$ and $\Gamma_{opt} = 4g_r^2/\kappa$. I will also assume that the drive is very close to perfectly detuned. This allows me to only keep the $\chi_c[\omega]$'s not found with more narrowly varying features. I will set the others to their approximate value near cavity resonance $\chi_c[\omega_c] = 2/\kappa$. The output spectrum in the weak coupling limit is

$$S_{a_{out}a_{out}}[\omega] = n_l^{th} + \kappa\kappa_l \left(n_c^{th} - n_l^{th}\right) |\chi_c[\omega]|^2 + \frac{4g_r^2 \kappa_l \Gamma_{tot}}{\kappa^2} \left(n_m^f - 2n_c^{th} + n_l^{th}\right) |\chi_{m,eff}[\omega - \omega_r]|^2 , (3.76)$$

which exhibits a constant background due to extra input fluctuations, a wide spectral component filtered by the cavity susceptibility due to extra thermal cavity fluctuations, and a narrow feature filtered by the mechanical susceptibility due to the final occupancy of the mechanical oscillator.

If the cavity is instead driven with a blue-detuned drive at $\omega_b \approx \overline{\omega}_c + \Omega_m$, the sideband of interest is the lower sideband and I set $\chi_m[\omega - \omega_b] = 0$ and $\chi_c[-\omega + 2\omega_b] = 0$. I once again assume weak coupling and a close to perfectly detuned drive, but in this case, that requires setting $n_m^0 = -1$ and $\Gamma_{opt} = -4g_b^2/\kappa$. The output spectrum is

$$\begin{aligned} S_{a_{out}a_{out}}[\omega] &= n_l^{th} + \kappa\kappa_l \left(n_c^{th} - n_l^{th}\right) |\chi_c[\omega]|^2 \\ &\quad + \frac{4g_b^2 \kappa_l \Gamma_{tot}}{\kappa^2} \left(n_m^f + 1 + 2n_c^{th} - n_l^{th}\right) |\chi_{m,eff}[-\omega + \omega_b]|^2 . \end{aligned} \tag{3.77}$$

It is important to notice how the presence of thermal cavity occupancy n_c^{th} and extra input noise n_l^{th} affects the red and blue-detuned cases. In the former (latter), cavity occupancy decreases (increases) the size of the sideband, while input noise increases (decreases) the size of the sideband. It is thus extremely important to independently measure n_c^{th} and n_l^{th} in order to correctly infer the mechanical occupancy from a measurement of the output fields.

The last case I'll consider is if the cavity drive is applied on-resonance at $\overline{\omega}_c$, no longer making any assumption about the relative values of κ and Ω_m. For this case, all of the χ's are important, but the expression can be simplified a bit by the fact that $\chi_c[-\omega + 2\overline{\omega}_c] = \chi_c^*[\omega]$ and the two

sidebands are far separated in frequency compared to their widths. The output spectrum is

$$S_{a_{\text{out}}a_{\text{out}}}[\omega] \approx n_{\text{l}}^{\text{th}} + \kappa\kappa_{\text{l}}\left(n_{\text{c}}^{\text{th}} - n_{\text{l}}^{\text{th}}\right)|\chi_{\text{c}}[\omega]|^2 \tag{3.78}$$
$$+ \frac{4g^2\kappa_{\text{l}}\Gamma_{\text{m}}}{(\kappa^2 + 4\Omega_{\text{m}}^2)^2}\left(\left(n_{\text{m}}^{\text{f}} - 2n_{\text{c}}^{\text{th}} + n_{\text{l}}^{\text{th}}\right)\kappa^2 + 4\left(n_{\text{m}}^{\text{f}} - n_{\text{l}}^{\text{th}}\right)\Omega_{\text{m}}^2\right)|\chi_{\text{m}}[\omega - \overline{\omega}_{\text{c}}]|^2$$
$$+ \frac{4g^2\kappa_{\text{l}}\Gamma_{\text{m}}}{(\kappa^2 + 4\Omega_{\text{m}}^2)^2}\left(\left(n_{\text{m}}^{\text{f}} + 1 + 2n_{\text{c}}^{\text{th}} - n_{\text{l}}^{\text{th}}\right)\kappa^2 + 4\left(n_{\text{m}}^{\text{f}} + 1 + n_{\text{l}}^{\text{th}}\right)\Omega_{\text{m}}^2\right)|\chi_{\text{m}}[-\omega + \overline{\omega}_{\text{c}}]|^2.$$

To get this expression, I used the approximations

$$\chi_{\text{c}}[\omega]^2\chi_{\text{m}}[\omega - \overline{\omega}_{\text{c}}] + \chi_{\text{c}}^*[\omega]^2\chi_{\text{m}}^*[\omega - \overline{\omega}_{\text{c}}] \quad \approx \quad \frac{\Gamma_{\text{m}}}{4}\left(\kappa^2 - 4\Omega_{\text{m}}\right)|\chi_{\text{c}}[\omega]|^4\,|\chi_{\text{m}}[\omega - \overline{\omega}_{\text{c}}]|^2, \quad (3.79)$$

$$\chi_{\text{c}}[\omega]\chi_{\text{m}}[\omega - \overline{\omega}_{\text{c}}] + \chi_{\text{c}}^*[\omega]\chi_{\text{m}}^*[\omega - \overline{\omega}_{\text{c}}] \quad \approx \quad \frac{\kappa\Gamma_{\text{m}}}{2}|\chi_{\text{c}}[\omega]|^2\,|\chi_{\text{m}}[\omega - \overline{\omega}_{\text{c}}]|^2, \tag{3.80}$$

$$\chi_{\text{c}}[\omega]^2\chi_{\text{m}}^*[-\omega + \overline{\omega}_{\text{c}}] + \chi_{\text{c}}^*[\omega]^2\chi_{\text{m}}[-\omega + \overline{\omega}_{\text{c}}] \quad \approx \quad \frac{\Gamma_{\text{m}}}{4}\left(\kappa^2 - 4\Omega_{\text{m}}\right)|\chi_{\text{c}}[\omega]|^4\,|\chi_{\text{m}}[-\omega + \overline{\omega}_{\text{c}}]|^2, (3.81)$$

$$\chi_{\text{c}}[\omega]\chi_{\text{m}}^*[-\omega + \overline{\omega}_{\text{c}}] + \chi_{\text{c}}^*[\omega]\chi_{\text{m}}[-\omega + \overline{\omega}_{\text{c}}] \quad \approx \quad \frac{\kappa\Gamma_{\text{m}}}{2}|\chi_{\text{c}}[\omega]|^2\,|\chi_{\text{m}}[-\omega + \overline{\omega}_{\text{c}}]|^2. \tag{3.82}$$

The first two approximations are only good for $\omega \approx \overline{\omega}_{\text{c}} + \Omega_{\text{m}}$, while the second two are only good for $\omega \approx \overline{\omega}_{\text{c}} - \Omega_{\text{m}}$. It is interesting to see how n_{c}^{th} and n_{l}^{th} affect the on-resonance drive measurement differently in the resolved or unresolved sideband limits. In the resolved sideband limit, cavity noise is irrelevant, as the sidebands are not located near the cavity frequency, whereas input noise interferes with the mechanical occupancy with the opposite sign as it did in the red and blue-detuned drive cases. In the unresolved sideband limit, the extra noises add with the same sign as for the red and blue-detuned drive cases.

In all drive cases, if the extra noises are zero, the upper sideband is proportional to n_{m}^{f}, while the lower sideband is proportional to $n_{\text{m}}^{\text{f}} + 1$. This is generally referred to as 'sideband asymmetry'. This asymmetry indicates the quantum nature of the effective mechanical oscillator. When viewed in terms of the backaction mechanical occupancy introduced above, the asymmetry can also be viewed as a consequence of the photon field shot noise (as is discussed in [81]).

3.1.9 Dressed cavity response

In this section, I will calculate the response of the cavity to a small probe tone at ω_{p}, in the presence of a strong drive tone at ω_{d}. The amplitude of the probe tone is small enough that it

should not change the cavity or mechanical parameters. If I were to start from Equations 2.85-2.88, I would use the input $\hat{a}_{\mathrm{in}} = \alpha_{\mathrm{in,d}}e^{j\omega_{\mathrm{d}}t} + \alpha_{\mathrm{in,p}}e^{j\omega_{\mathrm{p}}t}$, set all of the noise operators to zero, and then linearize around the driving field. However, I have already done a lot of this work in the previous sections, and I can just use the solution for $\hat{a}_1$ (Equation 3.23), making the replacements $\hat{\xi}_{\mathrm{l}}[\omega] \to \alpha_{\mathrm{in,p}}\delta[\omega - \omega_{\mathrm{p}}]$ and $\hat{\xi}_{\mathrm{r,0,m}} = 0$:

$$\hat{a}_1[\omega] = \frac{\chi_{\mathrm{c}}[\omega]\left(1 - g^2\chi_{\mathrm{c}}^*[-\omega + 2\omega_{\mathrm{d}}]\left(\chi_{\mathrm{m}}[\omega - \omega_{\mathrm{d}}] - \chi_{\mathrm{m}}^*[-\omega + \omega_{\mathrm{d}}]\right)\right)}{1 + g^2\left(\chi_{\mathrm{c}}[\omega] - \chi_{\mathrm{c}}^*[-\omega + 2\omega_{\mathrm{d}}]\right)\left(\chi_{\mathrm{m}}[\omega - \omega_{\mathrm{d}}] - \chi_{\mathrm{m}}^*[-\omega + \omega_{\mathrm{d}}]\right)}\sqrt{\kappa_{\mathrm{l}}}\alpha_{\mathrm{in,p}}\delta[0]. \quad (3.83)$$

Substituting this into the expression for the dressed cavity response (Equation 2.89), I find (remember that $i = 2$ for the transmission geometry and $i = 1$ for the reflection geometry) that this quantity is

$$S_{i1}[\omega_{\mathrm{p}}] = \frac{\alpha_{\mathrm{out,p}}}{\alpha_{\mathrm{in,p}}} = N_i - \sqrt{\kappa_{\mathrm{l}}}\frac{\hat{a}_1[\omega_{\mathrm{p}}]}{\alpha_{\mathrm{in,p}}\delta[0]} \quad (3.84)$$

$$= \boxed{N_2 - \kappa_{\mathrm{l}}\frac{\chi_{\mathrm{c}}[\omega_{\mathrm{p}}]\left(1 - g^2\chi_{\mathrm{c}}^*[-\omega_{\mathrm{p}} + 2\omega_{\mathrm{d}}]\left(\chi_{\mathrm{m}}[\omega_{\mathrm{p}} - \omega_{\mathrm{d}}] - \chi_{\mathrm{m}}^*[-\omega_{\mathrm{p}} + \omega_{\mathrm{d}}]\right)\right)}{1 + g^2\left(\chi_{\mathrm{c}}[\omega] - \chi_{\mathrm{c}}^*[-\omega_{\mathrm{p}} + 2\omega_{\mathrm{d}}]\right)\left(\chi_{\mathrm{m}}[\omega_{\mathrm{p}} - \omega_{\mathrm{d}}] - \chi_{\mathrm{m}}^*[-\omega_{\mathrm{p}} + \omega_{\mathrm{d}}]\right)}} \quad (3.85)$$

$$= \boxed{N_2 - \kappa_{\mathrm{l}}\chi_{\mathrm{c}}[\omega_{\mathrm{p}}] + g^2\kappa_{\mathrm{l}}\chi_{\mathrm{c}}^2[\omega_{\mathrm{p}}]\left(\chi_{\mathrm{m,eff}}[\omega_{\mathrm{p}} - \omega_{\mathrm{d}}] - \chi_{\mathrm{m,eff}}^*[-\omega_{\mathrm{p}} + \omega_{\mathrm{d}}]\right)}. \quad (3.86)$$

The second boxed expression makes it clear that in the absence of drive photons ($g = 0$), the cavity resumes its bare response, and that for large drives, there are extra features shaped like the total mechanical susceptibility.

This dressed response is zero on resonance for an optimally red-detuned drive in the resolved sideband limit when $4g^2/\Gamma_{\mathrm{m}} = 2\kappa_{\mathrm{l}} - \kappa$. This is the point where the impedance between itinerant photons in the microwave drive is matched to the impedance of the circuit. In this case, those photons are turned into mechanical phonons at the same rate that phonons are dissipated from the mechanical oscillator, and so they are completely absorbed. Note that this point is only possible for an over-coupled circuit in the reflection geometry ($\kappa_{\mathrm{l}} > \kappa/2$).

3.2 Two cavity drives

Two very interesting effects appeared in the previous section for the case of an on-resonance drive: sideband asymmetry of the measurement (see Equation 3.79) and quantum backaction of

photon fluctuations on the mechanical oscillator (see Equation 3.59). If the system is far in the re-solved sideband regime, an on-resonant drive results in extremely attenuated sidebands. Therefore, I might like to apply a red or blue-detuned drive in order to enhance these sidebands. However, for the quantum backaction measurement, this will result in a very large dynamic radiation pressure force, dwarfing the quantum backaction. I can get around this fact by applying two drive tones, one red-detuned and one blue-detuned, such that the net dynamic radiation pressure force is zero, once again allowing access to the quantum backaction piece.

A similar difficulty and solution arise for the sideband asymmetry measurement. The asymmetry is most visible when the mechanical oscillator has very few phonons, so I would like to apply a red-detuned drive to cool the oscillator to low occupancy. Unfortunately, this will even further sup-press the lower sideband. However, adding a second, blue-detuned, drive of smaller amplitude than the red-detuned one will allow measurement of its lower sideband while still cooling the oscillator.

Thus, the ideal strategy for seeing both quantum backaction and sideband asymmetry in the far resolved sideband regime is to apply two drives, one red-detuned and one blue-detuned. In this section I will follow a similar procedure to the previous section for one drive, only this time I will include a second drive. Therefore, some of the discussion and definitions of the quantities I calculate will not be repeated. This situation will require more assumptions than the one-drive case, namely that the drives are close to optimally red and blue-detuned and that the system is in the far sideband resolved regime.

3.2.1 Input assumptions

In this section, I will once again solve Equations 2.85-2.88, this time given that there are two inputs, one approximately red-detuned at $\omega_r \approx \omega_c - \Omega_m$ and one approximately blue-detuned at $\omega_b \approx \omega_c + \Omega_m$:

$$\alpha_{\text{in}}[t] = \alpha_{\text{in,r}} e^{j\omega_r t} + \alpha_{\text{in,b}} e^{j\omega_b t}. \tag{3.87}$$

I can assume that $\hat{a}$ and $\hat{a}_{\text{out}}$ have large components at ω_{r} and ω_{b} and smaller components at other frequencies and that $\hat{b}$ also has a steady state value and smaller fluctuating piece:

$$\hat{a}[t] \quad = \alpha_{\text{r}} e^{j\phi_{\text{r}}} e^{j\omega_{\text{r}}t} + \alpha_{\text{b}} e^{j\phi_{\text{b}}} e^{j\omega_{\text{b}}t} + \hat{a}_1[t], \qquad\qquad \hat{b}[t] = b_0[t] + \hat{b}_1[t], \qquad\qquad (3.88)$$

$$\hat{a}^{\dagger}[t] \quad = \alpha_{\text{r}} e^{-j\phi_{\text{r}}} e^{-j\omega_{\text{r}}t} + \alpha_{\text{b}} e^{-j\phi_{\text{b}}} e^{-j\omega_{\text{b}}t} + \hat{a}_1^{\dagger}[t], \qquad \hat{b}^{\dagger}[t] = b_0^*[t] + \hat{b}_1^{\dagger}[t],$$

$$\hat{a}_{\text{out}}[t] = \alpha_{\text{out,r}} e^{j\omega_{\text{r}}t} + \alpha_{\text{out,b}} e^{j\omega_{\text{b}}t} + \hat{a}_{\text{out,1}}[t]. \qquad\qquad (3.89)$$

Here, $\alpha_{\text{in,0}}$ and $\alpha_{\text{out,0}}$ are generally complex, but α_{r} and α_{b} are real and are related to the photon numbers by $n_{\text{r}} = \alpha_{\text{r}}^2$ and $n_{\text{b}} = \alpha_{\text{b}}^2$. I apologize for the confusing notation between the red drive photon number n_{r} and the right port thermal photon occupancy n_{r}^{th}. However, the superscript and context should always distinguish the two symbols.

3.2.2 Steady state solution

To zero-ith order (*i.e.* when $\hat{a}_1$, $\hat{b}_1$, and the $\hat{\xi}_i$'s are zero), solving the equations of motion gives

$$b_0[t] \quad = \frac{jg_0 \left(1 + 2\left(\alpha_{\text{r}}^2 + \alpha_{\text{b}}^2 + 2\alpha_{\text{r}}\alpha_{\text{b}} \cos\left[(\omega_{\text{b}} - \omega_{\text{r}})t + \phi_{\text{b}} - \phi_{\text{r}}\right]\right)\right)}{\Gamma_{\text{m}} - 2j\Omega_{\text{m}}}, \qquad (3.90)$$

$$\alpha_{\text{in,r}} \quad = \frac{\alpha_{\text{r}} e^{j\phi_{\text{r}}}}{\sqrt{\kappa_{\text{l}}}\chi_{\text{c}}[\omega_{\text{r}}]}, \qquad \alpha_{\text{in,b}} = \frac{\alpha_{\text{b}} e^{j\phi_{\text{b}}}}{\sqrt{\kappa_{\text{l}}}\chi_{\text{c}}[\omega_{\text{b}}]}, \qquad\qquad (3.91)$$

$$\alpha_{\text{out,r}} \quad = (N_2 - \kappa_{\text{l}}\chi_{\text{c}}[\omega_{\text{r}}])\alpha_{\text{in,r}}, \qquad \alpha_{\text{out,b}} = (N_2 - \kappa_{\text{l}}\chi_{\text{c}}[\omega_{\text{b}}])\alpha_{\text{in,b}}, \qquad (3.92)$$

where $\overline{\omega}_{\text{c}} = \omega_{\text{c}} + g_0(b_0[t] + b_0^*[t])$ is the new, shifted, cavity resonance frequency. The number of drive photons in the cavity and the output power from each drive are the same as if they were used independently.

3.2.3 Linearized equations of motion

Plugging the derived steady-state values into the equations of motion gives the linearized equations of motion:

$$
\dot{\hat{a}}_1[t] = -\left(\frac{\kappa}{2} - j\overline{\omega}_c\right)\hat{a}_1[t] + j\left(e^{j(\omega_r t + \phi_r)}g_r + e^{j(\omega_r t + \phi_b)}g_b\right)\left(\hat{b}_1[t] + \hat{b}_1^\dagger[t]\right) \tag{3.93}
$$
$$
+ \sum_{i=l,r,0} \sqrt{\kappa_i}\hat{\xi}_i[t],
$$

$$
\dot{\hat{b}}_1[t] = -\left(\frac{\Gamma_m}{2} - j\Omega_m\right)\hat{b}_1[t] + j\left(e^{-j(\omega_r t + \phi_r)}g_r + e^{-j(\omega_b t + \phi_b)}g_b\right)\hat{a}_1[t] \tag{3.94}
$$
$$
+ j\left(e^{j(\omega_r t + \phi_r)}g_r + e^{j(\omega_b t + \phi_b)}g_b\right)\hat{a}_1^\dagger[t] + \sqrt{\Gamma_m}\hat{\xi}_m[t],
$$

where $g_r \equiv g_0\sqrt{n_r}$ and $g_b \equiv g_0\sqrt{n_b}$ are the photon enhanced coupling rates. Multiplying these equations by $e^{-j\omega t}$ and integrating gives the linearized equations of motion and their conjugates in the frequency domain:

$$
\frac{\hat{a}_1[\omega]}{\chi_c[\omega]} = jg_r e^{j\phi_r}(\hat{b}_1[\omega - \omega_r] + \hat{b}_1^\dagger[\omega - \omega_r]) \tag{3.95}
$$
$$
+ jg_b e^{j\phi_b}(\hat{b}_1[\omega - \omega_b] + \hat{b}_1^\dagger[\omega - \omega_b]) + \sum_{i=l,r,0} \sqrt{\kappa_i}\hat{\xi}_i[\omega],
$$

$$
\frac{\hat{a}_1^\dagger[-\omega]}{\chi_c^*[\omega]} = -jg_r e^{-j\phi_r}(\hat{b}_1^\dagger[-\omega + \omega_r] + \hat{b}_1[-\omega + \omega_r]) \tag{3.96}
$$
$$
- jg_b e^{-j\phi_b}(\hat{b}_1^\dagger[-\omega + \omega_b] + \hat{b}_1[-\omega + \omega_b]) + \sum_{i=l,r,0} \sqrt{\kappa_i}\hat{\xi}_i^\dagger[-\omega],
$$

$$
\frac{\hat{b}_1[\omega]}{\chi_m[\omega]} = jg_r\left(e^{j\phi_r}\hat{a}_1^\dagger[\omega - \omega_r] + e^{-j\phi_r}\hat{a}_1[\omega + \omega_r]\right) \tag{3.97}
$$
$$
+ jg_b\left(e^{j\phi_b}\hat{a}_1^\dagger[\omega - \omega_b] + e^{-j\phi_b}\hat{a}_1[\omega + \omega_b]\right) + \sqrt{\Gamma_m}\hat{\xi}_m[\omega],
$$

$$
\frac{\hat{b}_1^\dagger[-\omega]}{\chi_m^*[\omega]} = -jg_r\left(e^{-j\phi_r}\hat{a}_1[-\omega + \omega_r] + e^{j\phi_r}\hat{a}_1^\dagger[-\omega - \omega_r]\right) \tag{3.98}
$$
$$
- jg_b\left(e^{-j\phi_b}\hat{a}_1[-\omega + \omega_b] + e^{j\phi_b}\hat{a}_1^\dagger[-\omega - \omega_b]\right) + \sqrt{\Gamma_m}\hat{\xi}_m^\dagger[-\omega],
$$

where, as in the one-drive case, $\chi_c[\omega] \equiv \left[\frac{\kappa}{2} + j(\omega - \overline{\omega}_c)\right]^{-1}$ and $\chi_m[\omega] \equiv \left[\frac{\Gamma_m}{2} + j(\omega - \Omega_m)\right]^{-1}$ are the cavity and mechanical susceptibilities.

Unlike in the one-drive case, the many frequencies in these four equations mean that they are an infinite set of coupled equations and can not be written in terms of only four variables, and

thus cannot be solved directly for $\hat{a}_1[\omega]$ and $\hat{b}_1[\omega]$. However, I can eliminate all of the $\hat{a}_1$'s and write them as equations for just the $\hat{b}_1$'s. This makes sense because I will first only be interested in the state of the mechanics and will not care about the cavity fields until I calculate the output spectrum. These equations for only the $\hat{b}_1$'s are the following:

$$\frac{\hat{b}_1[\omega]}{\chi_{\mathrm{m}}[\omega]} = c_0[\omega]\left(\hat{b}_1[\omega] + \hat{b}_1^\dagger[\omega]\right) - c_1^*[-\omega]\left(\hat{b}_1[\omega - \Delta W] + \hat{b}_1^\dagger[\omega - \Delta W]\right) \qquad (3.99)$$
$$+ c_1[\omega]\left(\hat{b}_1[\omega + \Delta W] + \hat{b}_1^\dagger[\omega + \Delta W]\right) + \hat{c}_{\mathrm{noise}}[\omega],$$

$$\frac{\hat{b}_1^\dagger[-\omega]}{\chi_{\mathrm{m}}^*[\omega]} = c_0^*[\omega]\left(\hat{b}_1^\dagger[-\omega] + \hat{b}_1[-\omega]\right) - c_1[-\omega]\left(\hat{b}_1^\dagger[-\omega + \Delta W] + \hat{b}_1[-\omega + \Delta W]\right) \quad (3.100)$$
$$+ c_1^*[\omega]\left(\hat{b}_1^\dagger[-\omega - \Delta W] + \hat{b}_1[-\omega - \Delta W]\right) + \hat{c}_{\mathrm{noise}}^\dagger[-\omega],$$

$$c_0[\omega] = -g_{\mathrm{r}}^2\left(\chi_{\mathrm{c}}[\omega + \omega_{\mathrm{r}}] - \chi_{\mathrm{c}}^*[-\omega + \omega_{\mathrm{r}}]\right) - g_{\mathrm{b}}^2\left(\chi_{\mathrm{c}}[\omega + \omega_{\mathrm{b}}] - \chi_{\mathrm{c}}^*[-\omega + \omega_{\mathrm{b}}]\right), \qquad (3.101)$$

$$c_1[\omega] = -e^{-j(\phi_{\mathrm{b}} - \phi_{\mathrm{r}})}g_{\mathrm{r}}g_{\mathrm{b}}\left(\chi_{\mathrm{c}}[\omega + \omega_{\mathrm{b}}] - \chi_{\mathrm{c}}^*[-\omega + \omega_{\mathrm{r}}]\right), \qquad (3.102)$$

$$\hat{c}_{\mathrm{noise}}[\omega] = jg_{\mathrm{r}}e^{-j\phi_{\mathrm{r}}}\chi_{\mathrm{c}}[\omega + \omega_{\mathrm{r}}]\sum_i \sqrt{\kappa_i}\hat{\xi}_i[\omega + \omega_{\mathrm{r}}]$$
$$+ jg_{\mathrm{r}}e^{j\phi_{\mathrm{r}}}\chi_{\mathrm{c}}^*[-\omega + \omega_{\mathrm{r}}]\sum_i \sqrt{\kappa_i}\hat{\xi}_i^\dagger[\omega - \omega_{\mathrm{r}}] \qquad (3.103)$$
$$+ jg_{\mathrm{b}}e^{-j\phi_{\mathrm{b}}}\chi_{\mathrm{c}}[\omega + \omega_{\mathrm{b}}]\sum_i \sqrt{\kappa_i}\hat{\xi}_i[\omega + \omega_{\mathrm{b}}]$$
$$+ jg_{\mathrm{b}}e^{j\phi_{\mathrm{b}}}\chi_{\mathrm{c}}^*[-\omega + \omega_{\mathrm{r}}]\sum_i \sqrt{\kappa_i}\hat{\xi}_i^\dagger[\omega - \omega_{\mathrm{b}}] + \sqrt{\Gamma_{\mathrm{m}}}\hat{\xi}_{\mathrm{m}}[\omega].$$

Here, $\Delta W = \omega_{\mathrm{b}} - \omega_{\mathrm{r}}$ and I note that $c_0[\omega] = -c_0^*[-\omega]$.

3.2.4 Assumptions used to simplify the 2-drive case

Equations 3.99 couple the field $\hat{b}_1[\omega]$ to $\hat{b}_1$ fields and their daggers at all frequencies $\omega + s\Delta W$, for integer s. Therefore, in order to solve these equations for $\hat{b}[\omega]$, I must approximate away terms that are small to obtain a solvably small system of equations. I will eventually be interested in calculating the mechanical spectrum near $\omega = \Omega_{\mathrm{m}}$. Thus, I am interested in solving for $\hat{b}[\Omega_{\mathrm{m}}]$ and $\hat{b}^\dagger[-\Omega_{\mathrm{m}}]$. The fields $\hat{b}_1[\omega]$ and $\hat{b}_1^\dagger[\omega]$ are proportional to $\chi_{\mathrm{m}}[\omega]$ and $\chi_{\mathrm{m}}^*[-\omega]$, respectively. Thus, if $\chi_{\mathrm{m}}[\omega + s\Delta W]$ is negligible for some integer s, then so is $\hat{b}_1[\omega + s\Delta W]$. The only χ_{m}'s that are significant near $\omega = \Omega_{\mathrm{m}}$ in the resolved sideband limit are $\chi_{\mathrm{m}}[\omega]$, $\chi_{\mathrm{m}}[-\omega + \Delta W]$, and their complex conjugates. Thus, the only fields that contribute near $\omega = \Omega_{\mathrm{m}}$ are $\hat{b}[\omega]$, $\hat{b}^\dagger[-\omega]$, $\hat{b}[-\omega + \Delta W]$, and

$\hat{b}^\dagger[\omega - \Delta W]$. Note that if the system were not in the resolved sideband limit, it would not be possible to truncate the equations like this and the system would not be easily solvable. The field $\hat{b}[\omega]$ only couples to $\hat{b}^\dagger[\omega - \Delta W]$ and $\hat{b}^\dagger[-\omega]$ only couples to $\hat{b}[\omega - \Delta W]$, so this reduces Equations 3.99 to two coupled equations to solve for $\hat{b}[\omega]$ and two for $\hat{b}^\dagger[-\omega]$:

$$\frac{\hat{b}_1[\omega]}{\chi_{\mathrm{m}}[\omega]} = c_0[\omega]\hat{b}_1[\omega] - c_1^*[-\omega]\hat{b}_1^\dagger[\omega - \Delta W] + \hat{c}_{\mathrm{noise}}[\omega], \tag{3.104}$$

$$\frac{\hat{b}_1^\dagger[\omega - \Delta W]}{\tilde{\chi}_{\mathrm{m}}^*[\omega]} = \tilde{c}_0^*[\omega]\hat{b}_1^\dagger[\omega - \Delta W] - \tilde{c}_1[-\omega]\hat{b}_1[\omega] + \hat{\tilde{c}}_{\mathrm{noise}}^\dagger[-\omega], \tag{3.105}$$

$$\frac{\hat{b}_1^\dagger[-\omega]}{\chi_{\mathrm{m}}^*[\omega]} = c_0^*[\omega]\hat{b}_1^\dagger[-\omega] - c_1[-\omega]\hat{b}_1[\Delta W - \omega] + \hat{c}_{\mathrm{noise}}^\dagger[-\omega], \tag{3.106}$$

$$\frac{\hat{b}_1[\Delta W - \omega]}{\tilde{\chi}_{\mathrm{m}}[\omega]} = \tilde{c}_0[\omega]\hat{b}_1[\Delta W - \omega] - \tilde{c}_1^*[-\omega]\hat{b}_1^\dagger[-\omega] + \hat{\tilde{c}}_{\mathrm{noise}}[\omega]. \tag{3.107}$$

Here, I have defined tilded functions to make the expressions simpler: $\tilde{c}_0[\omega] \equiv c_0[-\omega + \Delta W]$, $\tilde{c}_1[\omega] \equiv c_1[-\omega + \Delta W]$, $\hat{\tilde{c}}_{\mathrm{noise}}[\omega] \equiv \hat{c}_{\mathrm{noise}}[-\omega + \Delta W]$, and $\tilde{\chi}_{\mathrm{m}}[\omega] \equiv \chi_{\mathrm{m}}[-\omega + \Delta W]$. Solving these equations results in the solutions

$$\hat{b}_1[\omega] = \frac{\chi_{\mathrm{m}}[\omega]\left(\left(1 - \tilde{c}_0^*[\omega]\tilde{\chi}_{\mathrm{m}}^*[\omega]\right)\hat{c}_{\mathrm{noise}}[\omega] - c_1^*[-\omega]\tilde{\chi}_{\mathrm{m}}^*[\omega]\hat{\tilde{c}}_{\mathrm{noise}}^\dagger[-\omega]\right)}{\left(1 - c_0[\omega]\chi_{\mathrm{m}}[\omega]\right)\left(1 - \tilde{c}_0^*[\omega]\tilde{\chi}_{\mathrm{m}}^*[\omega]\right) - c_1^*[-\omega]\tilde{c}_1[-\omega]\chi_{\mathrm{m}}[\omega]\tilde{\chi}_{\mathrm{m}}^*[\omega]}, \tag{3.108}$$

$$\hat{b}_1^\dagger[-\omega] = \frac{\chi_{\mathrm{m}}^*[\omega]\left(\left(1 - \tilde{c}_0[\omega]\tilde{\chi}_{\mathrm{m}}[\omega]\right)\hat{c}_{\mathrm{noise}}^\dagger[-\omega] - c_1[-\omega]\tilde{\chi}_{\mathrm{m}}[\omega]\hat{\tilde{c}}_{\mathrm{noise}}[\omega]\right)}{\left(1 - c_0^*[\omega]\chi_{\mathrm{m}}^*[\omega]\right)\left(1 - \tilde{c}_0[\omega]\tilde{\chi}_{\mathrm{m}}[\omega]\right) - c_1[-\omega]\tilde{c}_1^*[-\omega]\chi_{\mathrm{m}}^*[\omega]\tilde{\chi}_{\mathrm{m}}[\omega]}. \tag{3.109}$$

Plugging in for the $\hat{c}_{\mathrm{noise}}$ terms and re-writing in terms of coefficients, I get

$$\hat{b}_1[\omega] = p_1[\omega]\hat{\xi}_{\mathrm{m}}^\dagger[\omega - \omega_{\mathrm{b}} + \omega_{\mathrm{r}}] + p_2[\omega]\hat{\xi}_{\mathrm{m}}[\omega] \tag{3.110}$$

$$+ p_3[\omega]\sum_i \sqrt{\frac{\kappa_i}{\kappa}}\hat{\xi}_i^\dagger[\omega - \omega_{\mathrm{b}}] + p_4[\omega]\sum_i \sqrt{\frac{\kappa_i}{\kappa}}\hat{\xi}_i[\omega + \omega_{\mathrm{r}}],$$

$$\hat{b}_1^\dagger[-\omega] = p_1^*[\omega]\hat{\xi}_{\mathrm{m}}[-\omega + \omega_{\mathrm{b}} - \omega_{\mathrm{r}}] + p_2^*[\omega]\hat{\xi}_{\mathrm{m}}^\dagger[-\omega] \tag{3.111}$$

$$+ p_3^*[\omega]\sum_i \sqrt{\frac{\kappa_i}{\kappa}}\hat{\xi}_i[-\omega + \omega_{\mathrm{b}}] + p_4^*[\omega]\sum_i \sqrt{\frac{\kappa_i}{\kappa}}\hat{\xi}_i^\dagger[-\omega - \omega_{\mathrm{r}}].$$

3.2.5   Phonon spectrum and mechanical occupancy

The phonon spectrum for the two-drive scheme is

$$
\begin{aligned}
S_{bb}[\omega] &= \left\langle \hat{b}^\dagger[-\omega]\hat{b}[\omega] \right\rangle \tag{3.112}\\
&= |p_1[\omega]|^2 \left\langle \hat{\xi}_{\mathrm{m}}[-\omega + \omega_{\mathrm{b}} - \omega_{\mathrm{r}}]\hat{\xi}_{\mathrm{m}}^\dagger[\omega - \omega_{\mathrm{b}} + \omega_{\mathrm{r}}] \right\rangle + |p_2[\omega]|^2 \left\langle \hat{\xi}_{\mathrm{m}}^\dagger[-\omega]\hat{\xi}_{\mathrm{m}}[\omega] \right\rangle \\
&\quad + |p_3[\omega]|^2 \sum_{i,j} \frac{\sqrt{\kappa_i \kappa_j}}{\kappa} \left\langle \hat{\xi}_i[-\omega + \omega_{\mathrm{b}}]\hat{\xi}_j^\dagger[\omega - \omega_{\mathrm{b}}] \right\rangle \tag{3.113}\\
&\quad + |p_4[\omega]|^2 \sum_{i,j} \frac{\sqrt{\kappa_i \kappa_j}}{\kappa} \left\langle \hat{\xi}_i^\dagger[-\omega - \omega_{\mathrm{r}}]\hat{\xi}_j[\omega + \omega_{\mathrm{r}}] \right\rangle \\
&= |p_1[\omega]|^2 \left(n_{\mathrm{m}}^{\mathrm{th}} + 1\right) + |p_2[\omega]|^2 \, n_{\mathrm{m}}^{\mathrm{th}} + |p_3[\omega]|^2 \left(n_{\mathrm{c}}^{\mathrm{th}} + 1\right) + |p_4[\omega]|^2 \, n_{\mathrm{c}}^{\mathrm{th}}. \tag{3.114}
\end{aligned}
$$

The coefficients $p_i[\omega]$ can be messy to calculate in full. However, they are much simpler if I make either of two assumptions, which seem to be valid for the cases I am interested in. The first is that $\chi_{\mathrm{m}}[-\omega + \Delta W] = 0$. This approximation is valid if the sidebands are separated by many mechanical linewidths. This will be the case for both the sideband asymmetry and quantum backaction measurements, where we want to be able to clearly distinguish the two sidebands. However, this approximation will not be valid if the sidebands overlap. In that case, $\chi_{\mathrm{m}}[-\omega+\Delta W] = \chi_{\mathrm{m}}^*[\omega]$ is clearly not zero. The alternative assumption is that $c_1[\omega] = 0$. This assumption is valid if the drives are symmetrical about the cavity frequency (regardless of whether the sidebands overlap or not). The only case where I might like the sidebands to overlap would be a measurement of quantum backaction evasion (see the discussion of this effect as a limiting case below), where the drive powers are equal. This is likely best accomplished with the sidebands centered in the cavity, so it seems reasonable that at least one of these two assumptions would be valid. If neither of them are true (if the sidebands are overlapping and significantly detuned from the cavity frequency), then the mechanical spectrum is very complicated and cannot be reduced to a Lorentzian.

Either of these assumptions leads to a substantial simplification of the mechanical field, letting me easily identify the effective mechanical susceptibility:

$$
\hat{b}[\omega] = \frac{\chi_{\mathrm{m}}[\omega]\hat{c}_{\mathrm{noise}}[\omega]}{1 - c_0[\omega]\chi_{\mathrm{m}}[\omega]}, \qquad\qquad \chi_{\mathrm{m,eff}}[\omega] = \frac{\chi_{\mathrm{m}}[\omega]}{1 - c_0[\omega]\chi_{\mathrm{m}}[\omega]}. \tag{3.115}
$$

Either of these assumptions also leads to the following simplification of the spectrum:

$$S_{bb}[\omega] = \frac{\Gamma_m n_m^{th} + g_b^2 \left(n_c^{th} + 1\right) |\chi_c[-\omega + \omega_b]|^2 + g_r^2 n_c^{th} |\chi_c[\omega - \omega_r]|^2}{|1 - c_0[\omega]\chi_m[\omega]|^2} |\chi_m[\omega]|^2 \quad (3.116)$$

$$= \left(\Gamma_m n_m^{th} + \frac{x_{zp}^2}{\hbar^2} S_{FF}^b[-\omega]\left(n_c^{th} + 1\right) + \frac{x_{zp}^2}{\hbar^2} S_{FF}^r[\omega] n_c^{th}\right) |\chi_{m,eff}[\omega]|^2 \quad (3.117)$$

$$\approx \left(\Gamma_m n_m^{th} + \Gamma_{opt,b} n_{m,b}^0 \left(n_c^{th} + 1\right) + \Gamma_{opt,r} \left(n_{m,r}^0 + 1\right) n_c^{th}\right) |\chi_{m,eff}[\omega]|^2 \quad (3.118)$$

$$\approx \boxed{\left(\Gamma_m n_m^{th} + \left(n_c^{th} + n_m^0 + 2n_c^{th} n_m^0\right) \Gamma_{opt}\right) |\chi_{m,eff}[\omega]|^2}. \quad (3.119)$$

In the second step, I replaced the cavity susceptibilities with the force spectral density due to the red or blue drive alone. The total force spectrum is $S_{FF}[\omega] = S_{FF}^r[\omega] + S_{FF}^b[\omega]$. In the third step, I approximated the force spectral densities by evaluating them at Ω_m and writing them in terms of $\Gamma_{opt,d}$ and $n_{m,d}^0$ for each drive alone. The total optomechanically induced linewidth is $\Gamma_{opt} = \Gamma_{opt,r} + \Gamma_{opt,b}$ while the total mechanical occupancy in the absence of mechanical damping and cavity photons is

$$\Gamma_{opt} n_m^0 = \frac{x_{zp}^2}{\hbar^2} S_{FF}[-\Omega_m] = \frac{x_{zp}^2}{\hbar^2}\left(S_{FF}^r[-\Omega_m] + S_{FF}^b[-\Omega_m]\right) = \Gamma_{opt,r} n_{m,r}^0 + \Gamma_{opt,b} n_{m,b}^0. \quad (3.120)$$

To get the final boxed expression for S_{bb}, I used the fact that $n_{m,r}^0 = 0$ and $n_{m,b}^0 = -1$. This results in the same expression as for the 1-drive case, now with the quantities Γ_{opt} and n_m^0 including contributions from both drives. The total mechanical occupancy is then also the same as in the 1-drive case:

$$\boxed{n_m^f = \frac{n_m^{th}\Gamma_m + \left(n_c^{th} + n_m^0 + 2n_c^{th} n_m^0\right) \Gamma_{opt}}{\Gamma_m + \Gamma_{opt}}}. \quad (3.121)$$

3.2.6 Important limits of the mechanical occupancy

Clearly, if one drive is turned off or substantially smaller than the other drive, this expression limits to the one-drive case with only a red or blue detuned drive. The most notable thing that is different than in the two-drive case happens if I apply red and blue-detuned drives that are equal in strength, $g_r = g_b = g$. Then the mechanical occupation becomes

$$n_m^f = n_m^{th} + n_m^{ba} = n_m^{th} + \frac{4g^2}{\kappa\Gamma_m}\left(2n_c^{th} + 1\right). \quad (3.122)$$

Once again, I find a situation in which the dynamical radiation pressure is absent and the quantum backaction heating due to fluctuations of the input field is visible. Comparison to Equation 3.59, the on-resonance single drive case, shows that (in the resolved sideband limit), the quantum backaction piece is stronger here by a factor of $4\Omega_{\mathrm{m}}^2/\kappa^2$. This is because the quantum backaction is filtered by the cavity and so should be much stronger when the sidebands are centered in the cavity rather than off to the sides. Thus, in the resolved sideband limit, the mechanical oscillator will exhibit far more quantum backaction motion when driven by two, equally strong, red and blue-detuned tones than when driven by a single tone on resonance.

3.2.7   Output field spectrum

I will next calculated the output fields for the system. Similarly to how I wrote the frequency-domain Langevin equations in terms of only $\hat{b}_1$'s above, I can instead write them in terms of only $\hat{a}_1$'s. Here I show the equation for $\hat{a}[\omega]$ (just take it's dagger to find the one for $\hat{a}^\dagger[-\omega]$):

$$
\frac{\hat{a}_1[\omega]}{\chi_{\mathrm{c}}[\omega]} = k_0[\omega]\hat{a}_1[\omega] + k_{1,\mathrm{r}}\hat{a}_1^\dagger[\omega - 2\omega_{\mathrm{r}}] + k_{1,\mathrm{b}}\hat{a}_1^\dagger[\omega - 2\omega_{\mathrm{b}}] + k_2[\omega]\hat{a}_1^\dagger[\omega - \omega_{\mathrm{r}} - \omega_{\mathrm{b}}] \tag{3.123}
$$
$$
+ k_{3,\mathrm{b}}[\omega]\hat{a}_1[\omega - \omega_{\mathrm{b}} + \omega_{\mathrm{r}}] + k_{3,\mathrm{r}}[\omega]\hat{a}_1[\omega - \omega_{\mathrm{r}} + \omega_{\mathrm{b}}] + \hat{k}_{\mathrm{noise}}[\omega],
$$

$$
k_0[\omega] = -g_{\mathrm{b}}^2\left(\chi_{\mathrm{m}}[\omega - \omega_{\mathrm{b}}] - \chi_{\mathrm{m}}^*[-\omega + \omega_{\mathrm{b}}]\right) - g_{\mathrm{r}}^2\left(\chi_{\mathrm{m}}[\omega - \omega_{\mathrm{r}}] - \chi_{\mathrm{m}}^*[-\omega + \omega_{\mathrm{r}}]\right), \tag{3.124}
$$

$$
k_{1,r}[\omega] = -e^{2j\phi_{\mathrm{r}}}g_{\mathrm{r}}^2\left(\chi_{\mathrm{m}}[\omega - \omega_{\mathrm{r}}] - \chi_{\mathrm{m}}^*[-\omega + \omega_{\mathrm{r}}]\right), \tag{3.125}
$$

$$
k_2[\omega] = -e^{j(\phi_{\mathrm{b}}+\phi_{\mathrm{r}})}g_{\mathrm{r}}g_{\mathrm{b}}\left(\chi_{\mathrm{m}}[\omega - \omega_{\mathrm{r}}] - \chi_{\mathrm{m}}^*[-\omega + \omega_{\mathrm{r}}] + \chi_{\mathrm{m}}[\omega - \omega_{\mathrm{b}}] - \chi_{\mathrm{m}}^*[-\omega + \omega_{\mathrm{b}}]\right) \tag{3.126}
$$

$$
k_{3,r}[\omega] = -e^{j(\phi_{\mathrm{r}}-\phi_{\mathrm{b}})}g_{\mathrm{b}}g_{\mathrm{r}}\left(\chi_{\mathrm{m}}[\omega - \omega_{\mathrm{r}}] - \chi_{\mathrm{m}}^*[-\omega + \omega_{\mathrm{r}}]\right), \tag{3.127}
$$

$$
\hat{k}_{\mathrm{noise}}[\omega] = je^{j\phi_{\mathrm{r}}}g_{\mathrm{r}}\sqrt{\Gamma_{\mathrm{m}}}\left(\hat{\xi}_{\mathrm{m}}[\omega - \omega_{\mathrm{r}}]\chi_{\mathrm{m}}[\omega - \omega_{\mathrm{r}}] + \hat{\xi}_{\mathrm{m}}^\dagger[\omega - \omega_{\mathrm{r}}]\chi_{\mathrm{m}}^*[-\omega + \omega_{\mathrm{r}}]\right)
$$
$$
+ je^{j\phi_{\mathrm{b}}}g_{\mathrm{b}}\sqrt{\Gamma_{\mathrm{m}}}\left(\hat{\xi}_{\mathrm{m}}[\omega - \omega_{\mathrm{b}}]\chi_{\mathrm{m}}[\omega - \omega_{\mathrm{b}}] + \hat{\xi}_{\mathrm{m}}^\dagger[\omega - \omega_{\mathrm{b}}]\chi_{\mathrm{m}}^*[-\omega + \omega_{\mathrm{b}}]\right) \tag{3.128}
$$
$$
+ \sum_i \sqrt{\kappa_i}\hat{\xi}_i[\omega].
$$

Also similarly to the $\hat{b}_1$'s, the field $\hat{a}_1[\omega]$ is proportional to $\chi_{\mathrm{c}}[\omega]$. I will only be interested in frequencies near the cavity frequency because that is where the sidebands of interest are centered. The only χ_{c}'s that are significant near $\omega = \omega_{\mathrm{c}}$ are $\chi_{\mathrm{c}}[\omega]$, $\chi_{\mathrm{c}}[-\omega + \omega_{\mathrm{r}} + \omega_{\mathrm{b}}]$, and their complex

conjugates. This leaves the following two equations and their daggers:

$$\frac{\hat{a}_1[\omega]}{\chi_c[\omega]} = k_0[\omega]\hat{a}_1[\omega] + k_2[\omega]\hat{a}_1^\dagger[\omega - \omega_r - \omega_b] + \hat{k}_{\text{noise}}[\omega], \qquad (3.129)$$

$$\frac{\hat{a}_1^\dagger[\omega - \omega_r - \omega_b]}{\tilde{\chi}_c^*[\omega]} = \tilde{k}_0^*[\omega]\hat{a}_1^\dagger[\omega - \omega_r - \omega_b] + \tilde{k}_2^*[\omega]\hat{a}_1[\omega] + \hat{\tilde{k}}_{\text{noise}}^\dagger[-\omega], \qquad (3.130)$$

where I have defined $\tilde{k}_0[\omega] \equiv k_0[-\omega + \omega_r + \omega_b]$, $\tilde{k}_2[\omega] \equiv k_2[-\omega + \omega_r + \omega_b]$, $\hat{\tilde{k}}_{\text{noise}}[\omega] \equiv \hat{k}_{\text{noise}}[-\omega + \omega_r + \omega_b]$, and $\tilde{\chi}_c[\omega] \equiv \chi_c[-\omega + \omega_r + \omega_b]$ to make the expressions simpler. Solving these equations gives

$$\hat{a}_1[\omega] = \frac{\chi_c[\omega]\left(\left(1 - \tilde{k}_0^*[\omega]\tilde{\chi}_c^*[\omega]\right)\hat{k}_{\text{noise}}[\omega] + k_2[\omega]\tilde{\chi}_c^*[\omega]\hat{\tilde{k}}_{\text{noise}}[-\omega]\right)}{(1 - k_0[\omega]\chi_c[\omega])\left(1 - \tilde{k}_0^*[\omega]\tilde{\chi}_c^*[\omega]\right) - k_2[\omega]\tilde{k}_2^*[\omega]\chi_c[\omega]\tilde{\chi}_c^*[\omega]} \qquad (3.131)$$

and its dagger. Substituting the solution for $\hat{a}_1$ into Equation 2.88 for $\hat{a}_{\text{out},1}$, writing out $\hat{k}_{\text{noise}}$, and writing the expression in terms of coefficients gives (with $N_1 \leftrightarrow N_2$ for the reflection geometry)

$$\hat{a}_{\text{out},1}[\omega] = N_2\hat{\xi}_l[\omega] + N_1\hat{\xi}_r[\omega] + h_1[\omega]\hat{\xi}_m^\dagger[\omega - \omega_b] + h_2[\omega]\hat{\xi}_m[\omega - \omega_r] \qquad (3.132)$$

$$+ h_3[\omega]\sum_i \sqrt{\frac{\kappa_i}{\kappa}}\hat{\xi}_i^\dagger[\omega - \omega_r - \omega_b] + h_4[\omega]\sum_i \sqrt{\frac{\kappa_i}{\kappa}}\hat{\xi}_i[\omega],$$

$$\hat{a}_{\text{out},1}^\dagger[-\omega] = N_2^*\hat{\xi}_l^\dagger[-\omega] + N_1^*\hat{\xi}_r^\dagger[-\omega] + h_1^*[\omega]\hat{\xi}_m[-\omega + \omega_b] + h_2^*[\omega]\hat{\xi}_m^\dagger[-\omega + \omega_r] \qquad (3.133)$$

$$+ h_3^*[\omega]\sum_i \sqrt{\frac{\kappa_i}{\kappa}}\hat{\xi}_i[-\omega + \omega_r + \omega_b] + h_4^*[\omega]\sum_i \sqrt{\frac{\kappa_i}{\kappa}}\hat{\xi}_i^\dagger[-\omega].$$

The output spectrum is thus (computed in a similar manner as for the one-drive case)

$$\begin{aligned}
S_{a_{\text{out}}a_{\text{out}}}[\omega] &= |h_1[\omega]|^2\left(n_m^{\text{th}} + 1\right) + |h_2[\omega]|^2 n_m^{\text{th}} + |h_3[\omega]|^2\left(n_c^{\text{th}} + 1\right) + |h_4[\omega]|^2 n_c \\
&\quad + \left(|N_2|^2 + N_2 h_4^*[\omega]\sqrt{\frac{\kappa_l}{\kappa}} + N_2^* h_4[\omega]\sqrt{\frac{\kappa_l}{\kappa}}\right)n_l^{\text{th}} \\
&\quad + \left(|N_1|^2 + N_1 h_4^*[\omega]\sqrt{\frac{\kappa_l}{\kappa}} + N_1^* h_4[\omega]\sqrt{\frac{\kappa_l}{\kappa}}\right)n_r^{\text{th}}.
\end{aligned} \qquad (3.134)$$

Computing the coefficients here would just be messy and is straightforward to do if needed, so I won't write them here. Instead, I'll specify to some interesting limiting cases to give some understanding of the important effects we're interested in.

3.2.8 Limiting cases of the output spectrum

I assume from here on that the feed line has a purely real impedance: $N_2 = 1$, $N_1 = 0$. I also set the mechanical susceptibilities for the upper blue and lower red sidebands are zero: $\chi_m[\omega - \omega_b] = \chi_m[-\omega + \omega_r] = 0$. I also always assume weak coupling.

I will first look at the case where the sidebands are separated in frequency by many mechanical linewidths. In this case, there are three contributions to the output spectrum: the wide background features that are not accompanied by any χ_m's, the features associated with the upper red sideband where $\chi_m[-\omega + \omega_b] = 0$, and the features associated with the lower blue sideband where $\chi_m[\omega - \omega_r] = 0$. For the sideband features, I will assume the sidebands are well inside the cavity linewidth and that I can evaluate $\chi_c[\omega]$ at $\overline{\omega}_c$. I also write the output in terms of the effective mechanical susceptibility. The spectrum is

$$
\begin{aligned}
S_{a_{\text{out}}a_{\text{out}}}[\omega] \;=\; & n_l^{\text{th}} + \kappa\kappa_l\left(n_c^{\text{th}} - n_l^{\text{th}}\right)|\chi_c[\omega]|^2 \\
& + \frac{4g_r^2\kappa_l\Gamma_{\text{tot}}}{\kappa^2}\left(n_m^f - 2n_c^{\text{th}} + n_l^{\text{th}}\right)|\chi_{m,\text{eff}}[\omega - \omega_r]|^2 \\
& + \frac{4g_b^2\kappa_l\Gamma_{\text{tot}}}{\kappa^2}\left(n_m^f + 1 + 2n_c^{\text{th}} - n_l^{\text{th}}\right)|\chi_{m,\text{eff}}[-\omega + \omega_b]|^2 .
\end{aligned}
\tag{3.135}
$$

This solution displays all of the behavior I anticipated at the beginning of the section: the sideband expressions are identical to those for the red or blue-detuned single drive, but now both sidebands are measurable at the same time. If the red drive is larger than the blue drive, it is possible to cool the mechanical oscillator to low occupancy while still observing the n_m^f, $n_m^f + 1$ sideband asymmetry. If the drives instead have equal amplitudes, the net dynamical backaction will be zero, allowing a measurement of the quantum backaction by looking at either sideband.

The other case of interest is the one when the sidebands are exactly overlapped $\omega_r = \overline{\omega}_c - \Omega_m$ and $\omega_b = \overline{\omega}_c + \Omega_m$ and the number of drive photons from the two drives are equal $g_r = g_b = g$. Now, $\chi_m[\omega - \omega_r] = \chi_m^*[-\omega + \omega_b]$ and the sidebands are completely inseparable. I once again assume that the sidebands are well inside the cavity linewidth and that I can evaluate $\chi_c[\omega]$ at $\overline{\omega}_c$ for the

sideband term. The output spectrum is

$$S_{a_{\text{out}}a_{\text{out}}}[\omega] = n_{\text{l}}^{\text{th}} + \kappa\kappa_{\text{l}}\left(n_{\text{c}}^{\text{th}} - n_{\text{l}}^{\text{th}}\right)|\chi_{\text{c}}[\omega]|^2 + \frac{4g^2\kappa_{\text{l}}\Gamma_{\text{m}}}{\kappa^2}\left(2n_{\text{m}}^{\text{th}} + 1\right)|\chi_{\text{m}}[\omega - \omega_{\text{r}}]|^2. \quad (3.136)$$

Notice that the sideband height here is proportional to $2n_{\text{m}}^{\text{th}} + 1$. In contrast, the spectrum with equal drives but not overlapping sidebands has a summed sideband height proportional to $2n_{\text{m}}^{\text{f}} + 1$, which includes a contribution from quantum backaction. Thus, the quantum backaction has disappeared from the overlapping sideband measurement. The measurement scheme with two drives and overlapping sidebands is thus termed 'backaction evasion'. This effect arises because the number of photons in the cavity is modulated at $2\Omega_{\text{m}}$, effectively measuring only one quadrature of the mechanical motion. Therefore, the extra backaction motion will be added only to the quadrature orthogonal to the measured quadrature.

3.2.9   Dressed cavity response

As with the one-drive case, I have already done most of the work required to find the dressed cavity response for two drives. I can just use the solution for $\hat{a}_1$ (Equation 3.131), making the replacements $\hat{\xi}_{\text{l}}[\omega] \to \alpha_{\text{p}}\delta[\omega - \omega_{\text{p}}]$ and $\hat{\xi}_{\text{r},0,\text{m}} = 0$, and plug into Equation 2.88 to find the response:

$$S_{i1}[\omega_{\text{p}}] = N_i - \kappa_{\text{l}}\frac{\chi_{\text{c}}[\omega]\left(1 - \tilde{k}_0^*[\omega]\tilde{\chi}_{\text{c}}^*[\omega]\right)}{(1 - k_0[\omega]\chi_{\text{c}}[\omega])\left(1 - \tilde{k}_0^*[\omega]\tilde{\chi}_{\text{c}}^*[\omega]\right) - k_2[\omega]\tilde{k}_2^*[\omega]\chi_{\text{c}}[\omega]\tilde{\chi}_{\text{c}}^*[\omega]}, \quad (3.137)$$

where again $i = 1$ for reflection and $i = 2$ for transmission geometry.

In the scenario where the sidebands are separated by many linewidths but still relatively centered in the cavity, I can separate the contributions from the cavity and each sideband and use the effective mechanical susceptibility to write an approximate expression for the cavity response:

$$S_{i1}[\omega_{\text{p}}] = N_i - \kappa_{\text{l}}\chi_{\text{c}}[\omega_{\text{p}}] + \kappa_{\text{l}}\chi_{\text{c}}[\omega_{\text{p}}]^2\left(g_{\text{r}}^2\chi_{\text{m,eff}}[\omega_{\text{p}} - \omega_{\text{r}}] - g_{\text{b}}^2\chi_{\text{m,eff}}^*[\omega_{\text{b}} - \omega_{\text{p}}]\right). \quad (3.138)$$

For the case where the sidebands overlap exactly and the two drives are centered about the cavity frequency and of equal strength, I recover the bare cavity response

$$S_{i1}[\omega_{\text{p}}] = N_i - \kappa_{\text{l}}\chi_{\text{c}}[\omega_{\text{p}}]. \quad (3.139)$$

3.3   Cavity optomechanics in the time-domain

To this point in this chapter, I have dealt with steady state solutions of Equations 2.85-2.88. Now, I turn to the situation where the drive tones are turned on and off in time. If I apply a strong red-detuned drive tone, I will find that the linearized interaction Hamiltonian resembles a beam-splitter Hamiltonian. This means that photons and phonons can be exchanged. We have already seen this in the steady state case of mechanical cooling: a red-detuned drive caused the phonons coupled to a relatively warm thermal bath to be exchanged with photons coupled to a much cooler bath, thereby cooling the mechanical oscillator. In the time-domain, I can think about turning this coupling on and off by turning the red-detuned drive (which I will call the transfer field) on and off. I characterize the strength of the transfer by either the transfer optomechanical coupling $g_{\mathrm{T}}[t]$ or the optomechanically induced mechanical damping rate $\Gamma_{\mathrm{T}}[t] = 4g_{\mathrm{T}}[t]^2/\kappa$.

One application that this control of the coupling allows is mechanical storage of information initially contained in the input or cavity fields (this is investigated experimentally in Chapter 11). The coupling is initially turned on to transfer the information from the cavity into the mechanical oscillator. It is then turned off for some time, isolating the information from the cavity and storing it in the mechanical oscillator. Lastly, the coupling is turned back on, transferring the information back into the cavity or output fields. The choice of cavity vs. input/output (itinerant) fields depends on the strength of the coupling tone. If the coupling between cavity and mechanics is much weaker than the cavity coupling, $2g < \kappa$, then the state leaks into or out of the cavity fast enough that the state is never entirely contained in the cavity, and the transfer is essentially between the mechanical oscillator and the itinerant fields. Conversely, if the coupling is very strong, $2g > \kappa$, then the state of the mechanics is swapped with that of the cavity faster than information can enter or escape from the cavity. In our experiment, the mechanical loss rate is much slower than the cavity's ($\Gamma_{\mathrm{m}} \ll \kappa$). Therefore, we would like to skip the cavity entirely, and thus work in the limit of weaker coupling.
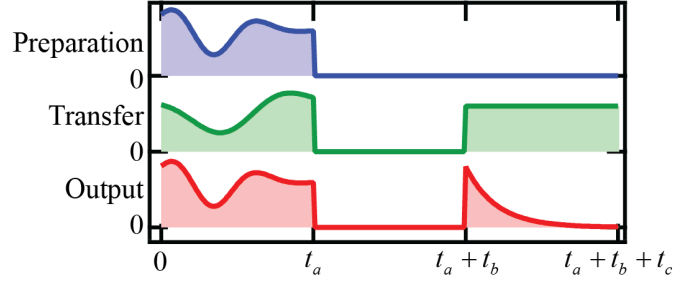
Figure 3.2: Pulse storage timing diagram. The goal is to transfer an arbitrary preparation signal at the cavity resonance (blue) into the mechanical oscillator and then later retrieve it. I apply a strong, red-detuned transfer drive (green) between times 0 and t_a, which will be shaped in time to optimally complete the transfer process. From time t_a to t_b, the signal will be stored in the mechanical oscillator. At time $t_\mathrm{a} + t_\mathrm{b}$, the transfer drive will again be turned on to read out the state of the mechanical oscillator. There will be some unwanted power that leaks out of the cavity during the initial transfer process - this power normalized to the input preparation power is what I call the leakage. The power that is retrieved from the cavity in the third process normalized to the input preparation power is the efficiency of storage.

3.3.1   Simplification of the equations of motion

The problem solved in this section is how to shape the envelope of the transfer (strong, red-detuned) pulse in time in order to optimally store and retrieve an arbitrary known preparation (weak, on resonance) tone in the mechanics (see Figure 3.2). Very similar theoretical and experimental work has been done by many groups, both for storing and retrieving an itinerant state from a mechanical oscillator [82, 83, 84, 85, 86, 87], and by transferring a state from one electromagnetic field to another, via a mechanical intermediary [88, 89, 90, 91].

I will optimize the transfer efficiency by comparing the energy stored and retrieved to the input preparation field energy. The optimal envelope should not depend on whether the state is classical or quantum, noisy or noiseless. These characteristics are likely to affect the fidelity of the stored and retrieved state, but not the total power conversion. I will thus ignore all noise terms in the equations of motion. For simplicity, I will assume the feed line has no reactive components. The Heisenberg-Langevin equations and output equation, without noise, in the reflection geometry

are:

$$\dot{a}[t] = -\left(\frac{\kappa}{2} - j\omega_c\right) a[t] + jg_0 \left(b[t] + b^\dagger[t]\right) a[t] + \sqrt{\kappa_l}\alpha_{in}[t], \tag{3.140}$$

$$\dot{b}[t] = -\left(\frac{\Gamma_m}{2} - j\Omega_m\right) b[t] + jg_0 \left(a^\dagger[t]a[t] + \frac{1}{2}\right), \tag{3.141}$$

$$a_{out}[t] = a_{in}[t] - \sqrt{\kappa_l}a[t]. \tag{3.142}$$

I have left off the hats because without noise, these equations are essentially classical. I will assume a strong red-detuned drive and a weaker signal of interest at the cavity resonant frequency. The cavity and output fields of interest will be near the cavity frequency, while the mechanical fields of interest will be near the mechanical frequency. Thus, the field assumptions are:

$$\alpha_{in}[t] = \alpha_{in,T}[t]e^{j\omega_T t} + \alpha_{in,p}[t]e^{j\bar{\omega}_c t}, \tag{3.143}$$

$$a[t] = \alpha_T[t]e^{j\phi_T}e^{j\omega_T t} + a_1[t]e^{j\bar{\omega}_c t}, \tag{3.144}$$

$$b[t] = b_0[t] + b_1[t]e^{j\Omega_m t}, \tag{3.145}$$

$$\alpha_{out}[t] = \alpha_{out,T}[t]e^{j\omega_T t} + \alpha_{out,p}[t]e^{j\bar{\omega}_c t}, \tag{3.146}$$

where $\alpha_{in,T}$ is the input amplitude for the large transfer drive and $\alpha_{in,p}$ is the input amplitude for the weaker preparation field. The cavity state amplitude due to the transfer drive is α_T. The α_{in}'s are complex, while ϕ_T accounts for the phase associated with the real α_T. I will linearize the equations of motion around the large transfer drive ($\alpha_{in,T}[t] \gg \alpha_{in,p}[t]$ and $\alpha_T[t] \gg a_1[t]$). The steady state part of the mechanical state is $b_0[t]$, while $b_1[t]$ accounts for deviations from this.

The zeroth order values (with $a_1[t]$, $b_1[t]$, $\alpha_{in,p}[t]$, and $\alpha_{out,p}[t]$ set to zero in Equations 3.140-3.142) are

$$b_0[t] = \frac{jg_0(1 + 2\alpha_T[t]^2)}{\Gamma_m - 2j\Omega_m}, \qquad \alpha_{in,T}[t] = \frac{e^{j\phi_T}}{\sqrt{\kappa_l}} \left(\frac{\alpha_T[t]}{\chi_c[\omega_T]} + \dot{\alpha}_T[t]\right), \tag{3.147}$$

$$\alpha_{out,T}[t] = \alpha_{in,T}[t] - \sqrt{\kappa_l}\alpha_T[t]e^{j\phi_T}, \tag{3.148}$$

where $\bar{\omega}_c = \omega_c + g_0(b_0 + b_0^*)$ and the linearized Langevin equations are

$$\dot{a}_1[t] = -\frac{\kappa}{2}a_1[t] + je^{j\phi_T}g_T[t]b_1[t] + \sqrt{\kappa_l}\alpha_{in,p}[t], \tag{3.149}$$

$$\dot{b}_1[t] = -\frac{\Gamma_m}{2}b_1[t] + je^{-j\phi_T}g_T[t]a_1[t]. \tag{3.150}$$

Here, $g_{\mathrm{T}}[t] = g_0 \alpha_{\mathrm{T}}[t]$ is the transfer coupling rate and I have made a rotating wave approximation to get rid of fields at frequencies that are strongly suppressed by the cavity.

The next simplification I will make will be to adiabatically eliminate the cavity mode dynamics. Generally, this means removing the rapidly changing dynamics from the equations of motion, leaving equations to solve for the more slowly-varying quantities. A similar argument is presented in reference [92, Appendix B], but for a different system of interest. The essential assumptions for this approximation are:

$$g_{\mathrm{T}}[t] \ll \kappa, \qquad \dot{g}_{\mathrm{T}}[t] \ll \frac{\kappa}{2} g_{\mathrm{T}}[t], \qquad \Gamma_{\mathrm{m}} \ll \kappa, \qquad \dot{\alpha}_{\mathrm{in,p}}[t] \ll \frac{\kappa}{2} \alpha_{\mathrm{in,p}}[t]. \qquad (3.151)$$

I will re-write the fields in the equations of motion as $a_1[t] = e^{-\kappa t/2} A[t]$ and $b_1[t] = e^{-\Gamma_{\mathrm{m}} t/2} B[t]$ to make them easier to integrate:

$$\dot{A}[t] = e^{\kappa t/2} \left(j e^{j\phi_{\mathrm{T}}} g_{\mathrm{T}}[t] b_1[t] + \sqrt{\kappa_{\mathrm{l}}} \alpha_{\mathrm{in,p}}[t] \right) \qquad (3.152)$$

$$= e^{(\kappa - \Gamma_{\mathrm{m}})t/2} j e^{j\phi_{\mathrm{T}}} g_{\mathrm{T}}[t] B[t] + e^{\kappa t/2} \sqrt{\kappa_{\mathrm{l}}} \alpha_{\mathrm{in,p}}[t], \qquad (3.153)$$

$$\dot{B}[t] = e^{-(\kappa - \Gamma_{\mathrm{m}})t/2} j e^{-j\phi_{\mathrm{T}}} g_{\mathrm{T}}[t] A[t]. \qquad (3.154)$$

I can then integrate the A equation

$$A[t] = \int_{-\infty}^{t} \left(e^{(\kappa - \Gamma_{\mathrm{m}})t'/2} j e^{j\phi_{\mathrm{T}}} g_{\mathrm{T}}[t'] B[t'] + e^{\kappa t'/2} \sqrt{\kappa_{\mathrm{l}}} \alpha_{\mathrm{in,p}}[t'] \right) dt'. \qquad (3.155)$$

I can integrate both terms by parts, using the assumptions stated above to kill the $\dot{\alpha}_{\mathrm{in,p}}$ and $\dot{g}_{\mathrm{T}}$ pieces:

$$\frac{d}{dt} \left(e^{\kappa t/2} \alpha_{\mathrm{in,p}}[t] \right) = \frac{\kappa}{2} e^{\kappa t/2} \alpha_{\mathrm{in,p}}[t] + e^{\kappa t/2} \dot{\alpha}_{\mathrm{in,p}}[t] \approx \frac{\kappa}{2} e^{\kappa t/2} \alpha_{\mathrm{in,p}}[t], \qquad (3.156)$$

$$\frac{d}{dt} \left(e^{(\kappa - \Gamma_{\mathrm{m}})t/2} g_{\mathrm{T}}[t] B[t] \right) = \frac{\kappa - \Gamma_{\mathrm{m}}}{2} e^{(\kappa - \Gamma_{\mathrm{m}})t/2} g_{\mathrm{T}}[t] B[t] + e^{(\kappa - \Gamma_{\mathrm{m}})t/2} \dot{g}_{\mathrm{T}}[t] B[t] \qquad (3.157)$$

$$+ e^{(\kappa - \Gamma_{\mathrm{m}})t/2} g_{\mathrm{T}}[t] \dot{B}[t]$$

$$\approx \frac{\kappa - \Gamma_{\mathrm{m}}}{2} e^{(\kappa - \Gamma_{\mathrm{m}})t/2} g_{\mathrm{T}}[t] B[t] + e^{(\kappa - \Gamma_{\mathrm{m}})t/2} g_{\mathrm{T}}[t] \dot{B}[t], \qquad (3.158)$$

$$\int_{-\infty}^{t} e^{\kappa t'/2} \alpha_{\mathrm{in,p}}[t'] dt' \approx \frac{2}{\kappa} e^{\kappa t/2} \alpha_{\mathrm{in,p}}[t], \qquad (3.159)$$

$$\int_{-\infty}^{t} e^{(\kappa - \Gamma_{\mathrm{m}})t'/2} g_{\mathrm{T}}[t'] B[t'] dt' \approx \frac{2}{\kappa - \Gamma_{\mathrm{m}}} e^{(\kappa - \Gamma_{\mathrm{m}})t/2} g_{\mathrm{T}}[t] B[t] \qquad (3.160)$$

$$- \frac{2}{\kappa - \Gamma_{\mathrm{m}}} \int_{-\infty}^{t} e^{(\kappa - \Gamma_{\mathrm{m}})t'/2} g_{\mathrm{T}}[t'] \dot{B}[t'] dt'.$$

Substituting in the equation for $\dot{B}[t]$, I write $A[t]$ as

$$A[t] = \frac{2\sqrt{\kappa_l}}{\kappa} e^{\kappa t/2} \alpha_{\text{in,p}}[t] + \frac{2je^{j\phi_T}}{\kappa - \Gamma_m} e^{(\kappa - \Gamma_m)t/2} g_T[t]B[t] + \frac{2}{\kappa - \Gamma_m} \int_{-\infty}^{t} g_T[t']^2 A[t']dt'. \quad (3.161)$$

I could substitute this solution for $A[t]$ into the last term and integrate by parts again to get the next order terms in $g_T[t]/\kappa$:

$$\begin{aligned}
A[t] &= \frac{2\sqrt{\kappa_l}}{\kappa} e^{\kappa t/2} \alpha_{\text{in,p}}[t] + \frac{2je^{j\phi_T}}{\kappa - \Gamma_m} e^{(\kappa - \Gamma_m)t/2} g_T[t]B[t] \quad &(3.162)\\
&\quad + \frac{4\sqrt{\kappa_l}}{\kappa} \frac{g_T[t]^2}{\kappa(\kappa + \Gamma_m)} e^{\kappa t/2} \alpha_{\text{in,p}}[t] + 4je^{j\phi_T} \frac{g_T[t]^3}{(\kappa - \Gamma_m)^3} e^{(\kappa - \Gamma_m)t/2} B[t] + \mathcal{O}\left(\frac{g_T[t]}{\kappa}\right)^4.
\end{aligned}$$

However, the approximation that $g_T[t] \ll \kappa$ means that we can keep just the zeroth and first order terms. Going back to the original variables $a_1[t]$ and $b_1[t]$ and making the approximation $\Gamma_m \ll \kappa$ gives

$$a_1[t] = e^{-\kappa t/2}A[t] \approx \frac{2}{\kappa}\left(je^{j\phi_T}g_T[t]b_1[t] + \sqrt{\kappa_l}\alpha_{\text{in,p}}[t]\right), \quad (3.163)$$

$$\dot{a}_1[t] = -\frac{\kappa}{2}a_1[t] + je^{j\phi_T}g_T[t]b_1[t] + \sqrt{\kappa_l}\alpha_{\text{in,p}}[t] \approx 0. \quad (3.164)$$

I find that the derivative of $a_1[t]$ is negligible compared to $\kappa a_1[t]/2$ in these approximations (see Figure 3.3 to see how they compare for reasonable experimental parameters). Often, this result
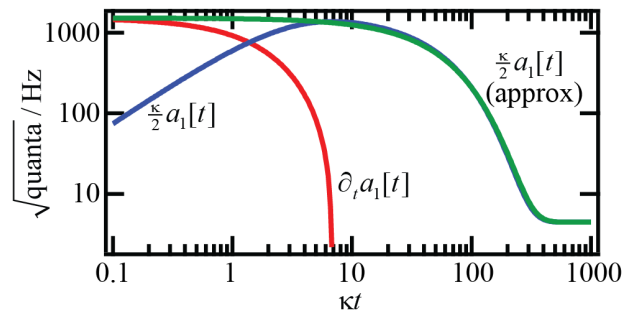
Figure 3.3: Adiabatic approximation validity on different timescales. The different terms in the equation of motion for $a_1[t]$ are plotted versus κt. The values of terms $\dot{a}_1[t]$ (red) and $\kappa a_1[t]/2$ (blue) are plotted on the y-axis as a function of κt for experimentally reasonable parameters. The derivative $\dot{a}_1[t]$ is much smaller than $\kappa a_1[t]/2$ for times greater than $\approx 2\kappa$. The adiabatic approximation involves setting $\dot{a}_1[t] = 0$, changing the value of $\kappa a_1[t]/2$ to be the sum of the two terms (shown in green).

is just stated as the approximation associated with adiabatic elimination (see reference [84]). The physical interpretation of this is that the cavity field tracks the input and mechanical states and does not depend on its own history. This makes sense because κ, the rate that the cavity loses information, is much larger than any other rate in the problem.

Substituting the solution for a_1 into the Langevin equation for b_1 leaves me with only one equation of motion to solve:

$$\dot{b}[t] + \left(\frac{\Gamma_m}{2} + \frac{2g_T[t]^2}{\kappa}\right) b[t] = \frac{2je^{-j\phi_T}\sqrt{\kappa_l}g_T[t]\alpha_{\text{in,p}}[t]}{\kappa}. \tag{3.165}$$

This is a first order differential equation for b_1 of form $\dot{b}_1[t] + P[t]b_1[t] = Q[t]$ which can be solved via the method of integrating factors.

3.3.2 Integrating factor solutions

First order differential equations of the form $\dot{b}_1[t] + P[t]b_1[t] = Q[t]$ can be solved using integrating factors, as follows. I will assume there is some function $\mu[t]$ such that

$$\partial_t\left(\mu[t]b_1[t]\right) = \mu[t]Q[t], \tag{3.166}$$

$$\mu[t]b_1[t] = \mu[t_0]b_1[t_0] + \int_{t_0}^t \mu[t']Q[t']dt', \tag{3.167}$$

$$b_1[t] = \boxed{\frac{1}{\mu[t]}\left(\mu[t_0]b_1[t_0] + \int_{t_0}^t \mu[t']Q[t']dt'\right)}. \tag{3.168}$$

I can then write a differential equation and solution for $\mu[t]$:

$$\dot{\mu}[t] = \frac{\mu[t]Q[t] - \mu[t]\dot{b}_1[t]}{b_1[t]} = \frac{\mu[t]P[t]b_1[t]}{b_1[t]} = \mu[t]P[t], \tag{3.169}$$

$$\mu[t] = \boxed{\exp\left[\int_{t_0}^t P[t']dt\right]}. \tag{3.170}$$

The boxed equations, along with Equations 3.163 and 3.142, allow me to find all of the fields given some input transfer and preparation fields.

I will divide the problem of state storage in the mechanical oscillator into three sections in time: the transfer, the storage, and the retrieval, illustrated in Figure 3.2. I will treat these three sections independently, using the final state of the system from one section as the initial condition of

the next. This is an approximation but is valid if the time for each section is long compared with the dynamics of the fields. During the transfer section, for times $0 \leq t \leq t_{\mathrm{a}}$, an arbitrary preparation signal $\alpha_{\mathrm{in,p}}[t]$ is transferred into the mechanical oscillator by a time-dependent transfer field with optomechanical coupling $g_{\mathrm{T}}[t]$. I assume the mechanical oscillator begins in state $b_1[0] = 0$, so the fields in the first time section are

$$\mu[t] = \exp\left[\int_0^t \left(\frac{\Gamma_{\mathrm{m}}}{2} + \frac{2}{\kappa}g_{\mathrm{T}}^2[t'']\right) dt''\right], \tag{3.171}$$

$$b_1[t] = 2je^{-j\phi_{\mathrm{T}}}\frac{\sqrt{\kappa_{\mathrm{l}}}}{\kappa}\frac{1}{\mu[t]}\int_0^t \mu[t']g_{\mathrm{T}}[t]\alpha_{\mathrm{in,p}}[t']dt', \tag{3.172}$$

$$\alpha_{\mathrm{out,p}}[t] = \left(1 - 2\frac{\kappa_{\mathrm{ext}}}{\kappa}\right)\alpha_{\mathrm{in,p}}[t] - \frac{2}{\kappa}je^{j\phi_{\mathrm{T}}}\sqrt{\kappa_{\mathrm{l}}}g_{\mathrm{T}}[t]b_1[t]. \tag{3.173}$$

For the storage section, $t_{\mathrm{a}} \leq t \leq t_{\mathrm{a}} + t_{\mathrm{b}}$, the storage and preparation fields are turned off, isolating the mechanical oscillator from the cavity. The fields during this section of time are

$$\mu[t] = \exp\left[\int_{t_{\mathrm{a}}}^t \frac{\Gamma_{\mathrm{m}}}{2}dt'\right] = e^{\Gamma_{\mathrm{m}}(t-t_{\mathrm{a}})/2}, \tag{3.174}$$

$$b_1[t] = \frac{1}{\mu[t]}b_1[t_{\mathrm{a}}] = b_1[t_{\mathrm{a}}]e^{-\Gamma_{\mathrm{m}}(t-t_{\mathrm{a}})/2}, \tag{3.175}$$

$$\alpha_{\mathrm{out,p}}[t] = 0. \tag{3.176}$$

During the third section of time, $t_{\mathrm{a}} + t_{\mathrm{b}} \leq t \leq t_{\mathrm{a}} + t_{\mathrm{b}} + t_{\mathrm{c}}$, the signal is retrieved by turning the transfer field back on, with constant transfer rate Γ_{out}. As the efficiency of the storage is only dependent on the total retrieved power, I can make this readout transfer constant in time. If a specific output pulse temporal profile were desired, I could instead shape the output transfer to achieve that profile. The fields during the third section of time are

$$\mu[t] = \exp\left[\int_{t_{\mathrm{a}}+t_{\mathrm{b}}}^t \frac{(\Gamma_{\mathrm{m}} + \Gamma_{\mathrm{out}})}{2}dt'\right] = e^{(\Gamma_{\mathrm{m}}+\Gamma_{\mathrm{out}})(t-t_{\mathrm{a}}-t_{\mathrm{b}})/2}, \tag{3.177}$$

$$b_1[t] = \frac{1}{\mu[t]}b[t_{\mathrm{a}} + t_{\mathrm{b}}] = e^{-(\Gamma_{\mathrm{m}}+\Gamma_{\mathrm{out}})(t-t_{\mathrm{a}}-t_{\mathrm{b}})/2}b[t_{\mathrm{a}} + t_{\mathrm{b}}], \tag{3.178}$$

$$\alpha_{\mathrm{out,p}}[t] = -je^{j\phi_{\mathrm{T}}}\sqrt{\frac{\Gamma_{\mathrm{out}}\kappa_{\mathrm{l}}}{\kappa}}b_1[t]. \tag{3.179}$$

Ideally, all of the preparation power would be transferred into the mechanical oscillator such that no power leaked out of the cavity during the first time section. That power would then be

recovered in the third time section. I define the efficiency and leakage of the storage as

$$\mathcal{E} = \frac{\int_{t_a+t_b}^{t_a+t_b+t_c} |\alpha_{\text{out,p}}[t]|^2 \, dt}{\int_0^{t_a} |\alpha_{\text{in,p}}[t]|^2 \, dt} \qquad \text{and} \qquad L = \frac{\int_0^{t_a} |\alpha_{\text{out,p}}[t]|^2 \, dt}{\int_0^{t_a} |\alpha_{\text{in,p}}[t]|^2 \, dt}. \tag{3.180}$$

Note that L is just the measured leakage energy and there will also be energy lost via dissipation through the internal port of the cavity. Thus, $\mathcal{E}$ and L do not in general add up to one. The denominators of $\mathcal{E}$ and L are just a function of the preparation state, which is specified at the beginning of the problem. Thus, optimizing the efficiency is equivalent to optimizing the numerator. I can re-write the expression for the efficiency numerator in terms of the fields found above

$$|\alpha_{\text{out,p}}[t]|^2 = \frac{\Gamma_{\text{out}}\kappa_l}{\kappa} |b_1[t]|^2 \tag{3.181}$$

$$= \frac{\Gamma_{\text{out}}\kappa_l}{\kappa} e^{-(\Gamma_{\text{out}}+\Gamma_m)(t-t_a-t_b)} |b_1[t_a+t_b]|^2 \tag{3.182}$$

$$= \frac{\Gamma_{\text{out}}\kappa_l}{\kappa} e^{-(\Gamma_{\text{out}}+\Gamma_m)(t-t_a-t_b)} e^{-\Gamma_m t_b} |b_1[t_a]|^2, \tag{3.183}$$

$$\int_{t_a+t_b}^{t_a+t_b+t_c} |\alpha_{\text{out,p}}[t]|^2 \, dt = \frac{\Gamma_{\text{out}}\kappa_l}{\kappa} e^{-\Gamma_m t_b} |b_1[t_a]|^2 \int_{t_a+t_b}^{t_a+t_b+t_c} e^{-(\Gamma_{\text{out}}+\Gamma_m)(t-t_a-t_b)} dt \tag{3.184}$$

$$= \frac{\Gamma_{\text{out}} \left(1 - e^{-(\Gamma_{\text{out}}+\Gamma_m)t_c}\right)}{\Gamma_{\text{out}}+\Gamma_m} \frac{\kappa_l}{\kappa} e^{-\Gamma_m t_b} |b_1[t_a]|^2 \tag{3.185}$$

$$= \frac{\Gamma_{\text{out}} \left(1 - e^{-(\Gamma_{\text{out}}+\Gamma_m)t_c}\right)}{\Gamma_{\text{out}}+\Gamma_m} \tag{3.186}$$

$$\times \frac{4\kappa_l^2 e^{-\Gamma_m t_b}}{\kappa^3} \left| \int_0^{t_a} \frac{\mu[t']}{\mu[t_a]} g_T[t']\alpha_{\text{in,p}}[t']dt' \right|^2.$$

Here, I see that maximizing the efficiency is also equivalent to maximizing the state in the mechanical oscillator at time t_a or optimizing the integral $\int_0^{t_a} (\mu[t']/\mu[t_a]) \, g_T[t']\alpha_{\text{in,p}}[t']dt'$. This is then an optimization problem of a functional, which can be solved by finding a stationary point of the functional with respect to $g_T[t]$.

3.3.3   Optimization of efficiency

I can re-write the function I want to optimize as

$$\int_0^{t_a} \frac{\mu[t']}{\mu[t_a]} g_T[t']\alpha_{in,p}[t']dt' = \int_0^{t_a} \exp\left[-\int_{t'}^{t_a}\left(\frac{\Gamma_m}{2}+\frac{2}{\kappa}g_T^2[t'']\right)dt''\right]g_T[t']\alpha_{in,p}[t']dt' \quad (3.187)$$

$$= \sqrt{\frac{\kappa}{2}}\int_0^{t_a}e^{\Gamma_m t'/2}\alpha_{in,p}[t']\sqrt{h[t']\dot{h}[t']}dt' \quad (3.188)$$

$$= \sqrt{\frac{\kappa}{2}}\int_0^{t_a}\mathcal{F}\left[t',h[t'],\dot{h}[t']\right]dt' \quad (3.189)$$

Here, $h[t] \equiv \exp\left[-\frac{2}{\kappa}\int_t^{t_a}g_T^2[t'']dt''\right]$ is a function that allowed me to write the argument $\mathcal{F}$ of the integral as a function of only $h[t]$, its derivative, and t. By calculus of variations, this integral will find a stationary point (optimum) of the integral only if $\mathcal{F}\left[t',h[t'],[\dot{h}][t']\right] = e^{\Gamma_m t'/2}\alpha_{in,p}[t']\sqrt{h[t']\dot{h}[t']}$ solves the Euler-Lagrange equation:

$$0 = \frac{\partial\mathcal{F}}{\partial h[t']} - \frac{d}{dt'}\left(\frac{\partial\mathcal{F}}{\partial\dot{h}[t']}\right) \quad (3.190)$$

$$= \frac{1}{2}e^{\Gamma_m t'/2}\alpha_{in,p}[t']\sqrt{\frac{\dot{h}[t']}{h[t']}} - \frac{d}{dt'}\left(\frac{1}{2}e^{\Gamma_m t'/2}\alpha_{in,p}[t']\sqrt{\frac{h[t']}{\dot{h}[t']}}\right) \quad (3.191)$$

$$= \frac{1}{2}e^{\Gamma_m t'/2}\left\{\alpha_{in,p}[t']\sqrt{\frac{\dot{h}[t']}{h[t']}} - \frac{\Gamma_m}{2}\alpha_{in,p}[t']\sqrt{\frac{h[t']}{\dot{h}[t']}} - \dot{\alpha}_{in,p}[t']\sqrt{\frac{h[t']}{\dot{h}[t']}} - \alpha_{in,p}[t']\frac{d}{dt'}\left(\sqrt{\frac{h[t']}{\dot{h}[t']}}\right)\right\}.$$

This gives me a first order differential equation and solution for $g_T^a[t']$:

$$\frac{d}{dt'}\left(\sqrt{\frac{h[t']}{\dot{h}[t']}}\right) = \sqrt{\frac{\dot{h}[t']}{h[t']}} - \frac{\Gamma_m}{2}\sqrt{\frac{h[t']}{\dot{h}[t']}} - \frac{\dot{\alpha}_{in,p}[t']}{\alpha_{in,p}[t']}\sqrt{\frac{h[t']}{\dot{h}[t']}}, \quad (3.192)$$

$$\frac{d}{dt'}\left(\frac{1}{g_T[t']}\right) = \frac{2}{\kappa}g_T[t'] - \left(\frac{\Gamma_m}{2} + \frac{\dot{\alpha}_{in,p}[t']}{\alpha_{in,p}[t']}\right)\frac{1}{g_T[t']}, \quad (3.193)$$

$$\dot{g}_T[t'] = -\frac{2}{\kappa}g_T[t']^3 + \left(\frac{\Gamma_m}{2} + \frac{\dot{\alpha}_{in,p}[t']}{\alpha_{in,p}[t']}\right)g_T[t'], \quad (3.194)$$

$$g_T[t] = \boxed{\sqrt{\frac{\kappa}{2}}\frac{e^{\Gamma_m t/2}\alpha_{in,p}[t]}{\sqrt{\frac{\kappa}{2}\left(\frac{\alpha_{in,p}[0]}{g_T[0]}\right)^2 + 2\int_0^t e^{\Gamma_m t'}\alpha_{in,p}[t']^2 dt'}}}. \quad (3.195)$$

Note here that the optimization procedure produced the optimal pulse shape **given** some initial condition for the transfer field $g_T[0]$. It did not produce an optimal pulse shape over all $g_T[0]$. Therefore, for a given preparation pulse shape, I will still need to vary $g_T[0]$ to see which value gives the best efficiency while keeping $g_T[t]$ within experimentally realizable values.

3.3.4   Pulse shaping examples

In this section I will use the above solutions to solve for the optimal transfer pulse shape and system fields for several trial preparation pulses: the rising exponential, the falling exponential, the Gaussian, and the half wave sine squared pulse. These pulses and their optimal transfer fields are shown in Figure 3.4 for an array of values of $g_\mathrm{T}[0]$. The efficiencies and maximum $g_\mathrm{T}[t]$ for these values are shown in Figure 3.5. All of these graphs are created using the following system parameters: $t_\mathrm{a} = 500\ \mu\mathrm{s}$, $\kappa = 2\pi \times 370\ \mathrm{kHz}$, $\Gamma_\mathrm{p} = 32\ \mathrm{kHz}$ (Γ_p is the preparation exponential or Gaussian rate below). For the plots, I assume that the second transfer (readout) pulse is on sufficiently long to read out the entire state ($t_\mathrm{c} \to \infty$). I also set $\Gamma_\mathrm{m} = 0$ for the plots in order to better compare the different pulse shapes. This removes the factor of mechanical decoherence and instead makes the efficiency only dependent on the transfer process. Note that I keep Γ_m and t_c finite in the analytic expressions below.

3.3.4.1   Rising exponential

For the input field $\alpha_{\mathrm{in,p}}[t] = Ae^{\Gamma_\mathrm{p}(t-t_\mathrm{a})/2}$ (Figure 3.4(a)), the efficiency is maximized for the transfer coupling rate

$$g_\mathrm{T}[t] = \frac{\sqrt{\kappa(\Gamma_\mathrm{m} + \Gamma_\mathrm{p})}e^{(\Gamma_\mathrm{m}+\Gamma_\mathrm{p})t/2}}{2\sqrt{e^{(\Gamma_\mathrm{m}+\Gamma_\mathrm{p})t} - 1 + \delta^{-2}}}. \tag{3.196}$$

Here, $\delta \equiv 2g_\mathrm{T}[0]/\sqrt{\kappa(\Gamma_\mathrm{m} + \Gamma_\mathrm{p})}$ quantifies the initial transfer rate in dimensionless units. The efficiency for the rising exponential is

$$\mathcal{E} \;=\; \frac{\eta_\mathrm{st}^2 e^{-\Gamma_\mathrm{m}t_\mathrm{b}}\Gamma_\mathrm{out}\Gamma_\mathrm{p}}{(\Gamma_\mathrm{out} + \Gamma_\mathrm{m})(\Gamma_\mathrm{p} + \Gamma_\mathrm{m})}\frac{\left(1 - e^{-(\Gamma_\mathrm{out}+\Gamma_\mathrm{m})t_\mathrm{c}}\right)\left(1 - e^{-(\Gamma_\mathrm{p}+\Gamma_\mathrm{m})t_\mathrm{a}}\right)^2 \delta^2}{(1 - e^{-\Gamma_\mathrm{p}t_\mathrm{a}})\left(\left(1 - e^{-(\Gamma_\mathrm{p}+\Gamma_\mathrm{m})t_\mathrm{a}}\right)\delta^2 + e^{-(\Gamma_\mathrm{p}+\Gamma_\mathrm{m})t_\mathrm{a}}\right)} \tag{3.197}$$

This efficiency is maximized for infinite δ, but in practice δ will be limited by experimental constraints. The efficiency is ultimately limited (even for ideal conditions $\{t_\mathrm{a}, t_\mathrm{c}\} \to \infty$ and $\Gamma_\mathrm{m} = 0$) to η_st^2, where $\eta_\mathrm{st} = \kappa_\mathrm{l}/\kappa$ is the state transfer efficiency of one transfer (there are two factors in the total efficiency, one for the initial transfer and one for the readout).
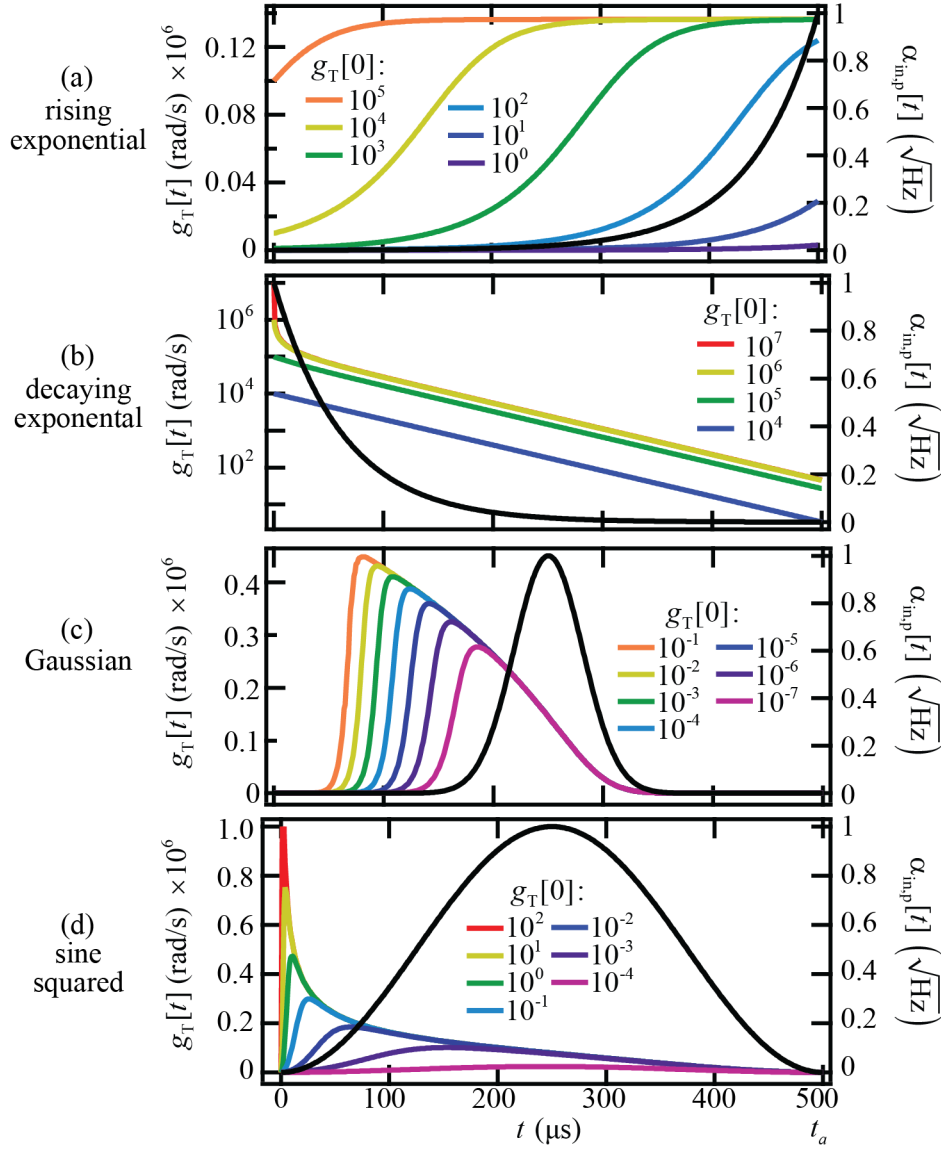
Figure 3.4: Optimal transfer pulse shaping results. The input preparation and optimal transfer fields are shown as a function of time. The preparation field is shown in black for each pulse shape and corresponds to the right axis. It is normalized to have an amplitude of one. The colored traces are the optimal transfer pulse shapes for several different values of $g_\text{T}[0]$, shown in the legends. (a) Rising exponential. (b) Decaying exponential. Note that for this graph only, the left y-axis is plotted logarithmically. Otherwise, it would be impossible to see the transfer pulses. (c) Gaussian. (d) Sine squared half-wave pulse.
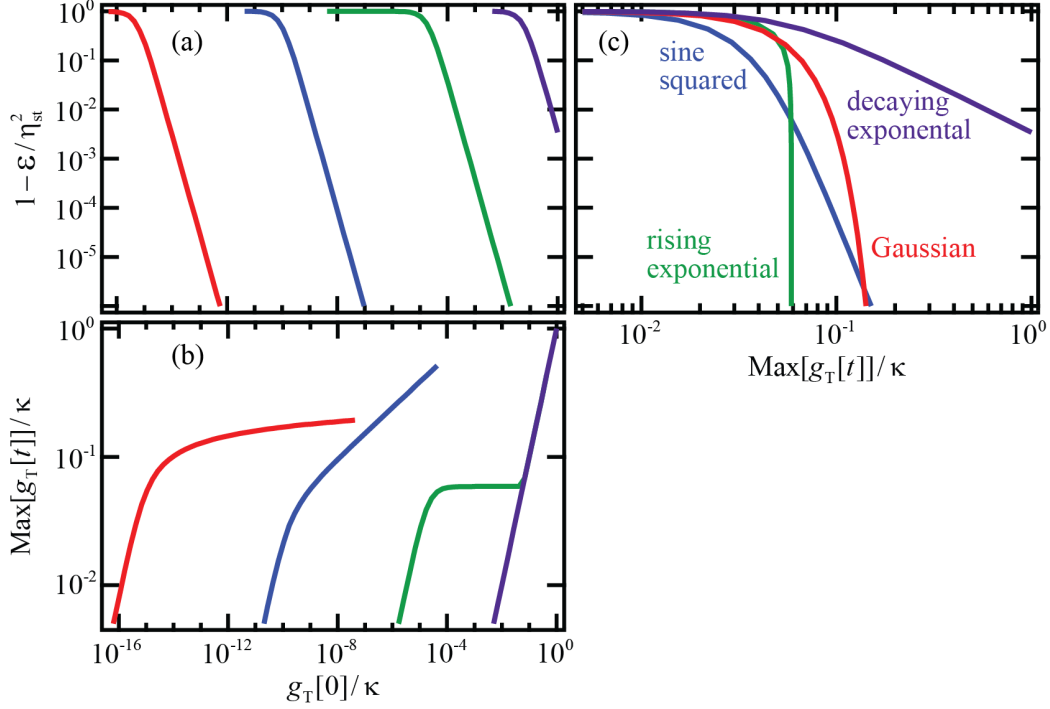
Figure 3.5: Transfer efficiency for different pulse shapes: Rising exponential (green), decaying exponential (purple), Gaussian (red), and sine squared (blue). (a) Efficiency as a function of different values of $g_T[0]$. I have plotted the y-axis as $1 - \mathcal{E}/\eta_{st}^2$ on a logarithmic scale to highlight efficiencies near the maximum achievable value. The efficiency improves with larger $g_T[0]$ for all four pulse shapes. However, this graph hides the fact that improvements in efficiency come at the cost of increasingly large transfer fields. (b) Maximum value of $g_T[t]$ as a function of different values of $g_T[0]$. (c) Parametric plot of efficiency as a function of maximum value of $g_T[t]$. This graph is the most useful as it displays efficiency achievable as a function of maximum $g_T[t]$ allowable. Keep in mind that the solutions I have derived are only valid in the weak coupling limit $\Gamma_T[t]/\kappa \ll 1$. This plot shows that high efficiency is most easily achieved for the rising exponential and least easily achieved for the decaying exponential.

3.3.4.2 Decaying exponential

For the input field $\alpha_{in,p}[t] = Ae^{-\Gamma_p t/2}$ (Figure 3.4(b)), the efficiency is maximized for the transfer coupling rate

$$g_T[t] = \frac{\sqrt{\kappa(\Gamma_p - \Gamma_m)}e^{-(\Gamma_p-\Gamma_m)t/2}}{2\sqrt{1 - e^{-(\Gamma_p-\Gamma_m)t} + \delta^{-2}}}. \tag{3.198}$$

Here, $\delta \equiv 2g_{\mathrm{T}}[0]/\sqrt{\kappa(\Gamma_{\mathrm{p}} - \Gamma_{\mathrm{m}})}$ quantifies the initial transfer rate in dimensionless units. The efficiency for the falling exponential is

$$\mathcal{E} = \frac{\eta_{\mathrm{st}}^2 e^{-\Gamma_{\mathrm{m}}(t_{\mathrm{a}} + t_{\mathrm{b}})} \Gamma_{\mathrm{out}} \Gamma_{\mathrm{p}}}{(\Gamma_{\mathrm{out}} + \Gamma_{\mathrm{m}})(\Gamma_{\mathrm{p}} - \Gamma_{\mathrm{m}})} \frac{\left(1 - e^{-(\Gamma_{\mathrm{out}} + \Gamma_{\mathrm{m}})t_{\mathrm{c}}}\right)\left(1 - e^{-(\Gamma_{\mathrm{p}} - \Gamma_{\mathrm{m}})t_{\mathrm{a}}}\right)^2 \delta^2}{\left(1 - e^{-\Gamma_{\mathrm{p}} t_{\mathrm{a}}}\right)\left(\left(1 - e^{-(\Gamma_{\mathrm{p}} - \Gamma_{\mathrm{m}})t_{\mathrm{a}}}\right)\delta^2 + 1\right)}. \tag{3.199}$$

Once again, this is maximized for infinite δ and is ultimately limited to η_{st}^2.

3.3.4.3 Gaussian

For the input field $\alpha_{\mathrm{in,p}}[t] = Ae^{-\Gamma_{\mathrm{p}}^2(t - t_{\mathrm{a}}/2)^2/2}$ (Figure 3.4(c)), the efficiency is maximized for the transfer coupling rate

$$g_{\mathrm{T}}[t] = \frac{\sqrt{\kappa \Gamma_{\mathrm{p}}} e^{-\Gamma_{\mathrm{p}}^2(t - t_{\mathrm{a}}/2)^2/2} e^{\Gamma_{\mathrm{m}}(t - t_{\mathrm{a}}/2)/2} e^{-\Gamma_{\mathrm{m}}^2/(8\Gamma_{\mathrm{p}}^2)}}{\pi^{1/4}\sqrt{2}\sqrt{\mathrm{erf}\left[\frac{\Gamma_{\mathrm{m}} + \Gamma_{\mathrm{p}}^2 t_{\mathrm{a}}}{2\Gamma_{\mathrm{p}}}\right] - \mathrm{erf}\left[\frac{\Gamma_{\mathrm{m}} + \Gamma_{\mathrm{p}}^2(t_{\mathrm{a}} - 2t)}{2\Gamma_{\mathrm{p}}}\right] + \delta^{-2}}} \tag{3.200}$$

Here, $\delta \equiv g_{\mathrm{T}}[0]\exp\left[\left((\Gamma_{\mathrm{m}} + \Gamma_{\mathrm{p}}^2 t_{\mathrm{a}})/(2\Gamma_{\mathrm{p}})\right)^2/2\right]\pi^{1/4}\sqrt{2}/\sqrt{\kappa\Gamma_{\mathrm{p}}}$ quantifies the initial transfer rate in dimensionless units and $\mathrm{erf}[x]$ is the error function. The efficiency for the Gaussian is

$$\mathcal{E} = \frac{\eta_{\mathrm{st}}^2 \Gamma_{\mathrm{out}} e^{-\Gamma_{\mathrm{m}}\left(\frac{t_{\mathrm{a}}}{2} + t_{\mathrm{b}} - \frac{\Gamma_{\mathrm{m}}}{4\Gamma_{\mathrm{p}}^2}\right)}}{\Gamma_{\mathrm{out}} + \Gamma_{\mathrm{m}}} \frac{\left(1 - e^{-(\Gamma_{\mathrm{out}} + \Gamma_{\mathrm{m}})t_{\mathrm{c}}}\right)\delta^2\left(\mathrm{erf}\left[\frac{\Gamma_{\mathrm{m}} + \Gamma_{\mathrm{p}}^2 t_{\mathrm{a}}}{2\Gamma_{\mathrm{p}}}\right] - \mathrm{erf}\left[\frac{\Gamma_{\mathrm{m}} - \Gamma_{\mathrm{p}}^2 t_{\mathrm{a}}}{2\Gamma_{\mathrm{p}}}\right]\right)^2}{2\mathrm{erf}\left[\frac{\Gamma_{\mathrm{p}} t_{\mathrm{a}}}{2}\right]\left(\delta^2\left(\mathrm{erf}\left[\frac{\Gamma_{\mathrm{m}} + \Gamma_{\mathrm{p}}^2 t_{\mathrm{a}}}{2\Gamma_{\mathrm{p}}}\right] - \mathrm{erf}\left[\frac{\Gamma_{\mathrm{m}} - \Gamma_{\mathrm{p}}^2 t_{\mathrm{a}}}{2\Gamma_{\mathrm{p}}}\right]\right) + 1\right)} \tag{3.201}$$

3.3.4.4 Sine squared half-wave pulse

For the input field $\alpha_{\mathrm{in,p}}[t] = A\sin^2\left[\pi t/t_{\mathrm{a}}\right]$ (Figure 3.4(d)), the expressions for $g_{\mathrm{T}}[t]$ is easy to find by using Equation 3.195, but is more complicated (and less easy to display as a simple expression) than for the previous examples. The integrals in Equation 3.187 can also not be done analytically. However, everything can be solved numerically, given values for all of the system parameters. This is what I have done to create the graphs in Figures 3.4(d) and 3.5.

Chapter 4

Theory III: Interferometric linear measurement

In Sections 3.1 and 3.2, I derived expressions for the field spectral density $S_{a_{\text{out}}a_{\text{out}}}[\omega]$ immediately at the output of the optomechanical system. In this chapter, I will relate the voltage spectral densities that we measure to $S_{a_{\text{out}}a_{\text{out}}}[\omega]$.

In the following sections I use the fact that the cavity output fields in Section 3.1 took the form

$$\hat{a}_{\text{out},1}[\omega] = \sum_{i=\{\text{m},\text{l},\text{r},0\}} \left\{ \alpha_i[\omega]\hat{\xi}_i[\omega - \omega_i'] + \beta_i[\omega]\hat{\xi}_i^\dagger[\omega + \omega_i' - 2\omega_{\text{d}}] \right\}, \tag{4.1}$$

where the sum is over the mechanical (m), left port (l), right port (r), and internal (0) cavity operators, $\omega_{\text{m}}' = \omega_{\text{d}}$, and $\omega_{\text{l}}' = \omega_{\text{r}}' = \omega_0' = 0$. The frequency dependent coefficients of each operator are contained in the α_i's and β_i's. The output fields in Section 3.2 took the same form, but with $\omega_{\text{d}} \to (\omega_{\text{r}} + \omega_{\text{b}})/2$, $\omega_{\text{m}}' = \omega_{\text{r}}$, and $\omega_{\text{l}}' = \omega_{\text{r}}' = \omega_0' = 0$. As each $\hat{\xi}_i$ operator only enters the expression for $\hat{a}_{\text{out}}$ at a single frequency, there are only a few nonzero combinations of $\hat{a}_{\text{out},1}$ and $\hat{a}_{\text{out},1}^\dagger$:

$$\left\langle \hat{a}_{\text{out},1}^\dagger[\omega_1]\hat{a}_{\text{out},1}[\omega_2] \right\rangle = S_{a_{\text{out}}a_{\text{out}}}[\omega_2]\delta_{\omega_1,-\omega_2}, \tag{4.2}$$

$$\left\langle \hat{a}_{\text{out},1}[\omega_1]\hat{a}_{\text{out},1}^\dagger[\omega_2] \right\rangle = (S_{a_{\text{out}}a_{\text{out}}}[\omega_1] + 1)\delta_{\omega_1,-\omega_2}, \tag{4.3}$$

$$\left\langle \hat{a}_{\text{out},1}[\omega_1]\hat{a}_{\text{out},1}[\omega_2] \right\rangle = -e^{2j\phi_{\text{d}}}S_{\text{cross}}[\omega_{\text{d}} - \omega_1]\delta_{\omega_1+\omega_2,2\omega_{\text{d}}}, \tag{4.4}$$

$$\left\langle \hat{a}_{\text{out},1}^\dagger[\omega_1]\hat{a}_{\text{out},1}^\dagger[\omega_2] \right\rangle = -e^{-2j\phi_{\text{d}}}S_{\text{cross}}^*[\omega_{\text{d}} + \omega_2]\delta_{\omega_1+\omega_2,-2\omega_{\text{d}}}, \tag{4.5}$$

where for the single drive case, ϕ_{d} and ω_{d} are the phase and frequency of the drive, and for the two drive case, $\phi_{\text{d}} \to (\phi_{\text{r}} + \phi_{\text{b}})/2$ and $\omega_{\text{d}} \to (\omega_{\text{r}} + \omega_{\text{b}})/2$. The spectral densities are related to the α's

and β's above by

$$S_{a_{\text{out}}a_{\text{out}}}[\omega] = \sum_{i=\{\text{m,l,r,0}\}} \left\{ |\alpha_i[\omega]|^2 n_i^{\text{th}} + |\beta_i[\omega]|^2 (n_i^{\text{th}} + 1) \right\}, \qquad (4.6)$$

$$S_{a_{\text{out}}a_{\text{out}}}[\omega] + 1 = \sum_{i=\{\text{m,l,r,0}\}} \left\{ |\alpha_i[\omega]|^2 (n_i^{\text{th}} + 1) + |\beta_i[\omega]|^2 n_i^{\text{th}} \right\}, \qquad (4.7)$$

$$S_{\text{cross}}[\omega] = -e^{-2j\phi_{\text{d}}} \sum_{i=\{\text{m,l,r,0}\}} \left\{ \alpha_i[\omega_{\text{d}} + \omega]\beta_i[\omega_{\text{d}} - \omega]n_i^{\text{th}} + \alpha_i[\omega_{\text{d}} - \omega]\beta_i[\omega_{\text{d}} + \omega](n_i^{\text{th}} + 1) \right\}. \quad (4.8)$$

I have defined the terms $S_{\text{cross}}[\omega]$ in a way that will highlight their interference with the $S_{a_{\text{out}}a_{\text{out}}}[\omega]$'s. For the specific output field results found in Sections 3.1, the cross terms turn out to be zero for a red or blue drive or any heterodyne measurement ($\omega_{\text{LO}} \neq \omega_{\text{d}}$). The one case where they do not vanish is when the detection is homodyne and there is a single, on-resonant drive. Making only the approximations that $N_2 = 1$, $\omega_{\text{LO}} = \omega_{\text{d}} = \overline{\omega}_{\text{c}}$, and $\chi_{\text{m}}[-\Omega_{\text{m}}] = 0$ (true for a high-Q mechanical oscillator), the cross terms satisfy the identity

$$S_{\text{cross}}[\omega] + S_{\text{cross}}^*[\omega] = g^2 \kappa_l \Gamma_{\text{m}}(1 + 2n_{\text{m}}^{\text{f}})|\chi_{\text{c}}[\overline{\omega}_{\text{c}} + \omega]|^2 |\chi_{\text{m}}[\omega]|^2 \qquad (4.9)$$

$$= S_{a_{\text{out}}a_{\text{out}}}^g[\overline{\omega}_{\text{c}} - \omega] + S_{a_{\text{out}}a_{\text{out}}}^g[\overline{\omega}_{\text{c}} + \omega]. \qquad (4.10)$$

Here, I have used a superscript g to indicate the g-dependent part of the spectral density:

$$S_{a_{\text{out}}a_{\text{out}}}^g[\omega] = S_{a_{\text{out}}a_{\text{out}}}[\omega] - S_{a_{\text{out}}a_{\text{out}}}^{g\to 0}[\omega]. \qquad (4.11)$$

This division of notation is important, as the cross terms only interfere with the g-dependent part of the spectral density, which contains information about the mechanical sidebands and is proportional to g^2. The cross terms do not affect the g-independent part of the spectral density, which is the contribution in the absence of optomechanical coupling ($g \to 0$) and contains information only about the cavity and input field thermal populations (it is zero in the absence of thermal photons).

The cross terms can also be nonzero in the case where there are two equal drives, one close to optimal red-detuning $\omega_{\text{r}} = \overline{\omega}_{\text{c}} - \Omega_{\text{m}} - \epsilon$ and one close to optimal blue $\omega_{\text{b}} = \overline{\omega}_{\text{c}} + \Omega_{\text{m}} + \epsilon$, with the sidebands separated by many mechanical linewidths but still within the cavity linewidth ($\Gamma_{\text{m}} \ll \epsilon \ll \kappa$). If the local oscillator frequency is centered between the two sidebands at $\omega_{\text{LO}} = \overline{\omega}_{\text{c}}$,

they are folded on top of each other and the measured frequency is $\omega \approx \epsilon$. In this case, the cross terms take the form

$$S_{\text{cross}}[\omega] + S^*_{\text{cross}}[\omega] \;=\; g^2 \kappa_{\text{l}} \Gamma_{\text{m}} (1 + 2 n_{\text{m}}^{\text{f}}) |\chi_{\text{c}}[\overline{\omega}_{\text{c}} + \omega]|^2 |\chi_{\text{m}}[\Omega_{\text{m}} - \omega + \epsilon]|^2 \tag{4.12}$$

$$\;=\; S^g_{a_{\text{out}} a_{\text{out}}}[\overline{\omega}_{\text{c}} - \omega] + S^g_{a_{\text{out}} a_{\text{out}}}[\overline{\omega}_{\text{c}} + \omega] \tag{4.13}$$

Note that these cross term relations are specific to the optomechanical model used in Sections 3.1 and 3.2.

4.1   Linear, interferometric measurement

I could imagine detecting the signal at the output of the cavity by just putting a microwave voltage detector at the output of the cavity and directly measuring the voltage spectral density at high frequency. However, it is technically difficult to digitize and store data taken at gigahertz frequencies, so we typically use an interferometric scheme to mix the signal down to lower frequency (usually in the kilohertz or megahertz range). In a homodyne detection, a single input signal is split into two parts traveling along different arms of an interferometer, the signal arm and the local oscillator arm. The signal arm contains the system of interest, which imparts a phase shift on the signal. Interfering this signal with the local oscillator (LO) allows the relative phase to be measured. Homodyne ($\omega_{\text{LO}} = \omega_{\text{d}}$) and heterodyne ($\omega_{\text{LO}} \neq \omega_{\text{d}}$) detection can both be done in either the optical or microwave regime (Figure 4.1). In the optical case, the interference is done using a beam splitter and the detector is a photodetector. In the microwave case, a frequency mixer is used to mix the signal with the local oscillator to produce a low frequency voltage signal which can be digitized. Appendix D.1 details the relevant field transformations for beam splitters and photodetectors in the optical case and explains how these elements can be combined to form a single-quadrature or two-quadrature detector. As the physics behind the microwave and optical cases is identical, I use this optical realization to model all interferometric detection. This chapter relies heavily on the results in appendix D.1 and I thus recommend reading it first.

In the case of an on-resonant drive for an optomechanical system, homodyne detection folds
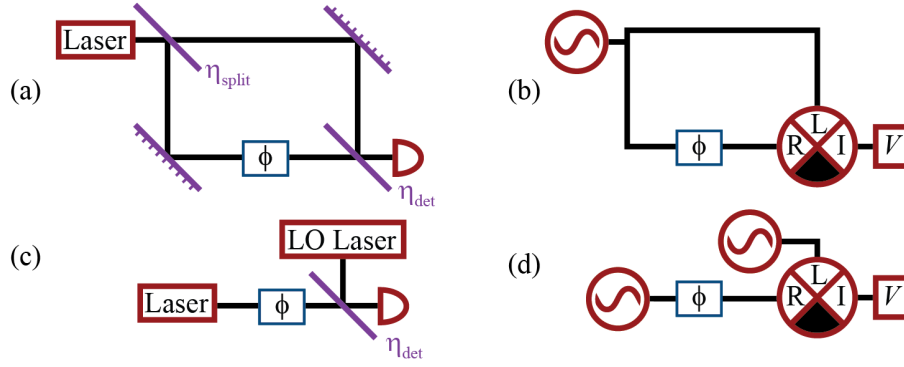
Figure 4.1: Interferometric detection. (a) Homodyne detection in the optical regime. A single laser tone is split into two pieces, one of which interacts with the system of interest in the signal arm of the interferometer. The other arm acts as a local oscillator. Using a photodetector to measure the interference of the two tones then allows a measurement of the phase shift due to the system of interest in the signal arm. (b) Homodyne detection in the microwave regime. The final beam splitter and photodetector are replaced by a frequency mixer and a voltage detector. (c,d) Heterodyne detection in the optical and microwave regimes. These are the same as homodyne detection except that the local oscillator is provided by a different source at a different frequency. As explained in Appendix D.1, η_{LO} must be large ($\eta_{\mathrm{LO}} \gg 1 - \eta_{\mathrm{LO}}$) in order to avoid adding extra noise to the measurement. In the homodyne case, η_{split} is not particularly consequential so long as the local oscillator power is much larger than the signal power (which could also be accomplished by attenuation or drive tone cancellation in the signal arm.)

the two sidebands on top of each other. Mathematically, this is evidenced by the cross terms introduced above being nonzero, allowing interference that can result in a better signal to noise than for heterodyne. In the case of the two driving tones considered in Section 3.2, the equivalent of homodyne detection is to place the LO at the cavity resonance, once again folding the sidebands on top of each other. However, in many cases heterodyne detection is preferable - for instance when the signal frequency of interest from homodyne detection is too large, or when (as is the case for a far-detuned drive) homodyne detection does not provide an improvement in signal to noise. Heterodyne detection would also be necessary for a sideband asymmetry measurement because the information of interest is in the differences between the two sidebands. Therefore, from here on, I only consider homodyne detection in the case where the single drive is near cavity resonance or where the two drives are equal in magnitude. For all other cases, the heterodyne result is the one that is relevant.

4.2   Single quadrature measurement

In Appendix D.1, I define two quadratures[1]of the field $\hat{d}[\omega]$ incident on a linear detector:

$$\hat{X}[\omega] = \hat{X}^\dagger[\omega] \quad = \quad \hat{d}[\omega + \omega_{\mathrm{LO}}] + \hat{d}^\dagger[\omega - \omega_{\mathrm{LO}}], \tag{4.14}$$

$$\hat{Y}[\omega] = \hat{Y}^\dagger[\omega] \quad = \quad -j(\hat{d}[\omega + \omega_{\mathrm{LO}}] - \hat{d}^\dagger[\omega - \omega_{\mathrm{LO}}]). \tag{4.15}$$

A linear detector modeled as just a beam splitter followed by a photodetector measures an intensity $\hat{I}$ only dependent on a single quadrature of the incident field (Equation D.9):

$$\hat{I}[\omega] = \hat{I}^\dagger[\omega] \quad = \quad A_{\mathrm{LO}}\sqrt{\eta_{\mathrm{LO}}(1 - \eta_{\mathrm{LO}})}\left(-\sin[\phi_{\mathrm{LO}}]\hat{X}[\omega] + \cos[\phi_{\mathrm{LO}}]\hat{Y}[\omega]\right), \tag{4.16}$$

where A_{LO} and ϕ_{LO} are the amplitude and phase of the local oscillator, and η_{LO} is the detection efficiency. In this chapter, I calculate the measured intensity spectrum for a linear detection of the output field from an optomechanical system. I introduce a beam splitter with transmission η placed between the system of interest and the detector to account for any loss[2]. The field incident on the linear detector is then $\hat{d}_{\mathrm{in}} = \sqrt{\eta}\hat{a}_{\mathrm{out}} + j\sqrt{1 - \eta}\hat{\xi}_{\mathrm{vac}}$. Using the results in Appendix D.1 (specifically Equation D.15) and writing in terms of $S_{\mathrm{cross}}[\omega]$, I find

$$
\begin{aligned}
S_{II}^{\mathrm{photon}}[\omega] \quad = \quad & \frac{1}{2\eta} + \frac{1}{2}\left(S_{a_{\mathrm{out}}a_{\mathrm{out}}}[\omega_{\mathrm{LO}} - \omega] + S_{a_{\mathrm{out}}a_{\mathrm{out}}}[\omega_{\mathrm{LO}} + \omega]\right) \\
& + \frac{1}{2}\left(e^{2j(\phi_{\mathrm{LO}} - \phi_{\mathrm{d}})}S_{\mathrm{cross}}^*[\omega] + e^{-2j(\phi_{\mathrm{LO}} - \phi_{\mathrm{d}})}S_{\mathrm{cross}}[\omega]\right)\delta_{\omega_{\mathrm{LO}},\omega_{\mathrm{d}}},
\end{aligned}
\tag{4.17}
$$

where $S_{II}^{\mathrm{photon}}[\omega]$ is the intensity spectral density written in photon units. For a heterodyne measurement, the cross terms are zero and the previous expression reduces to

$$
\begin{aligned}
S_{II}^{\mathrm{photon}}[\omega] \quad = \quad & \frac{1}{2\eta} + \frac{1}{2}\left(S_{a_{\mathrm{out}}a_{\mathrm{out}}}[\omega_{\mathrm{LO}} - \omega] + S_{a_{\mathrm{out}}a_{\mathrm{out}}}[\omega_{\mathrm{LO}} + \omega]\right) \tag{4.18} \\
= \quad & \frac{1}{2\eta} + \frac{1}{2}\left(S_{a_{\mathrm{out}}a_{\mathrm{out}}}^{g\to 0}[\omega_{\mathrm{LO}} - \omega] + S_{a_{\mathrm{out}}a_{\mathrm{out}}}^{g\to 0}[\omega_{\mathrm{LO}} + \omega]\right) \tag{4.19} \\
& + \frac{1}{2}\left(S_{a_{\mathrm{out}}a_{\mathrm{out}}}^{g}[\omega_{\mathrm{LO}} - \omega] + S_{a_{\mathrm{out}}a_{\mathrm{out}}}^{g}[\omega_{\mathrm{LO}} + \omega]\right).
\end{aligned}
$$

---

[1] Note that the quadratures I use are always defined as a sum of a field at one frequency and a daggered field at a different frequency, where those two frequencies are symmetric about the LO frequency. Specifically, they are not the real and imaginary part of the microwave or optical field at a single frequency.

[2] The beam splitter transmission (or quantum efficiency) η can be related to an effective number of added noise photons n_{add} via $\eta = (1 + 2n_{\mathrm{add}})^{-1}$ such that the constant factor in front of the right-hand side of the single-quadrature expressions for $S_{II}[\omega]$ becomes $1/(2\eta) = 1/2 + n_{\mathrm{add}}$.

For a homodyne measurement with an on-resonant single drive or two equal red and blue-detuned drives, the cross terms can maximally interfere with the spectral terms (for the choice $\phi_{\mathrm{LO}} = \phi_{\mathrm{d}}$)[3]:

$$
\begin{aligned}
S_{II}^{\mathrm{photon}}[\omega] \;=\; & \frac{1}{2\eta} + \frac{1}{2}\left(S_{a_{\mathrm{out}}a_{\mathrm{out}}}^{g\to 0}[\omega_{\mathrm{LO}} - \omega] + S_{a_{\mathrm{out}}a_{\mathrm{out}}}^{g\to 0}[\omega_{\mathrm{LO}} + \omega]\right) \\
& + \left(S_{a_{\mathrm{out}}a_{\mathrm{out}}}^{g}[\omega_{\mathrm{LO}} - \omega] + S_{a_{\mathrm{out}}a_{\mathrm{out}}}^{g}[\omega_{\mathrm{LO}} + \omega]\right).
\end{aligned}
\tag{4.20}
$$

The homodyne and heterodyne cases both have the same half-photon contribution from added noise and the same contribution from the $S_{a_{\mathrm{out}}a_{\mathrm{out}}}^{g\to 0}[\omega]$ terms (which contain only information about thermal photons). The difference in the two expressions is the factor of two enhancement of the $S_{a_{\mathrm{out}}a_{\mathrm{out}}}^{g}[\omega]$ terms in the homodyne case. As these terms contain the information of interest about the mechanical sidebands, this coefficient results in an obvious factor of two improvement in the signal to noise of the measurement. However, there is another factor of two improvement when using homodyne detection, as both $S_{a_{\mathrm{out}}a_{\mathrm{out}}}^{g}[\omega_{\mathrm{LO}} - \omega]$ and $S_{a_{\mathrm{out}}a_{\mathrm{out}}}^{g}[\omega_{\mathrm{LO}} + \omega]$ contain sideband information (as opposed to only one of these terms in the heterodyne case). This results in an overall factor of four improvement in signal to noise when using homodyne over heterodyne single-quadrature detection.

4.3   Two-quadrature measurement

In Appendix D.1, I model a linear detector measuring both quadratures of the incident field as a 50/50 beam splitter followed by two single-quadrature linear detectors, one of which has an LO that is ninety degrees out of phase. The two measured intensities then correspond to two orthogonal quadratures of the incident field (Equations D.17 and D.19, ignoring added noise for the moment):

$$
\frac{\sqrt{2}\,\hat{I}_{\mathrm{I}}[\omega]}{A_{\mathrm{LO}}\sqrt{\eta_{\mathrm{LO}}(1 - \eta_{\mathrm{LO}})}} \;=\; -\sin[\phi_{\mathrm{LO}}]\hat{X}[\omega] + \cos[\phi_{\mathrm{LO}}]\hat{Y}[\omega],
\tag{4.21}
$$

$$
\frac{\sqrt{2}\,\hat{I}_{\mathrm{Q}}[\omega]}{A_{\mathrm{LO}}\sqrt{\eta_{\mathrm{LO}}(1 - \eta_{\mathrm{LO}})}} \;=\; \sin[\phi_{\mathrm{LO}}]\hat{Y}[\omega] + \cos[\phi_{\mathrm{LO}}]\hat{X}[\omega].
\tag{4.22}
$$

---

[3] In this dissertation, I only consider the choices $\phi_{\mathrm{LO}} = \phi_{\mathrm{d}}$ and $\phi_{\mathrm{LO}} = \phi_{\mathrm{d}} + \pi/2$, which maximally constructively and destructively interfere with the spectral terms. However, other choices for ϕ_{LO} can lead to complicated interferences. In particular, for $\cos[\phi_{\mathrm{d}} - \phi_{\mathrm{LO}}] = \pm(3 + 4n_{\mathrm{m}}^{\mathrm{th}} + 4n_{\mathrm{m}}^{\mathrm{ba}})^{-1/2}$, the S_{cross} terms will interfere to create maximal squeezing of the vacuum noise. This is the effect observed in [57, 56].

I once again introduce a beam splitter with transmission η placed between the system of interest and the detector to account for any loss[4]. Using Equation D.21 and writing in terms of $S_{\text{cross}}[\omega]$, the intensity spectral densities for the I and Q quadratures and the quadrature combination $\hat{I}_\theta = \left(e^{j\theta} \hat{I}_\text{I} + e^{-j\theta} \hat{I}_\text{Q} \right)/\sqrt{2}$ are

$$S_{I_\text{I(Q)} I_\text{I(Q)}}^{\text{photon}}[\omega] = \frac{1}{\eta} + \frac{1}{2}\left(S_{a_\text{out} a_\text{out}}[\omega_\text{LO} - \omega] + S_{a_\text{out} a_\text{out}}[\omega_\text{LO} + \omega] \right) \tag{4.23}$$
$$\pm \frac{1}{2}\left(e^{2j(\phi_\text{LO} - \phi_\text{d})} S^*_{\text{cross}}[\omega] + e^{-2j(\phi_\text{LO} - \phi_\text{d})} S_{\text{cross}}[\omega] \right) \delta_{\omega_\text{LO}, \omega_\text{d}},$$
$$S_{I_\theta I_\theta}^{\text{photon}}[\omega] = \frac{1}{\eta} + \frac{1 - \sin[2\theta]}{2} S_{a_\text{out} a_\text{out}}[\omega_\text{LO} - \omega] + \frac{1 + \sin[2\theta]}{2} S_{a_\text{out} a_\text{out}}[\omega_\text{LO} + \omega]. \tag{4.24}$$

The plus in the first equation corresponds to the in-phase intensity and the minus to the quadrature intensity. The equation for $S_{I_\theta I_\theta}$ is only valid for heterodyne measurement.

For heterodyne measurement, the information of interest is likely only contained in either $S_{a_\text{out} a_\text{out}}[\omega_\text{LO} + \omega]$ or $S_{a_\text{out} a_\text{out}}[\omega_\text{LO} - \omega]$ and thus the best signal to noise occurs when measuring the combination intensity I_θ. A choice of $\theta = \pi/4$ optimizes the measurement for a signal with original frequency greater than ω_LO, while a choice of $\theta = -\pi/4$ optimizes the measurement for a signal with frequency less than ω_LO. This optimization leads to a result identical (up to an overall factor) to the heterodyne single-quadrature measurement. This can be understood, as the two-quadrature measurement results in twice as much noise, but also allows us to detect twice as much signal information.

For homodyne measurement, the signal in the in-phase channel is optimized (while the quadrature measurement is furthest from optimized) at $\phi_\text{LO} = \phi_\text{d}$:

$$S_{I_\text{I} I_\text{I}}^{\text{photon}}[\omega] = \frac{1}{\eta} + \frac{1}{2}\left(S_{a_\text{out} a_\text{out}}^{g \to 0}[\omega_\text{LO} - \omega] + S_{a_\text{out} a_\text{out}}^{g \to 0}[\omega_\text{LO} + \omega] \right) \tag{4.25}$$
$$+ \left(S_{a_\text{out} a_\text{out}}^{g}[\omega_\text{LO} - \omega] + S_{a_\text{out} a_\text{out}}^{g}[\omega_\text{LO} + \omega] \right),$$
$$S_{I_\text{Q} I_\text{Q}}^{\text{photon}}[\omega] = \frac{1}{\eta} + \frac{1}{2}\left(S_{a_\text{out} a_\text{out}}^{g \to 0}[\omega_\text{LO} - \omega] + S_{a_\text{out} a_\text{out}}^{g \to 0}[\omega_\text{LO} + \omega] \right). \tag{4.26}$$

---

[4] In the two quadrature expressions, I cannot just make the substitution $\eta = (1 + 2n_\text{add})^{-1}$ to write them in terms of added noise. As with two amplifiers in series, the noise from two beam splitters in series does not simply add. The effective added noise $n'_{\text{add},2}$ from a second beam splitter with transmission η_2 added in series with a beam splitter of transmission $\eta_1 = (1 + 2n_{\text{add},1})^{-1}$ is $n'_{\text{add},2} = n_{\text{add},2}/\eta_1$. In the case of the two-quadrature measurement, $\eta_1 = 1/2$ from the 50/50 beam splitter inside the linear detector, and $\eta_2 = \eta = (1 + 2n_\text{add})^{-1} = (1 + 2n'_\text{add}\eta_1)^{-1} = (1 + n'_\text{add})^{-1}$. The constant factor in front of the two-quadrature expressions then becomes $1/\eta = 1 + n'_\text{add}$.

The in-phase result is the same as the single-quadrature homodyne measurement, except with twice the added noise. Thus, using a two-quadrature detector to make a homodyne measurement always hurts the signal to noise by a factor of two.

4.4   Microwave detection and amplification

In the microwave regime, a frequency mixer and voltage detector replace the beam splitters and photodetectors in the discussion above (and in Appendix D.1). The voltage measured takes the place of the intensity, as both are a linear combination of fields and their daggers. The only difference is a normalization constant, but this can be absorbed into the proportionality between $S_{II}[\omega]$ and $S_{II}^{\mathrm{photon}}[\omega]$, which is not usually known (calibration of voltage to photon units or mechanical displacement units is discussed in Section 6.2).

The most notable difference between microwave and optical measurements is that microwave frequency mixers and detectors typically add many quanta of noise (the quantum efficiency η is very small). To decrease the effective loss, we amplify the signal prior to the linear detector (see Figure 4.2). The added noise at the input of the linear detector is then set by any loss (modeled as beam splitter with transmission η') prior to the amplifier, which can in practice be much smaller
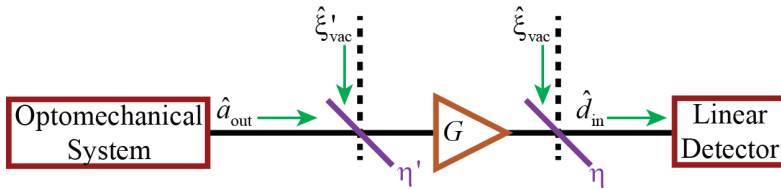
Figure 4.2: Model of amplification and added noise. Poor quantum efficiency η between the experiment and the detector can be overcome by adding an amplifier prior to that loss. The added noise is then set by the quantum efficiency η' before the amplifier.

than the detector noise:

$$\frac{1}{\sqrt{G\eta\eta'}}\hat{d}_{\text{in}} \;=\; \hat{a}_{\text{out}} + j\sqrt{\frac{1-\eta'}{\eta'}}\hat{\xi}'_{\text{vac}} + j\frac{1}{\sqrt{G}}\sqrt{\frac{1-\eta}{\eta\eta'}}\hat{\xi}_{\text{vac}} + \text{amplifier noise} \qquad (4.27)$$

$$\approx\; \hat{a}_{\text{out}} + j\sqrt{\frac{1-\eta'}{\eta'}}\hat{\xi}'_{\text{vac}} + \text{amplifier noise}. \qquad (4.28)$$

For large gain, the $\hat{\xi}_{\text{vac}}$ term can be made much smaller than the combination of the $\hat{\xi}'_{\text{vac}}$ term and added amplifier noise. Then the η dependence disappears and the added noise is set by only the loss prior to the amplifier. Note that the amplification will similarly make the half quanta of added noise due to a two quadrature linear detector measurement negligible.

4.4.1   Phase sensitive amplification

A phase-sensitive amplifier (such as a Josephson parametric amplifier, JPA) amplifies only one quadrature of the microwave field (as detailed in Appendix D.3.3):

$$X^{\text{J}}_{\text{in}}[\omega] \;=\; e^{-j\pi/4}\left(e^{-j\phi_{\text{P}}}\hat{c}_{\text{in},1}[\omega] + je^{j\phi_{\text{P}}}\hat{c}^{\dagger}_{\text{in},1}[\omega - 2\omega_{\text{J}}]\right), \qquad (4.29)$$

$$Y^{\text{J}}_{\text{in}}[\omega] \;=\; -e^{j\pi/4}\left(e^{-j\phi_{\text{P}}}\hat{c}_{\text{in},1}[\omega] - je^{j\phi_{\text{P}}}\hat{c}^{\dagger}_{\text{in},1}[\omega - 2\omega_{\text{J}}]\right), \qquad (4.30)$$

$$X^{\text{J}}_{\text{out}}[\omega] \;=\; 2L[\omega]X^{\text{J}}_{\text{in}}[\omega], \qquad\qquad Y^{\text{J}}_{\text{out}}[\omega] = \frac{Y^{\text{J}}_{\text{in}}[\omega]}{2L^{*}[\omega]}, \qquad (4.31)$$

where $\hat{c}_{\text{in(out)},1}$ is the input or output field from the JPA and $L[\omega]$ is the direct amplitude gain. When $\omega_{\text{LO}} = \omega_{\text{J}}$ and $\phi_{\text{LO}} = \phi_{\text{J}} - \pi/4$, the detected in-phase intensity (or voltage) is proportional to the amplified quadrature $X^{\text{J}}[\omega + \omega_{\text{J}}]$. Using a two-quadrature linear detector adds no additional information over a single-quadrature detector, as the quadrature intensity I_{Q} contains only deamplified information about Y^{J} (which will be hidden by the large detector noise). Thus, the choice to use a phase-sensitive amplifier sets the measurement as single quadrature, regardless of whether a one or two quadrature linear detection is used, and the results in Section 4.2 are the relevant ones for an interferometer containing a phase-sensitive amplifier.

4.4.2 Phase-insensitive amplification

A phase-insensitive amplifier (discussed in Appendix D.2) amplifies both quadratures of the microwave field equally, requiring an extra half quantum of added noise to preserve commutation relations. This is very similar to the situation of the two-quadrature linear detector. Thus, regardless of whether a single or two-quadrature linear detection is used after the amplifier, the two-quadrature results in Section 4.3 are the relevant ones for an interferometer containing a phase-insensitive amplifier. Although, in measuring only the in-phase quadrature, a single-quadrature detector may throw some of the available information away.

4.5 Quantum limits on detection

In this section I will evaluate the above single-quadrature intensity measurement expressions for the several important cases of optomechanical drives detailed in Sections 3.1 and 3.2 and convert them into displacement units. This can be accomplished, as we know that the displacement spectral density of actual mechanical motion should be

$$S_{xx}^{\mathrm{f}}[\omega] = 2x_{\mathrm{zp}}^2 \Gamma_{\mathrm{tot}} n_{\mathrm{m}}^{\mathrm{f}} |\chi_{\mathrm{m,eff}}[\omega]|^2, \tag{4.32}$$

such that the number of mechanical quanta is

$$n_{\mathrm{m}}^{\mathrm{f}} = \frac{1}{2x_{\mathrm{zp}}^2} \frac{1}{2\pi} \int_{-\infty}^{\infty} S_{xx}^{\mathrm{f}}[\omega] d\omega. \tag{4.33}$$

The measured intensity has a complicated proportionality to the displacement spectral density (which, in addition to mechanical and cavity parameters depends on the local oscillator amplitude, amplifier gains, quantum efficiencies, etc.) However, the area (and thus height) of the mechanical sideband in voltage or intensity units is proportional to the actual occupancy of the mechanical oscillator (and the proportionality coefficient can be calibrated, see Section 6.2). An apparent (or imprecision) number of mechanical quanta can be found by comparing the height of the measured background to the height of the sideband peak.

In this section, I will find the absolute limits on measurement imprecision and backaction for each drive case examined. I assume that there is no excess thermal noise ($n_{\mathrm{l}}^{\mathrm{th}} = n_{\mathrm{r}}^{\mathrm{th}} = n_{\mathrm{c}}^{\mathrm{th}} = 0$). This

makes all of the $S^{g \to 0}_{a_{\text{out}} a_{\text{out}}}[\omega]$ terms zero. The results for an optimal two-quadrature measurement can be found simply from the single-quadrature results, as they are always the same for heterodyne measurement and a factor of two worse in imprecision for a homodyne measurement.

4.5.1   Single red-detuned drive

One very important drive case is that of the red-detuned drive, as this results in the cooling and damping of the mechanical oscillator. I will specify to the resolved-sideband limit, as damping and cooling are both enhanced in this limit and mechanical ground state cooling is possible. The output spectrum in the weak-coupling regime (Equation 3.76), is then

$$S_{a_{\text{out}} a_{\text{out}}}[\omega] = S^{g}_{a_{\text{out}} a_{\text{out}}}[\omega] = \frac{4g^2 \kappa_{\text{l}} \Gamma_{\text{tot}}}{\kappa^2} n^{\text{f}}_{\text{m}} |\chi_{\text{m,eff}}[\omega - \omega_{\text{r}}]|^2. \tag{4.34}$$

For a red-detuned drive in the resolved-sideband limit, there is no advantage to making a homodyne measurement over a heterodyne (since the lower sideband is strongly filtered by the cavity response). A heterodyne measurement will mix the upper sideband centered at $\omega_{\text{r}} + \Omega_{\text{m}}$ down to frequency $\omega = |\omega_{\text{LO}} - (\omega_{\text{r}} + \Omega_{\text{m}} + \delta)|$, where δ is the detuning from the sideband center frequency. The optimal heterodyne intensity spectral density at this frequency is (from Equation 4.18)

$$S_{II}[\omega] \quad \propto \quad \frac{1}{2\eta} + \frac{2g^2 \kappa_{\text{l}} \Gamma_{\text{tot}}}{\kappa^2} n^{\text{f}}_{\text{m}} |\chi_{\text{m,eff}}[\Omega_{\text{m}} + \delta]|^2. \tag{4.35}$$

Re-writing this measured intensity spectrum as an inferred mechanical displacement spectrum gives

$$S^{\text{tot}}_{xx}[\omega] \quad = \quad S^{\text{imp}}_{xx}[\omega] + S^{\text{f}}_{xx}[\omega] = \frac{x^2_{\text{zp}} \kappa^2}{2g^2 \kappa_{\text{l}} \eta} + 2x^2_{\text{zp}} \Gamma_{\text{tot}} n^{\text{f}}_{\text{m}} |\chi_{\text{m,eff}}[\Omega_{\text{m}} + \delta]|^2. \tag{4.36}$$

Evaluating this spectral density on resonance and writing in terms of number of mechanical quanta gives

$$n^{\text{tot}}_{\text{m}} = n^{\text{imp}}_{\text{m}} + n^{\text{f}}_{\text{m}}, \qquad \text{where} \qquad n^{\text{imp}}_{\text{m}} = \frac{(1 + \mathcal{C}_{\text{r}})\kappa}{4\mathcal{C}_{\text{r}} \kappa_{\text{l}} \eta}. \tag{4.37}$$

I have written the imprecision in terms of the red drive cooperativity $\mathcal{C}_{\text{r}} = 4g^2/(\kappa \Gamma_{\text{m}})$, which is proportional to drive strength. The imprecision decreases with drive power until it saturates at

$\kappa/(4\kappa_\mathrm{l}\eta)$, which is at minimum $1/4$ for the reflection geometry or $1/2$ for the transmission geometry. These results are shown in Figure 4.3(a).

4.5.2 Single blue-detuned drive

The case of a single blue-detuned drive is very similar to the single red-detuned drive except that the radiation pressure damping is opposite in sign, leading to amplification of mechanical motion. Once again specializing to the resolved-sideband limit where radiation pressure effects are maximal, and assuming the weak coupling limit and absence of excess photon noise, the output spectrum (Equation 3.77) is

$$S_{a_\mathrm{out}a_\mathrm{out}}[\omega] = S^g_{a_\mathrm{out}a_\mathrm{out}}[\omega] = \frac{4g^2\kappa_\mathrm{l}\Gamma_\mathrm{tot}}{\kappa^2}(n^\mathrm{f}_\mathrm{m}+1)|\chi_\mathrm{m,eff}[-\omega+\omega_\mathrm{b}]|^2. \tag{4.38}$$

Once again, there is no advantage to making a homodyne measurement over a heterodyne (since this time the upper sideband is strongly filtered by the cavity response) and a heterodyne measurement will mix the lower sideband centered at $\omega_\mathrm{b} - \Omega_\mathrm{m}$ down to frequency $\omega = |\omega_\mathrm{LO} - (\omega_\mathrm{b} - \Omega_\mathrm{m} - \delta)|$. The inferred displacement spectral density and mechanical quanta are

$$S^\mathrm{tot}_{xx}[\omega] = S^\mathrm{imp}_{xx}[\omega] + S^\mathrm{f}_{xx}[\omega] + 2S^\mathrm{zp}_{xx}[\omega] = \frac{x^2_\mathrm{zp}\kappa^2}{2g^2\kappa_\mathrm{l}\eta} + 2x^2_\mathrm{zp}\Gamma_\mathrm{tot}(n^\mathrm{f}_\mathrm{m}+1)|\chi_\mathrm{m,eff}[\Omega_\mathrm{m}+\delta]|^2, \tag{4.39}$$

$$n^\mathrm{tot}_\mathrm{m} = n^\mathrm{imp}_\mathrm{m} + n^\mathrm{f}_\mathrm{m} + 2n^\mathrm{zp}_\mathrm{m}, \qquad n^\mathrm{imp}_\mathrm{m} = \frac{(1-\mathcal{C}_\mathrm{b})\kappa}{4\mathcal{C}_\mathrm{b}\kappa_\mathrm{l}\eta}. \tag{4.40}$$

The zero point spectral density is S^zp_{xx} and the zero point number of quanta is $n^\mathrm{zp}_\mathrm{m} = 1/2$. The blue drive cooperativity is $\mathcal{C}_\mathrm{b} = 4g^2/(\kappa\Gamma_\mathrm{m})$. This time, the number of imprecision quanta decreases to zero as the final mechanical occupation blows up at $\mathcal{C}_\mathrm{b} = 1$. These results for the blue drive are shown alongside those for the red drive in Figure 4.3(a).

4.5.3 Single on-resonance drive, homodyne detection

The case of a single, on-resonance drive is somewhat different from the red and blue detuned cases because there is no dynamical radiation pressure. Homodyne detection is often most preferable because the two sidebands can be folded on top of each other, increasing the signal to noise due to
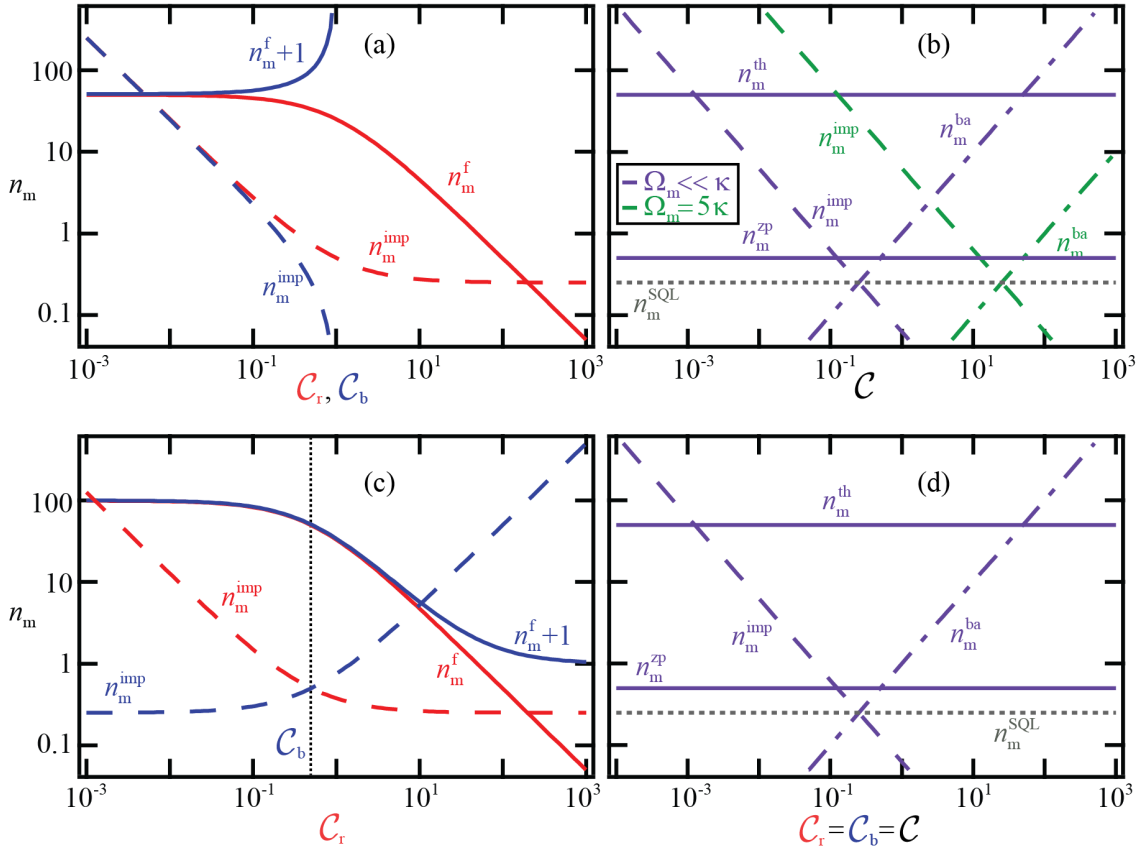
Figure 4.3: Mechanical occupancy contributions for various drive schemes. For all graphs, $\eta = 1$, $n_{\rm m}^{\rm th} = 50$, $\kappa_{\rm l} = \kappa$, and the best single-quadrature detection result is shown. Imprecisions (dashed), backactions (dash-dotted), and final or thermal and zero point (solid) occupancies are shown for each case. (a) Single red or single blue drive in the far resolved-sideband regime. The phonon occupancies are plotted as a function of cooperativity $\mathcal{C}_{\rm d} = 4g_{\rm d}^2/(\kappa\Gamma_{\rm m})$ for d = r and d = b. (b) Single, on-resonant drive. Phonon occupancies are measured with a homodyne detection scheme and plotted as a function of cooperativity. The results are shown in the unresolved sideband regime $\Omega_{\rm m} \ll \kappa$ (purple) and the resolved-sideband regime $\Omega_{\rm m} = 5\kappa$ (green). (c) Two drive scheme with unequal drives. The occupancies are plotted as a function of red drive cooperativity with the blue drive cooperativity fixed at $\mathcal{C}_{\rm b} = 0.5$ (vertical black dotted line). (d) Two drive scheme with equal drive strengths. Phonon occupancies are plotted as a function of equal cooperativity. The imprecision is that found in a homodyne, non-overlapping sidebands measurement. Comparison to (b) shows why the two drive scheme is preferable in the resolved-sideband regime.

their constructive interference. In the absence of excess photon noise, the output spectrum for an on-resonant drive (Equation 3.79) is

$$S_{a_{\text{out}}a_{\text{out}}}[\omega] = S_{a_{\text{out}}a_{\text{out}}}^{\text{mech}}[\omega] = \frac{4g^2\kappa_{\text{l}}\Gamma_{\text{m}}}{\kappa^2 + 4\Omega_{\text{m}}^2}\left(n_{\text{m}}^{\text{f}}|\chi_{\text{m}}[\omega - \overline{\omega}_{\text{c}}]|^2 + (n_{\text{m}}^{\text{f}} + 1)|\chi_{\text{m}}[-\omega + \overline{\omega}_{\text{c}}]|^2\right). \quad (4.41)$$

The optimal homodyne single-quadrature intensity (Equation 4.20) and the inferred displacement spectral density and occupancy are

$$S_{II}^{\text{photon}}[\omega] = \frac{1}{2\eta} + \frac{8g^2\kappa_{\text{l}}\Gamma_{\text{m}}}{\kappa^2 + 4\Omega_{\text{m}}^2}\left(n_{\text{m}}^{\text{f}} + \frac{1}{2}\right)|\chi_{\text{m}}[\Omega_{\text{m}} + \delta]|^2, \quad (4.42)$$

$$S_{xx}^{\text{tot}}[\omega] = S_{xx}^{\text{imp}}[\omega] + S_{xx}^{\text{f}}[\omega] + S_{xx}^{\text{zp}}[\omega] = \frac{x_{\text{zp}}^2\kappa(1+\nu)}{2\mathcal{C}\Gamma_{\text{m}}\kappa_{\text{l}}\eta} + 2x_{\text{zp}}^2\Gamma_{\text{m}}(n_{\text{m}}^{\text{f}} + \frac{1}{2})|\chi_{\text{m}}[\Omega_{\text{m}} + \delta]|^2 \quad (4.43)$$

$$n_{\text{m}}^{\text{tot}} = n_{\text{m}}^{\text{imp}} + n_{\text{m}}^{\text{th}} + n_{\text{m}}^{\text{zp}} + n_{\text{m}}^{\text{ba}} = \frac{(1+\nu)\kappa}{16\mathcal{C}\kappa_{\text{l}}\eta} + n_{\text{m}}^{\text{th}} + \frac{1}{2} + \frac{\mathcal{C}}{(1+\nu)}. \quad (4.44)$$

In the last line, the imprecision and backaction are written in terms of cooperativity $C = 4g^2/(\kappa\Gamma_{\text{m}})$ and a resolved sideband factor $\nu = 4\Omega_{\text{m}}^2/\kappa^2$. The product of the imprecision and backaction numbers of quanta is $n_{\text{m}}^{\text{imp}}n_{\text{m}}^{\text{ba}} = \kappa/(16\kappa_{\text{l}}\eta) \geq 1/16$. This minimum imprecision-backaction product is only met for a perfectly overcoupled cavity in the reflection geometry, measured with single-quadrature, quantum-efficient, homodyne detection. The minimum total added noise occurs when $n_{\text{m}}^{\text{imp}} = n_{\text{m}}^{\text{ba}} = n_{\text{m}}^{\text{SQL}} = 1/4$ and is called 'the standard quantum limit'. The minimum total number of quanta at the standard quantum limit is $n_{\text{m}}^{\text{tot}} = n_{\text{m}}^{\text{imp}} + n_{\text{m}}^{\text{ba}} + n_{\text{m}}^{\text{zp}} = 1$. The cooperativity required to reach the standard quantum limit is $\mathcal{C}^{\text{SQL}} = (1+\nu)/4$. Figure 4.3(b) shows the different occupation contributions resulting from an on-resonant cavity drive.

The standard quantum limit can be restated as a limit on the product of the imprecision displacement spectral density and the backaction force spectral density (both of which are frequency independent). These quantities, their product, and their values at the standard quantum limit are

$$S_{xx}^{\text{imp}} = \frac{x_{\text{zp}}^2\kappa(1+\nu)}{2\mathcal{C}\Gamma_{\text{m}}\kappa_{\text{l}}\eta}, \quad (4.45)$$

$$S_{FF}^{\text{ba}} = \frac{\hbar^2 S_{xx}^{\text{ba}}[\omega]}{x_{\text{zp}}^4|\chi_{\text{m,eff}}[\omega]|^2} = \frac{2\hbar^2\Gamma_{\text{m}}\mathcal{C}}{x_{\text{zp}}^2(1+\nu)}, \quad (4.46)$$

$$S_{xx}^{\text{imp}}S_{FF}^{\text{ba}} = \frac{\hbar^2\kappa}{\kappa_{\text{l}}\eta} \geq \hbar^2, \quad (4.47)$$

$$S_{xx}^{\text{SQL}} = \frac{2x_{\text{zp}}^2}{\Gamma_{\text{tot}}}, \quad\quad S_{FF}^{\text{SQL}} = \frac{\hbar^2\Gamma_{\text{tot}}}{2x_{\text{zp}}^2}. \quad (4.48)$$

Defining S_{xx}^{SQL} in terms of Γ_{tot} rather than Γ_{m} is inconsequential in the on-resonant drive case (because $\Gamma_{\mathrm{tot}} = \Gamma_{\mathrm{m}}$). However, this definition has the nice general property that

$$\frac{S_{xx}[\Omega_{\mathrm{m}}]}{4S_{xx}^{\mathrm{SQL}}} = \frac{\Gamma_{\mathrm{tot}}^2}{4} n_{\mathrm{m}}^{\mathrm{f}} |\chi_{\mathrm{m,eff}}[\Omega_{\mathrm{m}}]|^2 = n_{\mathrm{m}}^{\mathrm{f}}. \tag{4.49}$$

Thus, plotting an output spectrum in units of $S_{xx}[\omega]/(4S_{xx}^{\mathrm{SQL}})$ allows the mechanical occupancy to be directly read-off as the value on resonance.

4.5.4 Single on-resonance drive, heterodyne detection

While the minimum imprecision-backaction product for an on-resonant drive is achieved only for a homodyne measurement, there are a few technical reasons it might be preferable to do a heterodyne measurement. One is that the mechanical oscillator's resonant frequency may be too large to digitize easily. Another is that the amplifier may not have enough bandwidth to amplify both sidebands (for instance if $\kappa_{\mathrm{J}} < 2\Omega_{\mathrm{m}}$). A third is that it is necessary to measure the two sidebands independently in order to see sideband asymmetry. In these cases, it might be preferable to do a heterodyne measurement even if the imprecision is slightly higher. Here, I assume that I am interested in measuring the upper sideband. The lower sideband would give nearly identical results, with the replacement $n_{\mathrm{m}}^{\mathrm{f}} \to n_{\mathrm{m}}^{\mathrm{f}} + 1$. The optimal heterodyne intensity spectral density, inferred displacement spectral density, and number of phonons are

$$S_{II}^{\mathrm{photon}}[\omega] = \frac{1}{2\eta} + \frac{2g^2\kappa_{\mathrm{l}}\Gamma_{\mathrm{m}}}{\kappa^2 + 4\Omega_{\mathrm{m}}^2} n_{\mathrm{m}}^{\mathrm{f}} |\chi_{\mathrm{m}}[\omega - \overline{\omega}_{\mathrm{c}}]|^2, \tag{4.50}$$

$$S_{xx}^{\mathrm{tot}}[\omega] = \frac{2x_{\mathrm{zp}}^2\kappa(1+\nu)}{\mathcal{C}\kappa_{\mathrm{l}}\Gamma_{\mathrm{m}}\eta} + 2x_{\mathrm{zp}}^2\Gamma_{\mathrm{m}}n_{\mathrm{m}}^{\mathrm{f}} |\chi_{\mathrm{m}}[\omega - \overline{\omega}_{\mathrm{c}}]|^2, \tag{4.51}$$

$$n_{\mathrm{m}}^{\mathrm{tot}} = \frac{\kappa(1+\nu)}{4\mathcal{C}\kappa_{\mathrm{l}}\eta} + n_{\mathrm{m}}^{\mathrm{th}} + \frac{\mathcal{C}}{(1+\nu)}. \tag{4.52}$$

4.5.5 Generalized single-drive Heisenberg measurement relation

I can write the results of the previous few pages in a more generalized way. The general imprecision for a single-quadrature homodyne measurement ($\omega_{\mathrm{LO}} = \omega_{\mathrm{d}}$, identical to a heterodyne

measurement for off-resonant drive frequency) is

$$n_{\mathrm{m}}^{\mathrm{imp}} = \frac{\Gamma_{\mathrm{tot}}}{4g^2\eta\kappa_{\mathrm{l}}|\chi_{\mathrm{c}}[\omega_{\mathrm{d}} + \Omega_{\mathrm{m}}] - \chi_{\mathrm{c}}^*[\omega_{\mathrm{d}} - \Omega_{\mathrm{m}}]|^2}. \tag{4.53}$$

The generalized backaction fluctuations are

$$n_{\mathrm{m}}^{\mathrm{ba}} = \frac{g^2\kappa(1 + 2n_{\mathrm{c}}^{\mathrm{th}})}{2\Gamma_{\mathrm{tot}}} \left(|\chi_{\mathrm{c}}[\omega_{\mathrm{d}} - \Omega_{\mathrm{m}}]|^2 + |\chi_{\mathrm{c}}[\omega_{\mathrm{d}} + \Omega_{\mathrm{m}}]|^2\right). \tag{4.54}$$

The product of these two quantities realizes a Heisenberg uncertainty relation between measurement and perturbation of the motion:

$$
\begin{aligned}
n_{\mathrm{m}}^{\mathrm{imp}} n_{\mathrm{m}}^{\mathrm{ba}} &= \frac{\kappa(1 + 2n_{\mathrm{c}}^{\mathrm{th}})}{8\kappa_{\mathrm{l}}\eta} \frac{|\chi_{\mathrm{c}}[\omega_{\mathrm{d}} + \Omega_{\mathrm{m}}]|^2 + |\chi_{\mathrm{c}}[\omega_{\mathrm{d}} - \Omega_{\mathrm{m}}]|^2}{|\chi_{\mathrm{c}}[\omega_{\mathrm{d}} + \Omega_{\mathrm{m}}] - \chi_{\mathrm{c}}^*[\omega_{\mathrm{d}} - \Omega_{\mathrm{m}}]|^2} \tag{4.55} \\
&= \frac{\kappa(1 + 2n_{\mathrm{c}}^{\mathrm{th}})}{16\kappa_{\mathrm{l}}\eta} \left(1 + \frac{4\Delta^2}{\kappa^2 + 4\Omega_{\mathrm{m}}^2}\right) \geq \frac{1}{16}\left(1 + \frac{4\Delta^2}{\kappa^2 + 4\Omega_{\mathrm{m}}^2}\right). \tag{4.56}
\end{aligned}
$$

This uncertainty relation can be re-expressed in terms of displacement and force spectral densities:

$$S_{xx}^{\mathrm{imp}} S_{FF}^{\mathrm{ba}} = \left(\frac{8x_{\mathrm{zp}}^2}{\Gamma_{\mathrm{tot}}} n_{\mathrm{m}}^{\mathrm{imp}}\right)\left(\frac{2\hbar^2\Gamma_{\mathrm{tot}}}{x_{\mathrm{zp}}^2} n_{\mathrm{m}}^{\mathrm{ba}}\right) = 16\hbar^2 n_{\mathrm{m}}^{\mathrm{imp}} n_{\mathrm{m}}^{\mathrm{ba}} \geq \hbar^2\left(1 + \frac{4\Delta^2}{\kappa^2 + 4\Omega_{\mathrm{m}}^2}\right). \tag{4.57}$$

These relations recover the results obtained above for an on-resonant drive:

$$n_{\mathrm{m}}^{\mathrm{imp}} = \frac{(1 + \nu)\kappa}{16\mathcal{C}\kappa_{\mathrm{l}}\eta}, \qquad n_{\mathrm{m}}^{\mathrm{ba}} = \frac{\mathcal{C}(1 + 2n_{\mathrm{c}}^{\mathrm{th}})}{1 + \nu}, \qquad n_{\mathrm{m}}^{\mathrm{imp}} n_{\mathrm{m}}^{\mathrm{ba}} = \frac{\kappa(1 + 2n_{\mathrm{c}}^{\mathrm{th}})}{16\kappa_{\mathrm{l}}\eta} \geq \frac{1}{16}. \tag{4.58}$$

For an optimally red or blue-detuned drive they give:

$$n_{\mathrm{m}}^{\mathrm{imp}} = \frac{\kappa(1 + 4\nu(1 \pm \mathcal{C}))}{16\mathcal{C}\kappa_{\mathrm{l}}\eta(1 + \nu)} \approx \frac{\kappa(1 \pm \mathcal{C})}{4\mathcal{C}\kappa_{\mathrm{l}}\eta}, \qquad n_{\mathrm{m}}^{\mathrm{ba}} = \frac{\mathcal{C}(1 + 2n_{\mathrm{c}}^{\mathrm{th}})(1 + 2\nu)}{1 + 4\nu(1 \pm \mathcal{C})} \approx \frac{\mathcal{C}(1 + 2n_{\mathrm{c}}^{\mathrm{th}})}{2(1 \pm \mathcal{C})} \tag{4.59}$$

$$n_{\mathrm{m}}^{\mathrm{imp}} n_{\mathrm{m}}^{\mathrm{ba}} = \frac{\kappa(1 + 2n_{\mathrm{c}}^{\mathrm{th}})(1 + 2\nu)}{16\kappa_{\mathrm{l}}\eta(1 + \nu)} \geq \frac{1}{8}, \tag{4.60}$$

where the pluses are for the red-detuned case and the minuses are for the blue-detuned case.

4.5.6 Double drive scheme, sidebands not overlapping, heterodyne detection

In Section 3.2, I showed that in the far-resolved sideband regime both the sideband asymmetry and the quantum backaction could be enhanced by using two microwave drive tones, one optimally red-detuned and one optimally blue-detuned. For either of these measurements, it is preferable for

the sidebands to be spaced far apart compared to the mechanical linewidth. The output spectrum, ignoring excess photon noise, (Equation 3.136) is

$$S_{a_{\text{out}}a_{\text{out}}}[\omega] = \frac{4g_r^2\kappa_l\Gamma_{\text{tot}}}{\kappa^2}n_{\text{m}}^{\text{f}}|\chi_{\text{m,eff}}[\omega - \omega_r]|^2 + \frac{4g_b^2\kappa_l\Gamma_{\text{tot}}}{\kappa^2}(n_{\text{m}}^{\text{f}} + 1)|\chi_{\text{m,eff}}[-\omega + \omega_b]|^2. \qquad (4.61)$$

Assuming the local oscillator is not at the average frequency of the two drives ($\omega_{\text{LO}} \neq (\omega_r + \omega_b)/2$), the sidebands do not fold on top of each other and the results in the single-quadrature scheme for the red upper sideband are

$$S_{II}^{\text{photon}}[\omega] = \frac{1}{2\eta} + \frac{2g_r^2\kappa_l\Gamma_{\text{tot}}}{\kappa^2}n_{\text{m}}^{\text{f}}|\chi_{\text{m,eff}}[\Omega_{\text{m}} + \delta]|^2, \qquad (4.62)$$

$$S_{xx}^{\text{tot}}[\omega] = \frac{2x_{\text{zp}}^2\kappa}{\mathcal{C}_r\kappa_l\Gamma_{\text{m}}\eta} + 2x_{\text{zp}}^2 n_{\text{m}}^{\text{f}}\Gamma_{\text{tot}}|\chi_{\text{m,eff}}[\Omega_{\text{m}} + \delta]|^2, \qquad (4.63)$$

$$n_{\text{m}}^{\text{tot}} = \frac{\kappa(1 + \mathcal{C}_r - \mathcal{C}_b)}{4\mathcal{C}_r\kappa_l\eta} + n_{\text{m}}^{\text{f}}. \qquad (4.64)$$

The imprecision for the lower blue sideband is the same with $\mathcal{C}_r \to \mathcal{C}_b$ in the denominator. These imprecisions (and the accompanying final occupancies) are shown in Figure 4.3(c) for a fixed blue drive power as red drive power is increased. The backaction contribution to motion and the backaction-imprecision product for the red sideband are

$$n_{\text{m}}^{\text{ba}} = \frac{\mathcal{C}_r + \mathcal{C}_b}{2(1 + \mathcal{C}_r - \mathcal{C}_b)}, \qquad n_{\text{m,r}}^{\text{imp}}n_{\text{m}}^{\text{ba}} = \frac{\kappa(\mathcal{C}_r + \mathcal{C}_b)}{8\mathcal{C}_r\kappa_l\eta}. \qquad (4.65)$$

If the two drives are of equal strength $\mathcal{C}_r = \mathcal{C}_b = \mathcal{C}$, the backaction takes the form $n_{\text{m}}^{\text{ba}} = \mathcal{C}$ (Equation 3.122). The imprecision-backaction product is then $n_{\text{m}}^{\text{imp}}n_{\text{m}}^{\text{ba}} = \kappa/(4\kappa_l\eta) \geq 1/4$. This product may not seem impressive compared with the product achieved with an on-resonant drive. However, the cooperativity required to reach this point is $\mathcal{C} = 1/2$, making it considerably easier to achieve in the resolved sideband limit than that required with an on-resonant drive, $\mathcal{C} = (1 + \nu)/4$.

4.5.7   Double drive scheme, sidebands not overlapping, homodyne detection

If the interferometric measurement of the two-drive scheme is done with the local oscillator at $\omega_{\text{LO}} = (\omega_r + \omega_b)/2$ and the two drives are of equal strength $g_r = g_b = g$, the signal to noise can be improved in exactly the same way it was for the single on-resonance drive case when a homodyne

measurement was used. The measured frequency will be $\omega = |(\omega_{\rm b} - \omega_{\rm r})/2 - (\Omega_{\rm m} + \delta)|$ and the results are

$$S_{II}^{\rm photon}[\omega] \ = \ \frac{1}{2\eta} + \frac{8g^2\kappa_{\rm l}\Gamma_{\rm m}}{\kappa^2}(n_{\rm m}^{\rm f} + \frac{1}{2})|\chi_{\rm m}[\Omega_{\rm m} + \delta]|^2, \tag{4.66}$$

$$S_{xx}^{\rm tot}[\omega] \ = \ \frac{x_{\rm zp}^2\kappa}{2\mathcal{C}\Gamma_{\rm m}\kappa_{\rm l}\eta} + 2x_{\rm zp}^2\Gamma_{\rm m}(n_{\rm m}^{\rm f} + \frac{1}{2})|\chi_{\rm m}[\Omega_{\rm m} + \delta]|^2, \tag{4.67}$$

$$n_{\rm m}^{\rm tot} \ = \ \frac{\kappa}{16\mathcal{C}\kappa_{\rm l}\eta} + n_{\rm m}^{\rm th} + \frac{1}{2} + \mathcal{C}. \tag{4.68}$$

The imprecision-backaction product is then the same as for a single, on-resonant drive measured in the homodyne configuration: $n_{\rm m}^{\rm imp}n_{\rm m}^{\rm ba} = \kappa/(16\kappa_{\rm l}\eta) \geq 1/16$. However, as with the heterodyne two-drive detection above, this point is achieved at far less power ($\mathcal{C}^{\rm SQL} = 1/4$) than with the on-resonance drive ($\mathcal{C}^{\rm SQL} = (1+\nu)/4$) in the resolved sideband regime (compare Figure 4.3(b) and (d)).

4.5.8   Double drive scheme, sidebands overlapping

As I showed in Section 3.2, overlapping the two sidebands from two equal drives results in backaction evasion. This effect results from the fact that the mechanical state measured this way is stationary and the backaction force acts on the quadrature orthogonal to the one that is measured. In this case, the output spectrum is (Equation 3.136)

$$S_{a_{\rm out}a_{\rm out}}[\omega] \ = \ \frac{4g^2\kappa_{\rm l}\Gamma_{\rm m}}{\kappa^2}\left(2n_{\rm m}^{\rm th} + 1\right)|\chi_{\rm m}[\omega - \omega_{\rm r}]|^2 \tag{4.69}$$

The measured heterodyne intensity, inferred displacement spectral density, and mechanical occupation are

$$S_{II}^{\rm photon}[\omega] \ = \ \frac{1}{2\eta} + \frac{4g^2\kappa_{\rm l}\Gamma_{\rm m}}{\kappa^2}\left(n_{\rm m}^{\rm th} + \frac{1}{2}\right)|\chi_{\rm m}[\Omega_{\rm m} + \delta]|^2, \tag{4.70}$$

$$S_{xx}^{\rm tot}[\omega] \ = \ \frac{x_{\rm zp}^2\kappa}{\mathcal{C}\Gamma_{\rm m}\kappa_{\rm l}\eta} + 2x_{\rm zp}^2\Gamma_{\rm m}\left(n_{\rm m}^{\rm th} + \frac{1}{2}\right)|\chi_{\rm m}[\Omega_{\rm m} + \delta]|^2, \tag{4.71}$$

$$n_{\rm m}^{\rm tot} \ = \ \frac{\kappa}{8\mathcal{C}\kappa_{\rm l}\eta} + n_{\rm m}^{\rm th} + \frac{1}{2}. \tag{4.72}$$

The imprecision number of phonons for the overlapping sidebands is only half of that with non-overlapping sidebands. This makes sense from a quantum information standpoint because only one

quadrature of the mechanical field is measured (and thus an extra half quantum of added noise from measuring both quadratures is not required).

4.5.9 Summary of results

The imprecisions for situations in this section with large dynamical backaction (the single red and blue-detuned drives and two drives of unequal amplitude) are listed in Table 4.1(a). Imprecision and backaction occupations for situations with zero net dynamical backaction (the on-resonance drive and two drives of equal amplitude) are listed in Table 4.1(b).

(a)

drive	$n_{\mathrm{m}}^{\mathrm{imp}}$	$n_{\mathrm{m}}^{\mathrm{ba}}$	$n_{\mathrm{m}}^{\mathrm{imp}} n_{\mathrm{m}}^{\mathrm{ba}}$
red	$\kappa(1+\mathcal{C})/(4\kappa_{\mathrm{l}}\mathcal{C}\eta)$	$\mathcal{C}/(2(1+\mathcal{C}))$	$\kappa/(8\kappa_{\mathrm{l}}\eta)$
blue	$\kappa(1-\mathcal{C})/(4\kappa_{\mathrm{l}}\mathcal{C}\eta)$	$\mathcal{C}/(2(1-\mathcal{C}))$	$\kappa/(8\kappa_{\mathrm{l}}\eta)$
double (NO)	$\kappa(1+\mathcal{C}_{\mathrm{r}}-\mathcal{C}_{\mathrm{b}})/(4\kappa_{\mathrm{l}}\mathcal{C}_{\mathrm{d}}\eta)$	$(\mathcal{C}_{\mathrm{r}}+\mathcal{C}_{\mathrm{b}})/(2(1+\mathcal{C}_{\mathrm{r}}-\mathcal{C}_{\mathrm{b}}))$	$\kappa(\mathcal{C}_{\mathrm{r}}+\mathcal{C}_{\mathrm{b}})/(8\kappa_{\mathrm{l}}\mathcal{C}_{\mathrm{d}}\eta)$

(b)

drive	meas	$n_{\mathrm{m}}^{\mathrm{imp}}$	$n_{\mathrm{m}}^{\mathrm{ba}}$	$n_{\mathrm{m}}^{\mathrm{imp}} n_{\mathrm{m}}^{\mathrm{ba}}$
on-res	hetero	$\kappa(1+\nu)/(4\kappa_{\mathrm{l}}\mathcal{C}\eta)$	$\mathcal{C}/(1+\nu)$	$\kappa/(4\kappa_{\mathrm{l}}\eta)$
on-res	homo	$\kappa(1+\nu)/(16\kappa_{\mathrm{l}}\mathcal{C}\eta)$	$\mathcal{C}/(1+\nu)$	$\kappa/(16\kappa_{\mathrm{l}}\eta)$
double (NO)	hetero	$\kappa/(4\kappa_{\mathrm{l}}\mathcal{C}\eta)$	$\mathcal{C}$	$\kappa/(4\kappa_{\mathrm{l}}\eta)$
double (NO)	homo	$\kappa/(16\kappa_{\mathrm{l}}\mathcal{C}\eta)$	$\mathcal{C}$	$\kappa/(16\kappa_{\mathrm{l}}\eta)$
double (O)	hetero	$\kappa/(8\kappa_{\mathrm{l}}\mathcal{C}\eta)$	—	—

Table 4.1: Summary of imprecisions and backactions for different cavity drive cases. Quantities are written in terms of the cooperativity $\mathcal{C} = 4g^2/\kappa\Gamma_{\mathrm{m}}$, the resolved sideband factor $\nu = 4\Omega_{\mathrm{m}}^2/\kappa^2$, and the interferometer quantum efficiency η. The column 'drive' details the nature of the optomechanical drive. 'NO' indicates not-overlapping sidebands while 'O' indicates overlapping sidebands. (a) Results for cases where the net dynamical backaction is large, relevant for heterodyne detection in the resolved sideband limit. The two-drive result is thus for unequal amplitude drives and refers to the imprecision of the sideband associated with drive d. The results here apply to both single and two-quadrature detection as well as both homodyne and heterodyne detection. (b) Results for cases where the net dynamical backaction is negligible. The column 'meas' indicates 'homo' for homodyne measurement and 'hetero' for heterodyne. Thus, the two-drive cases are for equal amplitude drives ($g_{\mathrm{r}} = g_{\mathrm{b}} = g$). The results shown are all for single-quadrature detection. Two-quadrature detection results are the same except that the imprecision is a factor of two larger for homodyne cases.

<center>**Chapter 5**</center>

<center>**Device design and fabrication**</center>

In this chapter, I will discuss the different types of devices we have fabricated and measured. I will first explain the types of measurements of interest and the device parameters needed to optimize those measurements (Section 5.1). I will then discuss in detail the first major class of devices we made, namely ones with a wire or beam as the mechanical element (Section 5.2). As I will show, these devices do not achieve the best optomechanical coupling to date; however, they require less fabrication capabilities than the devices that have higher coupling and do achieve very high force sensitivity. I will first discuss the optimal parameters for this type of device and then explain their fabrication and achieved parameters. Lastly, I will briefly discuss devices with a suspended drum-like membrane as the mechanical oscillator, as fabricated by our colleagues at NIST (Section 5.3).

5.1 Quantities to optimize by fabrication

There are several quantities that can be designed on the device. For the cavity design, we control the cavity capacitance C, inductance L, coupling capacitance C_c, and device geometry (transmission or reflection), or put in other terms, the cavity resonant frequency ω_c, equivalent parallel RLC impedance[1] $Z_\mathrm{c} = \sqrt{L/C}$, and coupling rates κ_l and κ_r (these quantities were related

---

[1] The impedance $Z_\mathrm{c} = \sqrt{L/C}$ is the cavity impedance of the parallel RLC circuit equivalent to the actual circuit of interest. This should not be confused with the characteristic impedance of a transmission line, which is $Z_0 = \sqrt{\mathcal{L}/\mathcal{C}}$ where $\mathcal{L}$ and $\mathcal{C}$ are the inductance and capacitance per unit length of the transmission line. For a shorted $\lambda/4$ transmission line resonant circuit as in [10] and [45], $Z_\mathrm{c} = 4Z_0/\pi$, while for an open $\lambda/2$ resonant circuit as in [12], $Z_\mathrm{c} = 2Z_0/\pi$.

in Chapter 2).

For the mechanical design, we control the geometry and tension of the mechanical element. For a wire device, the geometry includes the length l, width w, thickness t, and spacing s between the wire and the ground plane. For a suspended membrane device, it includes the size and shape of the membrane and the height above the substrate. These mechanical parameters control the mechanical frequency Ω_{m}, mass m, and loss rate Γ_{m}. Both the cavity and mechanical parameters control the optomechanical coupling $G = d\omega_{\mathrm{c}}/dx$. Ideally, the best device would have both the highest optomechanical coupling and lowest mass possible. However, in practice, these two quantities trade off depending on fabrication parameters. Thus, it is important to see how measured quantities, such a force sensitivity or optomechanical control, depend on this compromise.

5.1.1   Optomechanical control

Many of the experiments of interest, such as dynamical radiation pressure cooling and amplification of mechanical motion (Sections 3.1-3.2), quantum backaction (Section 3.2), and preparation and readout of the mechanical oscillator in time (Section 3.3) are optimized by having a large single-photon optomechanical coupling g_0 between the mechanical oscillator and the cavity. The coupling can be written in terms of cavity and mechanical parameters

$$G = \frac{d\omega_{\mathrm{c}}}{dx} = \frac{d\omega_{\mathrm{c}}}{dC_{\mathrm{tot}}}\frac{dC_{\mathrm{tot}}}{dx} = \frac{-\omega_{\mathrm{c}}}{2C_{\mathrm{tot}}}\frac{dC_{\mathrm{tot}}}{dx} = \frac{-\omega_{\mathrm{c}}^2 Z_{\mathrm{c}}}{2}\frac{dC_{\mathrm{tot}}}{dx}, \tag{5.1}$$

$$g_0 = Gx_{\mathrm{zp}} = \frac{-\omega_{\mathrm{c}}^2 Z_{\mathrm{c}}}{2}\frac{dC_{\mathrm{tot}}}{dx}\sqrt{\frac{\hbar}{2m\Omega_{\mathrm{m}}}}, \tag{5.2}$$

where C_{tot} is the entire capacitance of the circuit ($C_{\mathrm{tot}} = C + C_{\mathrm{c}}$). From this expression, it is clear that it is preferable to have a large cavity frequency and large zero point motion (or small mechanical mass and resonance frequency). It is easy to see why the quantities G and x_{zp} trade off - in order to achieve a large change in capacitance per motion, the mechanical oscillator should have a large surface area. But in order to have a small mass, the mechanical oscillator should have small dimensions. Within the microwave regime, it is not possible to dramatically increase the cavity frequency above $\sim$10 GHz without making the energy comparable to the superconducting gap of

aluminum. For a given cavity frequency then, it is preferable to have large cavity impedance. This makes sense because in a higher impedance cavity, the mechanical motion will modulate a larger fraction of the total capacitance and thus have a higher participation ratio $C_{\text{tot}}^{-1}(dC_{\text{tot}}/dx)$.

I have so far only said that it is good to have a large g_0 (and by association a large maximum $g = g_0\sqrt{n_{\text{d}}}$). But large compared to what? There are three important thresholds of coupling that allow interesting physics. The easiest coupling benchmark to reach is that of large cooperativity $\mathcal{C} = 4g^2/(\kappa\Gamma_{\text{m}}) > 1$. For a red-detuned drive in the resolved sideband limit, a cooperativity equal to one allows doubling the mechanical linewidth and decreasing the mechanical occupancy by a factor of two. For a blue-detuned drive, it allows a decrease of the mechanical linewidth to zero and arbitrary amplification of mechanical motion. Cooperativity greater than or equal to one allows access to the standard quantum limit, both for a single drive in the unresolved sideband regime or equal red and blue-detuned drives in the resolved sideband regime. Cooperativity equal to one is also the coupling required to realize ideal conversion between itinerant photon and phonon energies for a red-detuned drive applied to a reflection geometry system in the resolved sideband limit.

The second interesting benchmark for the coupling is the quantum-enabled regime: $\tilde{\mathcal{C}} = 4g^2/(\kappa\Gamma_{\text{m}}n_{\text{m}}^{\text{th}}) > 1$. This quantity is a ratio between the rate of coupling to the rate of mechanical quantum decoherence (the rate that a single thermal phonon enters the mechanical oscillator). Having $\tilde{\mathcal{C}} > 1$ is thus required to transfer, store, and retrieve microwave states with energies on the order of a single photon. For a red-detuned drive in the resolved sideband regime, the quantum enabled regime allows cooling to a mechanical occupancy less than one. The onset of the quantum enabled regime is also the point where the quantum backaction motion of the mechanical oscillator becomes larger than its thermal motion, for either a single drive in the unresolved sideband regime or two equal drives in the resolved sideband regime.

The third coupling benchmark of interest is strong coupling: $\mathcal{S} = 4g^2/\kappa^2 > 1$. This regime allows the total mechanical linewidth to become equal to the cavity linewidth, causing the two resonant structures to undergo normal mode splitting. The onset of strong coupling, $\mathcal{S} = 1$, is also the point where the equations of motion are critically damped. Below this coupling, the equations

of motion are overdamped and application of a drive tone swaps itinerant photons to mechanical phonons and vice versa, but there is no oscillation of energy. For stronger couplings, the equations of motion are underdamped, and application of a drive tone causes energy to oscillate back and forth between the cavity and mechanical oscillator faster than it can be lost from the cavity. For example, strong coupling would be crucial for an experiment where the same cavity was coupled to both a mechanical oscillator and a qubit and the qubit was used to prepare arbitrary states of the mechanical oscillator. There are also many interesting things that can be done if an optomechanical system is in the single photon strong coupling regime: $4g_0^2/\kappa^2 > 1$ (see reference [93]). However, this regime is currently out of the reach of experiments.

The three different coupling regimes, written in terms of device parameters are

$$\mathcal{C} = \frac{4g^2}{\kappa\Gamma_{\mathrm{m}}} = \frac{2\hbar G^2 n_{\mathrm{d}}}{\kappa m \Omega_{\mathrm{m}} \Gamma_{\mathrm{m}}}, \qquad \tilde{\mathcal{C}} = \frac{4g^2}{\kappa\Gamma_{\mathrm{m}} n_{\mathrm{m}}^{\mathrm{th}}} = \frac{2\hbar^2 G^2 n_{\mathrm{d}}}{k_{\mathrm{B}} T \kappa m \Gamma_{\mathrm{m}}}, \qquad \mathcal{S} = \frac{4g^2}{\kappa^2} = \frac{2\hbar G^2 n_{\mathrm{d}}}{\kappa^2 m \Omega_{\mathrm{m}}}. \quad (5.3)$$

Here, k_{B} is Boltzmann's constant and T is the temperature of the mechanical oscillator. These expressions all benefit from large G, small κ, and small m. However, it is useful to see how they differ in their dependence on Γ_{m} and Ω_{m}.

5.1.2   Force sensitivity

An important experiment with a different goal than optomechanical control is that of force sensitivity. In this case, the idea is to detect some external force acting on the mechanical oscillator. The sensitivity to this force will be limited by mechanical motion due to sources other than this force: namely thermal, backaction and imprecision motion. Assuming that the power used to measure is high enough to decrease the imprecision below the thermal noise but not yet high enough to create backaction motion comparable to the thermal motion, the force sensitivity will be limited by the thermal force spectrum: $S_{FF}^{\mathrm{th}} = 4k_{\mathrm{B}} T m_{\mathrm{eff}} \Gamma_{\mathrm{m}}$, where m_{eff} is the effective mass of the mechanical oscillator, discussed in Appendix E. The best force sensitivity is achieved by having the smallest mass and mechanical loss and does not depend at all on the coupling strength (as long as it is high enough to reach the regime where thermal noise is much larger than imprecision noise).

In experiments, we observe that this simple picture is not quite true. In practice, the mechanical oscillator heats up as a function of incident microwave power, P_{in}. Using the data from references [10] and [76], it is possible to make an empirical law for this dependence (Figure 5.1). Fitting the two sets of data to power laws (shown in red), I find $T_{\text{m}} = 29P_{\text{in}}^{0.35}$ for reference [10] and $T_{\text{m}} = 71P_{\text{in}}^{0.14}$, where T_{m} here is in millikelvin and P_{in} is in picowatts. Compromising between the two with a power law of $T_{\text{m}} \propto P_{\text{in}}^{1/4}$ (shown as a black line), I find a reasonable approximation to the data. In this case, the extra noise due to this thermal backaction force on the mechanics will hurt the force sensitivity as a function of power. It is therefore optimal to work at a power where the imprecision and thermal backaction are in some sense balanced. The power dependence of the two contributions at the mechanical resonance goes as

$$S_{FF}^{\text{th}} = 4\alpha m_{\text{eff}}\Gamma_{\text{m}}P_{\text{in}}^{1/4} \qquad \text{and} \qquad S_{FF}^{\text{imp}} = \beta\frac{m_{\text{eff}}^2\Omega_{\text{m}}^2\Gamma_{\text{m}}^2}{G^2 P_{\text{in}}}. \tag{5.4}$$

Here, I have used α to replace k_{B} and the proportionality constant of the power to temperature
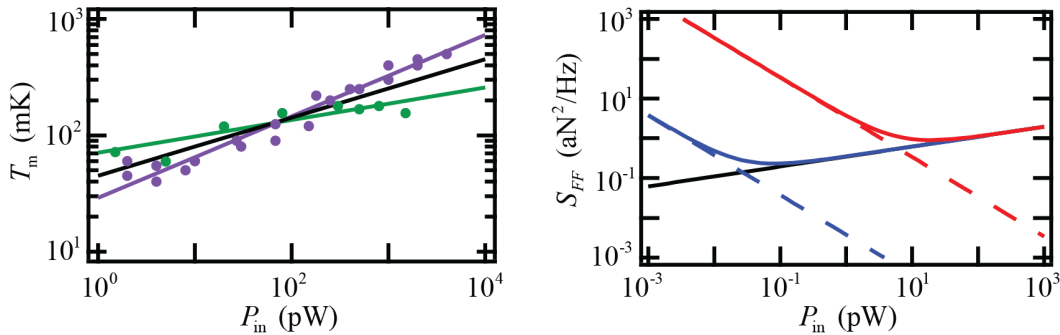
Figure 5.1: Power dependence of mechanical temperature in wire devices. (a) Mechanical temperature as a function of incident microwave power. The data is from references [10] (purple) and [76] (green). The purple and green lines are power law fits to the data, while the black line is a compromise between the two power laws. As the microwave power increases, the mechanical oscillator is parasitically heated. (b) Force sensitivity as a function of incident power when parasitic heating is taken into account. The power dependent thermal force spectral density is shown as a black line. The imprecision (dashed line) and total (solid line) force spectral densities are shown for two different coupling strengths, $G = 2\pi \times 1$ kHz/nm (red) and $G = 2\pi \times 30$ kHz/nm (blue). The best force sensitivity and power required are both lower for larger coupling. This graph was made with device parameters similar to those of reference [76].

relation and β to store the cavity parameters and geometry as well as the added noise of the measurement. The power that minimizes the total force noise on resonance is as follows.

$$\frac{d}{dP_{\text{in}}}\left(S_{\text{F}}^{\text{th}} + S_{\text{F}}^{\text{imp}}\right) = \alpha m_{\text{eff}}\gamma_{\text{m}}P_{\text{in}}^{-3/4} - \frac{\beta m_{\text{eff}}^2\Omega_{\text{m}}^2\Gamma_{\text{m}}^2}{G^2 P_{\text{in}}^2} = 0, \tag{5.5}$$

$$P_{\text{in}}^{\text{optimal}} = \left(\frac{\beta m_{\text{eff}}\Omega_{\text{m}}^2\Gamma_{\text{m}}}{\alpha G^2}\right)^{4/5}, \tag{5.6}$$

$$\left(S_{\text{F}}^{\text{th}} + S_{\text{F}}^{\text{imp}}\right)_{\text{min}} = 5\alpha^{4/5}\beta^{1/5}\left(\frac{m_{\text{eff}}^3\Omega_{\text{m}}\Gamma_{\text{m}}^3}{G}\right)^{2/5}. \tag{5.7}$$

In this case, I find that the force sensitivity once again depends almost linearly with small mass and mechanical loss. But I now also find that the force sensitivity is improved by small mechanical frequency and large optomechanical coupling.

5.2   Wire devices

When we began studying optomechanics, our fabrication capabilities were limited. Thus, we wanted to make a device that only required using planar fabrication techniques such as simple lithography with no structures suspended above the chip. We opted to suspend the mechanical element by etching away the silicon substrate rather than creating extra sacrificial layers. To form an optomechanical device in a planar geometry, the mechanical oscillator must modulate a capacitance between two pieces of metal in the same plane. A long wire is then the best choice for maximizing surface length while also maximizing motion in the plane. We also chose to make the cavity and mechanical oscillator out of aluminum because it is superconducting at low temperatures and unharmed by the silicon etching. In this section, I will talk about the best design parameters for such a wire device, how it is fabricated, and the parameters we were able to achieve.

5.2.1   Wire device design

In this section, I will try to find relationships to predict the mechanical resonance frequency, mechanical linewidth, and optomechanical coupling based on design parameters. That will allow me to write the quantities of interest above in terms of design parameters to see how the experimental

quantities of interest can be optimized by design choices.

5.2.1.1   Mechanical resonance frequency

For a wire under high tension, the frequency of the fundamental mode can be found from the speed v of propagation along the wire:

$$\Omega_{\mathrm{m}} = 2\pi \times \frac{v}{2l} = 2\pi \times \frac{1}{2l}\sqrt{\frac{\tau}{m/l}} = 2\pi \times \frac{1}{2l}\sqrt{\frac{E_{\mathrm{Al}}\epsilon wt}{\rho_{\mathrm{Al}}wt}} = 2\pi \times \left(\frac{1}{2}\sqrt{\frac{E_{\mathrm{Al}}\epsilon}{\rho_{\mathrm{Al}}}}\right)\frac{1}{l} \qquad (5.8)$$

where τ is the tension, E_{Al} and ρ_{Al} are the Young's modulus and density of aluminum, and ϵ is the strain experienced by the aluminum. In the absence of tension (see [94, pgs. 233-236] with the understanding that I_y is incorrect and should be I_x), the resonance frequency is

$$\Omega_{\mathrm{m}} = \sqrt{\frac{EI_x}{\rho A}}\left(\frac{c_0}{l}\right)^2 = \sqrt{\frac{E_{\mathrm{Al}}(tw^3/12)}{\rho_{\mathrm{Al}}(wt)}}\left(\frac{c_0}{l}\right)^2 = 2\pi \times \left(1.03\sqrt{\frac{E_{\mathrm{Al}}}{\rho_{\mathrm{Al}}}}\right)\frac{w}{l^2}, \qquad (5.9)$$

where I_x is the polar moment of inertia about the direction of motion [94, pg. 204], A is the cross sectional area of the wire, and $c_0 = 4.73004$ specifies the mode shape of the lowest mechanical mode of a doubly-clamped beam. Note that while the expression for high-tension does not depend on t or w, this expression does and I would find a slightly different expression for the frequency of the out of plane mode: $\Omega_{\mathrm{m}} = 2\pi \times (1.03\sqrt{E/\rho})t/l^2$. More generally [95], the resonance frequency for any suspended wire or beam is

$$\boxed{\Omega_{\mathrm{m}} = 2\pi \times \left(1.03\sqrt{\frac{E_{\mathrm{Al}}}{\rho_{\mathrm{Al}}}}\right)\frac{w}{l^2}\sqrt{1 + \frac{\epsilon l^2}{3.4w^2}}}, \qquad (5.10)$$

which reduces to the above expressions for very high or low tension.

The tension turns out to be a very important, controllable quantity. Without annealing, we find that our aluminum films (and thus our wires) at room temperature are under compressive stress. When such a wire is cooled down, the aluminum shrinks more than the silicon, making the compressive stress smaller. The low-temperature resonant frequencies that we see for wires fabricated without annealing are consistent with little to no tension. We fabricate high-tension wires by annealing at a high temperature (specifically $340°$ C $= 613$ K). This makes the atoms

in the wire more mobile and they more quickly relax to their lowest energy configuration. There will now be some high temperature where the aluminum and silicon are the same length with no tension, and thus the aluminum will be under tension for lower temperatures. Because we cool the wires somewhat slowly, it is unlikely that this equilibrium temperature is 613 K, but it is above 300 K, as the annealed wires seem to be tensioned at room temperature. The equation governing thermal expansion is $dl/dT = \alpha[T]l$, where $\alpha[T]$ is the coefficient of thermal expansion. At high temperatures ($T > 100$ K), α is relatively constant, so I can integrate this equation to find the expected amount of expansion/contraction:

$$\alpha \int_{T_1}^{T_2} dT = \int_{l_1}^{l_2} \frac{dl}{l}, l_2 = l_1 e^{\alpha(T_2 - T_1)}. \tag{5.11}$$

The coefficients of thermal expansion for aluminum and silicon near room temperature are $\alpha_{Al} = 23 \times 10^6$ K^{-1} and $\alpha_{Si} = 3 \times 10^6$ K^{-1}. At low temperatures, I can look up the measured relative linear expansion coefficient $\Delta l/l$ referenced to room temperature in a book, such as in reference [96]. This gives nearly temperature independent values near zero Kelvin:

$$\left(\frac{\Delta l}{l}\right)_{Al} = \frac{l_{Al}[0 \text{ K}] - l_{Al}[300 \text{ K}]}{l_{Al}[300 \text{ K}]} = -0.004, \tag{5.12}$$

$$\left(\frac{\Delta l}{l}\right)_{Si} = \frac{l_{Si}[0 \text{ K}] - l_{Si}[300 \text{ K}]}{l_{Si}[300 \text{ K}]} = -0.0005. \tag{5.13}$$

If the aluminum and silicon are the same natural length l^* at temperature T^*, then the aluminum will want to shrink more than the silicon as it is cooled down. Because it is attached to the silicon, it cannot do this and will end up being the length of the silicon. Thus, the aluminum will experience a strain ϵ. The strains near room temperature (300 Kelvin) and near zero Kelvin are:

$$\epsilon[300 \text{ K}] = \frac{\Delta l}{l} = \frac{l_{Si}[300 \text{ K}] - l_{Al}[300 \text{ K}]}{l_{Al}[300 \text{ K}]} = \frac{l^* e^{\alpha_{Si}(300 - T^*)}}{l^* e^{\alpha_{Al}(300 - T^*)}} - 1 \tag{5.14}$$

$$= e^{(\alpha_{Si} - \alpha_{Al})(300 - T^*)} - 1, \tag{5.15}$$

$$\epsilon[0 \text{ K}] = \frac{\Delta l}{l} = \frac{l_{Si}[0 \text{ K}] - l_{Al}[0 \text{ K}]}{l_{Al}[0 \text{ K}]} = \frac{(1 - 0.0005)l_{Si}[300 \text{ K}]}{(1 - 0.004)l_{Al}[300 \text{ K}]} - 1 \tag{5.16}$$

$$= \frac{(1 - 0.0005)}{(1 - 0.004)} e^{(\alpha_{Si} - \alpha_{Al})(300 - T^*)} - 1. \tag{5.17}$$

The strain of the wire is related to the stress σ by Hooke's law $\sigma = E\epsilon$, where E is the Young's modulus. The tension τ is this stress times the cross sectional area of the wire: $\tau = \sigma wt = E_{Al}\epsilon wt$.

Assuming a range for equilibrium temperature 300 K< T^* < 600 K, I find that the strain (which, unlike the tension, does not depend on the wire dimensions) is $0 < \epsilon[300 \text{ K}] < 0.006$ and $0.004 < \epsilon[15$ mK$] < 0.010$.

5.2.1.2   Mechanical loss rate

The mechanical damping is not particularly easy to model, but can be estimated empirically from some general experimental trends we have observed (see Figure 5.2). This figure shows that the mechanical quality factor $Q_\text{m} \equiv \Omega_\text{m}/\Gamma_\text{m}$ increases at least linearly with Ω_m as tension is changed. It also indicates that for the lowest frequencies (in the absence of tension), $Q_\text{m} \sim 3000$, independent of length. So, I will make the assumptions that $Q_\text{m}[\tau = 0] = 3000$ and $\Gamma_\text{m}[\tau] = \Gamma_\text{m}[\tau = 0]$. From this I find that

$$\Gamma_\text{m}[\tau] = \frac{\Omega_\text{m}[\tau = 0]}{3000} = 2\pi \times \left(\frac{1.03}{3000} \sqrt{\frac{E_\text{Al}}{\rho_\text{Al}}} \right) \frac{w}{l^2} \approx \boxed{11 \frac{w}{l^2}}. \tag{5.18}$$
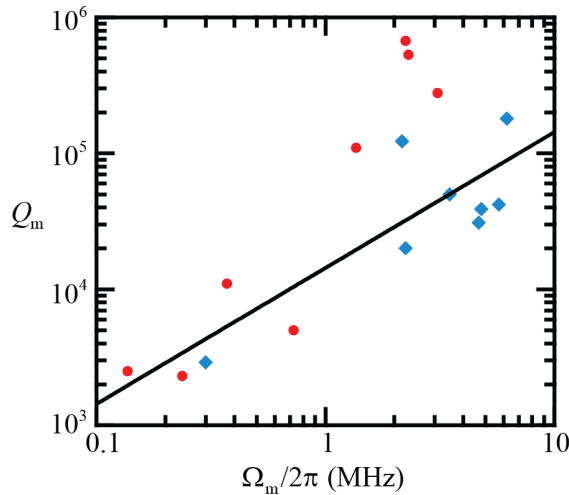
Figure 5.2: Measured mechanical quality factors of tensioned aluminum wire devices. The mechanical quality factor is shown as a function of mechanical resonance frequency for eight different 40 μm wires (blue squares) and eight 50 μm wires (red circles). The only difference between the eight devices in each data set is tension, which increases the mechanical frequency. The quality factor increases at least linearly with frequency (the black line corresponds to the average Γ_m for all devices). The data is from reference [97].

This expression, while empirical, gives some idea of the dependence of the mechanical linewidth on mechanical oscillator parameters. At the end of this section, this will enable me to write the quantities of interest from the previous section in terms of device parameters. A more sophisticated analysis of damping for wire oscillators, which came out after my analysis of wire devices presented here, can be found in reference [98].

5.2.1.3   Optomechanical coupling

The optomechanical coupling G for a mechanical oscillator coupled to a microwave circuit is (as found above)

$$G \equiv \frac{d\omega_{\mathrm{c}}}{dx} = \frac{-\omega_{\mathrm{c}}^2 Z_{\mathrm{c}}}{2} \frac{dC_{\mathrm{wire}}}{ds} \tag{5.19}$$

where C_{wire} and s are the capacitance and spacing between the wire and the ground plane. A change in position x of the wire is equivalent to a change of the spacing s. There are a few different ways to model the wire capacitance in order to find dC_{wire}/ds. Here, I model the wire and ground plane as two parallel wires or a coplanar stripline (CPS) (Figure 5.3). I also find more specific numerical results by simulating the full geometry.
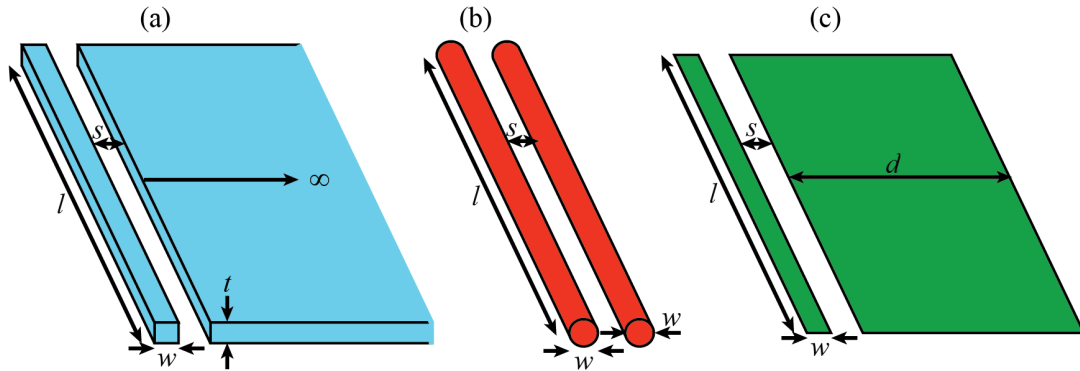

Figure 5.3: Models for wire capacitance. (a) Geometry of the device, involving a finite thickness wire of dimensions $l \times w \times t$ spaced by distance s from a relatively infinite ground plane. (b) Parallel wire geometry. (c) CPS geometry.

Parallel wire model

I can model a wire near an infinite ground plane as just two parallel wires (Figure 5.3(b)). This should give a lower bound on the capacitance for the geometry of interest. The formula for the capacitance of two parallel wires is:

$$
\begin{aligned}
C_{\text{wire}} &= \pi\epsilon_0 l \left(\ln \left[\frac{s+w}{w} + \sqrt{\left(\frac{s+w}{w}\right)^2 - 1} \right] \right)^{-1} \\
&= \pi\epsilon_0 l \left(\ln \left[\frac{s+w+\sqrt{s(s+2w)}}{w} \right] \right)^{-1}
\end{aligned}
\tag{5.20}
$$

$$
\boxed{ G = \frac{\omega_{\text{c}}^2 Z_{\text{c}} \pi \epsilon_0 l}{2\sqrt{s(s+2w)}} \left(\ln \left[\frac{s+w+\sqrt{s(s+2w)}}{w} \right] \right)^{-2} }.
\tag{5.21}
$$

CPS model

The capacitance between two uneven coplanar striplines (Figure 5.3(c)) is [99, pgs. 401-402]:

$$
C_{\text{wire}} = 2\epsilon_0 l \frac{K'[k]}{K[k]}, \qquad k' = \sqrt{\frac{w}{w+s}\frac{d}{d+s}} \xrightarrow{d\to\infty} \sqrt{\frac{w}{w+s}}.
\tag{5.22}
$$

Here, $K[k]$ is the complete elliptic integral[2] of the first kind and $K'[k] = K[k']$, where k' and k are complements: $k^2 + k'^2 = 1$; $k = \sqrt{s/(w+s)}$. It is possible to include the effect of finite thickness of the striplines [99, pg. 415] by using an effective spacing and width:

$$
s \to \overline{s} = s - \Delta, \qquad w \to \overline{w} = w + \Delta, \qquad \Delta \equiv \frac{5t}{4\pi}\left[1 + \ln\left(\frac{4\pi w}{t}\right) \right].
\tag{5.24}
$$

Reference [99] only endorses this method for $t/w \leq 0.1$, whereas we typically have $t/w \approx 1$, so we should be wary of results achieved this way, but they still may give some idea of how G scales with t. Obviously, this solution will be completely unusable for $\Delta > s$. The coupling G for the CPS model is

$$
\boxed{ G = -\epsilon_0 l \omega_{\text{c}}^2 Z_{\text{c}} \frac{d}{ds}\left(K\left[\sqrt{\frac{\overline{w}}{\overline{w}+\overline{s}}}\right] \Big/ K\left[\sqrt{\frac{\overline{s}}{\overline{w}+\overline{s}}}\right] \right) }.
\tag{5.25}
$$

---

[2] The definitions of the elliptical functions used in engineering texts are different from those in Mathematica due to a difference in the definition of the incomplete elliptic integral of the first kind (Elliptic F) [100, 101, 102, 103]:

$$
K[k]_{\text{engineering}} = \int_0^{\pi/2} \frac{d\theta}{\sqrt{1 - k^2\sin^2\theta}} = \text{EllipticK}[k^2]_{\text{mathematica}}.
\tag{5.23}
$$

Microwave Office simulation of CPS model

I can model the actual wire and ground plane CPS geometry with a finite thickness in microwave office. The details of these simulations can be found in Appendix F. Simulating for many different device parameters led to the following empirical formula for the coupling:

$$\boxed{G[s,l,t,w] = \frac{\omega_c^2 Z_c}{2} \frac{1.31 \times 10^{-11}}{s^{1.8}} \left(s^{0.9} + 16t\right) l}. \tag{5.26}$$

5.2.1.4 Wire device optimal parameters

There were several device optimization goals I set out at the beginning of the chapter. I would like to know how to design a device that either minimizes the force noise or maximizes the coupling to reach one of the three interesting coupling regimes. However, it is not always possible to optimize all design quantities at once. For instance, tension increases the resonance frequency, but also makes it much easier to make a successfully suspended device. Specifically, the longest suspended untensioned device we have ever made was 50 μm long, whereas the longest tensioned device was 150 μm long. Therefore, in some cases it may be preferable to add tension and increase the resonance frequency if it means that a longer length can be achieved.

In the absence of parasitic heating of the mechanical oscillator due to the microwave drive, the force spectral density is $S_{FF}^{th} \propto m_{eff}\Gamma_m \propto w^2 t/l$. This quantity is minimized by having a wire of the longest length and smallest width and thickness. Because this quantity is independent of mechanical resonance frequency, a device made to optimize force sensitivity would be a good example of one where we would increase tension to achieve a longer wire. When parasitic heating is taken into account, the optimal force sensitivity is

$$\left(S_{FF,min}^{tot}\right)^{5/2} \propto \frac{m_{eff}^3 \Omega_m \Gamma_m^3}{G} \propto \left(\frac{w^7 t^3 s^2}{s + 16t}\right) \frac{\Omega_m}{l^4}. \tag{5.27}$$

This quantity always benefits from long length and small width, thickness, and spacing. However, it is important to look at the compromise between length and resonance frequency on the right side of the expression. To understand the trade off, an untensioned wire with typical width $w = 150$ nm and longest length $l = 50$ μm would have the same force sensitivity as a tensioned one with

a typical strain $\epsilon \sim 0.006$ and length $l = 85$ μm. Thus, because adding tension allows wires of length longer than $l = 85$ μm, it is desirable. A similar trade off can be made between l and s. For example, it would be preferable to make the wire longer by a factor of 1.5 even at the cost of increasing the spacing by a factor of 2.5.

The first coupling value of merit was the cooperativity

$$\mathcal{C} = \frac{4g^2}{\kappa \Gamma_{\mathrm{m}}} \propto \frac{G^2}{m \Omega_{\mathrm{m}} \Gamma_{\mathrm{m}}} \propto \left(\frac{(s + 16t)^2}{w^2 t s^4} \right) \frac{l^3}{\Omega_{\mathrm{m}}}. \tag{5.28}$$

For this quantity, an untensioned wire of length $l = 50$ μm would be equivalent to a tensioned one of length $l = 95$ μm. Thus, the possibility of making tensioned wires longer than $l = 95$ μm makes adding tension desirable. The spacing and length trade off for a tensioned wire goes as l^4/s^2 or l^4/s^4, depending on the relationship between t and s. Thus, this case is more sensitive to spacing than the force sensitivity was. Here, unlike for force sensitivity where small thickness was always optimal, it is preferable to increase the thickness if it is larger than the spacing (to increase coupling) and preferable to decrease the thickness if it is smaller than the spacing (to decrease mass).

The second coupling of merit was the quantum-enabled regime

$$\tilde{\mathcal{C}} = \frac{4g^2}{\kappa \Gamma_{\mathrm{m}} n_{\mathrm{m}}^{\mathrm{th}}} \propto \frac{G^2}{m \Gamma_{\mathrm{m}}} \propto \frac{(s + 16t)^2 l^3}{w^2 t s^4}. \tag{5.29}$$

This case does not depend on resonant frequency at all, so adding tension to increase the length is always better. Again, it is preferable to increase the thickness if it is larger than the spacing and preferable to decrease the thickness if it is smaller than the spacing.

Lastly, the strong coupling limit is

$$\mathcal{S} = \frac{4g^2}{\kappa^2} \propto \frac{G^2}{m \Omega_{\mathrm{m}}} \propto \left(\frac{(s + 16t)^2}{w t s^4} \right) \frac{l}{\Omega_{\mathrm{m}}}. \tag{5.30}$$

To make a wire equivalent to the 50 μm long untensioned wire in this case would require a tensioned one of length $l = 190$ μm, which has not been achieved. Thus, this is the only example where an untensioned wire might ultimately be preferable over a tensioned one. Once again, it is preferable

to increase the thickness if it is larger than the spacing and preferable to decrease the thickness if it is smaller than the spacing.

5.2.2 Wire device fabrication

In this section, I will describe the wire device fabrication process in an illustrative way. The detailed step-by-step fabrication recipe can be found in Appendix G. The basic idea is to create a microwave circuit and mechanical wire, all fabricated out of a single layer of aluminum on an silicon substrate. A hole is then dry etched in the silicon under the wire in order to suspend (or release) it. During the etch process, the rest of the chip is protected by a layer of silicon oxide. Tension is added to the wire by annealing it at high temperature before the etch step.

Many of the steps in the following more detailed description involve photolithography or electron beam (e-beam) lithography, so I will first explain this process. Lithography (literally 'stone writing') is the process used to pattern a design onto the device. There are two main ways to do this. The first is to add material in a pattern on top of the device. The other is to remove material in a pattern from the device. Either way involves first making a kind of stencil out of a polymer resist. If material is to be added, it is then evaporated onto the device. When the resist is then removed, it takes with it (or 'lifts off') the material not intended to end up on the device. If instead material is to be removed from the device, the device is etched. The resist protects the areas where etching should not occur.

More specifically, the general lithographic process begins with baking the chip to remove any moisture, spinning a layer of resist on the chip, and then baking it again to set the resist. For photolithography, the chip is then aligned to the appropriately patterned photomask, making sure the chip is in contact with the photomask. The masked chip is exposed to ultraviolet light. For e-beam lithography, the electron beam in the scanning electron microscope (SEM) is used to write a pattern in the resist. Either of these processes makes exposed regions of the resist soluble in a developer. Thus, soaking the chip in developer causes the pattern to be left in the resist. The next step is to either evaporate metal or to etch the chip. If the former, metal is then evaporated in

an e-beam evaporator, after a short O_2 ash to promote the metal's adhesion to the surface. When the chip is then soaked in acetone, the resist is removed, leaving metal only in the places that were exposed. If the resist has a pattern for etching instead of evaporation, the chip is then either put in the etchant (for a wet etch such as hydrofluoric acid) or put in the reactive ion etcher (RIE) for a dry etch (such as SF_6). This etches the places that were exposed and leaves the unexposed regions unharmed.

I begin the wire device fabrication with a 1 cm square silicon chip with 150 nm thermal silicon oxide. There are several steps of lithography, so I begin by photolithographically patterning and evaporating titanium/gold alignment marks (Figure 5.4(a,b)). The titanium is critical to keep the gold from peeling off of the chip, while the gold creates marks that are easily visible in both the photo-aligner and the SEM.

I then photolithographically pattern small holes where the mechanical oscillator will eventually end up. As explained above, this starts by covering the chip with photoresist (Figure 5.5(a)) and exposing and developing the photoresist to leave the parts that were exposed bare of photoresist (Figure 5.5(b)). Next, I use buffered hydrofluoric acid to etch the silicon oxide, exposing the silicon in the holes (Figure 5.5(c)). I then remove the photoresist, leaving the bare chip with holes (Figures 5.5(d) and 5.4(c,d)).

Next, I do a double-layer resist process to create the microwave circuit and mechanical oscillator in a single aluminum layer. The reason for this double layer process is that the large features of the microwave circuit are most quickly made using photolithography, while the tiny lines and spaces required for the mechanical wire and spacing to the ground plane are only achievable with e-beam lithography. It is important to do the evaporation all as a single step to avoid oxides forming between the circuit and mechanical element which could prevent good electrical contact. The double-layer process involves spinning a layer of photoresist on top of a layer of poly(methyl methacrylate) (PMMA) (Figure 5.5(e)). I first photolithographically pattern the microwave resonator into the photoresist (Figure 5.5(f)). I then oxygen ash the device in the RIE. This eats away at both layers of resist, transferring the resonator pattern into the PMMA (Figure 5.5(g)). I then
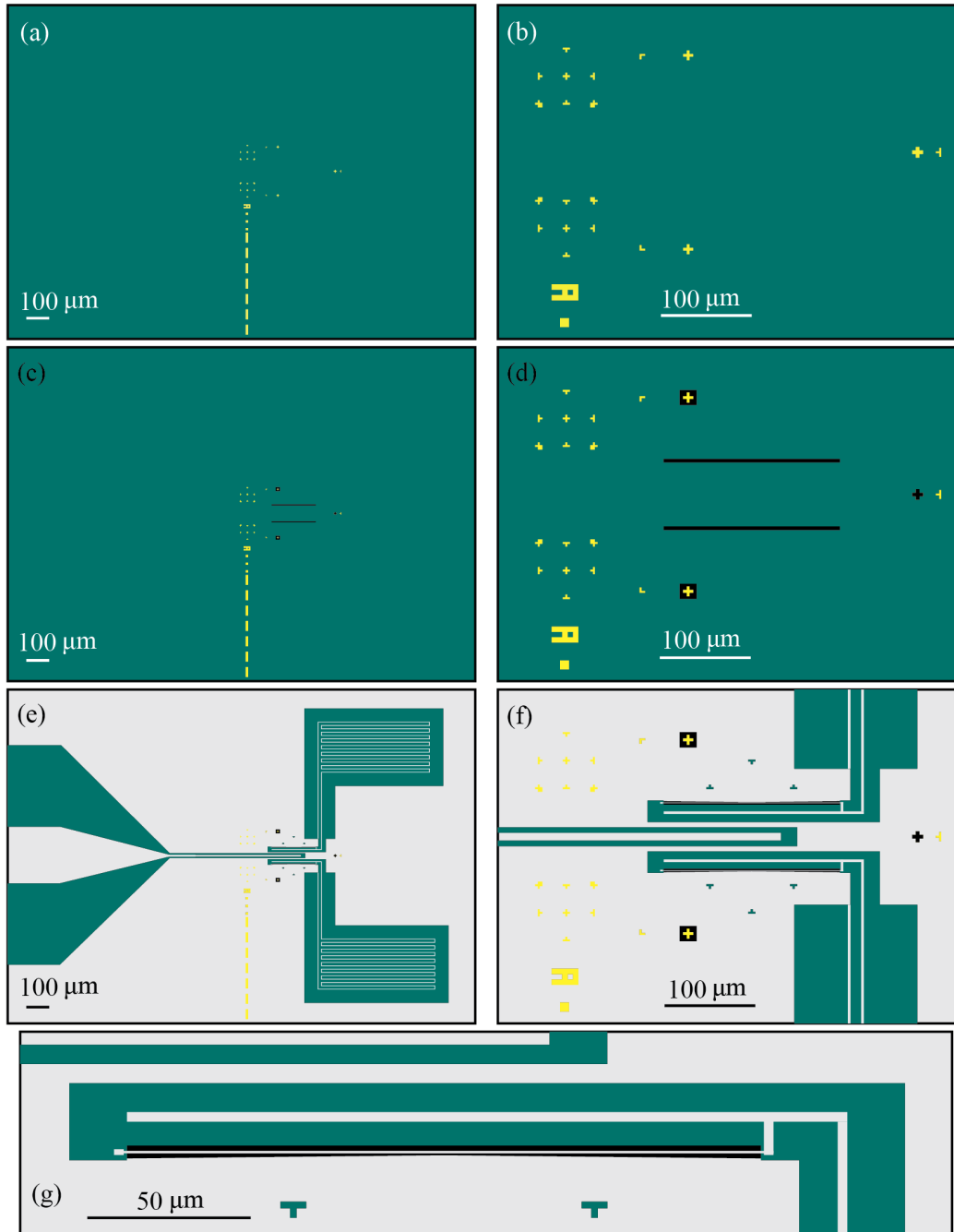
Figure 5.4: Illustrative top view of the fabrication process. The materials are silicon oxide (green), gold (yellow), silicon (black), and aluminum (light grey). (a,b) Gold alignment marks allow good alignment between holes, microwave resonators, and e-beam written wires. (c,d) Holes are patterned and etched in to the silicon oxide where the wire will end up. (e,f,g) The microwave circuit and mechanical element are patterned in a single layer of aluminum. The wire, ground plane adjacent to the wire, and wire supports are written together to ensure good alignment and spacing between these elements.
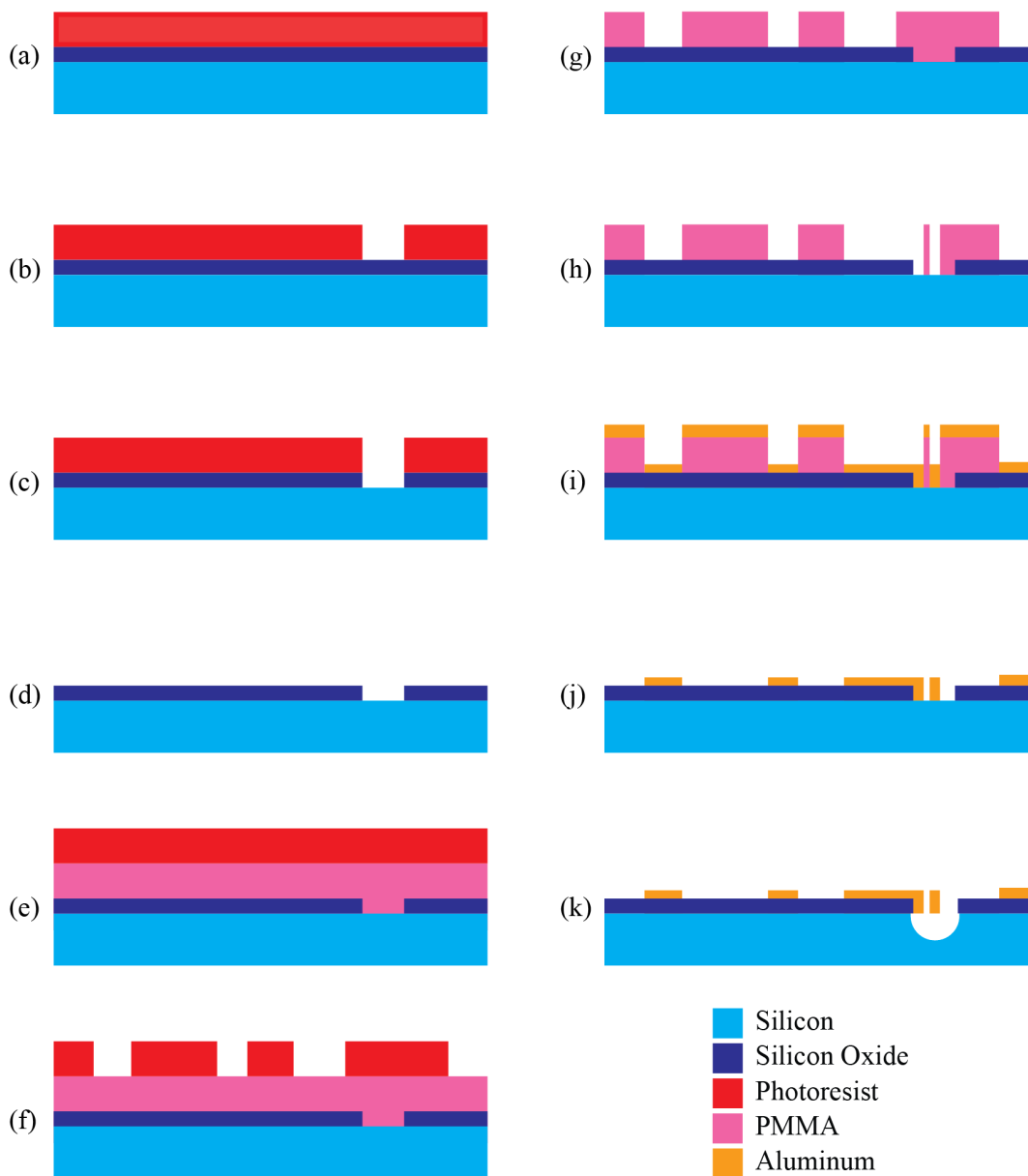
Figure 5.5: Illustrative side view of the fabrication process. (a) A silicon/silicon oxide chip is covered with photoresist. (b) Holes are exposed and developed in the photoresist where the wires will end up. (c) Holes are etched into the silicon oxide. (d) The photoresist is removed, leaving just the chip with holes in the silicon oxide. (e) The chip is covered with a double-layer resist: photoresist on top of PMMA. (f) The microwave circuit is exposed and developed into the photoresist. (g) The microwave circuit pattern is transferred to the PMMA by ashing. (h) The wire, supports, and ground plane are e-beam written and developed into the PMMA. (i) Aluminum is evaporated on the chip. (j) The PMMA is removed, leaving the circuit and wire as a single aluminum layer. (k) The silicon is etched out from under the wire, releasing it. The rest of the chip is protected from this etch by the silicon oxide.

write the wire, supports, and part of the ground plane nearest to the wire using e-beam lithography and develop the resist (Figure 5.5(h)). Writing the last bit of the ground plane in the e-beam step allows me to have fine control over the separation between the mechanical oscillator and ground plane. I then evaporate aluminum on the whole chip (Figure 5.5(i)). One key discovery was that the brief oxygen ash of the chip before evaporating the aluminum (which is generally good practice before evaporating as it makes the metal stick better) resulted in problems with later suspending the wires because they stuck to the substrate too much. The devices were far more successful when the oxygen ash was omitted. I finally lift off the remaining resist and unneeded metal by dissolving the PMMA in acetone, leaving the chip with the microwave resonator and mechanical oscillator in a single layer of aluminum (Figures 5.5(j) and 5.4(e,f,g)).

The next step is to anneal the chip by baking it in a 340 degree Celsius oven for half an hour. This causes the atoms in the chip to rearrange into a lower energy configuration at high temperature. When the device is then cooled back down, the aluminum will want to shrink more
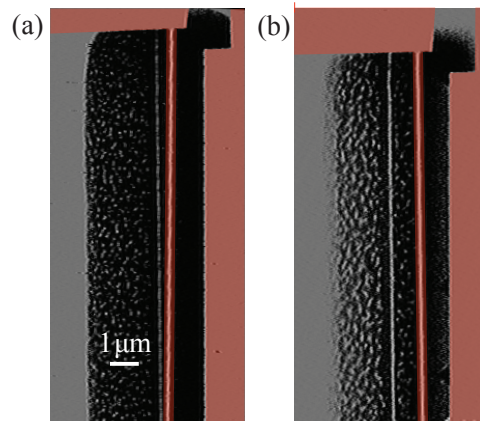
Figure 5.6: SEM images of the wire suspension process. The images show one end of a wire, taken at 30° rotation. Images that show the silicon and wire with good resolution tend to wash out the substrate, so I have false-colored the aluminum in red. The grey is the silicon oxide, while the rough black is the etched silicon. A line appears in the silicon where the wire has shaded the etching process. (a) Image of a wire which has only been partially released. The part of the wire touching the line is still stuck. (b) Image of the same wire after more etching where it is fully released. The wire is now parallel to the line on the bottom of the hole.

than the silicon, as its coefficient of thermal expansion is larger. Thus, the annealing process will put the aluminum under higher tension.

The very last step was to suspend the wires. I did this by doing an SF_6 etch in the RIE to etch away the silicon below the wires, releasing them (Figure 5.5(k)). It is possible to tell if a wire is released by looking at it in the SEM at an angle. There is usually a line where the silicon in the hole has been slightly less etched due to the shadow of the wire (see Figure 5.6). If the wire is
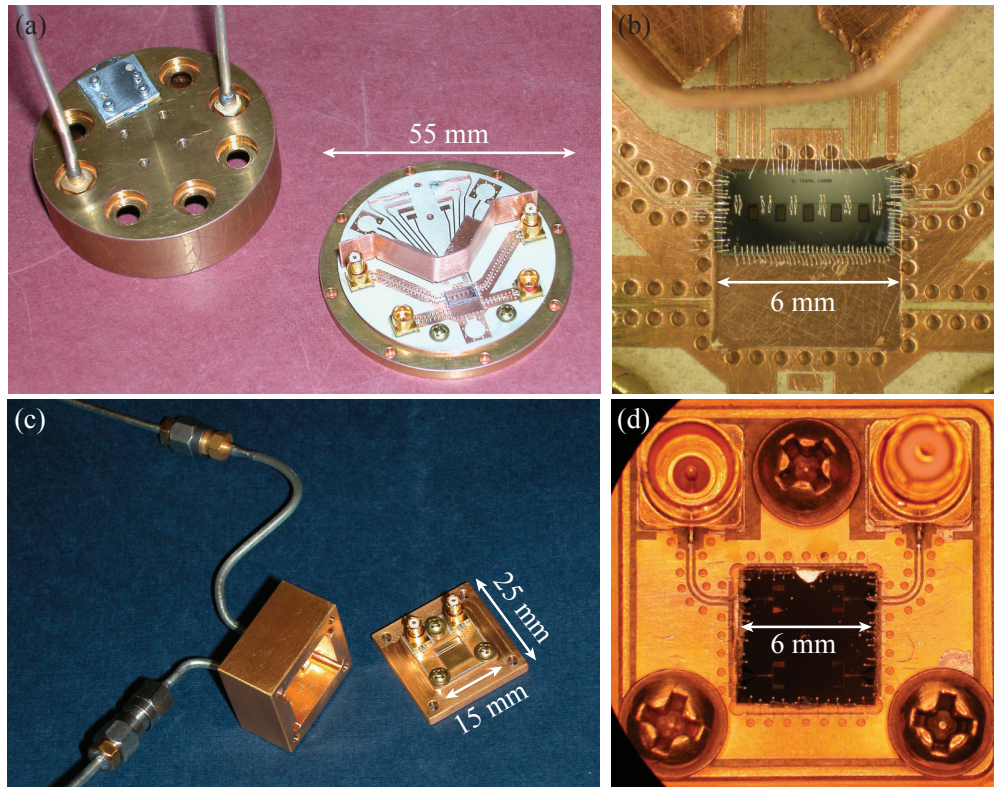
Figure 5.7: Images of device sample holders, which provide an interface between microwave cabling and the on-chip device. (a,b) Original round sample holder with up to four ports. The chip, now cut to a 6 mm square or half-square, is glued to a recessed area in the holder and the ground and center conductors of the holder are wire bonded to the chip. We also wire bonded unconnected grounds on the chip because we found it suppressed other unwanted modes. The vertical piece of metal on the circle board was implemented to break up modes of the sample box near the microwave frequencies of interest. The board interfaces with microwave cables via SMP bullet style connectors. (c,d) Improved sample holder for our experiment. It only has two microwave ports but has the benefit of being smaller, requiring less fridge space and eliminating box modes near the microwave frequencies of interest.
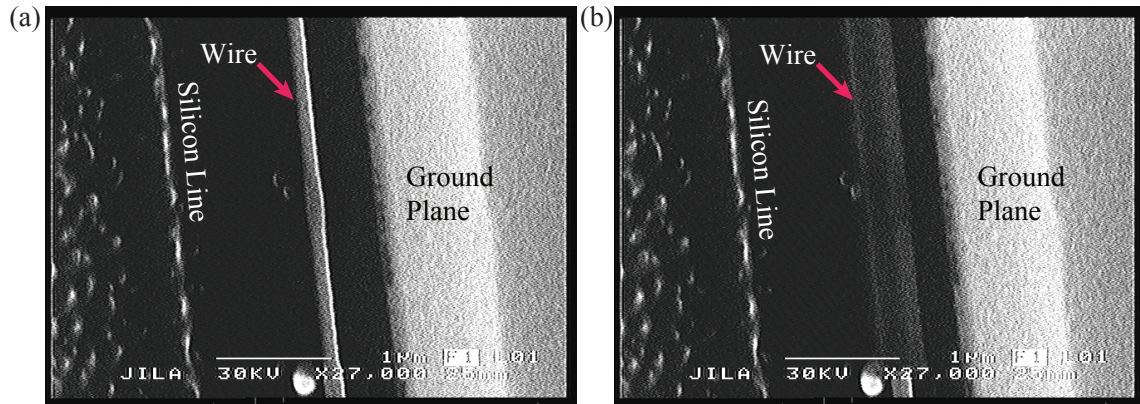
Figure 5.8: SEM images of wire actuation, taken at a 40° side view. (a) Undriven SEM image of the wire. It is suspended next to a ground plane and is parallel to the shadow line on the bottom of the silicon hole. (b) SEM image of the wire motion induced by a driving voltage of $-4V_{dc}$ and $2V_{pp}$ at the mechanical resonance frequency of 882 kHz. When cooled down, this device had a resonance frequency of 1.5 MHz [45].

parallel to this line and not stuck to the ground plane, then it is released. The release process can be further verified by driving the wire at room temperature in the SEM. We did this after the chip was wire bonded to the sample holder (Figure 5.7). We could then attach an AC voltage source to the center conductor of the chip and sweep the frequency until we found the mechanical resonance. At the mechanical resonance frequency, the voltage would drive the oscillator strongly, an effect that was visible in the SEM image (see Figure 5.8).

There were two visual concerns that we repeatedly noticed with my devices. One was that the aluminum film usually displayed many pinholes after annealing (Figure 5.9). This is potentially because the annealing was performed in air, rather than a reducing environment. The other visual concern that we noticed was that the double resist process created flagged edges on the aluminum resonator (Figure 5.9). This is because the resist pattern did not maintain perfectly sharp edges during the transferring of the resonator pattern to the PMMA. However, we did not abandon the double resist process because otherwise the microwave resonator and mechanical oscillator would have had to be evaporated separately, allowing for a layer of aluminum oxide to form between them and break electrical contact. Neither of these visual concerns seemed to prevent us from producing
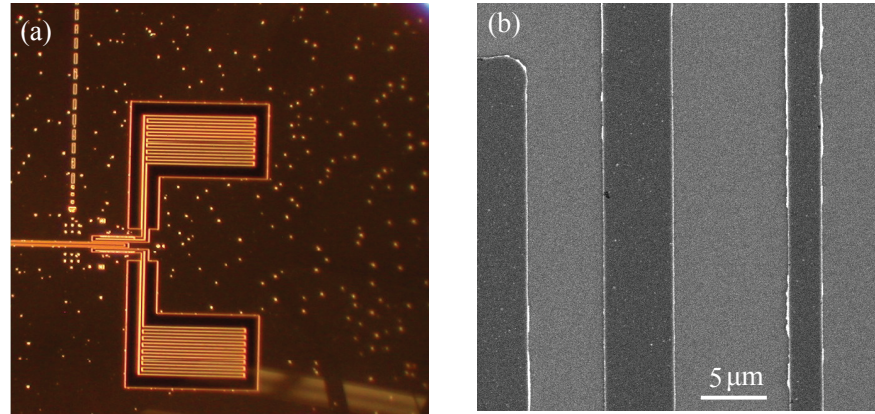
Figure 5.9: Images of visual fabrication concerns. (a) Optical image of a device after annealing. The aluminum film displays many pinholes. (b) SEM zoom-in of some of the aluminum traces (darker grey). The edges of the aluminum film display flags where they was torn during liftoff.
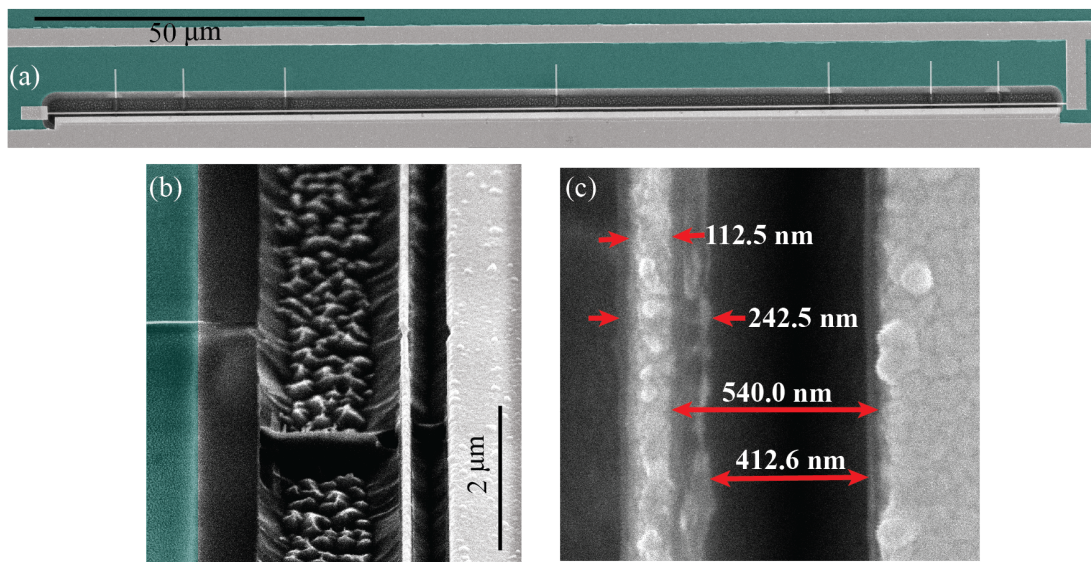
Figure 5.10: Images of a device released using the focused ion beam (FIB). (a) False-color SEM image of the wire. I have colored the silicon oxide green and the aluminum light grey. Remnants of the aluminum supports are visible on the opposite side of the hole from the ground plane. (b) False-color SEM image looking down the wire at a 52° tilt. The remnants of a support post are visible on the left, while imperfections from the cutting are left in the wire and ground plane where the support used to attach. In the silicon below the wire appears a line due to the shadow of the support during the RIE etch. (c) The e-beam attached to the FIB was superior to my typically-used e-beam, so it offered an opportunity to asses the true dimensions of the wire and spacing. The wire has a width of about 175 nm (determined by the single-pass line width of the e-beam writer). The spacing, here designed to be 600nm, is actually smaller by about 100nm.

devices with good microwave properties, so we did not fix them.

There is one other fabrication method that I used in an effort to make longer wires. As I showed in the previous section, devices with longer wires and closer spacing to the ground plane exhibit increased optomechanical coupling and are thus very desirable for our experiments. However, my experience was that the longer, closer wires tended to get stuck to the ground plane when they were released (even if they were under tension). This was a particularly frustrating experience because I was suspending them in the RIE, an environment with large and varying electric fields that I could neither see nor control. The solution to this problem was to pattern the mechanical oscillator with several orthogonal supports attaching it to the sides of the silicon oxide hole. Suspending the wire and supports in the RIE was then very easy and nearly always successful. The last step was to use a focused ion beam (FIB) to cut through the supports (see Figure 5.10). In this case, I could watch in real-time with an electron beam as the FIB cut the supports and control the cutting process. It was therefore a far more successful last step in the fabrication process. I found that the best strategy was to make a center support that went all the way across the hole and several others that only went half-way across. I would first cut all the short supports and lastly cut the long support in the middle. This way, the last cut generally pulled the wire **away** from the ground plane, making it much less likely to get stuck. The best device I was able to make this way was 150 μm long and only 350 nm from the ground plane. In the next section, I will compare this device to the ones we used for publications and a few others and will refer to it as the FIB device.

5.2.3   Parameters achieved with wire devices

In this section, I will describe the designs and parameters for our lab's three published wire devices, as well as those for my best wire device, discussed in the FIB section above (unpublished). I will also compare two other notable wire devices from other research groups. For ease of reference, I am going to name the wire devices A-F. Device G is not a wire device and will be introduced in the next section. The measured parameters for each device are listed in Table 5.1.

Device A [10] was the first published wire device from our lab. As such, it had modest

	A [10]	**B** [45]	**C** [76]	**D**	**E** [12]	**F** [14]	**G** [48]
length l (μm)	50	100	150	150	30	8.5	
width w (nm)	100	120	170	175	170	320	
thickness t (nm)	130	130	160	130	140	150	
spacing s (nm)	1000	1000	1000	350	75	10	
mass m (pg)	1.76	4.2	11	9.2	2.1	1.1	48
$\omega_{\rm c}/2\pi$ (GHz)	4.9	5.22	7.49	6.4	7.5	6.98	7.54
$Z_{\rm c}$ (Ω)	89	89	270	200	81	1266	569
$\kappa/2\pi$ (kHz)	490	230	2880	490	600	6200	200
$\Omega_{\rm m}/2\pi$ (MHz)	0.237	1.525	1.04	1.039	6.3	32.5	10.56
$\Gamma_{\rm m}/2\pi$ (Hz)	103	5.1	1.8	1.2	6.3	500	32
$G/2\pi$ (kHz/nm)	1.16	6.4	32	148	84	1,800	49,000

Table 5.1: Measured device parameters. Almost all parameters are either directly or indirectly extracted from the publications (aside from device D).

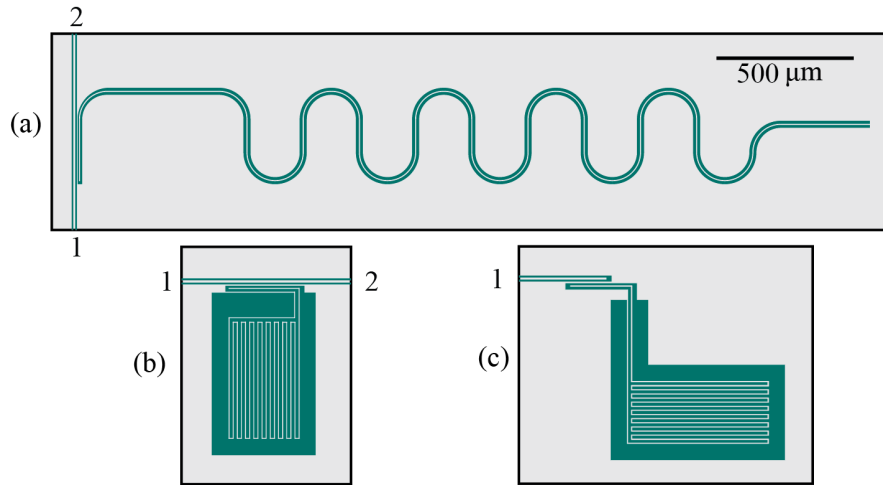Figure 5.11: Microwave circuit designs for different wire devices. Power is coupled on and off of the chip through a transmission line with either one or two ports. (a) Transmission line $\lambda/4$ resonant circuit in the transmission geometry [10, 45]. (b) High impedance design in the transmission geometry [76]. (c) High impedance design in the reflection geometry used for the best FIB-released wire device.

parameters. However, it is interesting as the only un-tensioned mechanical oscillator compared in this section (because it was not annealed). The circuit design for device A was a $\lambda/4$ transmission line resonant circuit in the transmission geometry (see Figure 5.11(a)).

Device B [45] was improved over device A by doubling the wire length and going to high tension where the mechanical linewidth was much smaller. This device was used to investigate radiation pressure cooling of the mechanical oscillator, presented in Chapter 8.1.

Device C [76] was further improved by again extending the wire length. Rather than using a transmission line microwave resonator, we implemented a higher impedance lumped-element circuit design (Figure 5.11(b)). This concentrated the capacitance near the wire, resulting in an increased participation ratio. This device was used to demonstrate a quantum efficient interferometric measurement of microwave fields, explained in Chapter 7.

Device D was created using the FIB to release the mechanical wire (as described above). This allowed me to decrease the spacing between the wire and ground plane substantially. This device also utilized a high impedance microwave circuit, but this time in the reflection geometry (Figure 5.11(c)). This device was not studied as extensively as all of the published devices, so the numbers quoted are from preliminary measurements.

Devices E [12] and F [14] are from the Schwab group at Cornell/Caltech and the Sillanpää group at Aalto University, respectively. I include them because these two devices offer a different approach to optimizing the quantities of interest. While I have attempted to increase coupling by making longer and longer wires, they have kept using shorter wires and instead focused on decreasing the spacing between the wire and ground plane. Their devices thus differ in many of the parameters and resulting quantities and it is interesting to see how all the different devices compare on the figures of merit I laid out at the beginning of this chapter.

I compare the calculated/simulated parameters to those measured in Figure 5.12. Figure 5.12(a) shows that the calculated mechanical resonance frequencies agree quite well with those measured. Device A is the floppiest, as expected because it is at low tension. Figure 5.12(b) shows the calculated and measured mechanical linewidths. These do not agree nearly as well.
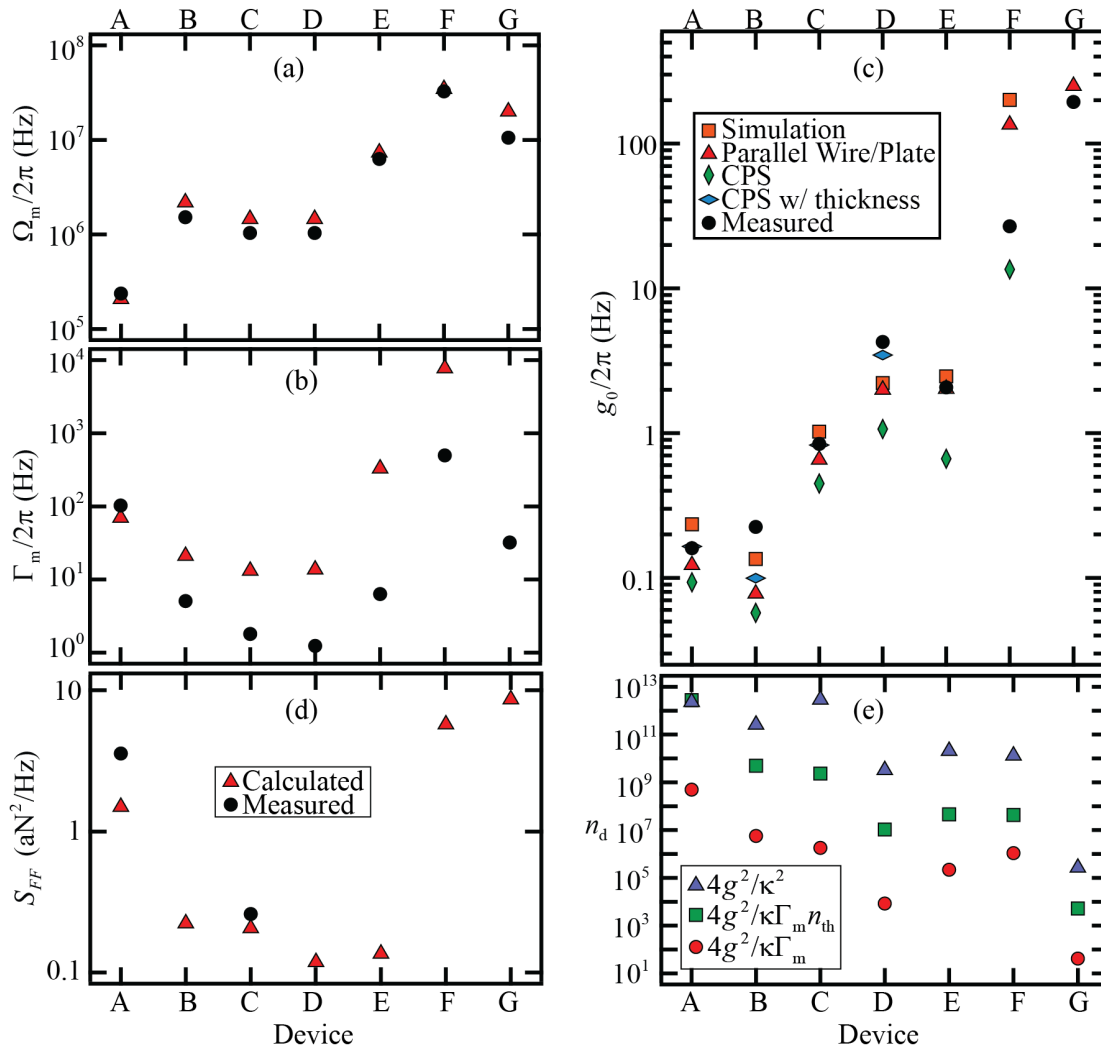
Figure 5.12: Comparison of device parameters for wire devices A-F and suspended membrane device G. (a) Mechanical resonance frequency measured (black circles) and calculated using Equations 5.10 and 5.31 (red triangles). The strain was set to zero for device A and to 0.006 for B-G. (b) Mechanical linewidth measured (black circles) and calculated using Equation 5.18 (red triangles). (c) Single-photon coupling rate measured (black circles) and calculated (see legend) using the three models and microwave office simulations presented in Sections 5.2.1.3 and 5.3 (and the zero point motion). (d) Force sensitivity measured (black circles) and calculated (red triangles) with a common mechanical oscillator temperature of 50 mK. (e) Number of drive photons required to reach each of the three important limits on optomechanical coupling.

However, that should be expected as the empirical expression I used for the expected values was found empirically using only short wires. The best mechanical linewidths come from devices B-E. Figure 5.12(c) compares all of the different models for wire to ground plane capacitance with the coupling actually measured. The parallel wire model seems to underestimate the coupling for the long wires while overestimating it for the shorter ones. The CPS model without thickness always underestimates the coupling. The CPS model with thickness does a good job predicting the coupling, but only in the regime for which it is applicable (it is invalid for the short wires). Overall, the models seem to agree well with the measurements for all wires except the very short one of device F. Device F exhibits by far the best single-photon coupling for a wire device. Figure 5.12(d) shows the calculated force sensitivity, simply using $S_{FF} = 4k_B T_m m_{\text{eff}} \Gamma_m$ and the measured parameters. I have assumed that the mechanical oscillators are all in thermal equilibrium at 50 mK. Devices B-E should have very good force sensitivity, in large part because of their superior mechanical linewidths. Figure 5.12(e) displays the three coupling limits of merit. I plot the number of photons that would be required to reach each of these limits. For device A, these are very large numbers, and none of the three would be achievable. However, for devices B-F, substantial cooling would be possible ($4g^2/\kappa\Gamma_m > 1$ at the highest powers).

5.3   Suspended membrane devices

In the previous section, I presented a class of planar devices that were conceived of with ease of fabrication in mind. As I showed, multiple groups have been able to push the parameters of these devices to quite impressive dimensions at the limits of fabrication, be it in terms of long wire length or of tiny spacing to the ground plane. However, the optomechanical coupling of these wire devices is ultimately limited by the fact that the wire makes up such a tiny fraction of the total circuit capacitance. In order to make the next strides forward in optomechanical coupling, it was thus necessary to move away from the planar geometry.

The first device to do this was made by our collaborators in Ray Simmonds' group at NIST. Using the vacuum gap capacitor technology that they have pioneered [104], they were able to
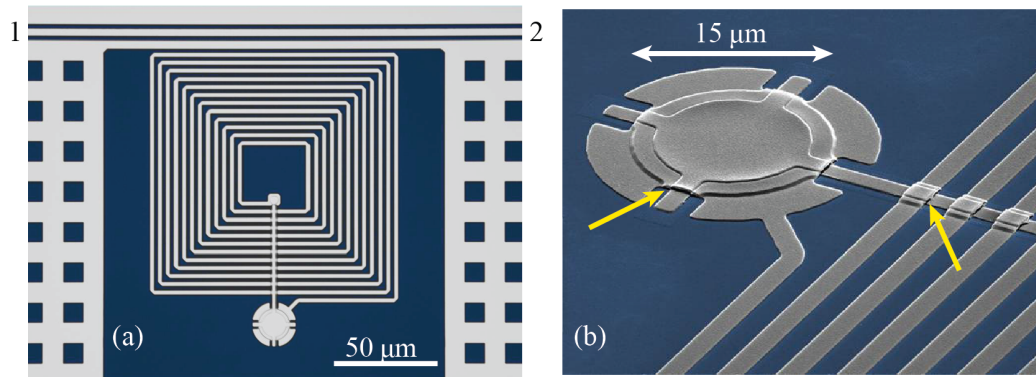
Figure 5.13: Images of a suspended membrane device, used in [15, 48, 66]. The sapphire substrate is shown in blue and the aluminum is grey. (a) The circular membrane mechanical oscillator (near the bottom of the image) is coupled to a large spiral inductor. Power is coupled into and out of the device through an inductively coupled feed line (at top, with ports labeled 1 and 2. (b) Zoom-in of the suspended membrane. Highlighted with yellow arrows are the vacuum gaps for the capacitor (left arrow), and a crossover of the inductor (right arrow).

create a device where the mechanical motion of a suspended membrane modulates nearly the entire capacitance of the microwave circuit. Their technology builds up the device in multiple layers, using a sacrificial layer between two layers of aluminum. When the sacrificial layer is etched away, they are left with two layers of metal separated by a very tiny 'vacuum gap'. This process can be used to suspend a membrane of metal, which can act both as a mechanical oscillator as well as the top plate of a parallel plate capacitor. The process can also be used to make bridges such that two traces of metal can cross each other, enabling the fabrication of a spiral inductor that has less stray capacitance than the meander inductors used in my wire devices. Their device is shown in Figure 5.13.

I will not go into the design and parameters of the suspended membranes in nearly the depth that I did for the wire devices; however, the mechanical resonance frequency and parallel plate capacitance are fairly quick to calculate, so I do it here. For a circular aluminum suspended membrane under high tension, the frequency of the fundamental mode can (as for the high tension

wire) be found from the speed v of propagation:

$$\Omega_{\mathrm{m}} = 2\pi \times v\lambda_{01} = 2\pi \times \frac{\alpha_{01}}{R}\sqrt{\frac{S}{m/(\pi R^2)}} = 2\pi \times \frac{\alpha_{01}}{R}\sqrt{\frac{\sigma t}{\rho_{\mathrm{Al}}t}} = 2\pi \times \frac{\alpha_{01}}{R}\sqrt{\frac{E_{\mathrm{Al}}\epsilon}{\rho_{\mathrm{Al}}}}, \tag{5.31}$$

where S is the surface tension, σ and ϵ are the stress and strain, and E_{Al} and ρ_{Al} are the Young's modulus and density of aluminum. The optomechanical coupling can be modeled using the formula for the simple parallel plate capacitor: $C_{\mathrm{membrane}} = \epsilon_0 \pi R^2/s$. The coupling is then

$$G = \frac{\omega_{\mathrm{c}}^2 Z_{\mathrm{c}}}{2}\frac{\epsilon_0 \pi R^2}{s^2}. \tag{5.32}$$

Device G in Table 5.1 and Figure 5.12 is the suspended membrane device in references [15] and [48]. Figure 5.12 shows that the equations above provide good predictions of the mechanical resonance frequency and optomechanical coupling for this device. This device has a larger mechanical resonance frequency and linewidth than many of the wire devices, but maintains a similar mechanical quality factor. It does not make the best force sensor, as the mass of the membrane is substantially larger than that of the wires. However, the impressiveness of this device is its large optomechanical coupling of $G = 2\pi \times 50$ MHz/nm. This enables it to reach all three of the coupling regimes with far fewer photons than any of the wire devices, and thus allows exploration of physics that was not within reach of the wire devices. This device was used to demonstrate strong coupling [15], cool the mechanical oscillator to the ground state ([48], Chapter 8.2), attempt to see sideband asymmetry and quantum backaction (Chapters 9 and 10), and demonstrate transfer of coherent itinerant microwave fields with the mechanical oscillator ([66], Chapter 11).

Chapter 6

Experimental calibrations

Several calibrations are similar between all of the experiments we perform. Here, I will discuss how we go from the measured voltage spectral density in Chapter 4 to units related to the optomechanical system (either the photons units $S_{II}^{\mathrm{photon}}[\omega]$ on the right-hand side of the intensity expressions in Chapter 4, or mechanical displacement $S_{xx}[\omega]$). The calibrations discussed eliminate the unknown proportionalities between $S_{II}[\omega]$ and $S_{II}^{\mathrm{photon}}[\omega]$ and determine the coupling g_0.

6.1   JPA gain calibration

The frequency dependence of the HEMT amplifier can generally be ignored, as it is close to flat over the frequency ranges present in our experiments. However, the JPA generally has a bandwidth of a few megahertz, meaning that it can be important to remove this frequency dependence. The frequency dependence of the JPA can be determined independent of the optomechanical cavity by injecting a probe tone at the input of the JPA (after the cavity) and then looking at the response at the output of the experiment. This response reveals the resonant frequency and bandwidth of the JPA (but not necessarily the absolute magnitude of JPA gain, as it also depends on the attenuation of the probe input line). In this way, the gain at any frequency can be referenced to the gain at any other frequency. The absolute value of the JPA gain can then be removed by referencing the amplitude of this probe tone measured with the JPA on to the same measured amplitude with the JPA off. This allows spectral data taken with the JPA to be put into effective 'JPA off' units. Figure 6.1 shows these transformations. The raw voltage spectral densities measured with the JPA
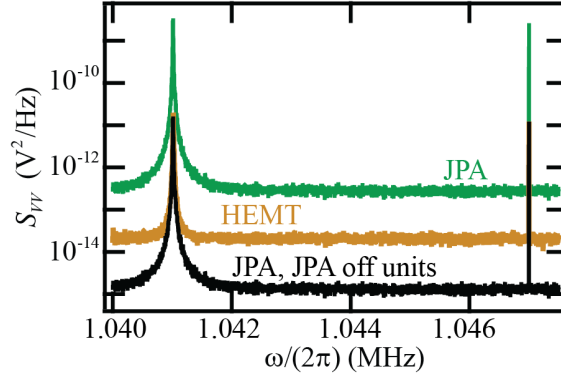
Figure 6.1: Measured voltage spectral densities. The raw data measured with the JPA on and off are shown in green and orange, respectively. The Lorentzian feature at ~ 1.041 MHz is the mechanical resonance, while the delta function at ~ 1.047 MHz is a calibration tone. The green data is scaled such that the calibration peaks will be equal in height, removing the JPA gain and resulting in the black data.

(green) and without the JPA (orange) are shown. Also included is the data with the JPA on, now transformed to remove the frequency dependence of the JPA gain and scaled into 'JPA off' units, making the two calibration tones of equal magnitude. The benefit of having the spectral data in 'JPA off' units is that it can be directly related to measurements of the output classical drive taken with the JPA off. These measurements cannot be taken with the JPA on, as the large drive tone will saturate the JPA if it is not canceled first.

6.2   Inferring mechanical motion from measured voltage spectral density

This section explains how we transform measured voltage spectral density data (in 'JPA off' units, if relevant) into data with optomechanical units (either the photon units $S_{II}^{\text{photon}}[\omega]$ on the right hand side of the equations in Chapter 4 or displacement spectral density units $S_{xx}[\omega]$). As the measured voltage spectral density is proportional to $S_{II}^{\text{photon}}[\omega]$, I relate the theory to the measurement with a proportionality constant λ:

$$S_{VV}[\omega] = \lambda S_{II}^{\text{photon}}[\omega]. \tag{6.1}$$

In general, λ depends on quantum efficiencies and amplifier gains (and could thus change day to day or even measurement to measurement).

The total drive power P_d can be measured by integrating the voltage spectral density about the drive frequency (measured with the same digitizing setup as the spectral data but with the JPA off if it is present):

$$
\begin{aligned}
Z_0 P_\mathrm{d} &= \frac{1}{2\pi} \int S_{V_\mathrm{d} V_\mathrm{d}}[\omega] d\omega = \frac{\lambda}{2\pi} \int S_{\mathrm{II,d}}^{\mathrm{photon}}[\omega] d\omega && (6.2) \\
&\approx \frac{\lambda}{2\pi} \int \frac{1}{2} \left(S_{a_\mathrm{out,d} a_\mathrm{out,d}}[\omega] + S_{a_\mathrm{out,d} a_\mathrm{out,d}}[2\omega_\mathrm{LO} - \omega] \right) d\omega = \frac{\lambda P_\mathrm{out}}{2\hbar\omega_\mathrm{d}} \left(1 + \delta_{\omega_\mathrm{LO},\omega_\mathrm{d}} \right), && (6.3)
\end{aligned}
$$

where P_out is the theoretical expression for the cavity output power given in Equation 3.7. The first two integrals are across the measured drive frequency $|\omega_\mathrm{LO} - \omega_\mathrm{d}|$, while the third integral is across the true drive frequency ω_d. In the second to last step, I assumed the drive power is large compared to any added noise power. Alternatively, λ can instead be related to the derivative of the measured drive voltage as a function of drive frequency:

$$
\left| \frac{dV_\mathrm{d}}{d\omega_\mathrm{d}} \right|^2 = \frac{\lambda}{2}(1 + \delta_{\omega_\mathrm{LO},\omega_\mathrm{d}}) \left| \frac{d\alpha_\mathrm{out}}{d\omega_\mathrm{d}} \right|^2 = \frac{\lambda}{2}(1 + \delta_{\omega_\mathrm{LO},\omega_\mathrm{d}}) \left| -\frac{d\alpha_\mathrm{out}}{d\overline{\omega}_\mathrm{c}} \right|^2 = \frac{\lambda(1 + \delta_{\omega_\mathrm{LO},\omega_\mathrm{d}})|N_i|^2 n_\mathrm{d}}{2\kappa_\mathrm{l}}. \quad (6.4)
$$

The inferred spectrum in Chapter 4 photon units is then

$$
\begin{aligned}
S_{II}^{\mathrm{photon}}[\omega] = \frac{S_{VV}[\omega]}{\lambda} &= \frac{S_{VV}[\omega] P_\mathrm{out}(1 + \delta_{\omega_\mathrm{LO},\omega_\mathrm{d}})}{2 Z_0 P_\mathrm{d} \hbar \omega_\mathrm{d}} && (6.5) \\
&= \left(\frac{S_{VV}[\omega]}{|dV_\mathrm{d}/d\omega_\mathrm{d}|^2} \right) \frac{|N_i|^2 n_\mathrm{d}(1 + \delta_{\omega_\mathrm{LO},\omega_\mathrm{d}})}{2\kappa_\mathrm{l}}. && (6.6)
\end{aligned}
$$

The inferred displacement spectral density can be found by relating the photon units to displacement spectral density units as done in Section 4.5. Note that this step depends on the details of the drive and interferometer and thus must be calculated independently for each case. As an example, if the voltage spectrum were measured using an on-resonant drive and a homodyne interferometer containing a JPA and then converted to 'JPA off' units, and the drive power was measured with the JPA off and $\omega_\mathrm{LO} \neq \omega_\mathrm{d}$, the displacement spectral density would be (from Equation 4.42)

$$
\frac{S_{xx}[\omega]}{x_\mathrm{zp}^2} = \frac{\kappa^2 + 4\Omega_\mathrm{m}^2}{4g^2 \kappa_\mathrm{l}} S_{II}^{\mathrm{photon}}[\omega] = \left(\frac{S_{V_\mathrm{I} V_\mathrm{I}}[\omega]}{Z_0 P_\mathrm{I,d}} \right) \frac{\kappa^2 + 4\Omega_\mathrm{m}^2}{32 g_0^2 \kappa_\mathrm{l}^2} |N_i \kappa - 2\kappa_\mathrm{l}|^2. \quad (6.7)
$$

Note that $S_{V_I V_I}[\omega]/(Z_0 P_d)$ and all of the other quantities in this expression are independently measured optomechanical parameters. In particular, converting measured data into displacement units does not depend on knowing the number of photons in the cavity.

As I said above, λ can change over time due to such things as amplifier gain changes. Rather than repeating the drive measurements above for each data point, we sometimes apply a calibrated force to the mechanical oscillator which lets us calibrate the relative change in λ between any two measurements. We do this by applying both a DC and AC voltage to the feed line such that the force on the mechanical oscillator is $F[\omega] = V_{DC} V_{AC}[\omega](dC_{fm}/dx)$, where C_{fm} here is the capacitance between the feed line and the mechanical oscillator. Let Λ be another proportionality constant which directly relates the measured voltage spectral density to the displacement spectral density ($\Lambda \propto \lambda$ but the relationship depends on the interferometer type). The voltage spectral density in the presence of mechanical drive force $F[\omega]$ is then

$$S_{V_I V_I}[\omega] = \Lambda S_{xx}[\omega] = \frac{\Lambda x_{zp}^4 S_{FF}[\omega]}{\hbar^2} |\chi_{m,eff}[\omega]|^2. \tag{6.8}$$

If the applied force is white (independent of frequency), then Λ can be related to the area A and linewidth Γ_{tot} of the measured Lorentzian spectrum:

$$S_{V_I V_I}[\omega] = \frac{A\Gamma_{tot}}{2\pi}|\chi_{m,eff}[\omega]|^2, \Lambda = \frac{A\Gamma_{tot}\hbar^2}{2\pi x_{zp}^4 S_{FF}}. \tag{6.9}$$

The displacement spectral density for any new measurement written in terms of a fully calibrated reference measurement is then

$$S_{xx}[\omega] = \frac{S_{V_I V_I}[\omega]}{\Lambda} = \frac{A_{ref}\Gamma_{tot,ref}}{A\Gamma_{tot}\Lambda_{ref}} S_{V_I V_I}[\omega], \tag{6.10}$$

where the critical assumption is that the force and zero point displacement do not change from measurement to measurement.

6.3 Optomechanical coupling calibration

The single-photon optomechanical coupling g_0 is found by using a temperature sweep to calibrate the mechanical output noise into quanta. The basic idea is that the area under the

mechanical peak in the output spectra with an on-resonance or very low power drive is proportional to $g_0^2 n_{\mathrm{m}}^{\mathrm{th}}$ and we expect that the mechanical oscillator is in equilibrium with the base temperature of the dilution refrigerator at high temperature ($T_{\mathrm{cryo}} \sim 100 - 300$ mK). We can determine the number of thermal mechanical phonons from the $S_{xx}[\omega]$ data:

$$g_0^2 n_{\mathrm{m}}^{\mathrm{th}} = \frac{g_0^2 S_{xx}^{\mathrm{th}}[\Omega_{\mathrm{m}}]}{4 S_{xx}^{\mathrm{SQL}}}. \tag{6.11}$$

Plotting this quantity as a function of fridge temperature T_{cryo} and using the equipartition theorem allows us to identify g_0 from the slope of the graph:

$$g_0^2 n_{\mathrm{m}}^{\mathrm{th}} = \frac{g_0^2 k_{\mathrm{B}}}{\hbar \Omega_{\mathrm{m}}} T_{\mathrm{cryo}}. \tag{6.12}$$

6.4 Amplifier added noise and cable loss

We calibrate the added noise of amplifiers and loss in our interferometer by switching between two calibrated noise sources (50 Ohm terminations), one at $T_{\mathrm{H}} = 4$ K and one at the fridge base temperature T_{cryo} (see Figure 6.2(a)). The source is switched to the base temperature termination during experiments to minimize the thermal input noise incident on the optomechanical system. However, switching to the 4 K source allows us to calibrate the added noises of the interferometer.

If the switch is switched to the cold load at T_{cryo}, then the number of microwave noise quanta at the input of the amplifier (see Figure 6.2(b)) will be

$$n_{\mathrm{in}}[T_{\mathrm{cryo}}] = \frac{1}{2} + \left(e^{\hbar \omega / (k_{\mathrm{B}} T_{\mathrm{cryo}})} - 1 \right)^{-1}, \tag{6.13}$$

regardless of any cold attenuation between the cold load and the amplifier. By using two different base temperatures of the fridge, $T_{\mathrm{cryo,1}}$ and $T_{\mathrm{cryo,2}}$, a Y-factor measurement can be made to determine the gain and added noise of the amplifier:

$$
\begin{aligned}
Y &= \frac{n_{\mathrm{out}}[T_{\mathrm{cryo,1}}]}{n_{\mathrm{out}}[T_{\mathrm{cryo,2}}]} = \frac{n_{\mathrm{in}}[T_{\mathrm{cryo,1}}] + n_{\mathrm{add}}}{n_{\mathrm{in}}[T_{\mathrm{cryo,2}}] + n_{\mathrm{add}}}, \tag{6.14} \\
n_{\mathrm{add}} &= \frac{n_{\mathrm{in}}[T_{\mathrm{cryo,1}}] - Y n_{\mathrm{in}}[T_{\mathrm{cryo,2}}]}{Y - 1}. \tag{6.15}
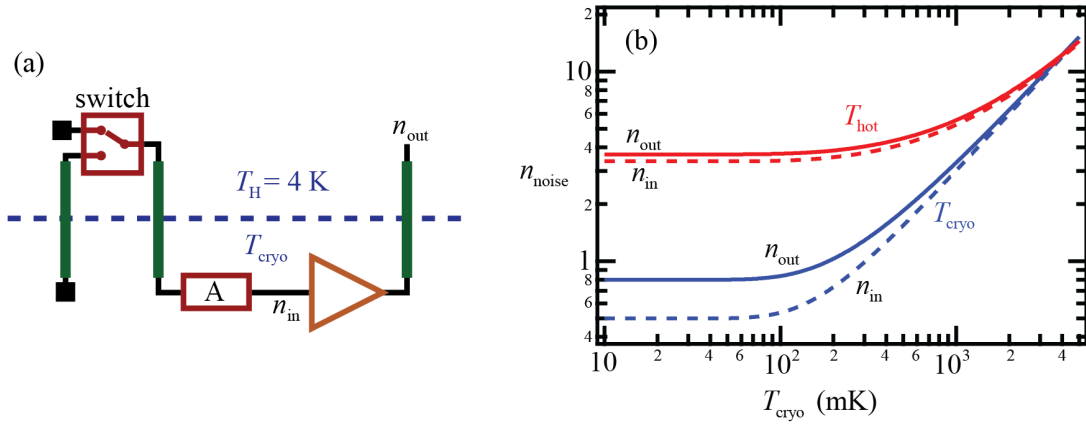\end{aligned}
$$

Figure 6.2: Calibration of interferometer added noise. (a) Calibrated noise setup. The amplifier input can be switched between one of two calibrated noise sources, one at T_H and one at T_{cryo}. Loss between the switch and amplifier is modeled as an attenuator with power attenuation A. Superconducting cables (green) are used to losslessly transition between temperatures. The number of microwave noise quanta at the input of the amplifier is n_{in}, while the number of measured noise quanta is n_{out}. (b) Theoretical noise quanta for calibration measurements using $\omega = 2\pi \times 7$ GHz, $n_{add} = 0.3$, $A=1/4$, $T_H = 4$ K. With the switch switched to T_{cryo} (blue), the input and output noise are independent of A and a measurement of the output noise reveals the amplifier gain (from the slope at high temperatures) and added noise (from the zero-temperature value). With the switch switched to T_H (red), the output noise is dependent on A and using the known values of G, n_{add}, and T_H allows a determination of A.

Here, Y and the n_{out}'s are measured values, while the n_{in}'s are calculated from the known temperatures via Equation 6.13.

To determine any cold attenuation between the calibrated noise source and the amplifier, the switch is switched to the hot load. This fixes the input noise temperature of the attenuation at T_H, while the attenuation itself is at temperature T_{cryo}. The number of microwave noise quanta at the output of loss with power attenuation A (at the input of the amplifier) is

$$n_{in}[T_{cryo}] = \frac{1}{2} + \frac{A}{e^{\hbar\omega/(k_B T_H)} - 1} + \frac{1 - A}{e^{\hbar\omega/(k_B T_{cryo})} - 1}. \tag{6.16}$$

Varying the base temperature of the fridge then varies only the temperature of the attenuation, allowing us to identify the loss A between the switch and the amplifier.

Chapter 7

Experiment I: Quantum efficient microwave measurement

In this chapter, I detail our realization of a quantum efficient microwave interferometer, which enabled us to make a measurement of our mechanical oscillator with an imprecision below the imprecision at the standard quantum limit. This result is critical to the exploration of the quantum behavior of mechanical oscillators, as the quantum motion must be resolvable above the measurement imprecision. Additionally, the improvement in interferometric measurement also resulted in an exquisite force sensitivity of the optomechanical system, potentially leading to future applications in ultrasensitive detection.

7.1 Review of quantum limits on measurement

In Section 4.5.3, I found expressions for the imprecision and backaction numbers of mechanical quanta in the presence of a single, on-resonance, cavity drive, using a homodyne interferometer containing a phase-sensitive amplifier:

$$n_{\mathrm{m}}^{\mathrm{tot}} = n_{\mathrm{m}}^{\mathrm{imp}} + n_{\mathrm{m}}^{\mathrm{ba}} + n_{\mathrm{m}}^{\mathrm{th}} + n_{\mathrm{m}}^{\mathrm{zp}}, \tag{7.1}$$

$$n_{\mathrm{m}}^{\mathrm{imp}} = \left(\frac{\kappa}{16\kappa_{\mathrm{l}}}\right) \frac{1+\nu}{\mathcal{C}}(1+2n_{\mathrm{add}}), \tag{7.2}$$

$$n_{\mathrm{m}}^{\mathrm{ba}} = \frac{\mathcal{C}}{1+\nu}. \tag{7.3}$$

In these equations, $n_{\mathrm{m}}^{\mathrm{th}}$ is the number of thermal quanta, $n_{\mathrm{m}}^{\mathrm{zp}} = 1/2$ is the half quanta of zero-point motion, $\mathcal{C} = 4g^2/(\kappa\Gamma_{\mathrm{m}})$ is the cooperativity and $\nu = 4\Omega_{\mathrm{m}}^2/\kappa^2$ is the resolved sideband factor. In

terms of displacement spectral densities, these are

$$S_{xx}^{\text{tot}}[\omega] \quad = \quad S_{xx}^{\text{imp}}[\omega] + S_{xx}^{\text{ba}}[\omega] + S_{xx}^{\text{th}}[\omega] + S_{xx}^{\text{zp}}[\omega], \tag{7.4}$$

$$S_{xx}^{\text{imp}}[\omega] \quad = \quad 4S_{xx}^{\text{SQL}} n_{\text{m}}^{\text{imp}}, \tag{7.5}$$

$$S_{xx}^{\text{ba(th,zp)}}[\omega] \quad = \quad 4S_{xx}^{\text{SQL}} n_{\text{m}}^{\text{ba(th,zp)}} \frac{\Gamma_{\text{m}}^2}{4} |\chi_{\text{m}}[\omega]|^2. \tag{7.6}$$

Quantum limits are imposed on the product of the imprecision and backaction:

$$n_{\text{m}}^{\text{imp}} n_{\text{m}}^{\text{ba}} \quad = \quad \frac{\kappa}{16\kappa_{\text{l}}}(1 + 2n_{\text{add}}) \geq \frac{1}{16}, \tag{7.7}$$

$$S_{xx}^{\text{imp}} S_{FF}^{\text{ba}} \quad = \quad 16\hbar^2 n_{\text{m}}^{\text{imp}} n_{\text{m}}^{\text{ba}} \geq \hbar^2. \tag{7.8}$$

The minimum total number of phonons as a function of cooperativity occurs at $\mathcal{C}^{\text{SQL}} = (1+\nu)/4$, where the imprecision and backaction phonon numbers are equal ($n_{\text{m}}^{\text{imp}} = n_{\text{m}}^{\text{ba}} = 1/4$). This is called the standard quantum limit and thus I define $n_{\text{m}}^{\text{SQL}} = 1/4$ or $S_{xx}^{\text{SQL}} = 2x_{\text{zp}}^2/\Gamma_{\text{tot}}$ to be the imprecision (or backaction) at this point.

7.2   Interferometric measurement setup

Our detailed homodyne interferometric scheme is shown in Figure 7.1. A single tone is split into three parts. The first is used to drive the optomechanical system, the second is used to pump the JPA, and the third provides the local oscillator to the mixer. The input lines are heavily attenuated to prevent thermal noise from room temperature from reaching the device. For this experiment, the device we use is in the transmission geometry. This necessarily hurts the imprecision at any given power by a factor of two, as $\kappa_{\text{l}} = \kappa_{\text{ext}}/2 \leq \kappa/2$. The added noise of the amplifiers and loss of microwave lines and components can be calibrated by switching between two different noise sources at the input of the experiment, as explained in Section 6.4. One source is thermalized to base temperature T_{cryo} (this is what we use while doing the actual experiment), while the other is at $T_{\text{H}} = 4$ K. Varying the base temperature of the cryostat with the switch switched to the hot termination allows us to identify 6 dB of total loss between the switch and JPA, 2 dB of which is estimated to be between the cavity and the JPA.
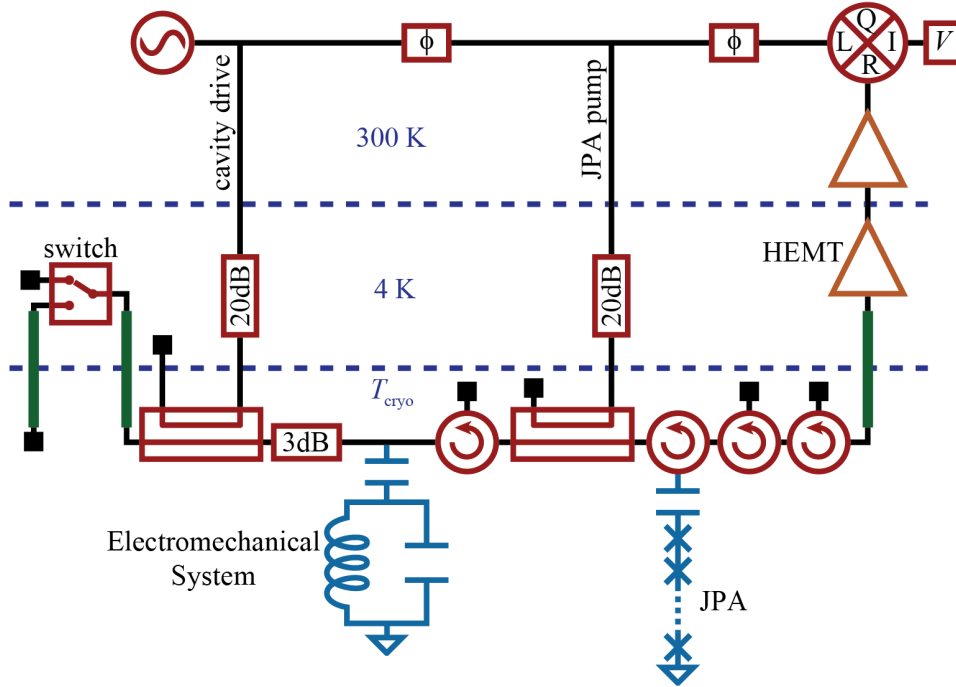
Figure 7.1: Interferometer diagram. A single microwave tone is divided in three parts to drive the cavity, pump the JPA, and provide the local oscillator to the mixer. A directional coupler is used at base temperature to combine the highly attenuated cavity drive with calibrated noise from one of two terminations determined by a switch. The drive signal then interacts with a transmission geometry optomechanical system. The output signal from the cavity reflects off of the JPA before being sent through an output chain of amplifiers to the mixer. Superconducting coaxial cables (green) are used between temperature stages to minimize loss. Cryogenic microwave circulators are used to prevent amplifier noise from reaching the optomechanical system.

Similar measurements (also explained in Section 6.4) allow us to identify that the added noise of the JPA is $n_{\text{add}}^{\text{JPA}} = 0.3$ and the added noise of the HEMT alone is $n_{\text{add}}^{\text{HEMT}} = 24.5$. When the JPA is on, the HEMT noise is effectively divided by ~ 20 dB of JPA gain, contributing 0.25 quanta of noise. The effective number of added noise photons from the loss and amplifiers can then be found:

$$\frac{1}{2} + n_{\text{add}} = 10^{0.2} \left(\frac{1}{2} + n_{\text{add}}^{\text{JPA}} + \frac{n_{\text{add}}^{\text{HEMT}}}{G^{\text{JPA}}} \right) = \frac{1}{2} + 1.16 \tag{7.9}$$

Despite the heavy attenuation on the input lines, we estimate the thermal input noise to be $n_{\text{l}}^{\text{th}} = 0.17$. This noise will add to the imprecision of the measurement. However, it will contribute negligibly to the thermal motion of the mechanical oscillator, as the occupancy in this experiment will always be large compared to 0.17 (no cooling is employed). The total added noise of the

interferometer utilizing the JPA is thus estimated to be $n_{\text{add}} + n_{\text{l}}^{\text{th}} = 1.3$. Without the JPA, loss between the JPA and HEMT is important and the total added noise we estimate is $n_{\text{add}} = 55$. This added noise value corresponds to a quantum efficiency of $\eta = 0.9\%$. This means that without the JPA, 99% of the signal is thrown away before the measurement - clearly a poor situation. With the JPA, the interferometer's quantum efficiency improves to $\eta = 27\%$, an efficiency comparable to those achieved in optical systems.

7.3   Device design and parameters

The device used for this experiment is the one labeled 'Device C' in Chapter 5. We realize this optomechanical system by embedding an aluminum mechanical wire in a superconducting microwave cavity. The wire has dimensions 150 μm ×170 nm ×160 nm, giving an estimated mass of $m = (11 \pm 2)$ pg. We can look at the output spectra to determine the mechanical resonance frequency $\Omega_{\text{m}} = 2\pi \times 1.04$ MHz and mechanical linewidth $\Gamma_{\text{m}} \approx 2\pi \times 1.8$ Hz (depending on power). The circuit is made from the same layer of aluminum as the wire and is designed to have a higher impedance than a $\lambda/4$ transmission line cavity (see Figure 5.11(b)). The bare cavity response is measured to extract the cavity resonance frequency $\omega_{\text{c}} = 2\pi \times 7.49$ GHz, cavity linewidth
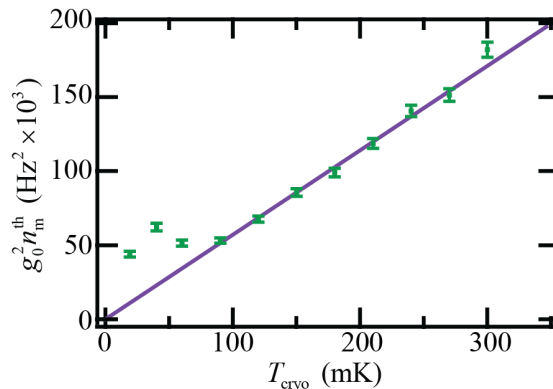
Figure 7.2: Optomechanical coupling calibration. The integrated voltage spectral density $S_{VV}[\omega]$ is proportional to $g_0^2 n_{\text{m}}^{\text{f}} \sim g_0^2 n_{\text{m}}^{\text{th}}$ through measurable proportionality constants. This quantity is plotted here as a function of cryostat temperature T_{cryo}. The slope of the linear (zero-offset) fit reveals the single-photon optomechanical coupling $g_0 = 2\pi \times 0.86 \pm 0.3$ Hz.

$\kappa = 2\pi \times 2.88$ MHz, and external coupling $\kappa_{\text{ext}} = 2\pi \times 2.5$ MHz. The cavity linewidth is designed to be comparable to the mechanical frequency ($\nu = 4\Omega_{\text{m}}^2/\kappa^2 = 0.52$) to aid in achieving the best possible measurement imprecision.

To calibrate the optomechanical coupling, we do a temperature sweep as described in Section 6.3. This is shown in Figure 7.2, where $g_0^2 n_{\text{m}}^{\text{f}} \approx g_0^2 n_{\text{m}}^{\text{th}}$ is plotted verses cryostat base temperature. At high temperatures, the mechanical oscillator tracks the cryostat temperature. At low temperatures, the mechanical occupancy saturates. We fit all but the lowest three temperatures to a line through zero to deduce the single photon coupling $g_0 = 2\pi \times 0.83 \pm 0.3$ Hz. Plugging in the zero point motion results in $G = g_0/x_{\text{zp}} = 2\pi \times (32 \pm 3)$ kHz/nm. The fractional uncertainty in G is larger than in g_0 because it includes the relatively large uncertainty in the mass. The value of G is independently confirmed to be $G = 2\pi \times (30 \pm 6)$ kHz/nm by measurements of the radiation pressure damping using a detuned cavity drive.

7.4 Imprecision below the standard quantum limit

The use of a more quantum-efficient interferometer to read out an optomechanical system clearly leads to an improvement in the measurement of mechanical motion. However, the quantitative figure of merit for efficient mechanical detection is the imprecision of the measurement in units of phonons. The imprecision number of phonons will be inversely proportional to the quantum efficiency of the interferometer and should decrease linearly with the number of drive photons. There is no theoretical limit on how small the imprecision can be. In this experiment, we investigate this imprecision as a function of drive power and show that the imprecision can be pushed below a quarter quantum (the value at the standard quantum limit).

For a series of drive powers, we measure the output voltage spectrum and transform it (as described in Section 6.2) into an inferred displacement spectral density. Figure 7.3(a) shows the highest power measurement made using an on-resonance drive and our homodyne interferometer including the JPA. Figure 7.3(b) shows the same measurement for a blue-detuned drive. Most notably, the imprecision (frequency independent background) in spectral density units is the same in
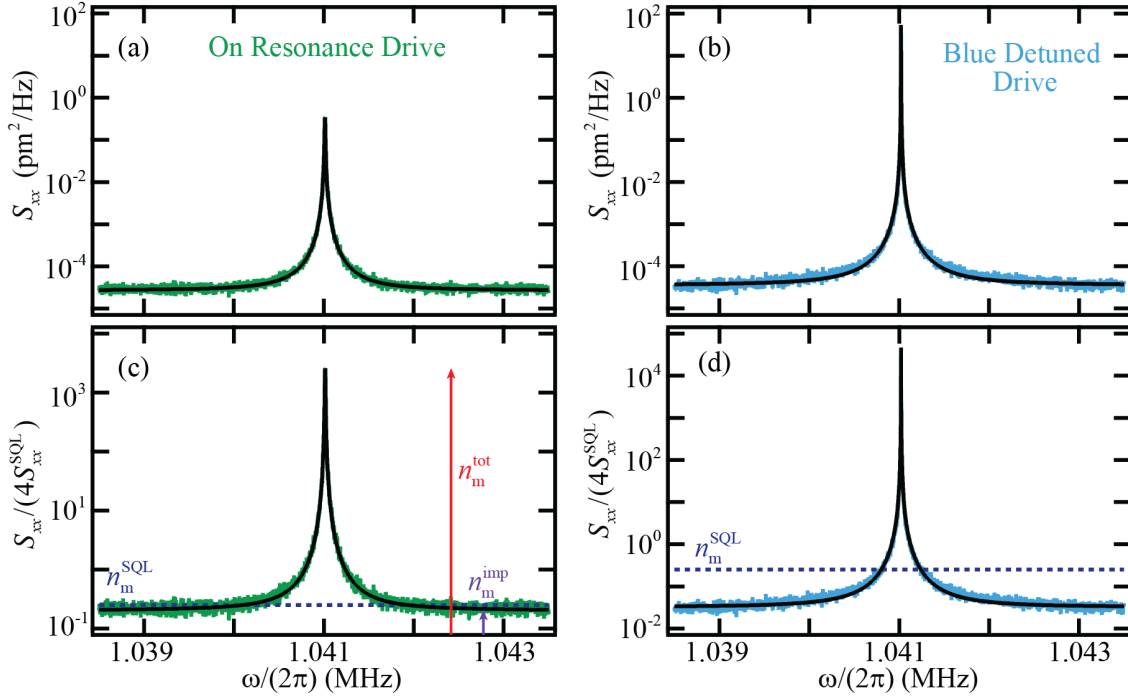
Figure 7.3: Inferred mechanical spectra in displacement and phonon units, (a,b) $S_{xx}[\omega]$ and (c,d) $S_{xx}[\omega]/(4S_{xx}^{\mathrm{SQL}})$, respectively. (a,c) Mechanical spectra in the presence of an on-resonant drive. The imprecision is below the imprecision at the standard quantum limit (dark blue dotted line). (b,d) Mechanical spectra in the presence of a blue-detuned drive. The absolute imprecision is the same as for the on-resonance drive, but the number of imprecision phonons can be arbitrarily small at the cost of amplified mechanical motion.

both cases. However, it is somewhat more convenient to plot the spectra in units of $S_{xx}[\omega]/(4S_{xx}^{\mathrm{SQL}})$, as in Figures 7.3(c,d). These units have the nice property that the number of phonons can be read off simply by looking at the data on resonance. Thus, the height of the frequency-independent background is $n_{\mathrm{m}}^{\mathrm{imp}}$ and the total height of the Lorentzian peak is $n_{\mathrm{m}}^{\mathrm{tot}}$. For the on-resonant drive, the measurement imprecision is below the imprecision at the standard quantum limit $n_{\mathrm{m}}^{\mathrm{SQL}} = 1/4$ (dash-dotted line). Quantitatively, the number of thermal quanta is $n_{\mathrm{th}} = 2600$ and the measurement imprecision is $n_{\mathrm{m}}^{\mathrm{imp}} = 0.2 \pm 0.0075 < n_{\mathrm{m}}^{\mathrm{SQL}}$. The imprecision in displacement spectral density units is $(S_{xx}^{\mathrm{imp}})^{1/2} = (4.8\pm0.4)$ fm/$\sqrt{\mathrm{Hz}}$. This fractional uncertainty is larger than the uncertainty in $n_{\mathrm{m}}^{\mathrm{imp}}$ because it includes the uncertainty in the mass of the mechanical oscillator. For the blue-detuned drive, the imprecision number of phonons can be arbitrarily small (as expected, see Figure 4.3(a)),

but at the cost of amplifying the mechanical motion. In Figure 7.3(d), the mechanical linewidth is reduced to $\Gamma_{\text{tot}} = 2\pi \times 0.67$ Hz, and the imprecision is $n_{\text{m}}^{\text{imp}} = 0.017$. However, the real mechanical motion is increased to $n_{\text{m}}^{\text{f}} = 5 \times 10^4$.

While only the highest power point is required to demonstrate that the imprecision is below that at the standard quantum limit, the entire power dependence of the imprecision can be used to confirm the excellent quantum efficiency of our interferometer. The number of quanta for the on-resonant drive as a function of incident drive power is shown in Figure 7.4(a). The number of thermal quanta (red circles) stays approximately constant as a function of power, while the number of imprecision quanta (purple squares) decreases with power. The very highest power points are taken from the data in Figure 7.3(c) and we once again see that the imprecision number of quanta is below the imprecision at the standard quantum limit, $n_{\text{m}}^{\text{SQL}} = 1/4$. The expected imprecisions given a perfect quantum-efficient interferometer and an interferometer with $n_{\text{add}} = 1.3$ are shown as solid and dashed lines, respectively. Both lines include the measured values of κ and Γ_{m} at each
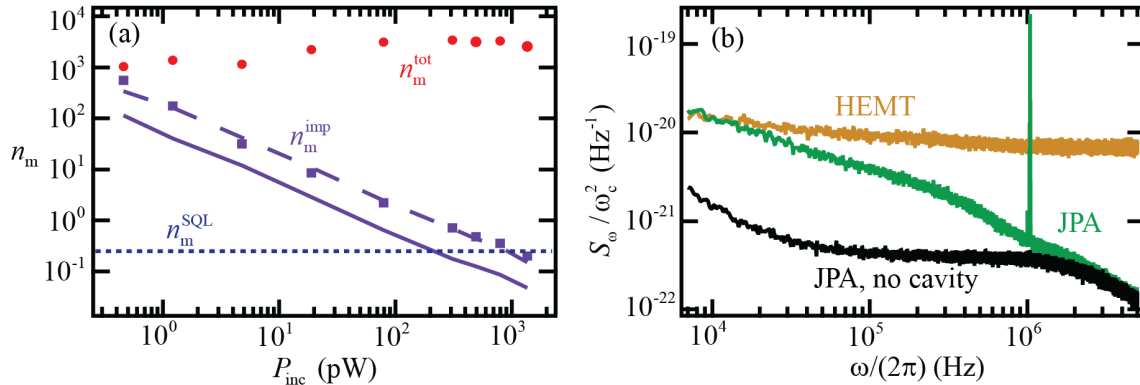
Figure 7.4: Power-dependence of the imprecision. (a) Imprecision (purple squares) and total (red circles) mechanical phonon numbers as a function of incident drive power. At the highest power (inferred from the data in figure 7.3(c)), the imprecision is below the imprecision at the standard quantum limit (dark blue dotted line). Expected imprecisions assuming a shot noise limited interferometer and an interferometer with $n_{\text{add}} = 1.3$ are shown as solid and dashed lines, respectively. (b) Cavity frequency noise limits the achievable imprecision. The JPA improves apparent cavity frequency noise (black) over using only a HEMT amplifier (orange) by reducing the added noise of the interferometer. However, when the cavity is driven, excess cavity frequency fluctuations dominate the apparent cavity fluctuations in the JPA case (green).

power, which is why the lines are not perfectly straight. Most notably, the line for $n_{\mathrm{add}} = 1.3$ agrees well with our data, confirming our added noise calibration and the fact that our interferometer is nearly shot-noise limited.

The theory introduced so far in this thesis would predict that the imprecision could have been improved even further by increasing the microwave power. However, the imprecision in this experiment was limited by a source of technical noise. Ultimately, any information we know about the mechanical position comes from our knowledge of the cavity frequency fluctuations (as the optomechanical coupling is dependent on $G = d\omega_{\mathrm{c}}/dx$). The imprecision discussed in the theory comes from the apparent cavity frequency fluctuations contributed by added microwave photons. The measured cavity frequency fluctuations are shown in Figure 7.4(b) for the highest power used in Figure 7.3. As expected, the frequency fluctuations measured using only a HEMT amplifier (orange) include a narrow Lorentzian peak at the mechanical frequency (corresponding to actual mechanical motion) and are otherwise dominated by apparent fluctuations from the interferometer added noise. Using the JPA but leaving the cavity drive off (black) improves these apparent fluctuations, reducing the imprecision of the measurement. However, when the cavity drive is turned back on (green), excess cavity frequency fluctuations dominate the imprecision. These fluctuations do not decrease with larger drive power, and thus limit the imprecision from being improved beyond what is presented above. This limitation could be decreased in future experiments by choosing materials, fabrication techniques, or cavity geometry to decrease the cavity frequency fluctuations or by increasing the optomechanical coupling g_0 to make those frequency fluctuations less important.

7.5   Force sensitivity

Once the imprecision is decreased below the thermal noise, a measurement of the optomechanical system is extremely sensitive to mechanical displacement and thus also any forces that may act on the mechanical oscillator. The sensitivity to an external force applied to the center of

the mechanical wire is limited by both the thermal and imprecision noise and is given by

$$S_{FF}^{\text{tot}}[\omega] \approx \frac{2\hbar^2\Gamma_{\text{m}}}{\mathbf{2}x_{\text{zp}}^2}\left(\frac{4n_{\text{m}}^{\text{imp}}}{\Gamma_{\text{m}}^2|\chi_{\text{m}}[\omega]|^2} + n_{\text{m}}^{\text{th}}\right) = \frac{\hbar^2\Gamma_{\text{m}}}{x_{\text{zp}}^2}\left(\frac{4n_{\text{m}}^{\text{imp}}}{\Gamma_{\text{m}}^2|\chi_{\text{m}}[\omega]|^2} + n_{\text{m}}^{\text{th}}\right). \tag{7.10}$$

The bold 2 comes from the use of the effective mass $m_{\text{eff}} = m/2$ at the center of the high-tension wire (see Appendix E):

$$x_{\text{zp,eff}}^2 = \frac{\hbar}{2m_{\text{eff}}\Omega_{\text{m}}} = \frac{\mathbf{2}\hbar}{2m\Omega_{\text{m}}} = \mathbf{2}x_{\text{zp}}^2. \tag{7.11}$$

Assuming the imprecision is smaller than the thermal occupation, the sensitivity to forces at the mechanical resonance frequency is

$$S_{FF}^{\text{tot}}[\Omega_{\text{m}}] = \frac{\hbar^2\Gamma_{\text{m}}}{x_{\text{zp}}^2}\left(n_{\text{m}}^{\text{imp}} + n_{\text{m}}^{\text{th}}\right) \approx \frac{\hbar^2\Gamma_{\text{m}}}{x_{\text{zp}}^2}n_{\text{m}}^{\text{th}} = 2k_{\text{B}}T_{\text{m}}m\Gamma_{\text{m}} = 4k_{\text{B}}T_{\text{m}}m_{\text{eff}}\Gamma_{\text{m}}, \tag{7.12}$$

where T_{m} is the thermal temperature of the mechanical oscillator. The bandwidth of the sensor (the region in frequency where the thermal contribution is larger than the imprecision one) is $\Gamma_{\text{m}}\sqrt{n_{\text{m}}^{\text{th}}/n_{\text{m}}^{\text{imp}} - 1}$.
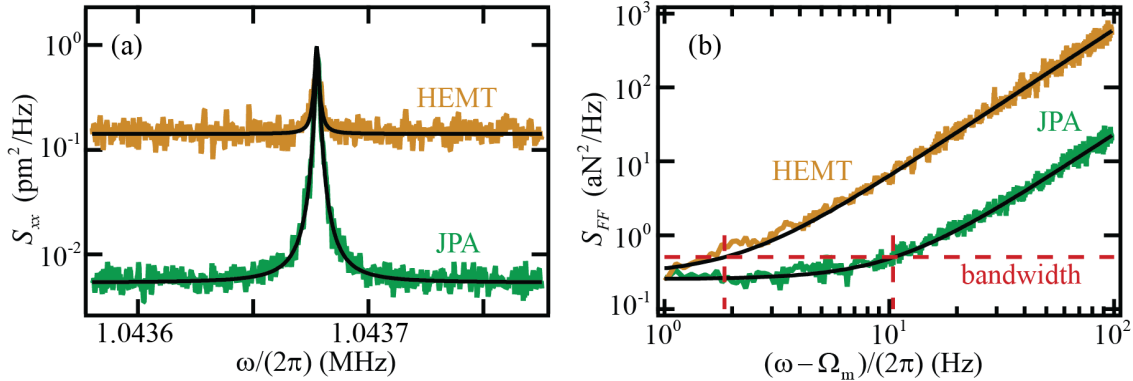
Figure 7.5: Force sensitivity. (a) Displacement spectral density measured with the JPA on (green) and off (orange) at low incident power $P_{\text{inc}} = 1$ pW. Using the JPA significantly improves the displacement imprecision. (b) The same data as in (a), now plotted as a force spectral density versus logarithmic frequency away from the mechanical resonance frequency. As the thermal motion is much larger than the imprecision even with the JPA off, the force sensitivity on resonance is not improved by turning the JPA on. However, the bandwidth of the force sensor (the region of frequency over which the sensor is not limited by the imprecision) is improved by a factor of five when the JPA is employed. This is indicated by a horizontal red dashed line at twice the force sensitivity on resonance and vertical red dashed lines at the frequencies where this is equal to the measured force sensitivity $S_{FF}^{\text{tot}}[\omega] \approx S_{FF}^{\text{imp}}[\omega] + S_{FF}^{\text{th}} = 2S_{FF}^{\text{th}}$.

Theoretically, the force sensitivity should be independent of power once the imprecision is small compared to the thermal motion. However, we observe that both T_{m} and Γ_{m} increase with power. Therefore, our best force sensitivity is achieved at low power $P_{\mathrm{inc}} = 1$ pW, one of the lowest powers used in Figure 7.4. The displacement and force spectral densities at this power are shown in Figure 7.5. The force sensitivity on resonance is $S_{FF}[\Omega_{\mathrm{m}}] = (0.26 \pm 0.04)$ aN^2/Hz, both with and without the JPA. However, the bandwidth of the sensor improves fivefold from $2\pi \times 1.85$ Hz to $2\pi \times 10.4$ Hz when the JPA is used (Figure 7.5(b), red dashed lines).

In this experiment, we were able to demonstrate the achievement of a nearly shot-noise limited interferometer in the microwave regime, an advance critical not only to our experiments in optomechanics, but also essential for any experiment where the information of interest is contained in microwave fields. This improvement in efficiency allowed an on-resonant drive measurement of a mechanical oscillator with an imprecision below the value at the standard quantum limit. This ultrasensitive measurement of mechanical motion will be essential to future detection of quantum states of the mechanical oscillator which could lead to squeezing of the mechanical mode, entanglement of mechanical motion and other quantum systems, and even investigations into fundamental quantum mechanical theory.

Chapter 8

Experiment II: Radiation pressure cooling to the mechanical ground state

Radiation pressure cooling of a mechanical oscillator into its ground state was a long-standing goal of the entire optomechanics community, as it is the first step toward realizing experiments exploring quantum mechanics in macroscopic mechanical oscillators. In this chapter, I will detail our experiments on cooling the mechanical oscillator using the radiation pressure of microwave photons. In Section 8.1, I detail our initial, proof of principle, cooling measurements from reference [45]. In Section 8.2, I explain how the advent of a device capable of reaching the strong-coupling regime as well as the implementation of the nearly shot-noise limited interferometry described in Chapter 7 allowed one of the first measurements of a macroscopic mechanical oscillator in its quantum ground state [48].

8.1   Initial realization of radiation pressure cooling

In our initial experiments exploring radiation pressure cooling in 2008 [45], we observed the radiation pressure induced changes to the mechanical susceptibility and demonstrated cooling of the mechanical oscillator from an occupancy of 700 down to 140 phonons. This initial attempt was done with an interferometer containing only a HEMT amplifier and a comparatively weakly coupled device to the one that follows.

8.1.1   Review of radiation pressure cooling theory in the weak-coupling limit

In Chapter 3.1, I found theoretical expressions for the radiation pressure induced damping Γ_{opt}, mechanical resonance frequency shift Ω_{opt}, final number of mechanical phonons $n_{\mathrm{m}}^{\mathrm{f}}$, and the cavity output operator spectrum $S_{a_{\mathrm{out}}a_{\mathrm{out}}}[\omega]$, in the presence of an optimally red-detuned drive $\omega_{\mathrm{r}} \approx \overline{\omega}_{\mathrm{c}} - \Omega_{\mathrm{m}}$, in the resolved sideband limit ($\Omega_{\mathrm{m}} \gg \kappa$). In the case where the added noise and final mechanical occupancy are relatively large compared to any photon occupancy, $n_{\mathrm{l}}^{\mathrm{th}}$ and $n_{\mathrm{c}}^{\mathrm{th}}$ can be ignored. Then these quantities in the weak coupling regime are (Equations 3.32, 3.57, and 3.76)

$$\Gamma_{\mathrm{tot}} = \Gamma_{\mathrm{m}} + \Gamma_{\mathrm{opt}} \;=\; \Gamma_{\mathrm{m}} + 4g^2 \left(\frac{\kappa}{\kappa^2 + 4(\Delta + \Omega_{\mathrm{m}})^2} - \frac{\kappa}{\kappa^2 + 4(\Delta - \Omega_{\mathrm{m}})^2} \right), \tag{8.1}$$

$$\Omega_{\mathrm{tot}} = \Omega_{\mathrm{m}} + \Omega_{\mathrm{opt}} \;=\; \Omega_{\mathrm{m}} + 4g^2 \left(\frac{\Delta + \Omega_{\mathrm{m}}}{\kappa^2 + 4(\Delta + \Omega_{\mathrm{m}})^2} + \frac{\Delta - \Omega_{\mathrm{m}}}{\kappa^2 + 4(\Delta - \Omega_{\mathrm{m}})^2} \right), \tag{8.2}$$

$$n_{\mathrm{m}}^{\mathrm{f}} \;=\; \frac{n_{\mathrm{m}}^{\mathrm{th}}\Gamma_{\mathrm{m}} + \left(n_{\mathrm{c}}^{\mathrm{th}} + n_{\mathrm{m}}^{0} + 2n_{\mathrm{c}}^{\mathrm{th}}n_{\mathrm{m}}^{0} \right)\Gamma_{\mathrm{opt}}}{\Gamma_{\mathrm{m}} + \Gamma_{\mathrm{opt}}} \approx \frac{n_{\mathrm{m}}^{\mathrm{th}}\Gamma_{\mathrm{m}}}{\Gamma_{\mathrm{m}} + \Gamma_{\mathrm{opt}}}, \tag{8.3}$$

$$S_{a_{\mathrm{out}}a_{\mathrm{out}}}[\omega] \;\approx\; g^2 \kappa_{\mathrm{l}} \Gamma_{\mathrm{tot}} n_{\mathrm{m}}^{\mathrm{f}} \left| \chi_{\mathrm{c}}[\omega] \right|^2 \left| \chi_{\mathrm{m,eff}}[\omega - \omega_{\mathrm{r}}] \right|^2. \tag{8.4}$$

In Chapter 4, I derived expressions to relate the intensity (or voltage) spectral density measured by an in-phase, linear, two-quadrature detector to the $S_{a_{\mathrm{out}}a_{\mathrm{out}}}[\omega]$'s (the relevant result for an interferometer only containing a HEMT amplifier). The measured spectrum at frequency $\omega = |\omega_{\mathrm{LO}} - (\omega_{\mathrm{r}} + \Omega_{\mathrm{m}} + \delta)|$, where δ is the detuning from the mechanical sideband peak, is

$$S_{I_{\mathrm{I}}I_{\mathrm{I}}}^{\mathrm{photon}}[\omega] \;=\; \frac{1}{\eta} + \frac{1}{2} \left(S_{a_{\mathrm{out}}a_{\mathrm{out}}}[\omega_{\mathrm{LO}} - \omega] + S_{a_{\mathrm{out}}a_{\mathrm{out}}}[\omega_{\mathrm{LO}} + \omega] \right) \tag{8.5}$$

$$\approx \frac{1}{\eta} + \frac{1}{2} g_{\mathrm{r}}^2 \kappa_{\mathrm{l}} \Gamma_{\mathrm{tot}} n_{\mathrm{m}}^{\mathrm{f}} \left| \chi_{\mathrm{c}}[\omega_{\mathrm{r}} + \Omega_{\mathrm{m}}] \right|^2 \left| \chi_{\mathrm{m,eff}}[\Omega_{\mathrm{m}} + \delta] \right|^2. \tag{8.6}$$

8.1.2   Device parameters and interferometric setup

The optomechanical device for this experiment is described in Chapter 5 as 'Device B'. The mechanical oscillator is an aluminum wire with dimensions 100 μm $\times$130 nm $\times$120 nm, resulting in a mass[1] of 4.2 pg. The bare mechanical frequency and linewidth (determined from the output spectra) are $\Omega_{\mathrm{m}} = 2\pi \times 1.525$ MHz and $\Gamma_{\mathrm{m}} \sim 2\pi \times 5$ Hz. The microwave circuit is a $\lambda/4$ transmission line resonator (see Figure 5.11(a)) in the transmission geometry ($\kappa_{\mathrm{l}} = \kappa_{\mathrm{ext}}/2$. The bare cavity response
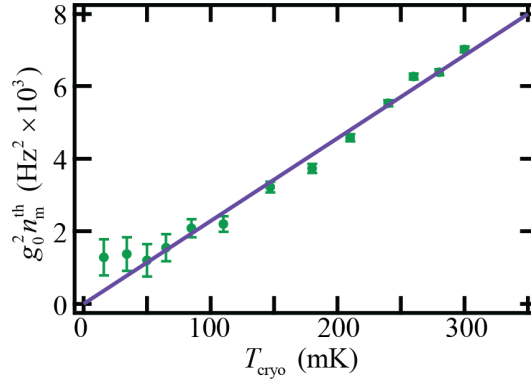
Figure 8.1: Optomechanical coupling calibration. The integrated voltage spectral density $S_{VV}[\omega]$ is proportional to $g_0^2 n_{\mathrm{m}}^{\mathrm{f}} \sim g_0^2 n_{\mathrm{m}}^{\mathrm{th}}$ through measurable proportionality constants. This quantity is plotted here as a function of cryostat temperature T_{cryo}. The slope of the linear (zero-offset) fit reveals the single-photon optomechanical coupling $g_0 = 2\pi \times 0.21$ Hz.

indicates a cavity resonance frequency and linewidth $\overline{\omega}_{\mathrm{c}} = 2\pi \times 5.22$ GHz and $\kappa = 2\pi \times 230$ kHz. The cavity linewidth is designed to be much smaller than the mechanical frequency, putting this device soundly in the resolved sideband limit (quantified by the resolved-sideband factor $\nu = 4\Omega_{\mathrm{m}}^2/\kappa^2 = 176$) and theoretically enabling cooling to the ground state (via the requirements outlined in Section 3.1.6).

To calibrate the optomechanical coupling, we do a temperature sweep as described in Section 6.3. This is shown in Figure 8.1, where $g_0^2 n_{\mathrm{m}}^{\mathrm{f}} \approx g_0^2 n_{\mathrm{m}}^{\mathrm{th}}$ is plotted verses cryostat base temperature. This measurement is done with a red-detuned drive, but at low enough drive power ($n_{\mathrm{d}} \approx 9 \times 10^5$, $\mathcal{C} \approx 0.14$) where radiation pressure effects should be negligible. At high temperatures, the mechanical oscillator is in equilibrium with the cryostat temperature. At low temperatures, the mechanical oscillator temperature saturates to ~ 50 mK, or $n_{\mathrm{m}}^{\mathrm{th}} \sim 700$. We fit all but the lowest two temperatures to a line through zero to deduce the single photon coupling $g_0 = 2\pi \times 0.21$ Hz. Dividing by the zero point motion results in $G = g_0/x_{\mathrm{zp}} = 2\pi \times 5.7$ kHz/nm.

---

[1] This is different from the number published in [45], as the mass used consistently throughout the published analysis was erroneously 6.2 pg rather than the true 4.2 pg. However, neither the single-photon coupling g_0, nor the radiation pressure induced damping, nor the final mechanical occupancy depend on mass. Therefore, consistently using the incorrect mass changes only the value for G and the units S_{xx}. The published achievements in damping and occupancy are unaffected.

This experiment was done with a heterodyne interferometer containing a HEMT amplifier only (Figure 8.2). The most notable component that was not contained in the interferometer in the previous chapter is a low frequency mechanical drive line that allows us to drive the mechanical oscillator near its resonance frequency. This low-frequency drive is combined with the microwave drive through a bias T, allowing it to modulate the voltage along the feed line, exerting a force on the mechanical oscillator. Sweeping this mechanical drive frequency then allows us to measure the response of the mechanical oscillator to this force.
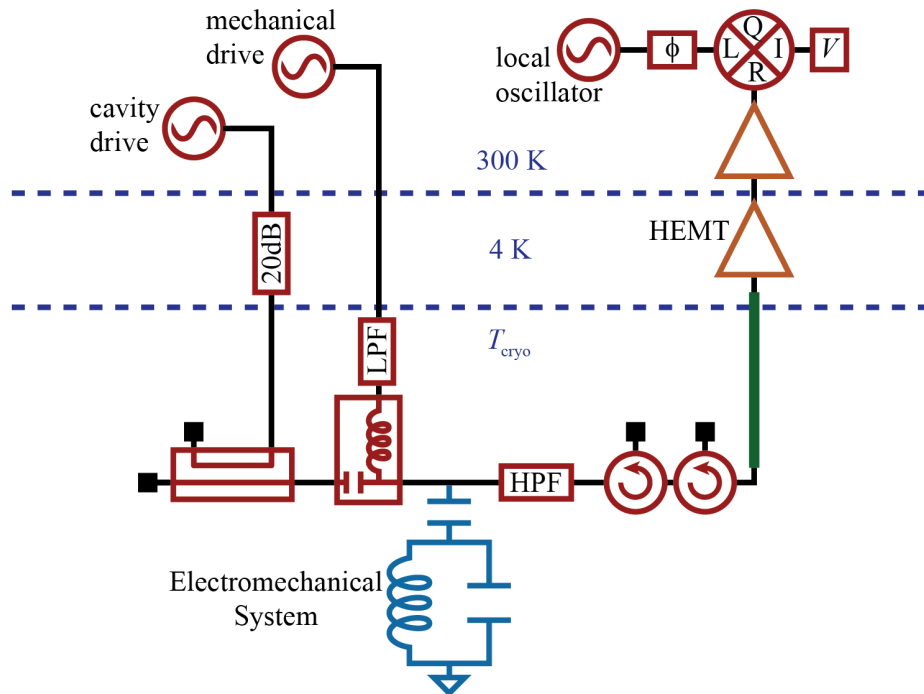
Figure 8.2: Interferometric measurement setup. The heterodyne interferometer is formed by interrogating the system of interest (here an electromechanical system) with a microwave cavity drive and then mixing the resulting microwave signal with a local oscillator at the output of the experiment. A bias T combines the cavity drive with a low-frequency ($\sim$ 1 MHz) mechanical drive. Once again, cryogenic circulators are used to block amplifier and thermal noise at 4K from reaching the optomechanical system.

8.1.3   Observed change in mechanical susceptibility

The presence of radiation pressure changes the mechanical susceptibility by changing the resonant frequency and linewidth of the mechanical oscillator (Equation 3.32). We investigate this by observing the change in the driven mechanical response as a function of microwave drive frequency while adjusting the incident power to keep the number of drive photons in the cavity constant at $n_{\rm d} = 8 \times 10^6$ ($\mathcal{C} \approx 1.2$), essentially measuring the effective mechanical susceptibility. At this power, the radiation pressure damping is slightly larger than the intrinsic mechanical damping. The mechanical resonance frequency and linewidth are plotted as a function of drive frequency in
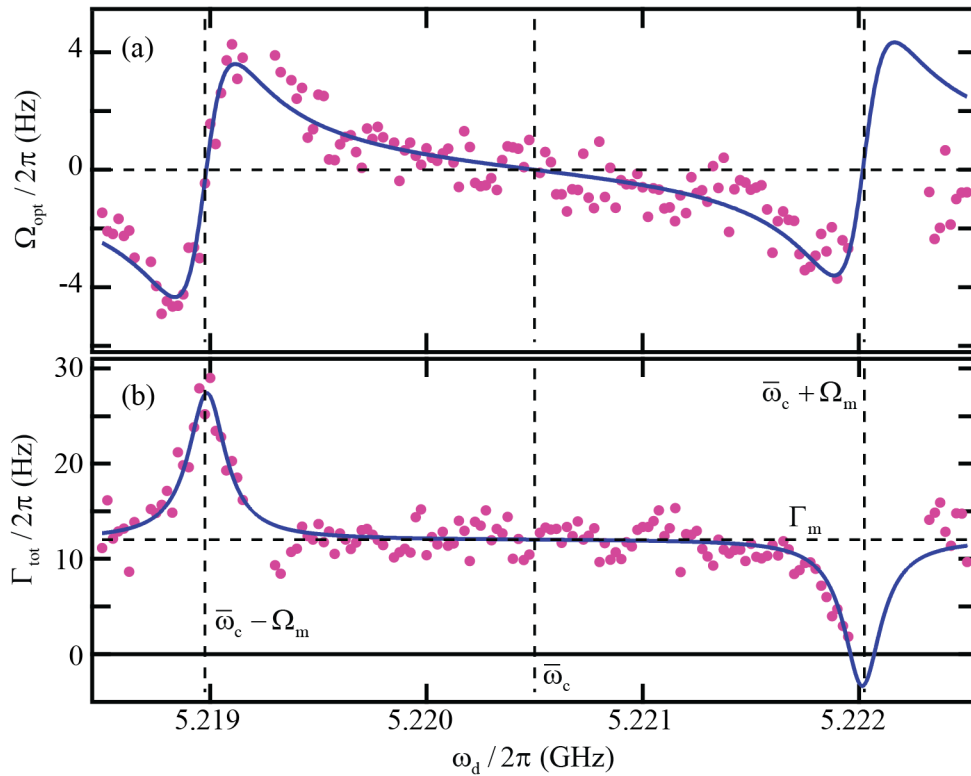
Figure 8.3: Optomechanically induced change in mechanical susceptibility. The optomechanically induced mechanical resonance frequency (a) and the total mechanical damping (b) are plotted as a function of drive frequency with the number of drive photons held constant. The intrinsic damping and frequency are shown as horizontal dashed lines. Vertical dashed lines indicate the cavity resonance frequency, as well as the optimally red and blue detuned frequencies $\overline{\omega}_{\rm c} \pm \Omega_{\rm m}$. The two quantities are fit concurrently (solid blue line) to Equations 3.32 with $n_{\rm d}$ as the only free parameter.

Figure 8.3 and fit with the theoretical equations found above. The only adjustable parameter in these fits is n_d and the value recovered agrees with estimates for the incident power within the 3 dB uncertainty of the input drive line attenuation. There are data points missing near $\omega_\mathrm{d} = \overline{\omega}_\mathrm{c} + \Omega_\mathrm{m}$, as expected, because this is where the mechanical oscillator is amplified to self-oscillation.

8.1.4 Cooling to 140 mechanical quanta

The radiation pressure damping measured in the previous section suggests that the mechanical oscillator was also being cooled by the radiation pressure. Theoretically, the final mechanical occupancy should be inversely proportional to the mechanical damping: $n_\mathrm{m}^\mathrm{f} = n_\mathrm{m}^\mathrm{th} \Gamma_\mathrm{m} / \Gamma_\mathrm{tot}$. However, to measure this thermal occupancy, we need to look at the output spectral density without a mechanical driving force. Here, I present the results of this thermal occupancy measurement as a function of red-detuned drive power.

One detail of this measurement is that the cavity becomes nonlinear at the highest microwave powers due to the non-linear electrodynamics of the cavity's aluminum superconducting film. As in the case of the optomechanical nonlinearity described in Section 3.1.2, this nonlinearity shifts the cavity resonance down in frequency and eventually causes the cavity to become bistable. This nonlinearity (prior to the bistability) does not prevent cooling measurements, but must be taken into account when finding the optimal red-detuned frequency. In order to determine this frequency, we make similar mechanical response measurements to the one in Figure 8.3, but now at constant incident power (rather than constant photon number) and only over the range of frequencies near optimal red-detuning (see Figure 8.4(a-b)). This allows us to determine the frequency of maximal damping (and thus maximal cooling) for each incident power, plotted in Figure 8.4(c).

Once the optimal drive frequency for cooling is established, we measure both the voltage spectrum without a mechanical drive and the driven mechanical response for each of a series of red drive powers. The spectrum without the mechanical drive is converted to displacement units by using the driven mechanical response to reference to the well-calibrated temperature sweep (which was calibrated by measuring the derivative of the output drive voltage as a function of drive
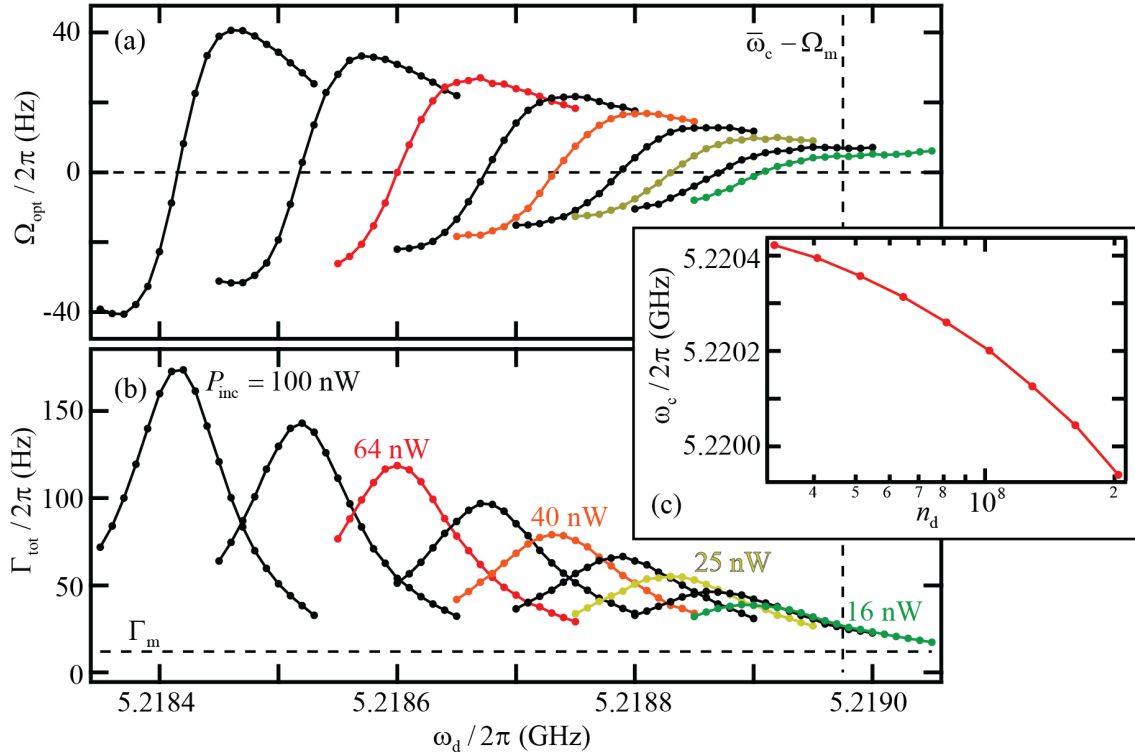
Figure 8.4: Calibration of optimal detuning for radiation pressure damping and cooling. Optomechanically induced mechanical resonance frequency (a) and total effective mechanical linewidth (b) as a function of drive frequency for the highest incident powers. The intrinsic (low power) optimal red-detuned frequency is shown as a vertical dashed line. The incident powers plotted are 1 dB steps from $P_{\mathrm{inc}} = 16$ nW (right, green) to $P_{\mathrm{inc}} = 100$ nW (left). As the power increases, the point of maximal damping (and therefore the cavity resonance frequency) shifts lower in frequency. The cavity linewidth (as inferred from the width of the damping curves) decreases as the power increases. The frequency point of maximal damping is chosen as the operating point for the cooling data. (c) Extracted cavity resonance frequency from the data in (a) and (b), now plotted as the number of drive photons in the cavity when optimally detuned.

frequency, see Section 6.2). The displacement spectral density is plotted in Figure 8.5 for several different drive powers. As the power is increased, the mechanical linewidth increases while the final occupancy decreases. The imprecision of the measurement also decreases with power for all powers, indicating that it is not limited by cavity frequency fluctuations as in references [10] and [76].

In Figure 8.6, the mechanical linewidth and final occupancy are plotted as a function of number of drive photons. The mechanical linewidth increases by a factor of 30 and at high power becomes linear in number of photons, as expected for radiation-pressure dominated damping. The
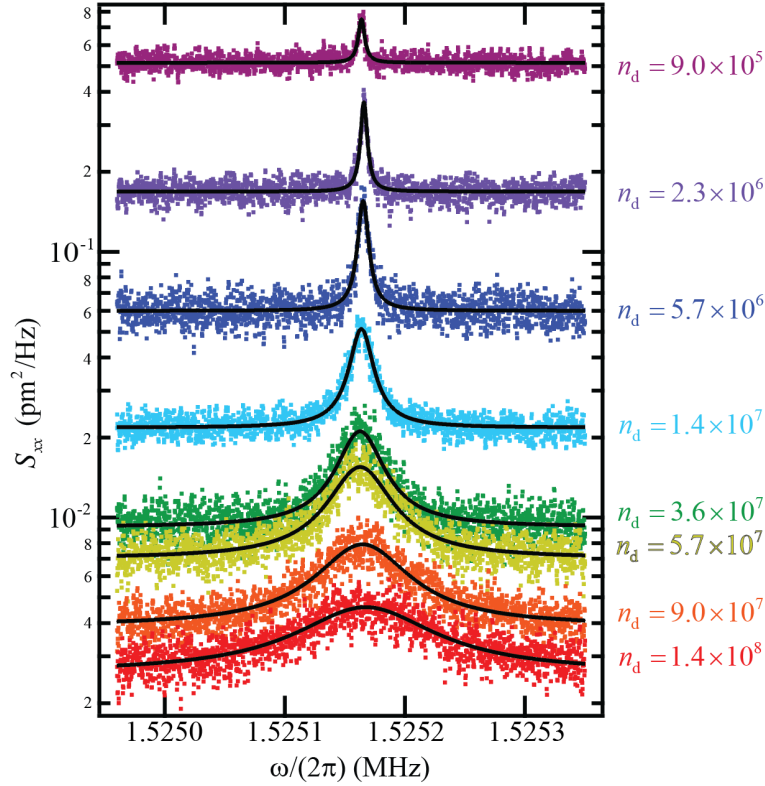
Figure 8.5: Mechanical spectra for several microwave drive powers. The displacement spectral density of the mechanical sideband is shown for drive photon numbers between 9×10^5 and 1.4×10^8 ($0.1 < \mathcal{C} < 21$). The highest four powers are drawn in the same four colors as in Figure 8.4. As the power is increased, the frequency-independent imprecision decreases. At the same time, the mechanical oscillator is damped (the linewidth increases) and cooled (the total area under the Lorentzian peak decreases - note the logarithmic scale).
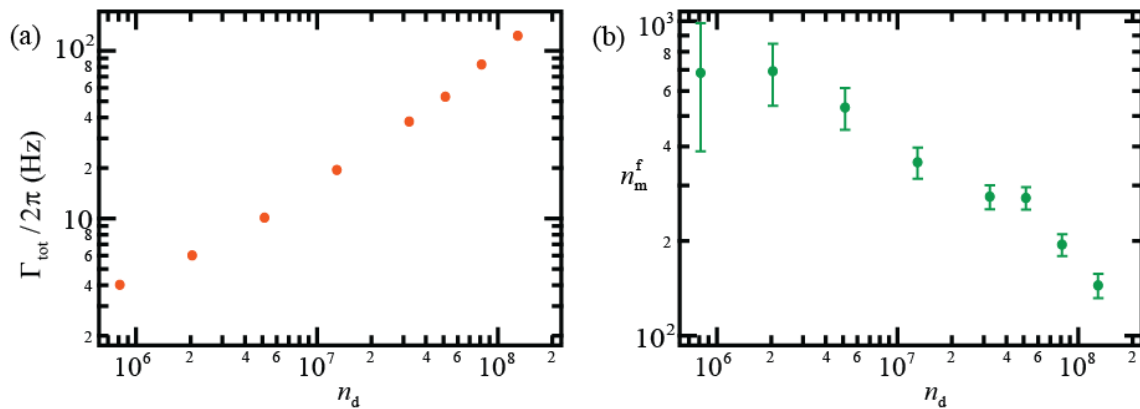
Figure 8.6: Summary of cooling data. (a) Total mechanical linewidth and (b) final mechanical occupancy as a function of number of drive photons. The mechanical oscillator is cooled from an initial occupancy of 700 quanta to a final occupancy of 140 quanta.

mechanical occupancy is cooled from 700 phonons to 140 ± 7 phonons, a factor of five. The discrepancy between this factor of 5 and the factor of 30 increase in linewidth can be understood because the large drive powers used may heat the mechanical oscillator thermal bath. This effect is compounded by the fact that we observe the intrinsic mechanical linewidth Γ_m to increase with temperature, thus coupling the oscillator more strongly to its warmer bath. The maximum number of inter-cavity drive photons, and thus the minimum final occupancy, is limited by the non-linearity of the cavity.

This experiment showed that radiation pressure dominated damping and cooling in the resolved sideband regime are feasible in a microwave electromechanical system containing a macroscopic mechanical oscillator. The cooling was limited by the number of allowed drive photons; thus, an improvement in optomechanical coupling could allow cooling to the ground state. Another necessary improvement for observing ground state cooling would be to integrate the system with a nearly shot noise limited measurement capable of discerning the final sub-phonon mechanical occupancy. The second half of this chapter presents the exciting results that came from these improvements.

8.2   Cooling to the quantum ground state

In the previous section, I described our initial experiment with radiation pressure damping and cooling. The experiment detailed in this chapter improves upon those results significantly by using a much more strongly coupled optomechanical system, thereby reducing the number of drive photons in the cavity required to cool the mechanical oscillator. For this experiment, we also implemented the nearly shot-noise limited interferometer presented in Chapter 7, enabling ultrasensitive detection of mechanical motion even as the mechanical oscillator was cooled to its ground state.

8.2.1 Review of radiation pressure cooling theory in the strong-coupling limit

The optomechanical device used in this experiment can reach the strong-coupling regime [15] $(2g > \kappa)$, so it will be generally best to use the expressions for the final number of mechanical phonons $n_{\rm m}^{\rm f}$ and the cavity output operator spectrum $S_{a_{\rm out}a_{\rm out}}[\omega]$ valid in the strong-coupling limit (Equations 3.63 and 3.75):

$$n_{\rm m}^{\rm f} = \frac{(4g^2 + \kappa^2)\Gamma_{\rm m}n_{\rm m}^{\rm th} + 4g^2\kappa n_{\rm c}^{\rm th}}{\kappa(4g^2 + \kappa\Gamma_{\rm m})} = \frac{(1 + \Gamma_{\rm opt}/\kappa)\Gamma_{\rm m}n_{\rm m}^{\rm th} + \Gamma_{\rm opt}n_{\rm c}^{\rm th}}{\Gamma_{\rm tot}}, \tag{8.7}$$

$$\begin{aligned} S_{a_{\rm out}a_{\rm out}}[\omega] &= |1 - N_1|^2 n_{\rm l}^{\rm th} + |N_1|^2 n_{\rm r}^{\rm th} \tag{8.8} \\ &\quad + \frac{\kappa_{\rm l}|\chi_{\rm c}[\omega]|^2}{|1 + g^2\chi_{\rm c}[\omega]\chi_{\rm m}[\omega - \omega_{\rm r}]|^2} \left(g^2\Gamma_{\rm m}(n_{\rm m}^{\rm th} - n_{\rm l}^{\rm th})|\chi_{\rm m}[\omega - \omega_{\rm r}]|^2 + \kappa(n_{\rm c}^{\rm th} - n_{\rm l}^{\rm th})\right) \\ &\quad + \frac{\kappa_{\rm l}(n_{\rm l}^{\rm th} - n_{\rm r}^{\rm th})}{|1 + g^2\chi_{\rm c}[\omega]\chi_{\rm m}[\omega - \omega_{\rm r}]|^2}{\rm Re}[N_1\chi_{\rm c}^*[\omega](1 + g^2\chi_{\rm c}[\omega]\chi_{\rm m}[\omega - \omega_{\rm r}])] \\ &\approx \frac{\kappa_{\rm l}|\chi_{\rm c}[\omega]|^2 \left(g^2\Gamma_{\rm m}n_{\rm m}^{\rm th}|\chi_{\rm m}[\omega - \omega_{\rm r}]|^2 + \kappa n_{\rm c}^{\rm th}\right)}{|1 + g^2\chi_{\rm c}[\omega]\chi_{\rm m}[\omega - \omega_{\rm r}]|^2}. \tag{8.9} \end{aligned}$$

In the last step, I have set $n_{\rm l}^{\rm th} = n_{\rm r}^{\rm th} = 0$, as is found to be the case for this experiment (this will be discussed below).

In Chapter 4, I found the expression for the intensity (or voltage) spectral density measured by an in-phase, linear, single-quadrature detector (the relevant result for an interferometer containing a JPA). In units of photon number (as in the right hand side of expressions in Chapter 4), this spectrum at frequency $\omega = |\omega_{\rm LO} - (\omega_{\rm r} + \Omega_{\rm m} + \delta)|$ is

$$\begin{aligned} S_{II}^{\rm photon}[\omega] &= \frac{1}{2\eta} + \frac{1}{2}\left(S_{a_{\rm out}a_{\rm out}}[\omega_{\rm LO} - \omega] + S_{a_{\rm out}a_{\rm out}}[\omega_{\rm LO} + \omega]\right) \tag{8.10} \\ &\approx \frac{1}{2\eta} + \frac{\kappa_{\rm l}|\chi_{\rm c}[\omega_{\rm r} + \Omega_{\rm m} + \delta]|^2 \left(g^2\Gamma_{\rm m}n_{\rm m}^{\rm th}|\chi_{\rm m}[\Omega_{\rm m} + \delta]|^2 + \kappa n_{\rm c}^{\rm th}\right)}{2|1 + g^2\chi_{\rm c}[\omega_{\rm r} + \Omega_{\rm m} + \delta]\chi_{\rm m}[\Omega_{\rm m} + \delta]|^2}. \tag{8.11} \end{aligned}$$

The measured spectral density can be related to photon units by comparing with the measured red-detuned drive power (as explained in Section 6.2):

$$\frac{S_{VV}[\omega]}{Z_0 P_{\rm r}} = \frac{2\hbar\omega_{\rm r}}{P_{\rm out,r}}S_{II}^{\rm photon}[\omega] \approx \frac{2\kappa_{\rm l}}{|N_2|^2 n_{\rm r}^{\rm th}\Omega_{\rm m}^2}S_{II}^{\rm photon}[\omega]. \tag{8.12}$$

The measured red drive power is $P_{\rm r} = (2\pi Z_0)^{-1}\int S_{VV}[\omega]d\omega$, where the integral is across the measured drive frequency. For low drive powers, when the coupling is weak and the cavity photon

occupancy is still negligible compared to the number of thermal phonons, the output spectrum can be transformed into mechanical displacement units and fit with a simple Lorentzian:

$$S_{xx}[\omega] \approx \frac{\kappa^2 x_{\text{zp}}^2}{g^2 \kappa_{\text{l}}} S_{II}^{\text{photon}}[\omega] = \frac{|N_2|^2 \kappa^2 \Omega_{\text{m}}^2}{2 G^2 \kappa_{\text{l}}^2} \left(\frac{S_{VV}[\omega]}{Z_0 P_{\text{r}}} \right) \tag{8.13}$$

$$= S_{xx}^{\text{SQL}} \left(4 n_{\text{m}}^{\text{imp}} + \Gamma_{\text{tot}}^2 n_{\text{m}}^{\text{f}} |\chi_{\text{m,eff}}[\Omega_{\text{m}} + \delta]|^2 \right). \tag{8.14}$$

The cavity parameters at each power can easily be extracted from the response of the cavity. At high power, the number of drive photons in the cavity (required to determine the cavity photon noise occupation n_{c}^{th}) can also be extracted from the dressed response. At low power, the dressed response does not reveal the number of drive photons, but this number can be inferred by comparing the measured output power to a power where the number is known. Once the cavity parameters and number of drive photons is known, the expressions in this section allow us to extract the cavity and mechanical occupancies from measurements of the voltage spectral density.

8.2.2   Device parameters and interferometric setup

In this experiment, we use a heterodyne interferometer including a Josephson parametric amplifier (see Figure 8.7). One microwave generator supplies the optomechanical drive and cancellation tones, both of which are heavily attenuated before reaching $T_{\text{cryo}} \sim 15$ mK. The drive tone interacts with the optomechanical system, picking up sidebands with information about the mechanical oscillator. It is then destructively interfered with the cancellation tone, so as not to overwhelm the JPA. This cancellation is maintained to the part-per-million level by using a feedback loop to control a voltage variable attenuator and phase shifter in the cancellation arm. Another microwave generator provides the JPA pump tone and the local oscillator to the interferometer. The JPA pump is 1.3 MHz higher in frequency than the cavity frequency so that the measurement is heterodyne, and it is also heavily attenuated before reaching the weakly coupled port of the JPA. The drive-canceled signal coming from the optomechanical system is amplified as it reflects off the strongly coupled port of the JPA and is subsequently amplified by HEMT and room temperature amplifiers before being mixed down and detected. A switch connects one of two calibrated noise
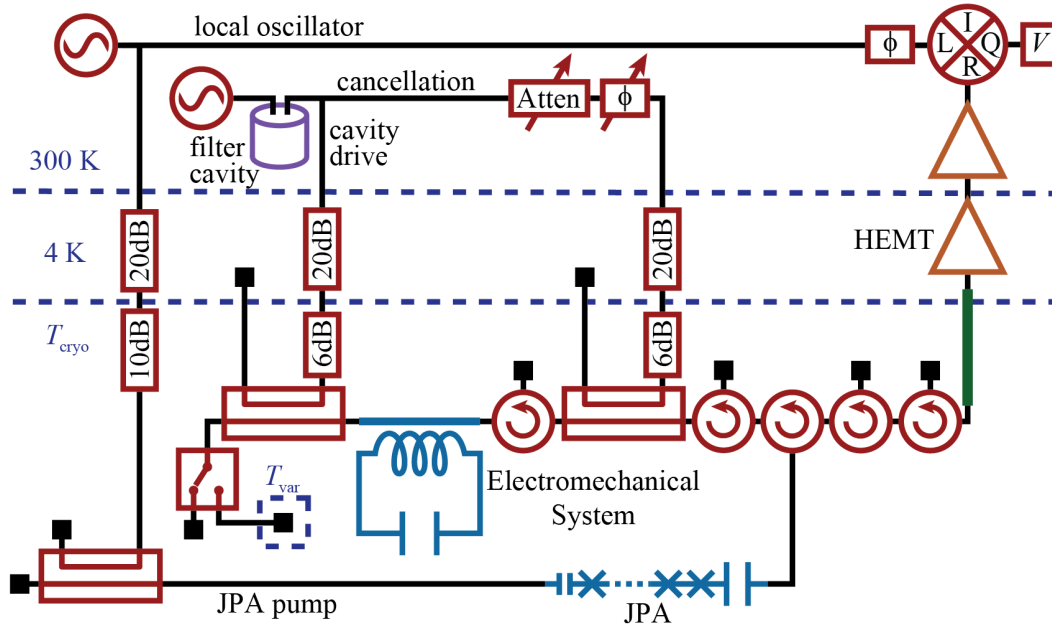
Figure 8.7: Interferometric measurement setup. Two microwave tones are each divided in two parts to form a heterodyne interferometer. The first tone is used to drive the transmission geometry electromechanical system and then cancel that drive tone prior to amplification. A filter cavity (purple) is used at the output of this generator to attenuate generator phase and amplitude noise. The second is used to pump the JPA and provide the local oscillator to the mixer. A switch is used to switch between two terminations, one at T_{cryo} and one attached to a variable temperature stage with temperature T_{var}. A superconducting coaxial cable (green) is used between temperature stages to minimize loss. Directional couplers (20 dB) are used at base temperature to minimize power being dissipated on the cold stage. Cryogenic circulators are used to define the input and output ports of the JPA and to isolate the experiment from amplifier and thermal noise at 4K.

sources (50 Ω terminations) to the input drive line. Varying the temperatures of these terminations allows Y-factor measurements of the amplifier added noises and microwave component losses (see Section 6.4). This allows us to determine that the total added noise of the amplifiers in this experiment is $n_{\mathrm{add}}^{\mathrm{amps}} \sim 0.5$. Combining this with the estimated 2.5 dB loss between the cavity and JPA gives a total added noise and interferometer quantum efficiency of $n_{\mathrm{add}} = 1.3$ and $\eta = 0.38$.

As in the experiment in Chapter 7, the introduction of a JPA into our interferometer vastly improves the quantum efficiency (and thus the signal to noise) of the measurement. The difference between a measurement with the JPA and one with only a HEMT is perhaps most apparent when the two inferred displacement spectral densities are plotted on a linear scale (Figure 8.8(a)). Using

the JPA improves the imprecision of the measurement by more than a factor of 30, reducing the integration time by a factor of 10^3 (as, from the Dicke-Radiometer formula, the uncertainty in the power P goes as $\sigma_P = P/\sqrt{B\tau}$ where B is the measurement bandwidth and τ is the integration time).

At high powers in the measurements that follow, we see a nonzero cavity noise occupancy ($n_c^{th} \sim 0.3$), which is much too large to be accounted for by the cryostat temperature (which would give $n_c^{th} = 0.04$). In an effort to determine whether this effect was caused by excess generator noise, we inserted a home-made filter cavity directly after the drive generator. We tune the filter cavity to maximize transmission at the drive frequency and suppress it by 40 dB at the optomechanical cavity frequency (see Figure 8.8(b)). The phase and amplitude noise of the generators we use are specified to be less than -150 dBc at 10 MHz detuning from the drive frequency. The filter cavity decreases this specification to sufficiently below the the microwave drive tone shot-noise level. Therefore, we are confident that the observed cavity noise is not a result of microwave generator noise. Additionally, we do not observe a difference in the cavity noise occupancy between when the cavity filter is present or removed, confirming that even without the filter cavity, generator noise is not the cause of the cavity occupancy. Moreover, the wide cavity part of the spectral density (ignoring the mechanical sidebands) should take the form

$$S_{a_{out}a_{out}}[\omega] = \kappa_l|\chi_c[\omega]|^2\kappa_0 n_0^{th} + |N_1 - \kappa_l\chi_c[\omega]|^2 n_r^{th} + |N_2 - \kappa_l\chi_c[\omega]|^2 n_l^{th} \tag{8.15}$$

where $\kappa_0 n_0^{th} = \kappa n_c^{th} - \kappa_l n_l^{th} - \kappa_r n_r^{th}$ and $\kappa_0 = \kappa - \kappa_l - \kappa_r$. The cavity occupancy we see is always a peak, not a dip, and always Lorentzian in form (despite the cavity response taking a Fano form). Thus, the cavity noise occupancy we see is best modeled as a warm thermal bath coupled to the cavity, and we set $n_r^{th} = n_l^{th} = 0$.

The optomechanical device for this experiment is described in Chapter 5 as 'Device G'. Unlike the previous experiments using wires as the mechanical oscillator, this device uses the drum-head vibrational mode of a suspended aluminum membrane. The circular membrane has diameter 15 μm and thickness 100 nm, resulting in a mass of 48 pg. The bare mechanical parameters are found
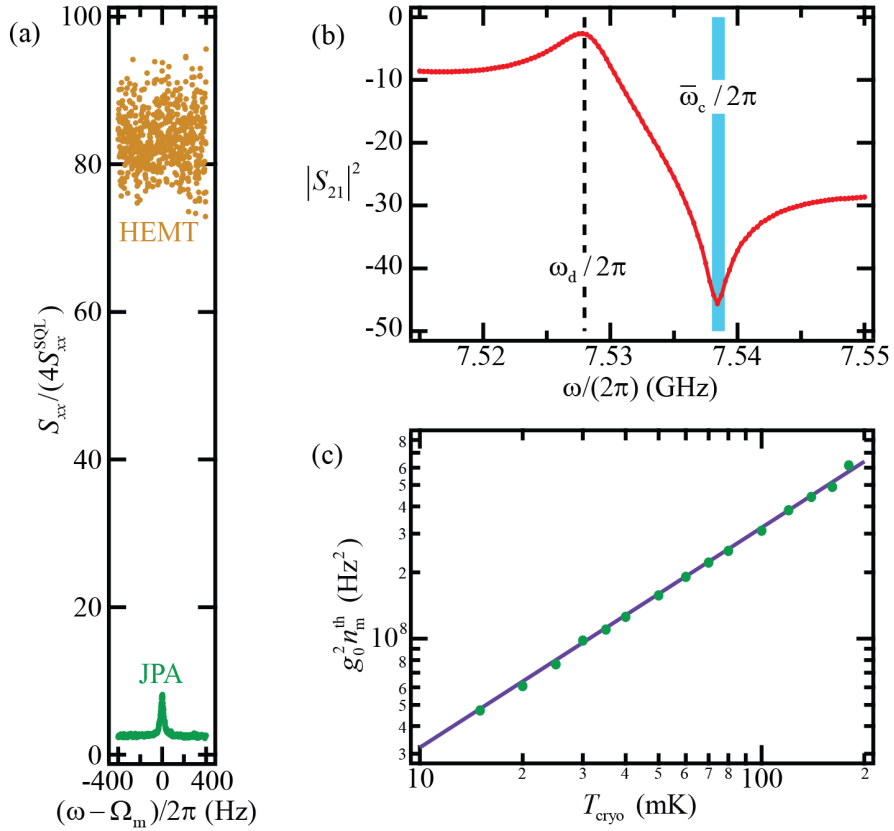
Figure 8.8: Interferometer and device calibration. (a) The interferometer quantum efficiency (and thus the measurement imprecision in number of mechanical phonons) improves by a factor of 30 when using the JPA (green) over only using the HEMT (orange). Here, the spectral density of a mechanical sideband is shown in both cases using the same drive power and integration time. (b) Filter cavity response. A resonant cavity is introduced following the microwave drive generator and tuned to be transparent at the drive frequency and attenuating at the cavity frequency (blue shaded region). The generator noise at the cavity frequency is suppressed by 40 dB, removing it as a potential cause of excess optomechanical cavity noise. (c) Optomechanical coupling calibration. The integrated voltage spectral density $S_{VV}[\omega]$ is proportional to $g_0^2 n_m^f \sim g_0^2 n_m^{th}$ through measurable proportionality constants and is plotted here as a function of cryostat temperature T_{cryo}. The slope of the linear (zero-offset) fit reveals the single-photon optomechanical coupling $g_0 = 2\pi \times 201$ Hz.

by measuring the output spectra of the device at low power and are $\Omega_m = 2\pi \times 10.56$ MHz and $\Gamma_m = 2\pi \times 32$ Hz. The factor of 10 increase of resonance frequency over the wire devices is beneficial, as the number of initial thermal phonons in the mechanical oscillator is then a factor of 10 less. The membrane is suspended 50 nm above another aluminum layer, forming a large parallel plate capacitor. This capacitor, in parallel with an inductor, leads to a bare microwave resonance

frequency, linewidth, and external coupling rate $\omega_{\text{c}} = 2\pi \times 7.54$ GHz, $\kappa = 2\pi \times 200$ kHz, and $\kappa_{\text{ext}} = 2\pi \times 133$ kHz. The resolved-sideband factor $\nu = 4\Omega_{\text{m}}^2/\kappa^2 = 1.1 \times 10^4$ puts this device far into the resolved-sideband regime, where cooling to the ground state is possible. Power is coupled in and out of the microwave resonator via a transmission geometry feed line inductively coupled to the spiral inductor.

To calibrate the optomechanical coupling, we do a temperature sweep as described in Section 6.3. The voltage spectral density is measured at several different temperatures. This measurement is done with a very weak red-detuned drive ($n_{\text{d}} \sim 3$, $\mathcal{C} \sim 0.08$), where radiation pressure effects are negligible. The voltage spectral density is converted into displacement units by also measuring the drive power at each point (as described in Section 6.2 and reviewed in the theory section above). The resulting occupancies are shown in Figure 8.8(c), where $g_0^2 n_{\text{m}}^{\text{f}} \approx g_0^2 n_{\text{m}}^{\text{th}}$ is plotted verses cryostat base temperature. At all temperatures including $T_{\text{cryo}} = 15$ mK, the mechanical oscillator is in equilibrium with the cryostat temperature, indicating that the initial mechanical occupancy at base temperature is $n_{\text{m}}^{\text{th}} \sim 30$. We fit the data to a line through zero to deduce the single photon coupling $g_0 = 2\pi \times 201$ Hz. Dividing by the zero point motion results in $G = g_0/x_{\text{zp}} = 2\pi \times 49 \pm 2$ MHz/nm.

8.2.3 Damping and cooling the mechanical oscillator to the quantum ground state

To investigate the effects of radiation pressure on the optomechanical system, we infer the cavity and mechanical states as a function of drive power while regulating the cryostat temperature at $T_{\text{cryo}} = 20$ mK. At each power, we measure the dressed response of the cavity to determine the cavity resonance frequency $\overline{\omega}_{\text{c}}$, linewidth κ, Fano parameter N_2, and (for high powers only) the optomechanical coupling g. We then measure the output spectrum near the mechanical sideband and convert it into units directly related to the optomechanical system ($S_{VV}[\omega]/(Z_0 P_{\text{d}})$ or $S_{xx}[\omega]$). This allows extraction of the total mechanical resonance frequency Ω_{tot} and linewidth Γ_{tot}, as well as the mechanical and cavity occupancies $n_{\text{m}}^{\text{imp}}$, n_{m}^{f}, and n_{c}^{th}.

Figure 8.9 shows the inferred spectral densities from our measurements. For low drive powers with $18 < n_{\text{d}} < 4.5 \times 10^3$ ($0.5 < \mathcal{C} < 113$), the spectra can be plotted in units of displacement

spectral density and fit to a simple Lorentzian (Figure 8.9(a)). Noting the logarithmic scale, we see that the imprecision of the measurement decreases with power, the mechanical linewidth increases, and the total area under the curve (shaded area) decreases. The final occupancy can easily be determined as $n_{\mathrm{m}} = S_{xx}[\Omega_{\mathrm{m}}]/(4S_{xx}^{\mathrm{SQL}})$. For larger drive powers with $4.5 \times 10^3 < n_{\mathrm{d}} < 1.8 \times 10^5$ ($113 < \mathcal{C} < 4500$), the cavity occupancy becomes important and the mechanical occupancy can no longer be simply determined from $S_{xx}[\Omega_{\mathrm{m}}]/(4S_{xx}^{\mathrm{SQL}})$. Instead, a correct inference of occupancies requires measuring the spectrum over a larger frequency range (of order κ rather than Γ_{tot}) and
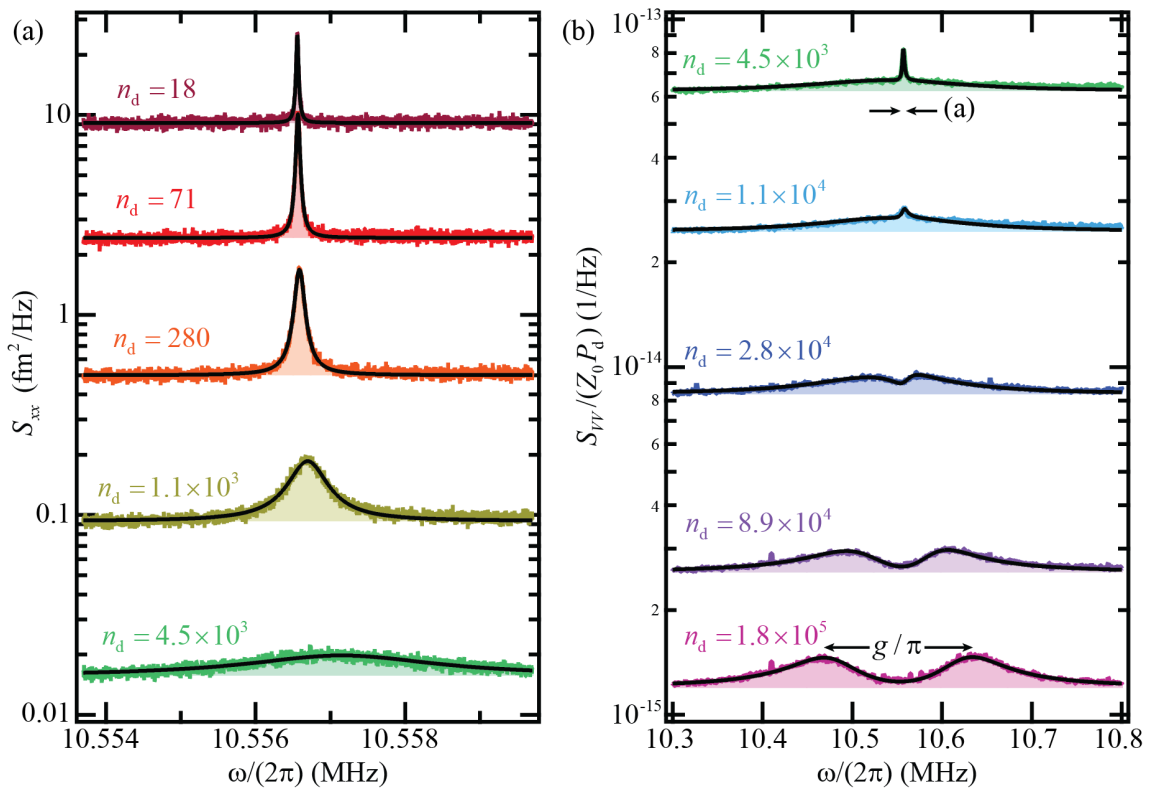
Figure 8.9: Inferred mechanical spectra in the presence of radiation pressure cooling and damping. (a) Inferred displacement spectral densities and fits for low powers. As the number of drive photons is increased, the imprecision (frequency-independent background) decreases, the mechanical damping (the Lorentzian linewidth) increases, and the mechanical temperature (shaded area under the peak) decreases. (b) Inferred spectra proportional to photon units and fits for high powers. Here, the data is shown over a larger frequency range where the nonzero cavity occupation is visible as a Lorentzian with the cavity linewidth and frequency. The lowest power data is the same as the highest power data in (a), and the frequency span of (a) is indicated for comparison. As the power is increased, the mechanical and cavity peaks interfere, eventually normal-mode splitting by g/π.

using the full expression for $S_{VV}[\omega]/(Z_0 P_{\rm r})$ to fit the data and extract $n_{\rm m}^{\rm f}$ and $n_{\rm c}^{\rm th}$. As the power is increased past $\mathcal{C} = 4g^2/(\kappa\Gamma_{\rm m}) > n_{\rm m}^{\rm th}/n_{\rm c}^{\rm th}$, the mechanical sideband destructively interferes with the cavity occupancy (this is called squashing) and eventually, for powers above $\mathcal{S} = 4g^2/\kappa^2 > 1/2$, the two harmonic oscillators undergo normal mode splitting.

The optomechanical parameters extracted from the spectra in Figure 8.9 are shown as functions of drive photon number in Figure 8.10. Figure 8.10(a) shows the imprecision in phonon units. The imprecision initially decreases as $1/n_{\rm d}$ but then saturates to $n_{\rm m}^{\rm imp} = 1.9$ as the mechanical linewidth becomes radiation-pressure dominated. Comparing to the expected value for a transmission geometry device, $n_{\rm m}^{\rm imp} = \kappa/(2\kappa_{\rm ext}\eta)$, gives a value of the quantum efficiency $\eta = 0.39$, which is consistent with the expectations from amplifier added noise and cable loss. The imprecision achieved with the JPA is critical to measuring mechanical motion with occupancies near one, as without the JPA it would be $n_{\rm m}^{\rm imp} = 70$ (a factor of $\sim 10^3$ in integration time, as mentioned previously). In displacement units, the minimum imprecision is $S_{xx}^{\rm imp} = 5.5 \times 10^{-4}$ fm^2/Hz and is not limited by cavity frequency fluctuations as in [10] and [76]. Figure 8.10(b) shows the various coupling rates as a function of drive photon number. The optomechanical coupling g increases as $\sqrt{n_{\rm d}}$ (as expected), while the total cavity linewidth κ is only weakly power-dependent. At low powers, the total mechanical linewidth $\Gamma_{\rm tot}$ is dominated by the intrinsic mechanical damping $\Gamma_{\rm m}$, while at high powers, it is dominated by radiation pressure damping $\Gamma_{\rm opt}$. The black line through this data is not a fit, but is rather calculated as $\Gamma_{\rm tot} = \Gamma_{\rm m} + 4g_0^2 n_{\rm d}/\kappa$, using the measured value of κ at each point. At the highest powers, $\Gamma_{\rm tot}$ becomes comparable to κ, and the cavity and mechanical modes hybridize into two normal modes.

Figure 8.10(c) shows the final mechanical and cavity occupancies as a function of drive photon number. At low powers, the mechanical oscillator is in equilibrium with the cryostat temperature $T_{\rm cryo} = 20$ mK, resulting in $n_{\rm m}^{\rm f} = n_{\rm m}^{\rm th} = 40$. No cavity noise photons are visible at low power within our 0.5 quanta measurement uncertainty. As the drive power is increased, the mechanical occupation decreases, at first following the weak-coupling expression for final occupancy, $n_{\rm m}^{\rm f} = \Gamma_{\rm m} n_{\rm m}^{\rm th}/\Gamma_{\rm tot}$, which decreases inversely to number of photons once the damping is radiation-
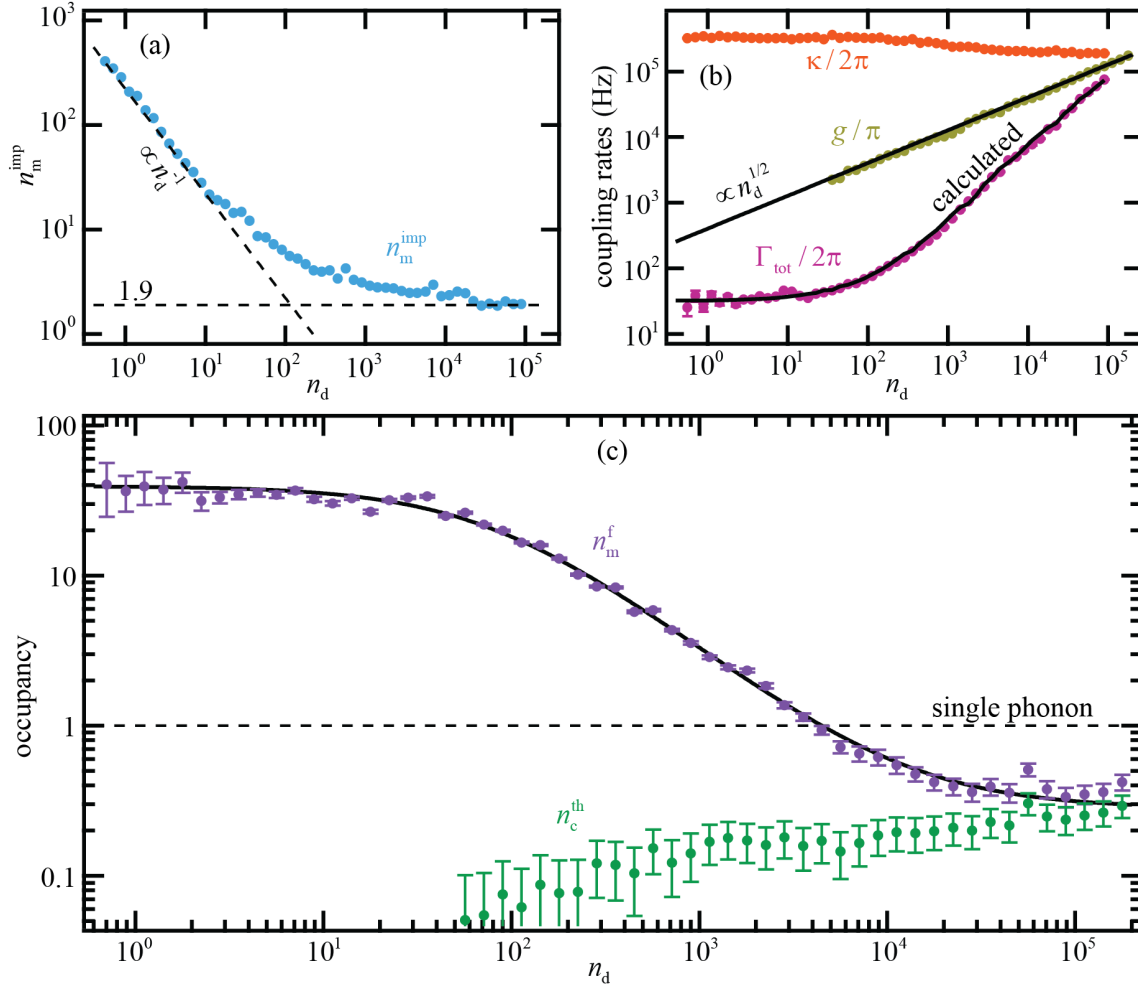
Figure 8.10: Results of radiation pressure damping and cooling as a function of drive photon number. (a) The imprecision number of photons decreases at low power but saturates at high power to 1.9 quanta, confirming the quantum efficiency of the interferometer as 39%. (b) The optomechanical coupling goes as $\sqrt{n_\mathrm{d}}$, while the cavity damping κ is relatively constant. The total mechanical linewidth follows the expected theoretical dependence (black line), given the measured values of κ, Γ_m, and g_0. (c) The radiation pressure damping in (b) is accompanied by cooling from $n_\mathrm{m}^\mathrm{f} = 40$ to 0.34 ± 0.05 phonons (shown in purple and fit with the black line), initializing the mechanical oscillator in its ground state. The cooling is ultimately limited by cavity noise photons n_c^th (shown in green).

pressure dominated. We observe the mechanical oscillator with an occupation of a single quanta at $n_\mathrm{d} \sim 4 \times 10^3$ photons ($\mathcal{C} \sim 100$). At higher powers, the onset of normal mode splitting and the presence of cavity noise photons slows the cooling rate until the final occupancy reaches its theoretical lower limit $n_\mathrm{m}^\mathrm{f} = \Gamma_\mathrm{m} n_\mathrm{m}^\mathrm{th}/\kappa + n_\mathrm{c}^\mathrm{th} \approx n_\mathrm{c}^\mathrm{th}$. We observe cooling to a final mechanical

occupancy of 0.34 ± 0.05 quanta, the first realization of ground-state radiation-pressure cooling of a macroscopic mechanical oscillator.

This experiment also achieved sensitivity near the Heisenberg limit found in Section 4.5. As derived there, the imprecision-backaction product for a red-detuned drive is

$$\sqrt{n_{\mathrm{m}}^{\mathrm{imp}} n_{\mathrm{m}}^{\mathrm{ba}}} = \sqrt{\frac{\kappa(1 + 2n_{\mathrm{c}})}{8\kappa_{\mathrm{l}}\eta}} \geq \frac{1}{\sqrt{8}} \approx 0.35. \tag{8.16}$$

Given the parameters in our experiment, we would expect this product to be approximately $\sqrt{n_{\mathrm{m}}^{\mathrm{imp}} n_{\mathrm{m}}^{\mathrm{ba}}} = 1.13$. We can measure an upper bound on this quantity by realizing that $n_{\mathrm{m}}^{\mathrm{ba}} = n_{\mathrm{m}}^{\mathrm{f}} + 1/2 - (n_{\mathrm{m}}^{\mathrm{th}} + 1/2)\Gamma_{\mathrm{m}}/\Gamma_{\mathrm{tot}} \leq n_{\mathrm{m}}^{\mathrm{f}} + 1/2$. Therefore, $\sqrt{n_{\mathrm{m}}^{\mathrm{imp}} n_{\mathrm{m}}^{\mathrm{ba}}} \leq \sqrt{n_{\mathrm{m}}^{\mathrm{imp}}(n_{\mathrm{m}}^{\mathrm{f}} + 1/2)}$. For our highest power point, we measure $n_{\mathrm{m}}^{\mathrm{f}} = 0.34$ and $n_{\mathrm{m}}^{\mathrm{imp}} = 1.9$. Substituting these numbers in reveals an upper limit on the imprecision-backaction product of $\sqrt{n_{\mathrm{m}}^{\mathrm{imp}} n_{\mathrm{m}}^{\mathrm{ba}}} \leq 1.26 = 3.57/\sqrt{8}$. This measured product is the closest experimental approach of the Heisenberg limit to date.

In this experiment, we utilized an electromechanical system capable of reaching the strong-coupling regime (which is shown in much more detail in reference [15]) to achieve ground state cooling of a macroscopic mechanical oscillator. This achievement was a long-standing goal of the field of optomechanics, as it is a critical first step toward using an optomechanical system for quantum information processing. This achievement opens the door for exciting future experiments, such as coherently storing microwave information in the mechanical oscillator, entangling photons and phonons, and coupling optical and microwave cavities via a mechanical oscillator.

Chapter 9

Experiment III: Two-drive sideband asymmetry

In Chapter 8, I described how we used the radiation pressure of microwave photons to damp and cool a macroscopic, megahertz frequency, mechanical oscillator to a phonon occupancy below a single quanta. This realization was an extremely important result, as it put the mechanical oscillator into the regime where quantum effects should be important. However, the measurement of average occupancy less than one did not by itself demonstrate that the mechanical oscillator behaved quantum mechanically. In fact, even if the system behaved completely classically down to zero temperature, it would still be possible to measure an average occupancy less than one (or energy less than some number $\hbar\Omega_{\mathrm{m}}$). Therefore, the next step is to observe something more suggestive of the quantum nature of the mechanical oscillator.

In this chapter, I present our efforts to measure the asymmetry between the upper and lower mechanical sidebands. As I found in Sections 3.1 and 3.2, the upper sideband should be proportional to the number of mechanical phonons $n_{\mathrm{m}}^{\mathrm{f}}$, while the lower sideband should be proportional to that number plus one ($n_{\mathrm{m}}^{\mathrm{f}} + 1 = n_{\mathrm{m}}^{\mathrm{f}} + 2n_{\mathrm{m}}^{\mathrm{zp}}$). This asymmetry can be understood as a consequence of the existence of the quantum mechanical ground state or as the result of commutation relations of the mechanical noise operators. It is still a semi-classical result; however, because the same effect could be created without quantum mechanics if, for example, each of the three cavity baths contributed exactly half a quantum of classical photon noise.

For this experiment, we measure the same suspended membrane device as in Chapter 8 (Device 'G' in Chapter 5). This device is far in the resolved-sideband regime, so a measurement of

the sideband asymmetry is best accomplished by using two drive tones, one approximately optimally red-detuned (at $\omega_{\mathrm{r}} \approx \overline{\omega}_{\mathrm{c}} - \Omega_{\mathrm{m}}$) and one approximately optimally blue-detuned (at $\omega_{\mathrm{b}} \approx \overline{\omega}_{\mathrm{c}} + \Omega_{\mathrm{m}}$). The drives will be situated so that the upper red and lower blue sideband frequencies are separated by many mechanical linewidths ($|\omega_{\mathrm{b}} - \omega_{\mathrm{r}} - 2\Omega_{\mathrm{m}}| \gg \Gamma_{\mathrm{tot}}$), making the occupancies of the two sidebands separately measurable. The two-drive scheme has a double benefit over a single drive in this regime - the radiation pressure control of the mechanical oscillator is maximal, while the readout of the mechanical sidebands is enhanced by their location near the cavity resonance frequency. The blue drive will have power large enough to enable readout of the lower mechanical sideband, but small enough compared to the red drive that the mechanical oscillator can still be damped and cooled to low occupancy.

In theory, this sideband asymmetry measurement should not be much more difficult than the cooling measurement in Chapter 8, as the spectral measurements should be calibrated in the same way and the theoretical form of $S_{a_{\mathrm{out}} a_{\mathrm{out}}}[\omega]$ for two drives is derived in Section 3.2. However, this experiment turns out to be much more difficult than the cooling one, as any calibration errors tend to have a differential effect on the sideband occupancies, ruining the asymmetry. In particular, determining the number of photons in the cavity from each drive has proven to be difficult to the point of prohibiting a rigorously defensible observation of the asymmetry. In this chapter, I will discuss our efforts to do this experiment and the complications encountered (and relegate the full details of the calibrations to Appendix H). I will conclude that the asymmetry is visible in our measurements, provided that we are allowed to adjust the relative photon number calibration in a reasonable, but not completely rigorous, way.

9.1   Review of two-drive measurement theory

As this is the same device and very similar measurement to that in Chapter 8.2, I will assume that there is no thermal photon measurement port occupancy: $n_{\mathrm{l}}^{\mathrm{th}} = n_{\mathrm{r}}^{\mathrm{th}} = 0$. I also specify to single-quadrature heterodyne measurement and assume the weak coupling limit, as I will not end up cooling into the strong coupling regime. However, I will not make the assumption that the

sidebands are exactly at the cavity resonance frequency or that the cavity is completely Lorentzian (as I did in Section 4.5).

Ignoring the lower red and upper blue sidebands (looking near $\omega = \bar{\omega}_c$ and thus setting $\chi_m[\omega_r - \omega] = \chi_m[\omega - \omega_b] = 0$), the dressed response, the measured spectrum in units of photons, the cavity output spectrum, and the final mechanical occupancies are

$$S_{21}[\omega] = N_2 - \frac{\kappa_l \chi_c (1 - \tilde{k}_0^* \tilde{\chi}_c^*)}{(1 - k_0[\omega]\chi_c)(1 - \tilde{k}_0^* \tilde{\chi}_c^*) - k_2 \tilde{k}_2^* \chi_c \tilde{\chi}_c^*}, \tag{9.1}$$

$$S_{II}^{\text{photon}}[|\omega_{\text{LO}} - \omega|] = \frac{1}{2\eta} + \frac{1}{2} S_{a_{\text{out}}a_{\text{out}}}[\omega], \tag{9.2}$$

$$S_{a_{\text{out}}a_{\text{out}}}[\omega] = \frac{\kappa_l |\chi_c|^2}{\left|(1 - k_0\chi_c)(1 - \tilde{k}_0^* \tilde{\chi}_c^*) - k_2 \tilde{k}_2^* \chi_c \tilde{\chi}_c^*\right|^2} \tag{9.3}$$

$$\times \left\{ \kappa n_c^{\text{th}} \left|1 - \tilde{\chi}_c^* (g_b^2 \chi_{m,r} - g_r^2 \chi_{m,b}^*)\right|^2 + g_r^2 g_b^2 \kappa (n_c^{\text{th}} + 1) |\tilde{\chi}_c^*|^2 \left|\chi_{m,r} - \chi_{m,b}^*\right|^2 \right.$$

$$+ g_b^2 \Gamma_m n_{m,b}^{\text{th}} |\chi_{m,b}|^2 \left|1 - (g_b^2 - g_r^2)\tilde{\chi}_c^* \chi_{m,r}\right|^2$$

$$\left. + g_r^2 \Gamma_m n_{m,r}^{\text{th}} |\chi_{m,r}|^2 \left|1 - (g_b^2 - g_r^2)\tilde{\chi}_c^* \chi_{m,b}^*\right|^2 \right\},$$

$$n_{m,b}^f = \frac{\Gamma_m n_{m,b}^{\text{th}} - n_c^{\text{th}} \Gamma_{\text{opt,b}} + (n_c^{\text{th}} + 1)\Gamma_{\text{opt,r}}}{\Gamma_{\text{tot}}}, \tag{9.4}$$

$$n_{m,r}^f = \frac{\Gamma_m n_{m,r}^{\text{th}} - (n_c^{\text{th}} + 1)\Gamma_{\text{opt,b}} + n_c^{\text{th}} \Gamma_{\text{opt,r}}}{\Gamma_{\text{tot}}}. \tag{9.5}$$

These expressions are written in terms of several short-hand symbols:

$$k_0 = k_0[\omega] = -g_r^2 \chi_{m,r} + g_b^2 \chi_{m,b}^*, \quad \tilde{k}_0^* = k_0^*[-\omega + \omega_r + \omega_b] = g_b^2 \chi_{m,r} - g_r^2 \chi_{m,b}^*, \tag{9.6}$$

$$k_2 \tilde{k}_2^* = k_2[\omega]k_2^*[-\omega + \omega_r + \omega_b] = -g_r^2 g_b^2 (\chi_{m,r} - \chi_{m,b}^*)^2, \tag{9.7}$$

$$\chi_{m,r} = \chi_m[\omega - \omega_r], \quad \chi_{m,b}^* = \chi_m^*[\omega_b - \omega], \quad \chi_c = \chi_c[\omega], \quad \tilde{\chi}_c^* = \chi_c^*[-\omega + \omega_r + \omega_b], \tag{9.8}$$

$$n_{m,b}^{\text{th}} = n_m^{\text{th}} + 1, \qquad n_{m,b}^f = n_m^f + 1, \qquad n_{m,r}^{\text{th}} = n_m^{\text{th}}, \qquad n_{m,r}^f = n_m^f. \tag{9.9}$$

The measured spectral density $S_{VV}[\omega]$ can be related to the spectrum in photon units $S_{II}^{\text{photon}}[\omega]$ through a parameter λ:

$$S_{VV}[\omega] = \lambda[\omega] S_{II}^{\text{photon}}[\omega], \tag{9.10}$$

$$Z_0 P_d = \frac{1}{2\pi} \int S_{V_d V_d}[\omega] d\omega = \frac{\lambda[\omega_d] P_{\text{out,d}}}{2\hbar\omega_d} = \lambda[\omega_d] \frac{n_d}{2\kappa_l} \left|\frac{N_2}{\chi_c[\omega_d]} - \kappa_l\right|^2. \tag{9.11}$$

If λ is frequency independent (as was the assumption made in all previous experiments, including cooling to the ground state), then this unit conversion can be simply made using only the measured output drive power and cavity parameters. In most experiments this is a reasonable assumption, as the HEMT amplifier gain is nearly frequency-independent over frequency ranges of order Γ_{tot} or κ. However, in this experiment the two drives are separated by 20 MHz, a frequency difference over which the HEMT gain, and thus λ, can differ by several percent[1]. Understanding the frequency dependence of λ is then critical for measuring sideband asymmetry, as ignoring the frequency dependence can have a differential effect on the sidebands. The most blatant signature of making this error is that the two inferred sideband occupancies will disagree at high occupancy (where both the quantum and classical models predict that they are equal). Measuring the full frequency dependence of λ is not an easy task, as a response measurement of the HEMT gain and output cables will necessarily be convolved with any frequency dependence of the input cables. As an easy approximation, I will therefore assume that the frequency dependence of $\lambda[\omega]$ is linear:

$$\lambda[\omega] = \frac{(\omega_{\text{r}} - \omega)\lambda[\omega_{\text{b}}] + (\omega - \omega_{\text{b}})\lambda[\omega_{\text{r}}]}{\omega_{\text{r}} - \omega_{\text{b}}}. \tag{9.13}$$

Given this assumption and knowledge of the values of $\lambda[\omega_{\text{r}}]$ and $\lambda[\omega_{\text{b}}]$, any measured voltage spectrum can then be put into photon units and fit to the theoretical expressions reviewed above.

9.2   Calibration of the two-drive experiment

In this section, I will discuss the calibration of the frequency-dependent parameter $\lambda[\omega]$ at ω_{r} or ω_{b}. Knowing one of these values is the same as knowing the number of photons in the cavity due the red or blue drive, as these quantities are related only by measurable cavity and drive parameters. As $\lambda[\omega]$ contains information about the amplifier gains, which can change over time,

---

[1] This frequency dependence would also have been present for the cooling experiment of Section 8.2. Ignoring the frequency dependence of λ leads to inferred quantities that are slightly different than the true values:

$$\frac{\eta}{\eta_{\text{true}}} = \frac{\lambda[\omega_c]}{\lambda[\omega_{\text{r}}]}, \quad \frac{g_0^2}{g_{0,\text{true}}^2} = \frac{\lambda[\omega_{\text{r}}]}{\lambda[\omega_c]}, \quad \frac{n_c^{\text{th}}}{n_{c,\text{true}}^{\text{th}}} = \frac{\lambda[\omega_{\text{r}}]}{\lambda[\omega_c]}, \quad n_{\text{m}}^{\text{f}} \approx n_{\text{m,true}}^{\text{f}} + 2(n_c^{\text{th}} - n_{c,\text{true}}^{\text{th}}). \tag{9.12}$$

However, these differences are not large enough to affect the main result of the cooling experiment - namely cooling to a mechanical occupancy of less than one quanta.

the assumption that it is constant from day to day is probably not a good one; however, it does seem to be constant over measurement sweeps taken on timescales of hours. I therefore re-calibrate $\lambda[\omega]$ for each separate sweep of temperature or power.

9.2.1   Calibration of red-drive voltage to photon unit conversion

The number of red-drive photons in the cavity (or $g_{\mathrm{r}} = g_0\sqrt{n_{\mathrm{r}}}$) is fairly straightforward to extract (in the same way as was done for the cooling experiment in Section 8.2) from the dressed cavity response measured with a high-power, red-detuned drive and the blue drive off. This calibration is discussed with some example data in Appendix H.1 and proves to be a straightforward way to determine g_{r} and $\lambda[\omega_{\mathrm{r}}]$. Assuming that ω_{r} is held fixed and that $\lambda[\omega_{\mathrm{r}}]$ has not changed since the calibration, this value (as well as the bare cavity parameters) allows us to go back and forth between the measured output power and the number of photons due to the red drive, regardless of the red and blue drive powers.

9.2.2   Calibration of blue-drive voltage to photon unit conversion

The number of blue-drive photons in the cavity proves to be much more difficult to determine than the number of red-drive photons. The different approaches we have attempted are detailed in Appendix H.2. We conclude there that the two-drive dressed response is not a reliable method of calibration, as the resulting data does not always match the predicted form from my model, is not always described by parameters consistent with those extracted from spectral data, and even in the best cases reveals more scattered values for the number of blue-drive photons than other methods. We also conclude that using the onset of mechanical parametric oscillation as an indication of equal red and blue photon numbers is neither adequately repeatable nor accurate. The most consistent method found for determining the number of blue-drive photons in the cavity is to measure the spectral sidebands of the mechanical oscillator at high-occupancy (when the net radiation pressure effects are small). In this case, we expect that the occupancies of the upper red and lower blue sidebands are approximately equal ($n_{\mathrm{m,r}}^{\mathrm{f}} = n_{\mathrm{m,b}}^{\mathrm{f}} = n_{\mathrm{m}}^{\mathrm{f}}$) and that the thermal cavity occupancy

affects them negligibly. Thus, even without calibrating the spectral data into optomechanical units, a measurement of the relative sideband amplitudes reveals $g_\mathrm{r}^2/g_\mathrm{b}^2$ (and thus combined with the red-drive calibration reveals g_b or $\lambda[\omega_\mathrm{b}]$). Unfortunately, the better measurements of asymmetry (two of which are presented later in this chapter) were all calibrated using the parametric oscillation method and must be adjusted to achieve reasonable results (this is discussed more in Appendix H and when these results are presented).

9.3   Interferometric setup and device

The interferometric setup (Figure 9.1) for this experiment is nearly identical to that of the ground state cooling experiment, except that there are now two input drives. The JPA pump is located about 600 kHz above the cavity frequency. As the interferometric setup at low temperatures has not changed from the ground state cooling experiment, the quantum efficiency is approximately $\eta = 0.38$, and we assume that $n_\mathrm{l}^\mathrm{th} = n_\mathrm{r}^\mathrm{th} = 0$, even without the filter cavity.

The optomechanical device for this experiment is also the same one as for the ground state cooling experiment (Device 'G' in Chapter 5). However, the device was thermally cycled between experiments, so some of the optomechanical parameters have slightly different values. The bare mechanical resonance frequency is $\Omega_\mathrm{m} = 2\pi \times 10.472$ MHz, the cavity resonance frequency is $\omega_\mathrm{c} = 2\pi \times 7.5887$ GHz, and the power dependent damping of the cavity is $2\pi \times 200$ kHz $< \kappa < 2\pi \times 500$ kHz.

To calibrate the optomechanical coupling, we again do a temperature sweep as described in Section 6.3. This sweep is done with both a red and a blue-detuned drive, but at low enough powers where radiation pressure effects should be small ($n_\mathrm{r} \approx n_\mathrm{b} \approx 17$, $\mathcal{C}_\mathrm{r} \approx \mathcal{C}_\mathrm{b} \approx 0.13$). The voltage spectral density of both the upper red and lower blue sidebands are measured four times at each of several different temperatures. The calibrated values of $\lambda[\omega_\mathrm{r}]$ and $\lambda[\omega_\mathrm{b}]$ for the temperature sweep (included in the calibration summary Figure H.6) are used to convert the measured voltage spectral density into displacement units. The resulting occupancies are shown in Figure 9.2, where $g_0^2 n_\mathrm{m}^\mathrm{f} \approx g_0^2 n_\mathrm{m}^\mathrm{th}$ is plotted verses cryostat base temperature for each sideband. The frequencies of the
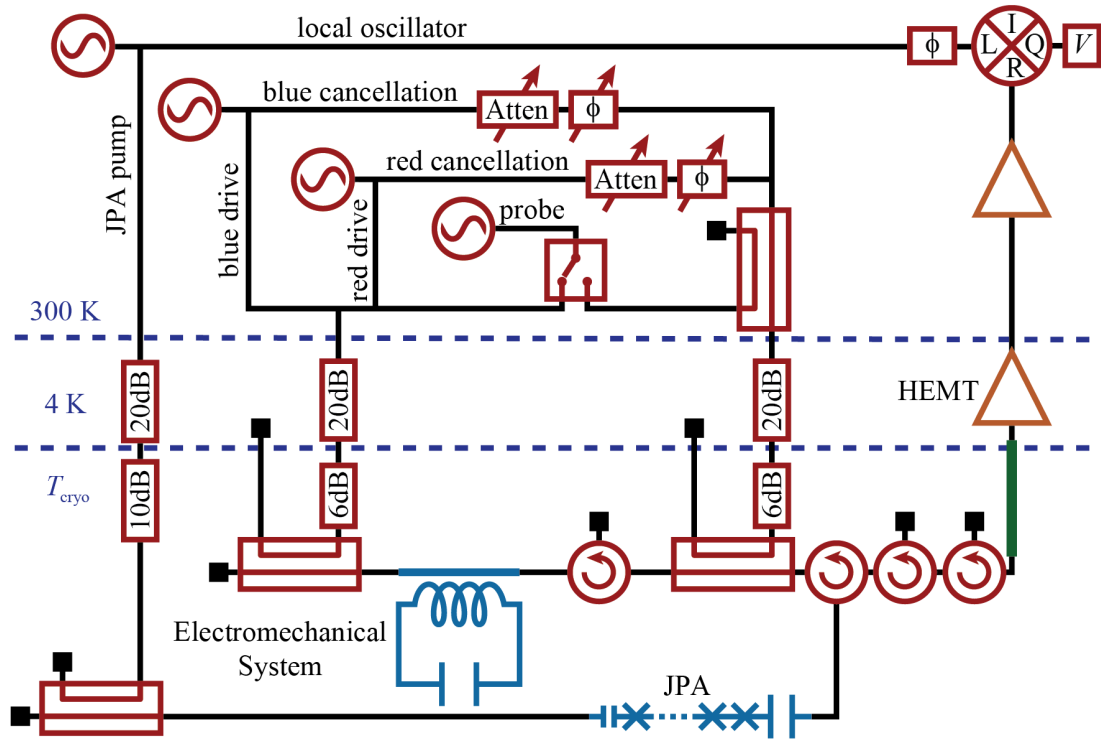
Figure 9.1: Interferometric measurement setup. We realize a heterodyne interferometer that measures only a single microwave quadrature in the same way as for the ground state cooling experiment in the previous chapter. However, now there are two input drives and two cancellations, one red detuned from the cavity resonance frequency and one blue detuned. A probe tone can be introduced into either the input line (for dressed response measurements of the cavity) or the cancellation line (for measurements of the JPA response and gain).

sidebands are shown relative to the cavity lineshape in the upper left of the figure. In the main figure, we see that the number of phonons is linear with cryostat temperature down to about 25 mK. Fitting the upper red sideband points (red triangles) to a line through zero and using equipartition results in a single-photon optomechanical coupling $g_0 = 2\pi \times 188.8$ Hz (red dashed line). Fitting only the lower blue sideband points (blue circles) results in $g_0 = 2\pi \times 185.7$ Hz (dashed blue line). The fact that these values are very close to each other indicates a very good calibration of the λ's. From now on, I use the average coupling value $g_0 = 2\pi \times 187.25$ Hz (shown as a black solid line).
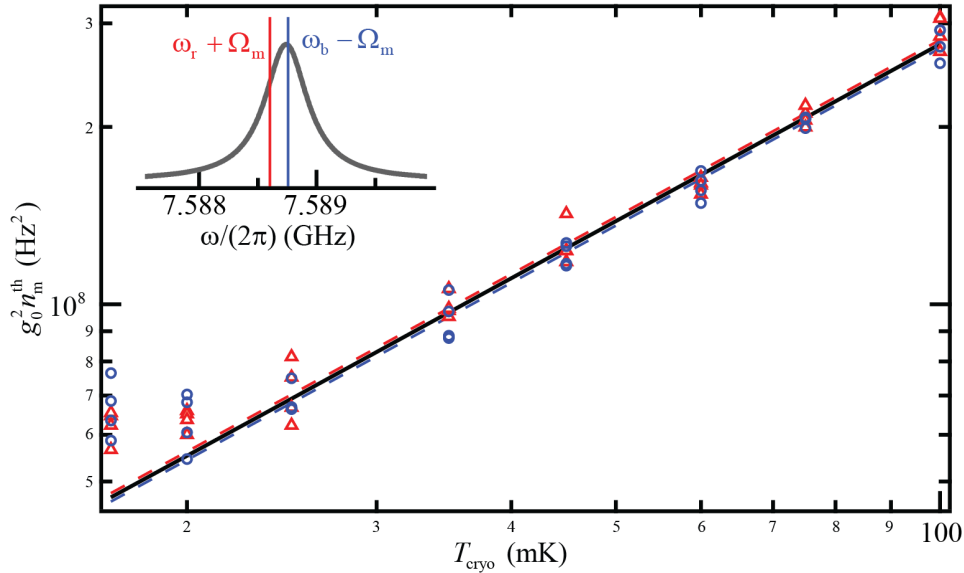
Figure 9.2: Optomechanical coupling calibration. The integrated voltage spectral density $S_{VV}[\omega]$ can be converted to $g_0^2 n_{\mathrm{m}}^{\mathrm{f}} \approx g_0^2 n_{\mathrm{m}}^{\mathrm{th}}$ using measurable proportionality constants. This quantity is plotted here as a function of cryostat temperature T_{cryo} for the upper red sideband (red triangles) and lower blue sideband (blue circles). The average slope of the linear (zero-offset) fits reveals the single-photon optomechanical coupling $g_0 = 2\pi \times 187.25$ Hz.

9.4 Measurements of sideband asymmetry

In this section I present two representative measurements of sideband asymmetry, labeled as data sets 11 and 14 to be consistent with the numbering in Appendix H. For each data set, the blue drive generator strength is kept constant while the red drive generator power is increased in steps of 1 dB, damping and cooling the mechanical oscillator to lower occupancy. The blue generator drive power is 3 dBm for both data sets, resulting in similar blue photon numbers of order $n_{\mathrm{b}} \sim 500$ ($\mathcal{C} \sim 5$). The number of red photons ranges from $n_{\mathrm{r}} \sim 500$ to $n_{\mathrm{r}} \sim 10^4$ ($5 < \mathcal{C} < 200$) within each data set. The insets of Figure 9.3 show the cavity lineshapes for the lowest (solid line) and highest (dashed line) red drive powers as well as the upper red and lower blue sideband frequencies. The main difference between these two data sets is that data set 11 has sidebands that are detuned by about $\kappa/3$ above the cavity, while data set 14 has sidebands nearly resonant with the cavity.

The conversion parameter $\lambda[\omega]$ is calibrated for each data set (as explained earlier in this

chapter and in Appendix H) and used (along with measured bare cavity parameters and output drive powers) to convert a raw voltage spectral density into photon units. The data is then fit according to the theory reviewed at the beginning of this chapter to extract the inferred final and imprecision occupancies for each sideband and the thermal cavity occupancy. These occupancies are plotted for each data set as a function of the red drive photon number in Figures 9.3(a,b). As expected, the final number of mechanical phonons extracted from each sideband decreases with red power. The cavity occupancy does not behave the same way that it did in the ground state cooling experiment. In that experiment, the cavity occupancy was negligible at low power and increased with red drive photons. Here, it seems to be surprisingly large when the two drives are similar in power and decreases with number of red photons, remaining small compared to the final occupancy of the
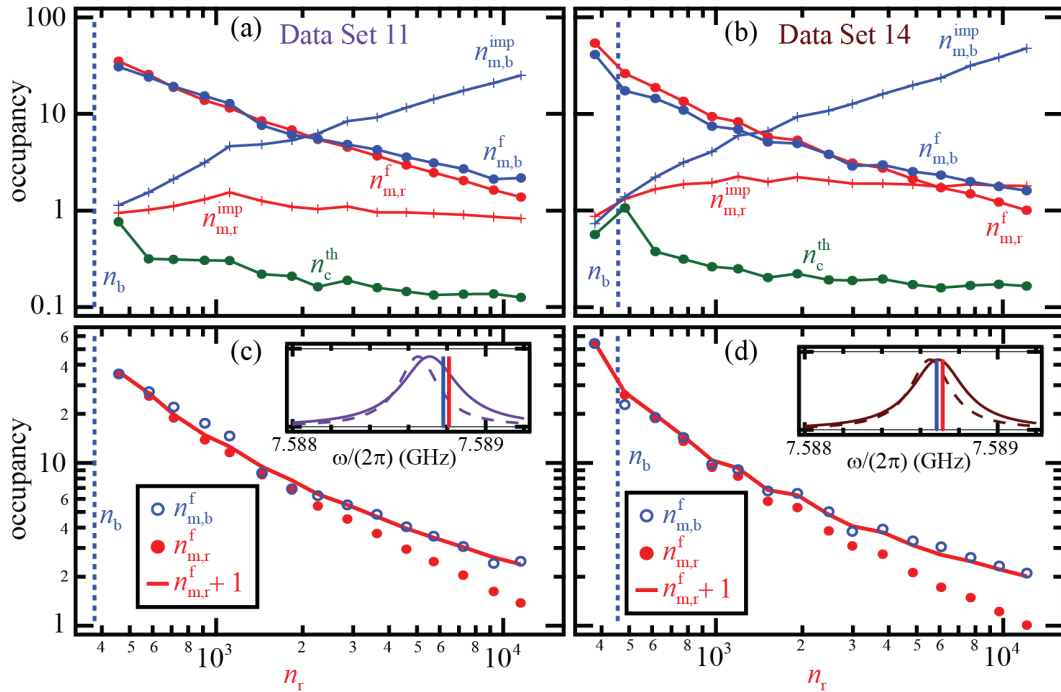
Figure 9.3: Measured sideband asymmetry as a function of red-drive photon number for data set 11 (a,c) and data set 14 (b,d). The cavity response and sideband frequencies for each data set are shown as insets. (a,b) Inferred final mechanical occupancies, imprecision, and thermal cavity occupancy as a function of number of red-drive photon number. (c,d) Comparison of upper red and lower blue final sideband occupancies. The lower blue occupancy is scales such that the red and blue occupancies are equal for the lowest power. The red line is the red data plus one.

mechanical oscillator even at the highest red powers. In Chapter 4, I found that the imprecision for the lower red sideband should be $n_{m,r}^{imp} = \kappa(1 + \mathcal{C}_r - \mathcal{C}_b)/(2\kappa_{ext}\mathcal{C}_r\eta)$ and limit to $\kappa/(2\kappa_{ext}\eta)$ at high red power. The blue lower sideband imprecision should be $n_{m,r}^{imp} = \kappa(1 + \mathcal{C}_r - \mathcal{C}_b)/(2\kappa_{ext}\mathcal{C}_b\eta)$, which increases as $\kappa n_r/(2\kappa_{ext}n_b\eta) \propto n_r$ at high red power. The measured imprecisions agree well with these expectations. The blue sideband imprecision at high red power is much larger than the final mechanical occupancy of that sideband. Further loss of signal-to-noise prevents us from measuring the blue sideband occupancy for larger red drive powers.

Figures 9.3(c,d) show the same results as Figures (a,b), but include only the final mechanical occupancies from each sideband, the true quantities of interest for this experiment. As discussed in Appendix H, I sadly do not trust the relative calibration of $\lambda[\omega_b]/\lambda[\omega_r]$ for either of these data sets, as the values for both sets were extracted using the parametric oscillation calibration method. I therefore make the best approximation to a valid high-occupancy calibration by scaling all of the final blue occupancies by a common factor (one for each data set) such that the highest occupancy points agree. This means of calibration is not particularly rigorous, as it uses the data set to calibrate itself. However, it is a reasonable thing to do if we want to understand what asymmetry we might see if we had an accurate calibration. The inferred final mechanical occupancies are plotted as points and a red line equal to the red data plus 1 has been added as a guide for the eye. We observe that the sideband asymmetry is visible and agrees well with our expectations.

In conclusion, we have observed a preliminary asymmetry of one between the occupancies of the upper red and lower blue sidebands using a two-drive scheme, but a rigorous quantitative determination of this asymmetry is highly dependent on careful, independent calibration of the y-axis, which we have not achieved. It could be possible, by combining the high-occupancy spectral calibration method with an asymmetry sweep using one of the above input drive configurations, to make a definitive claim of asymmetry. However, the fact that this device is highly power dependent, is not described by my theoretical model in the presence of two drives, and requires sensitive calibration of frequency dependent gains makes continuing to pursue this measurement more an exercise in calibration rather than an exploration of new and interesting physics. It might

instead be a wiser choice look for asymmetry with a different device in the un-resolved sideband regime.

Chapter 10

Experiment IV: Quantum backaction and backaction evasion

In this brief chapter, I discuss an interesting experiment that initially seemed possible with our suspended membrane device, but exhibited a very surprising limitation in the form of parametric oscillation. I will show only our very preliminary attempts to observe quantum backaction and backaction evasion and describe a likely explanation for the extremely low power limitation on backaction evasion due to mechanical parametric oscillation.

As the measurement of a mechanical oscillator becomes more and more sensitive, quantum mechanics dictates that this measurement necessarily imparts a backaction force onto the mechanical motion. This basic premise of quantum measurement is discussed more fully in the introduction of this dissertation, so I will just give a brief explanation here. The necessity that a strong measurement be accompanied by a backaction force comes about because the position and momentum of the oscillator are non-commuting observables. The Heisenberg uncertainty principle then requires that a measurement of the position with uncertainty $\Delta x_{\mathrm{m,meas}}$ be accompanied by a random perturbation of the momentum $\Delta p_{\mathrm{m,perturb}}$ large enough to satisfy $\Delta x_{\mathrm{m,meas}} \Delta p_{\mathrm{m,perturb}} \geq \hbar/2$. As the position and momentum are not constants of motion, this uncertainty in momentum evolves into an uncertainty in position a quarter of an oscillation later, leading to an uncertainty relation between measurement uncertainty and perturbation of the total mechanical motion. This can be expressed as $n_{\mathrm{m}}^{\mathrm{imp}} n_{\mathrm{m}}^{\mathrm{ba}} \geq 1/16$.

The addition of random backaction motion $n_{\mathrm{m}}^{\mathrm{ba}}$ due to a strong measurement was seen mathematically in the equations for the final mechanical occupancy in the absence of large radiation
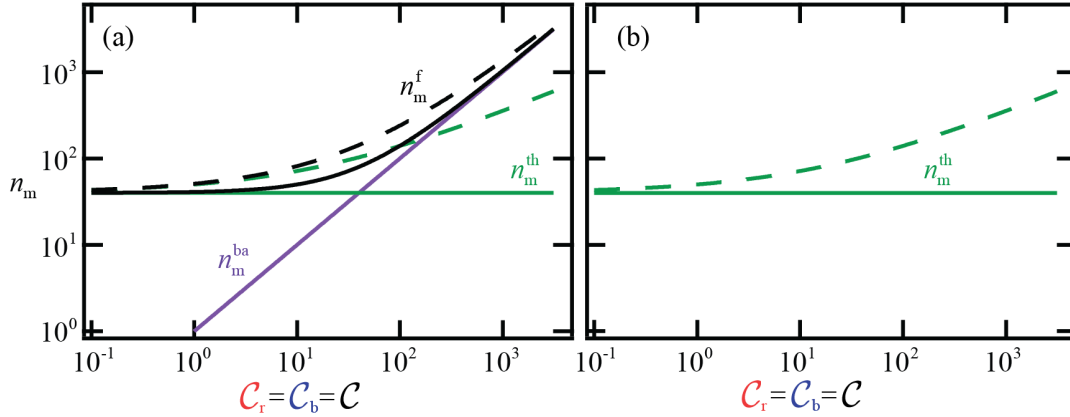
Figure 10.1: Mechanical occupancy contributions near the point where backaction motion becomes dominant. (a) Thermal (green), backaction (purple), and final (black) mechanical occupancies in the case where the sidebands are not overlapping. The case of ideal power-independent mechanical bath occupancy is shown as solid lines, and the case where the bath temperature rises with power is shown with dashed lines. (b) Contributions to the mechanical occupancy for a backaction-evading (overlapping sidebands) scheme. No backaction motion is visible, so the thermal contribution is measured directly.

pressure effects (with a single, on-resonance cavity drive or with two, equal-amplitude, red and blue-detuned drives). In this chapter, I focus on the two drive case, as it is the optimal scheme for observing quantum backaction with our far-resolved-sideband-regime device. Assuming the two drives have equal cooperativity $\mathcal{C}_r = \mathcal{C}_b = \mathcal{C} = 4g^2/(\kappa\Gamma_m)$, the final mechanical occupancy is $n_m^f = n_m^{th} + n_m^{ba} = n_m^{th} + \mathcal{C}(2n_c^{th} + 1)$.

The quantum backaction is real mechanical motion (as opposed to the apparent motion that we call imprecision) and is thus filtered by the mechanical response, making it hard to distinguish from the thermal motion of the oscillator. Figure 10.1(a) shows the thermal (green), backaction (purple), and final (black) mechanical occupancies for the two-drive scheme as a function of cooperativity. In order to observe the quantum backaction, the measurement strength must be strong enough for the backaction contribution to dominate the thermal contribution, causing an $n_m^f \propto \mathcal{C}$ dependence. Assuming $n_c \ll 1$, this requires cooperativity $\mathcal{C} > n_m^{th}$. Our device can accommodate drive photon numbers up to $n_d \approx 10^5$ (as in [48]), enabling $\mathcal{C} \approx 2 \times 10^3$. The thermal occupancy is only $n_m^{th} \approx 40$, so the quantum backaction seems like a reasonable effect to observe.

One complication to the above picture is that the mechanical oscillator thermal bath often heats up at large drive powers. This classical backaction that we observe is sub-linear in cooperativity (for example, as shown as dashed lines in Figure 10.1(a)), so the $n_m^f \propto \mathcal{C}$ dependence of the quantum backaction should still be observable at high enough cooperativity. However, its presence may increase the cooperativity requirement for observing quantum backaction and may make the transition between thermal and backaction dominated motion less stark.

A more definitive way to distinguish the classical from quantum backactions is to compare a measurement of quantum backaction to a backaction evasion measurement. In Section 3.2, I considered the output spectrum when the two drives were of equal strength ($g_r = g_b = g$) and the sidebands were overlapped. In this case, I found that the output spectrum was proportional to n_m^{th}, not n_m^f! Thus, despite backaction still being present on the oscillator, no sign of that backaction is present in the measurement. This effect arises because the overlapping-sidebands scheme measures only one quadrature of the mechanical motion, $\hat{X}_1 = \hat{x}\cos[\Omega_m t] - \hat{p}\sin[\Omega_m t]$. Because this quadrature and the orthogonal quadrature $\hat{X}_2 = \hat{x}\sin[\Omega_m t] + \hat{p}\cos[\Omega_m t]$ do not commute ($[\hat{X}_1, \hat{X}_2] = [\hat{x}, \hat{p}] = j\hbar$), a measurement of $\hat{X}_1$ is accompanied by the necessary backaction force on $\hat{X}_2$. However, unlike $\hat{x}$ and $\hat{p}$, in the resolved sideband limit the quadratures $\hat{X}_1$ and $\hat{X}_2$ are constants of motion, meaning that they do not evolve into each other. Thus, a continuous measurement of $\hat{X}_1$ can be made without contributing extra backaction motion to that quadrature. The mechanical occupancy contributions measured with a backaction evasion scheme are shown in Figure 10.1(b). No backaction motion is measurable, so the thermal motion (including any classical backaction heating) is easily determined. Thus, by comparing two measurements, one with the sidebands separated and one with them overlapping, a clear signature of quantum backaction should be visible.

Figure 10.2 shows some preliminary measurements we made in attempt to show that comparing results using a non-overlapping-sidebands scheme and a backaction evasion scheme would be feasible. In each part of the figure, the number of drive photons is fixed and the drive tone detunings are changed, going from well resolved sidebands (purple), to nearly overlapping sidebands
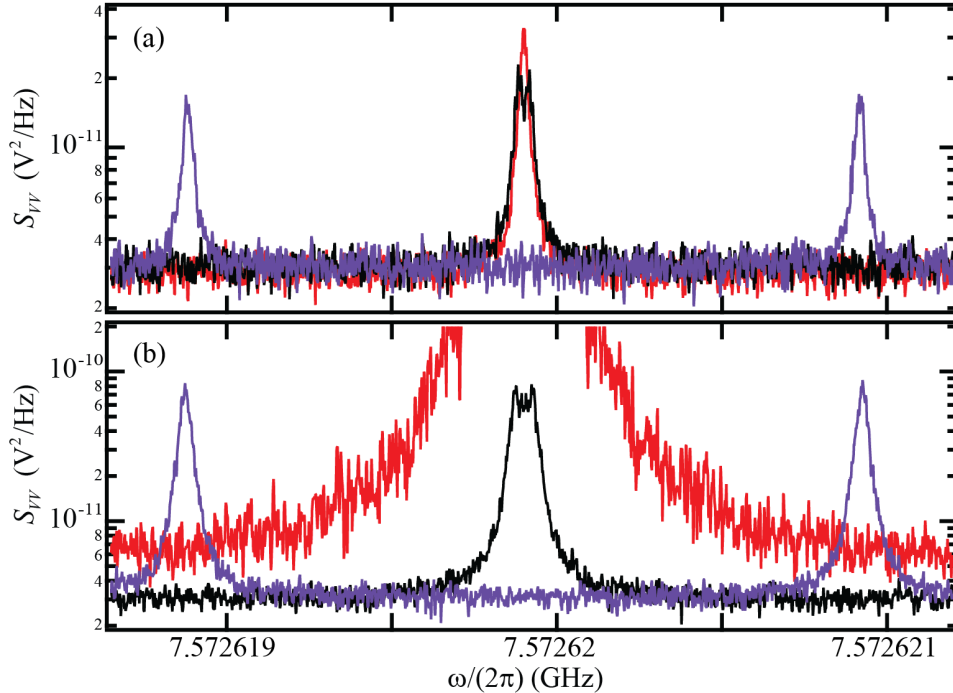
Figure 10.2: Parametric instability in the backaction evasion scheme. Each figure shows resolved sidebands (purple), slightly overlapped sidebands (black), and fully overlapped sidebands (red). (a) For $\mathcal{C} \approx 0.6$, the sidebands remain stable when overlapped. (b) For $\mathcal{C} \approx 2.3$, overlapping the sidebands causes parametric amplification of the mechanical motion.

(black), to completely overlapping sidebands (red). In Figure 10.2(a), the number of photons is $n_\mathrm{r} = n_\mathrm{b} \approx 28$ ($\mathcal{C} \approx 0.6$). The overlapped sidebands appear to be about twice the height of the resolved sidebands, as expected. Conversely, in Figure 10.2(a), where $n_\mathrm{r} = n_\mathrm{b} \approx 115$ ($\mathcal{C} \approx 2.3$), the sidebands seem well-behaved even as they are slightly overlapped, but the mechanical oscillator becomes unstable as the sidebands are fully overlapped.

Parametric instabilities during backaction-evasion are not particularly surprising. A parametric instability can arise any time the mechanical spring constant (and thus resonance frequency) is modulated at $2\Omega_\mathrm{m}$ and the strength of the modulation of Ω_m is larger than the mechanical damping. The total number of drive photons in the cavity (averaged over a cavity oscillation) due to

two equal-strength drives separated by exactly $2\Omega_m$ is

$$n_d[t] = \frac{CV[t]^2}{\hbar\omega_c} = \frac{C(V_0\cos[(\overline{\omega}_c+\Omega_m)t]+V_0\cos[(\overline{\omega}_c-\Omega_m)t])^2}{\hbar\omega_c} \tag{10.1}$$

$$= \frac{4CV_0^2}{\hbar\omega_c}\cos[\Omega_m t]^2\cos[\omega_c t]^2 = n_d\left(1+\cos[2\Omega_m t]\right), \tag{10.2}$$

where $V[t]$ is the voltage across the circuit capacitance C, and n_d without an argument is the usual time averaged number of drive photons. Thus, if the mechanical spring constant is dependent on number of photons in any way, it will be modulated at $2\Omega_m$, and a parametric instability can arise.

In fact, we had expected to see such an instability due to the second-order optomechanical coupling $\lambda = d^2\omega_c/dx^2$ (as observed in [105]). Including the second-order optomechanical coupling, the displacement-dependent part of the system energy is

$$E[x] = \frac{1}{2}k_s x^2 + \frac{1}{2}\left(C+\frac{dC}{dx}x+\frac{1}{2}\frac{d^2C}{dx^2}x^2\right)V[t]^2. \tag{10.3}$$

The effective mechanical spring constant (the coefficient of the x^2 term) is then

$$k_{s,\text{eff}} = k_s + \frac{1}{2}\frac{d^2C}{dx^2}V[t]^2 = k_s + \frac{\hbar\omega_c}{2C}\frac{d^2C}{dx^2}n_d(1+\cos[2\Omega_m t]), \tag{10.4}$$

which is modulated at $2\Omega_m$ with amplitude equal to the time-averaged static correction to k_s. This modulation will create parametric oscillation of the mechanical oscillator if the static resonance frequency correction (and therefore the modulation) is larger than Γ_m. The time-averaged mechanical resonance frequency (to first order) is

$$\Omega_{m,\text{eff}} = \sqrt{\frac{k_{s,\text{eff}}}{m}} \approx \Omega_m\left(1+\frac{k_{s,\text{eff}}-k_s}{2k_s}\right) = \Omega_m + \frac{\hbar\omega_c n_d}{4m\Omega_m C}\frac{d^2C}{dx^2} = \Omega_m + \Gamma_m\mathcal{C}\frac{\kappa}{\omega_c}\left(\frac{3}{4}-\frac{\omega_c\lambda}{4G^2}\right) \tag{10.5}$$

For a suspended membrane device, $\lambda/G^2 = -1/\omega_c$, the resonant frequency change is $\Gamma_m\mathcal{C}\kappa/\omega_c$, and the cooperativity required for instability is $\mathcal{C} \geq \omega_c/\kappa$. For our device, this instability should occur at $\mathcal{C} \approx 4\times 10^4$, far above the $\mathcal{C} \approx 2$ where we observe parametric oscillation.

The cause of the parametric oscillation we do observe is likely an effect that was investigated in detail in reference [16]. They observed an instability due to microwave power dissipated on the device heating the mechanical oscillator and changing its resonance frequency (and thus its spring

constant):

$$\Omega_{\mathrm{m,eff}} = \Omega_{\mathrm{m}} + \frac{d\Omega_{\mathrm{m}}}{dT_{\mathrm{m}}}\frac{dT_{\mathrm{m}}}{dP_{\mathrm{diss}}}\frac{dP_{\mathrm{diss}}}{dn_{\mathrm{d}}}n_{\mathrm{d}}[t], \tag{10.6}$$

$$k_{\mathrm{s,eff}} \approx k_{\mathrm{s}} + 2m\Omega_{\mathrm{m}}\frac{d\Omega_{\mathrm{m}}}{dT_{\mathrm{m}}}\frac{dT_{\mathrm{m}}}{dP_{\mathrm{diss}}}\frac{dP_{\mathrm{diss}}}{dn_{\mathrm{d}}}n_{\mathrm{d}}(1 + \cos[2\Omega_{\mathrm{m}}t]). \tag{10.7}$$

Here, T_{m} is the mechanical bath temperature and P_{diss} is the power dissipated at the device. We have not investigated this model in any detail to determine if the onset of our observed instability quantitatively matches this model; however, we do generally see heating of the mechanical oscillator with drive power and changes in mechanical resonance frequency with temperature. Additionally, the onset of instability observed in reference [16] occurred at $\mathcal{C} = 2.8$, a similar onset cooperativity to that of our observation. Therefore, this effect seems like a good candidate for explaining our observed parametric oscillation.

Chapter 11

Experiment V: State transfer between coherent itinerant microwave fields and a mechanical oscillator

The past several experimental chapters have detailed our efforts in pushing both measurement of mechanical motion and that mechanical motion itself into the quantum regime. These achievements were longstanding goals of the field, as they are critical prerequisites toward using optomechanical systems as tools in quantum information applications. Mechanical elements have exciting potential for quantum information, as their lifetimes can be very long, enabling storage of information. Additionally, mechanical oscillators can couple to many different kinds of systems, enabling transfer of quantum states between systems at vastly different frequencies. In particular, a mechanical oscillator could be used to couple a microwave and optical cavity, joining the quantum state preparation and manipulation strengths of superconducting circuit experiments with the quantum state storage and transmission strengths of the optical world.

The experiment described in this chapter [66] reveals our efforts to temporally control our optomechanical system, with the goal of transferring a microwave state into the mechanical oscillator, storing it there, and then retrieving it at a later time, a sequence that I analyzed the efficiency of in Chapter 3.3. We achieve coherent state transfer between itinerant microwave fields and the mechanical oscillator, even for itinerant fields with amplitudes of a single quanta. This transfer occurs on timescales far shorter than the quantum state lifetime of the mechanical oscillator, indicating the possibility of using this state transfer in the future to couple together different quantum systems or perform more complicated protocols.

In this experiment, we control the microwave fields incident on the cavity by applying a weak preparation field at the cavity resonance frequency. We also control the optomechanical coupling in time by turning on and off a much stronger, optimally red-detuned, transfer field. Most of this experiment is done with a weak-coupling limit transfer field $(2g_\mathrm{T} \ll \kappa)$. In this case, itinerant microwave fields leak into and out of the cavity fast enough that the state is never fully contained in the cavity and the transfer is essentially between itinerant microwaves and the mechanical oscillator. At the end of the chapter, I will show one measurement with a strong-coupling limit transfer field $(2g_\mathrm{T} \gg \kappa)$ that enables transfer of states directly between the cavity and mechanical oscillator; however, having the state occupy the cavity for any length of time is undesirable due to the relatively large coupling of the cavity to external and internal ports. Therefore, the best transfer is achieved in the weak-coupling regime $(2g_\mathrm{T} \ll \kappa)$.

The sequence of transfer and preparation fields for this experiment is illustrated in Figure 11.1. An initial preparation pulse is transfered into the mechanical oscillator by applying a constant transfer field. The transfer field is turned off at time t_a, isolating the mechanical oscillator and state of interest from the cavity. The transfer field is turned back on after a delay time t_b, transferring the
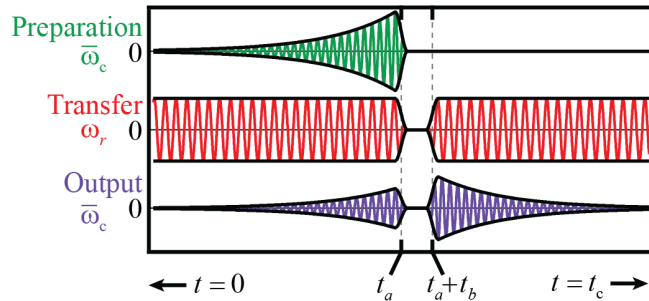

Figure 11.1: Sequence of fields for preparation, storage, and retrieval of an itinerant state. $0 < t < t_\mathrm{a}$: The microwave field at $\overline{\omega}_\mathrm{c}$ is prepared as a rising exponential to be optimally transferred into the mechanical oscillator by a constant transfer field at $\omega_\mathrm{r} = \overline{\omega}_\mathrm{c} - \Omega_\mathrm{m}$. Any microwaves not captured by the mechanical oscillator will reflect from the cavity and be measured at $\overline{\omega}_\mathrm{c}$. $t_\mathrm{a} < t < t_\mathrm{a} + t_\mathrm{b}$: Both input microwave fields are turned off, isolating the mechanical oscillator and state of interest from the cavity and output. $t_\mathrm{a} + t_\mathrm{b} < t < t_\mathrm{a} + t_\mathrm{b} + t_\mathrm{c}$: The transfer field is turned back on, coupling the mechanical state to the cavity and output environment, allowing read-out of the mechanical state.

mechanical state back out of the optomechanical system so that we can read it out. Measurement of the output of the system at the cavity frequency reveals the part of the preparation field not captured by the mechanical oscillator (for $0 < t < t_{\mathrm{a}}$) and the final retrieved state (for $t_{\mathrm{a}} + t_{\mathrm{b}} < t < t_{\mathrm{a}} + t_{\mathrm{b}} + t_{\mathrm{c}}$).

The device and interferometer we use for this experiment are essentially the same as for the ground state cooling and the sideband asymmetry measurements. However, we shorted one end of the microwave feedline, creating a boundary condition for one port of the cavity that results in the reflection geometry. Most of the device parameters remained the same, but the cavity couplings for the device in this configuration are $\kappa_{\mathrm{l}} = \kappa_{\mathrm{ext}} = 2\pi \times 275$ kHz and 320 kHz $< \kappa/(2\pi) < 360$ kHz.

11.1   Review and details of state transfer theory

The most critical requirement for coherent state transfer at quantum levels is that the transfer time be much faster than the rate of rethermalization from the mechanical bath. The transfer rate Γ_{l} between itinerant microwaves and the mechanical oscillator can be read off from the equation of motion for the oscillator (found in Chapter 3.3, assuming weak coupling, $\Gamma_{\mathrm{T}} \ll \kappa$, where $\Gamma_{\mathrm{T}} = 4g_{\mathrm{T}}^2/\kappa$):

$$\dot{b}_1[t] + \frac{1}{2}(\Gamma_{\mathrm{m}} + \Gamma_{\mathrm{T}})b_1[t] = je^{-j\phi_{\mathrm{T}}}\sqrt{\frac{\Gamma_{\mathrm{T}}\kappa_{\mathrm{l}}}{\kappa}}\alpha_{\mathrm{in,p}}[t] \quad \Rightarrow \quad \Gamma_{\mathrm{l}} = \frac{\Gamma_{\mathrm{T}}\kappa_{\mathrm{l}}}{\kappa}. \tag{11.1}$$

The total rate of transfer of itinerant photons to all channels (including the internal cavity bath) is Γ_{T}. The quantum decoherence rate Γ_{qu} for the mechanical oscillator to rethermalize by one phonon can be found by solving the mechanical equation of motion in the absence of coupling to the cavity (but in the presence of the mechanical bath) and solving for the time required for the

final occupancy to increase by a quantum:

$$\dot{b}_1[t] = -\frac{\Gamma_m}{2}b_1[t] + \sqrt{\Gamma_m}\xi_{m,1}[t], \tag{11.2}$$

$$b_1[t] = e^{-\Gamma_m t/2}\left(e^{\Gamma_m t_0/2}b_1[t_0] + \sqrt{\Gamma_m}\int_{t_0}^{t} e^{\Gamma_m t_1/2}\xi_{m,1}[t_1]dt_1\right), \tag{11.3}$$

$$n_m^f[t] = \left\langle b_1^\dagger[t]b_1[t]\right\rangle = e^{-\Gamma_m(t-t_0)}n_m^f[t_0] + (1 - e^{-\Gamma_m(t-t_0)})n_m^{th}, \tag{11.4}$$

$$n_m^f[t_0 + \Gamma_{qu}^{-1}] = n_m^f[t_0] + 1 \quad \Rightarrow \quad \Gamma_{qu} = \Gamma_m\left(\log\left[\frac{n_m^{th} - n_m^f[t_0]}{n_m^{th} - n_m^f[t_0] - 1}\right]\right)^{-1} \approx \Gamma_m n_m^{th}. \tag{11.5}$$

In the last line, I have made the approximation that $n_m^{th} \gg \{n_m^f, 1\}$. The comparison between the state transfer rate and quantum decoherence rate is most easily quantified by the cooperativity parameter $\tilde{C} = \Gamma_T/\Gamma_{qu} = 4g_T^2/(\kappa\Gamma_m n_m^{th})$. When $\tilde{C} \gg 1$, cooling of the mechanical ground state is possible, as is preparation of the mechanical oscillator in a coherent state. However, in order to faithfully transfer more complicated quantum states into the mechanical oscillator, it must also be true that the rate of transfer is much larger than the rate for a single thermal phonon to enter the mechanical oscillator ($\Gamma_l/\Gamma_{qu} \gg 1$). For our experiment, $\Gamma_{qu} = 2\pi \times 1.75$ kHz. The transfer rate used for most of the experiment is $\Gamma_T = 2\pi \times 7$ kHz and the maximum possible transfer rate is limited by the onset of strong coupling to $\Gamma_T = \kappa = 2\pi \times 340$ kHz. The ratio $\kappa_l/\kappa = \Gamma_l/\Gamma_T = 0.8$. Thus, both $\tilde{C} = \Gamma_T/\Gamma_{qu} \gg 1$ and $\Gamma_l/\Gamma_{qu} \gg 1$ are conditions easily met by our experiment. We therefore assume in the rest of the analysis that the mechanical bath can be ignored during state transfer (for $0 < t < t_a$ and $t_a + t_b < t < t_a + t_b + t_c$). However, we include and observe the effect of the mechanical bath during the storage time (when the mechanical oscillator is isolated from the cavity), such that $n_m^f[t_a + t_b] = (1 - e^{-\Gamma_m t_b})n_m^{th} + e^{-\Gamma_m t_b}n_m^f[t_a]$.

In Chapter 3.3, I solved the equations of motion in the time domain for each of the fields in each section of time (assuming weak coupling, $\Gamma_T \ll \kappa$, and no sources of noise). I found that a rising exponential preparation field $\alpha_{in,p}[t] = Ae^{\Gamma_p(t-t_a)/2}$ is nearly optimally transferred to the mechanical oscillator by a constant transfer pulse. Here, I extend this analysis to include sources of noise: for $0 < t < t_a$ and $t_a + t_b < t < t_a + t_b + t_c$, I include the various sources of photon noise but continue to treat the mechanical oscillator noiselessly (based on the assumption that the mechanical rethermalization rate is smaller than the transfer rate). For $t_a < t < t_a + t_b$, I include

the mechanical bath, as the mechanical oscillator is decoupled from the cavity. The solutions for the mechanical and output fields in each section of time for the rising exponential preparation and constant transfer fields are then:

$$0 \leq t \leq t_\mathrm{a}: \qquad g_\mathrm{T}[t] = \frac{\sqrt{\kappa \Gamma_\mathrm{T}}}{2}, \qquad \alpha_\mathrm{in,p}[t] = A e^{\Gamma_\mathrm{p}(t-t_\mathrm{a})/2},$$

$$b_1[t] = A e^{\Gamma_\mathrm{p}(t-t_\mathrm{a})/2} \frac{2 j e^{-j\phi_\mathrm{T}}}{\Gamma + \Gamma_\mathrm{p} + \Gamma_\mathrm{m}} \sqrt{\frac{\Gamma \kappa_\mathrm{l}}{\kappa}} (1 - e^{-(\Gamma + \Gamma_\mathrm{p} + \Gamma_\mathrm{m})t/2}), \tag{11.6}$$

$$a_\mathrm{out,p}[t] = \left(1 - \frac{2\kappa_\mathrm{l}}{\kappa}\right) \hat{\xi}_{\mathrm{l},1}[t] - \frac{2\sqrt{\kappa_\mathrm{l}\kappa_\mathrm{i}}}{\kappa} \hat{\xi}_{\mathrm{i},1}[t] \tag{11.7}$$

$$+ A e^{\Gamma_\mathrm{p}(t-t_\mathrm{a})/2} \left(1 - \frac{2\kappa_\mathrm{l}(\Gamma_\mathrm{p} + \Gamma_\mathrm{m} + \Gamma e^{-(\Gamma + \Gamma_\mathrm{p} + \Gamma_\mathrm{m})t/2})}{\kappa(\Gamma + \Gamma_\mathrm{p} + \Gamma_\mathrm{m})}\right),$$

$$t_\mathrm{a} \leq t \leq t_\mathrm{a} + t_\mathrm{b}: \qquad g_\mathrm{T}[t] = \alpha_\mathrm{in,p}[t] = 0,$$

$$b_1[t] = e^{-\Gamma_\mathrm{m}(t-t_\mathrm{a})/2} b_1[t_\mathrm{a}], \tag{11.8}$$

$$a_\mathrm{out,p}[t] = \left(1 - \frac{2\kappa_\mathrm{l}}{\kappa}\right) \hat{\xi}_{\mathrm{l},1}[t] - \frac{2\sqrt{\kappa_\mathrm{l}\kappa_\mathrm{i}}}{\kappa} \hat{\xi}_{\mathrm{i},1}[t], \tag{11.9}$$

$$n_\mathrm{m}^\mathrm{f}[t_\mathrm{a} + t_\mathrm{b}] = (1 - e^{-\Gamma_\mathrm{m} t_\mathrm{b}}) n_\mathrm{m}^\mathrm{th} + e^{-\Gamma_\mathrm{m} t_\mathrm{b}} n_\mathrm{m}^\mathrm{f}[t_\mathrm{a}] \tag{11.10}$$

$$= (1 - e^{-\Gamma_\mathrm{m} t_\mathrm{b}}) n_\mathrm{m}^\mathrm{th} + e^{-\Gamma_\mathrm{m} t_\mathrm{b}} \frac{4 A^2 \Gamma_\mathrm{T} \kappa_\mathrm{l}}{(\Gamma_\mathrm{T} + \Gamma_\mathrm{p} + \Gamma_\mathrm{m})^2 \kappa}, \tag{11.11}$$

$$t_\mathrm{a} + t_\mathrm{b} \leq t \leq t_\mathrm{a} + t_\mathrm{b} + t_\mathrm{c}: \qquad g_\mathrm{T}[t] = \frac{\sqrt{\kappa \Gamma_\mathrm{T}}}{2}, \qquad \alpha_\mathrm{in,p} = 0,$$

$$b_1[t] = e^{-(\Gamma + \Gamma_\mathrm{m})(t-t_\mathrm{a}-t_\mathrm{b})/2} b_1[t_\mathrm{a} + t_\mathrm{b}], \tag{11.12}$$

$$a_\mathrm{out,p}[t] = \left(1 - \frac{2\kappa_\mathrm{l}}{\kappa}\right) \hat{\xi}_{\mathrm{l},1}[t] - \frac{2\sqrt{\kappa_\mathrm{l}\kappa_\mathrm{i}}}{\kappa} \hat{\xi}_{\mathrm{i},1}[t] \tag{11.13}$$

$$- j e^{j\phi_\mathrm{T}} \sqrt{\frac{\Gamma \kappa_\mathrm{l}}{\kappa}} e^{-(\Gamma + \Gamma_\mathrm{m})(t-t_\mathrm{a}-t_\mathrm{b})/2} b_1[t_\mathrm{a} + t_\mathrm{b}].$$

Assuming that $\{\Gamma_\mathrm{T}, \Gamma_\mathrm{p}\} \gg \{\Gamma_\mathrm{m}, t_\mathrm{a}^{-1}, t_\mathrm{c}^{-1}\}$, the efficiency and leakage of the storage process take the approximate forms

$$\mathcal{E} = \frac{\int_{t_\mathrm{a}+t_\mathrm{b}}^{t_\mathrm{a}+t_\mathrm{b}+t_\mathrm{c}} |\langle \alpha_\mathrm{out,p}[t] \rangle|^2 \, dt}{\int_0^{t_\mathrm{a}} |\alpha_\mathrm{in,p}[t]|^2 \, dt} \approx \frac{\Gamma_\mathrm{T}}{\Gamma_\mathrm{p}} \left(\frac{2\Gamma_\mathrm{p} \kappa_\mathrm{l}}{(\Gamma_\mathrm{T} + \Gamma_\mathrm{p})\kappa}\right)^2 e^{-\Gamma_\mathrm{m} t_\mathrm{b}}, \tag{11.14}$$

$$L = \frac{\int_0^{t_\mathrm{a}} |\langle \alpha_\mathrm{out,p}[t] \rangle|^2 \, dt}{\int_0^{t_\mathrm{a}} |\alpha_\mathrm{in,p}[t]|^2 \, dt} \approx \left(1 - \frac{2\Gamma_\mathrm{p} \kappa_\mathrm{l}}{(\Gamma_\mathrm{T} + \Gamma_\mathrm{p})\kappa}\right)^2. \tag{11.15}$$

The efficiency is maximized for $\Gamma_\mathrm{T} = \Gamma_\mathrm{p}$ (note that this is not the point of minimum leakage for $\kappa_\mathrm{l} \neq \kappa$). When this condition is realized, the efficiency $\mathcal{E} = (\kappa_\mathrm{l}/\kappa)^2 e^{-\Gamma_\mathrm{m} t_\mathrm{b}}$ is composed of the

mechanical state decay during the storage time and a squared state transfer efficiency $\eta_{\mathrm{st}} = \kappa_1/\kappa$ (one factor for the capture and one for the release).

Calculating the efficiency of the transfer process reveals the total energy transfered; however, we would also like to understand the noise properties of the output state (and thus both the coherent and thermal (noise) contributions of the inferred mechanical state at time $t_{\mathrm{a}} + t_{\mathrm{b}}$). Taking the traditional Fourier transform of the time-dependent voltage does not make sense for this experiment given the decaying exponential nature of the output fields. However, we can make an analogous transformation of the output voltage using optimally chosen basis functions:

$$\check{V}_1[\omega] = \int_0^\infty e^{-\Gamma_{\mathrm{T}} t/2} \cos[\omega t] V[t + t_{\mathrm{a}} + t_{\mathrm{b}}] dt, \tag{11.16}$$

$$\check{V}_2[\omega] = \int_0^\infty e^{-\Gamma_{\mathrm{T}} t/2} \sin[\omega t] V[t + t_{\mathrm{a}} + t_{\mathrm{b}}] dt. \tag{11.17}$$

In the limit where $\Gamma_{\mathrm{T}} \to 0$, we recover the traditional voltages in the frequency domain:

$$\check{V}_1[\omega] = \int \cos[\omega t] V[t] dt = \mathrm{Re}[V[\omega]], \tag{11.18}$$

$$\check{V}_2[\omega] = \int \sin[\omega t] V[t] dt = \mathrm{Im}[V[\omega]], \tag{11.19}$$

$$\check{V}_1[\omega]^2 + \check{V}_2[\omega]^2 = S_{VV}[\omega]. \tag{11.20}$$

Using the derived expression above for the recovered output field $a_{\mathrm{out,p}}[t]$, the relation between output and measured fields $V[t] = \sqrt{\lambda} V^{\mathrm{photon}}[t]$ (see Section 6.2), and the heterodyne single-quadrature interferometer transformations (see Chapter 4), the measured voltage can be written in terms of the mechanical state quadratures at time $t_{\mathrm{a}} + t_{\mathrm{b}}$ (ignoring all noise sources for now). The $\check{V}$'s at the sideband frequency can then be related to these mechanical quadratures (similarly to how we related the output voltage spectral density $S_{VV}[\omega_{\mathrm{LO}} - \omega_{\mathrm{sideband}}]$ to $n_{\mathrm{m}}^{\mathrm{f}} = S_{xx}[\Omega_{\mathrm{m}}]/S_{xx}^{\mathrm{SQL}}$ in the steady state experiments):

$$X_1[t_{\mathrm{a}} + t_{\mathrm{b}}] = -\frac{1}{2}\left(e^{-j\phi} b_1[t_{\mathrm{a}} + t_{\mathrm{b}}] + e^{j\phi} b_1^\dagger[t_{\mathrm{a}} + t_{\mathrm{b}}]\right) = \sqrt{\frac{2\Gamma_{\mathrm{T}}}{\lambda \eta_{\mathrm{st}}}} \check{V}_1[\omega_{\mathrm{LO}} - \overline{\omega}_{\mathrm{c}}], \tag{11.21}$$

$$X_2[t_{\mathrm{a}} + t_{\mathrm{b}}] = \frac{j}{2}\left(e^{-j\phi} b_1[t_{\mathrm{a}} + t_{\mathrm{b}}] - e^{j\phi} b_1^\dagger[t_{\mathrm{a}} + t_{\mathrm{b}}]\right) = \sqrt{\frac{2\Gamma_{\mathrm{T}}}{\lambda \eta_{\mathrm{st}}}} \check{V}_2[\omega_{\mathrm{LO}} - \overline{\omega}_{\mathrm{c}}], \tag{11.22}$$

$$n_{\mathrm{m}}^{\mathrm{f}}[t_{\mathrm{a}} + t_{\mathrm{b}}] = \left\langle X_1[t_{\mathrm{a}} + t_{\mathrm{b}}]^2 + X_2[t_{\mathrm{a}} + t_{\mathrm{b}}]^2 \right\rangle = \frac{2\Gamma_{\mathrm{T}}}{\lambda \eta_{\mathrm{st}}} \left\langle \check{V}_1[\omega_{\mathrm{LO}} - \overline{\omega}_{\mathrm{c}}]^2 + \check{V}_2[\omega_{\mathrm{LO}} - \overline{\omega}_{\mathrm{c}}]^2 \right\rangle \tag{11.23}$$

Here, the mechanical quadratures measured are chosen by $\phi = \phi_{\mathrm{LO}} - \phi_{\mathrm{T}} + (\omega_{\mathrm{LO}} - \overline{\omega}_{\mathrm{c}})(t_{\mathrm{a}} + t_{\mathrm{b}})$ and the brackets indicate ensemble averages. Including sources of cavity and interferometer noise and calculating the basis function transformation with frequency $\omega \neq \omega_{\mathrm{LO}} - \overline{\omega}_{\mathrm{c}}$ results in

$$\frac{2\Gamma_{\mathrm{T}}}{\lambda \eta_{\mathrm{st}}} \left\langle \check{V}_1[\omega_{\mathrm{LO}} - \overline{\omega}_{\mathrm{c}} - \delta]^2 + \check{V}_2[\omega_{\mathrm{LO}} - \overline{\omega}_{\mathrm{c}} - \delta]^2 \right\rangle = \frac{\Gamma_{\mathrm{T}}^2 n_{\mathrm{m}}^{\mathrm{f}}[t_{\mathrm{a}} + t_{\mathrm{b}}]}{\Gamma_{\mathrm{T}}^2 + \delta^2} + \frac{1}{\eta \eta_{\mathrm{st}}}. \tag{11.24}$$

The inferred mechanical state is filtered by a Lorentzian profile with width $2\Gamma_{\mathrm{T}}$ and rides on an imprecision background set by the combination of the state transfer efficiency and the interferometer efficiency. This total efficiency can be found by calculating this quantity at $|\delta| \gg \Gamma_{\mathrm{T}}$. The total energy in the inferred mechanical quadratures (leaving the quadrature argument $[t_{\mathrm{a}} + t_{\mathrm{b}}]$ implied from here on) is then

$$\left\langle X_1^2 + X_2^2 \right\rangle = n_{\mathrm{m}}^{\mathrm{f}}[t_{\mathrm{a}} + t_{\mathrm{b}}] + \frac{1}{\eta \eta_{\mathrm{st}}}. \tag{11.25}$$

The coherent and noisy contributions to $n_{\mathrm{m}}^{\mathrm{f}}$ can be distinguished by calculating the relevant statistical quantities:

$$\langle X_1 \rangle^2 + \langle X_2 \rangle^2 = n_{\mathrm{m}}^{\mathrm{coh}}[t_{\mathrm{a}} + t_{\mathrm{b}}] = e^{-\Gamma_{\mathrm{m}} t_{\mathrm{b}}} \frac{4A^2 \Gamma_{\mathrm{T}} \eta_{\mathrm{st}}}{(\Gamma_{\mathrm{T}} + \Gamma_{\mathrm{p}})^2} \approx e^{-\Gamma_{\mathrm{m}} t_{\mathrm{b}}} \frac{A^2 \eta_{\mathrm{st}}}{\Gamma_{\mathrm{T}}}, \tag{11.26}$$

$$\left\langle (X_1 - \langle X_1 \rangle)^2 \right\rangle + \left\langle (X_2 - \langle X_2 \rangle)^2 \right\rangle = n_{\mathrm{m}}^{\mathrm{noise}}[t_{\mathrm{a}} + t_{\mathrm{b}}] + \frac{1}{\eta \eta_{\mathrm{st}}} = (1 - e^{-\Gamma_{\mathrm{m}} t_{\mathrm{b}}})n_{\mathrm{m}}^{\mathrm{th}} + \frac{1}{\eta \eta_{\mathrm{st}}}. \tag{11.27}$$

We therefore know how to infer all of the properties of the mechanical state at time $t_{\mathrm{a}} + t_{\mathrm{b}}$ from the voltage measured at the output of the experiment. The only unknown quantities in need of calibration are λ, which can be calibrated using a temperature sweep, and $\eta \eta_{\mathrm{st}}$, which can be determined using the detuned basis functions.

11.2   Coherent state transfer

We first demonstrate coherent state transfer of itinerant microwave states by applying the sequence of microwave fields shown in Figure 11.1 with fixed delay time $t_{\mathrm{b}} = 25$ μs. This time is chosen to be short enough that the total transfer and retrieval efficiency is degraded by less than 1%, but still long enough that any photons left in the cavity during storage should leak out long

before readout (in $\kappa^{-1} = 500$ ns). The exponential rising rate of the preparation field is fixed at $\Gamma_\mathrm{p} = 2\pi \times 6.4$ kHz and we vary the strength of the transfer field Γ_T. Figure 11.2(a) shows the (normalized) measured voltage $V[t]/A$ as a function of time for four different transfer strengths. This measurement does not require any calibration, as the voltages are normalized to the input preparation amplitude A, found by measuring the output voltage of the same preparation tone detuned away from the cavity. The time axis of all plots in this chapter has been shifted for ease of inspection such that $t_\mathrm{a} = 0$. When the transfer field is much weaker than the preparation rise rate ($\Gamma_\mathrm{T} < 2\pi \times 100$ Hz $ll\Gamma_\mathrm{p}$), the incident fields are badly impedance matched to the mechanical oscillator and they are simply reflected and measured in the first segment of time. For $\Gamma_\mathrm{T} = 2\pi \times 3.9$ kHz $\approx \Gamma_\mathrm{p}$, the systems are well matched and the output field in first time segment is indistinguishable from that that would be measured if the system were replaced by a 50 Ω termination. However, when the readout field is applied, the information is recovered, indicating that it was stored in the mechanical oscillator. When the transfer field is much larger than the
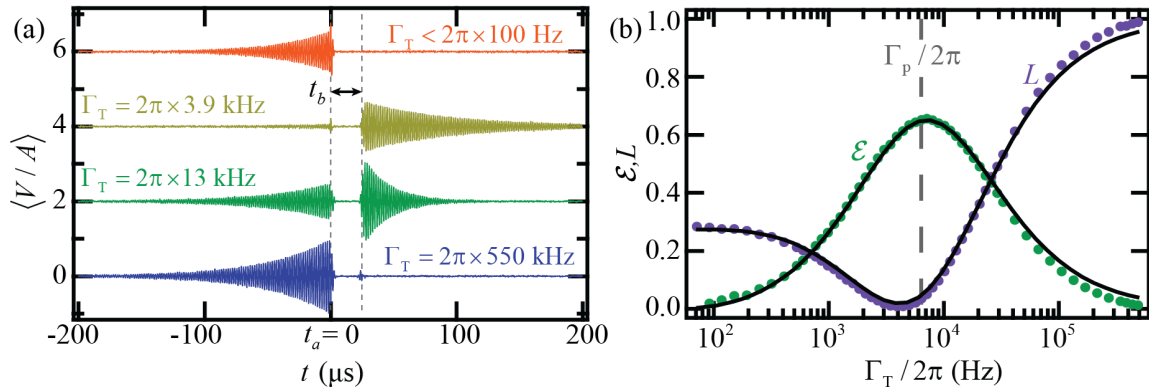

Figure 11.2: Coherent state transfer between itinerant photons and mechanical phonons. (a) Normalized output voltage measured as a function of time for four transfer strengths, each offset by 2 from the previous trace. Leakage is observed for $t < t_\mathrm{a}$ when the preparation and transfer fields are poorly matched. Efficient transfer of the preparation state to the mechanical oscillator and back is observed at $t_\mathrm{a} + t_\mathrm{b} < t < t_\mathrm{a} + t_\mathrm{b} + t_\mathrm{c}$ when the preparation rise rate and transfer field strength are similar. (b) Efficiency $\mathcal{E}$ (green) and leakage L (purple) as a function of transfer strength. The maximum efficiency occurs when $\Gamma_\mathrm{T} = \Gamma_\mathrm{p}$ (grey dashed line). The expected values given independently determined parameters (black lines) agree well with the data.

preparation rise rate ($\Gamma_T = 2\pi \times 550$ kHz $> \Gamma_p$), the transfer field is strong enought to transfer the itinerant state to the mechanical oscillator and back to the ininerant field before being captured by the mechanical oscillator. This once again results in energy being retrieved in the first section of time. Figure 11.2(b) shows the measured efficiency $\mathcal{E}$ and leakage L as a function of transfer drive strength. The efficiency is maximum when $\Gamma_T = \Gamma_p$, where it reaches 65%, implying a state transfer efficiency of $\eta_{st} = \sqrt{0.65} = 0.81 \pm 0.02$. This value agrees well with the cavity decay rates that we measure independently: $\eta_{st} = \kappa_l/\kappa = 0.80 \pm 0.01$. The full Γ_T dependence of $\mathcal{E}$ and L agrees well with the theoretical expressions presented above (plotted as black lines with no free parameters) and only deviates from this where the tranfer strength approaches the strong coupling regime.

11.3 Calibration of inferred mechanical state

In the above theory section, I detailed the transformations required to infer the coherent, noise, and apparent contributions to the number of mechanical quanta from the measured output voltage. The only quantities that required calibration were λ and $\eta\eta_{st}$. These two quantities can be calibrated using a temperature sweep of the mechanical oscillator in thermal equilibrium and inferences of the mechanical quadratures made with $|\delta| \gg \Gamma_T$. Figure 11.3(a) shows the inferred mechanical phonon number as a function of δ, the offset frequency of the basis functions used to optimally extract n_m^f. The red data shows this quantity when the mechanical state is in equilibrium with its bath at 25 mK. Even if the y-axis were not calibrated (if λ were not known), the ratio of the height of the Lorentzian peak to the background would give a measure of $n_m^{th}\eta\eta_{st}$. Figure 11.3(b) shows the measured number of thermal phonons $n_m^{th} = n_m^f[t_a + t_b] = \langle X_1^2 + X_2^2 \rangle - 1/(\eta\eta_{st})$ as a function of cryostat temperature. Each point on this graph is derived from 2000 inferences of the mechanical state (as shown in the inset). The delay time is set to $t_b = 75$ ms $\gg \Gamma_m^{-1}$, such that the mechanical state at $t_a + t_b$ is in equilibrium with the mechanical bath. The inferred phonon number follows the cryostat temperature linearly between 35 and 80 mK and saturates to 25 mK (50 quanta) at the base temperature of 15 mK. The range of linear dependence allows us
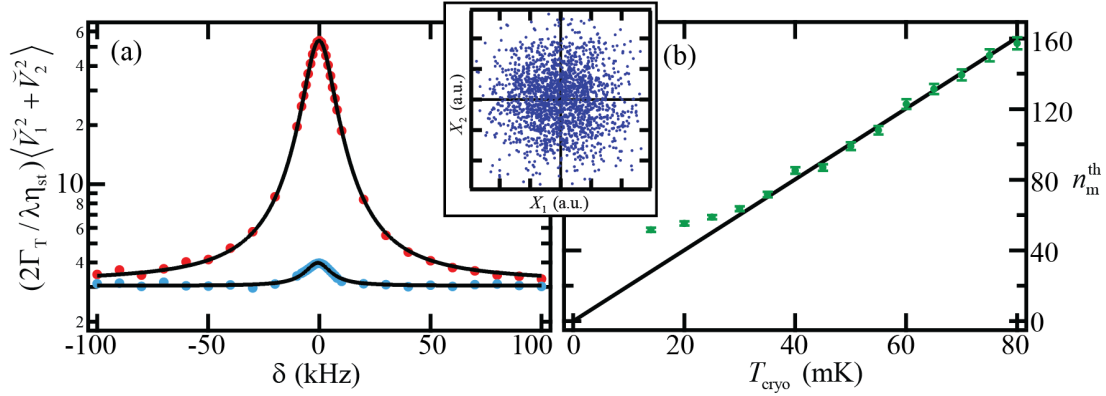
Figure 11.3: Calibration of phonon units and apparent mechanical motion. (a) The apparent motion (imprecision) can be calibrated by calculating the inferred mechanical occupancy with the basis functions detuned by $|\delta| \gg \Gamma_T$ from the frequency of optimal inference. (b) The conversion factor between measured voltage and inferred mechanical occupancy can be calibrated by measuring the mechanical oscillator in equilibrium with its bath as a function of cryostat temperature. (inset) Each point in the temperature sweep consists of 2000 inferences of the mechanical state.

to determine λ, thereby calibrating all future measurements into phonon units. Once λ is known, we can return to Figure 11.3(a) and find that the linear background of the 25 mK thermal state gives $(\eta\eta_{st})^{-1} = 3.1$. This indicates an interferometer efficiency of $\eta = 0.39$, consistent with the values obtained in the previous experiments with the same interferometer. Also shown in Figure 11.3(a) is the inferred thermal phonon contribution for a much lower entropy state (blue data). The extracted contributions for this state are $n_m^{noise} = 0.9$ and $(\eta\eta_{st})^{-1} = 3.1$, confirming that the imprecision of this measurement does not depend on the details of the measured state.

11.4   Phase-coherent state transfer at the single quanta level

We next investigate the noise properties of the inferred mechanical state to demonstrate preservation of the phase and amplitude of the prepared signal, even at single-photon itinerant input state amplitudes. We also estimate the quantum state lifetime of the mechanical oscillator by observing its coherent and thermal phonon contributions as a function of storage time.

In Figure 11.4(a), I again show the 2000 inferences of the mechanical quadratures for a 25 mK thermal state (now in phonon units) achieved by setting the delay time to $t_b = 75$ ms. This

distribution has no coherent component and obeys a two-dimensional Gaussian distribution. If we return to a delay time of $t_b = 25$ μs and set the preparation rise rate and transfer strength to $\Gamma_p = 2\pi \times 6.4$ kHz and $\Gamma_T = 2\pi \times 7$ kHz, respectively, we can further investigate states with a coherent contribution. We make 2000 inferences of the mechanical quadratures for each of four preparation phases, separated by 90 degree increments (shown as four different colors in Figure
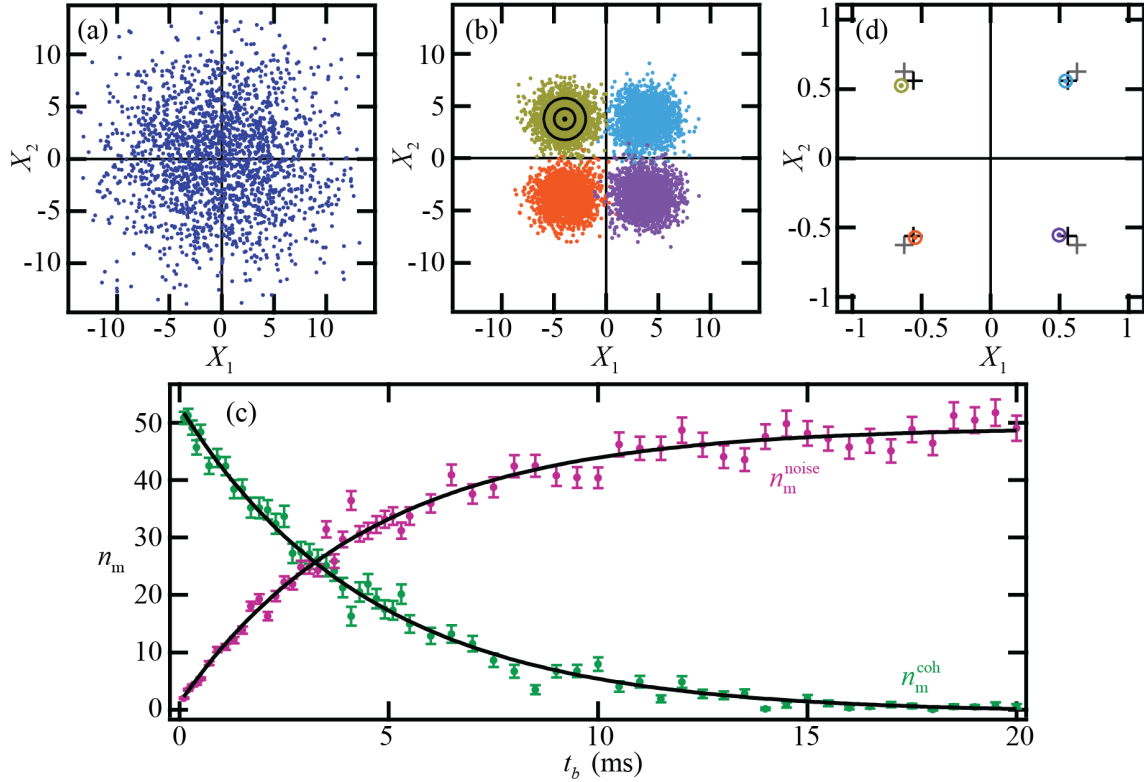

Figure 11.4: Phase-coherent state transfer. (a) Distribution of mechanical state inferences for a mechanical oscillator at equilibrium at 25 mK. (b) Distribution of mechanical state inferences given a state prepared with one of four $\pi/2$-rotated preparation phases (indicated by different colors). The radius of the large circle on the yellow data is the standard deviation $\sqrt{n_m^{\text{noise}} + 1/(\eta\eta_{\text{st}})}$ while the radius of the small circle is the minimum possible standard deviation given $\eta = \eta_{\text{st}} = 1$ and $n_m^{\text{noise}} = 0$. (c) Coherent and noise components of the mechanical occupancy as a function of storage time. The error bars are standard error of the mean for 500 measurements per point. The black lines are the theoretical expectations, given $\Gamma_m = 2\pi \times 35$ Hz as an independently determined parameter. (d) Mechanical state inferences as in (b), but with preparation amplitudes at the single photon level. The coherent component from 2000 inferences is shown as a colored dot surrounded by a circle with radius the standard error of the mean. The crosses show the expected values given measurements of the preparation fields for the known state transfer efficiency (black) and for ideal state transfer efficiency $\eta_{\text{st}} = 1$ (grey).

11.4(b)). The phase of the preparation pulse is preserved through the storage and recovery of the state. The inferred coherent and noise components of the final occupancy are $n_{\mathrm{m}}^{\mathrm{coh}} = 28.7 \pm 0.8$ and $n_{\mathrm{m}}^{\mathrm{noise}} = 0.9 \pm 0.1$. In the ground state cooling experiment (reference [48]), we found that the final mechanical occupancy was $n_{\mathrm{m}}^{\mathrm{f}} = 0.5$ for a cooling field with strength $\Gamma_{\mathrm{opt}} = 2\pi \times 7$ kHz. Therefore, we would expect that the final occupancy after the 25 μs storage would be $n_{\mathrm{m}}^{\mathrm{f}} = 0.8$, in reasonable agreement with the observed value. Figure 11.4(b) demonstrates that we can prepare and read out a mechanical state with less than one phonon of energy in a phase coherent way.

Figure 11.4(c) shows the evolution of the final mechanical state as a function of storage time. We choose the amplitude of the preparation pulse such that the coherent contribution at time t_{a} is $n_{\mathrm{m}}^{\mathrm{coh}}[t_{\mathrm{a}}] \approx A^2 \eta_{\mathrm{st}}/\Gamma_{\mathrm{T}} = 50 = n_{\mathrm{m}}^{\mathrm{th}}$. The evolution of both the coherent and noise components of the occupancy agree with the theoretical expectations, as $n_{\mathrm{m}}^{\mathrm{coh}}[t]$ exponentially decays in time at rate Γ_{m} and $n_{\mathrm{m}}^{\mathrm{noise}}[t]$ returns to $n_{\mathrm{m}}^{\mathrm{th}}$ at the same rate. This measurement strengthens our theoretical expectations that the quantum state lifetime of the mechanical oscillator is $\Gamma_{\mathrm{qu}}^{-1} = (\Gamma_{\mathrm{m}} n_{\mathrm{m}}^{\mathrm{th}})^{-1} = 90$ μs.

In order to test the preservation of phase and amplitude for transfered microwave states with amplitudes of less than one quanta, we make the same measurements as in Figure 11.4(b), but decrease the preparation field amplitude to the single (photon) quanta level. In Figure 11.4(d), we plot the average values (coherent component) of 2000 inferences of mechanical quadrature, again for each of four phases (colored dots). We also plot the expected results from measurements of the preparation field and knowledge of the state transfer efficiency (black crosses). The deviation of the measured values is consistent with statistical error and is below 0.1 quanta. Therefore, this measurement demonstrates phase-coherent state transfer and storage at the single quanta level.

11.5 State transfer in the strong coupling regime

Lastly, we investigate the maximum achievable transfer rate by increasing the transfer field strength into the strong coupling regime ($\Gamma_{\mathrm{T}} > \kappa$). In this regime, the state of interest is fully contained in the cavity before and after transfer, making the transfer process between cavity pho-
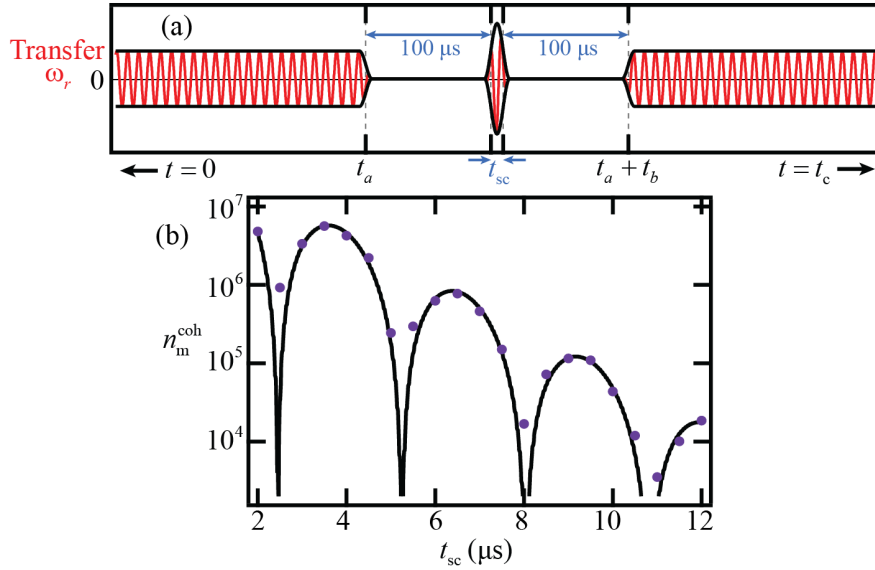
Figure 11.5: State transfer between the cavity and mechanical oscillator. (a) Sequence of fields for preparation, storage, exchange, storage, and retrieval of an itinerant microwave state. The exchange pulse transfers the state between the mechanical oscillator and the cavity. (b) The coherent component of the mechanical occupation alternately increases and disappears, indicating whether the energy ended up in the mechanical oscillator or the cavity at the end of the exchange. Several exchanges of energy are visible.

tons and the mechanical oscillator rather than between itinerant photons and the oscillator. To investigate this effect, we do the same (weak coupling limit) preparation and readout operations as before, but now introduce a strongly coupled, transfer (or exchange) pulse of duration t_{sc} during the storage segment (as illustrated in Figure 11.5(a)). We wait 100 μs before and after the exchange pulse to let the cavity fields decay away. Thus, the signal measured during the readout only contains information about the portion of the state that ended up in the mechanical oscillator after the exchange. The coherent contribution to the mechanical state can be inferred just as for the previous measurements in this chapter and is shown in Figure 11.5(b). By varying the time t_{sc}, we see exchanges of energy between the mechanical oscillator and cavity. The solid line is a fit using the equations of motion for the system and agrees well with the data for $\Gamma_T = 2.98\kappa$. Therefore, this measurement demonstrates that the transfer rate can exceed κ, but that the transfer is then between the cavity and the mechanical oscillator rather than itinerant photons and the oscillator.

The maximum rate for itinerant photon to mechanical oscillator transfer is κ.

In this chapter, I have described our efforts to transfer a prepared itinerant microwave state into the mechanical oscillator, store it there, and then retrieve it at a later time. We have demonstrated that such state transfers can take place on timescales far faster than the quantum decoherence rate of the mechanical oscillator. We have also shown that this process is phase coherent, even for input states at the level of a single photon. This achievement already provides an important tool - namely storage - to the world of microwave quantum information processing. Furthermore, it is a first step toward transferring quantum states between microwave and optical frequencies via a mechanical intermediary.

Chapter 12

Conclusions and future directions

This dissertation has focused on optomechanical systems, systems where the collective motional state of many atoms is coupled to an electromagnetic field. One of the two primary features of such systems is that mechanical motion changes the phase of the electromagnetic field, enabling sensitive inferences of that mechanical motion to be made. The other feature is that the electromagnetic field exerts a radiation pressure force back on the mechanical oscillator, enabling control of the mechanical state.

In addition to the general optomechanical theory presented to describe many of the interesting effects seen in optomechanical systems, this dissertation describes several of our experimental achievements using an electromechanical system. At the outset of my PhD work in 2007, our group had shown a proof of principle demonstration of electromechanical coupling between a nanomechanical wire oscillator and a microwave resonator [10]. Since then, we have improved on the ultrasensitive detection realized by our electromechanical system by realizing a quantum efficient microwave interferometer (Chapter 7, [76]). This interferometer is applicable not only for electromechanical experiments but also for any experiment that imprints information of interest onto the phase of a microwave field. Quantum efficient measurement allowed us to detect the motion of a mechanical oscillator with imprecision below that at the standard quantum limit and infer a force sensitivity of $S_{FF} = 0.26$ aN^2/Hz.

We have also made many improvements toward control of the mechanical state using the radiation pressure force of the microwave field. We showed initial radiation pressure cooling to 140

phonons [45] using a wire mechanical oscillator. We then improved upon the microwave interferometer and device employed to cool a suspended membrane mechanical oscillator to 0.34 phonons [48], the first achievement of radiation pressure cooling of a macroscopic mechanical oscillator to the ground state. We further demonstrated coherent state transfer between a mechanical oscillator and itinerant microwave fields, even at single photon signal amplitudes [66].

All of these improvements (and similar results in many of the other experiments in the field) have set the stage for investigations into optomechanical systems as tools for quantum information and basic tests of quantum physics. The immediate next step for our electromechanical experiment will be to create entangled states of photons and phonons, as discussed theoretically in [106]. Another parallel effort will be to devise an optomechanical device capable of simultaneously coupling to both microwave and optical fields [67]. This would allow quantum information to pass between these two different frequency regimes, making it possible to utilize the storage and long-distance transmission capabilities at optical frequencies while also taking advantage of the exquisite state preparation and manipulation available with superconducting qubits at microwave frequencies. We are also interested in making steps toward the realization of a system capable of exploring the intersection of quantum mechanics and gravitational theory, as proposed in [70, 71, 72, 73].

Bibliography

[1] M. Aspelmeyer, T. J. Kippenberg, and F. Marquardt, "Cavity optomechanics," arXiv:1303.0733, 2013. [Online]. Available: http://arxiv.org/abs/1303.0733

[2] B. Abbott, et al. (LIGO Scientific Collaboration), "Detector description and performance for the first coincidence observations between LIGO and GEO," Nuclear Instruments and Methods in Physics Research Section A: Accelerators, Spectrometers, Detectors and Associated Equipment, vol. 517, p. 154, 2004. [Online]. Available: http://dx.doi.org/10.1016/j.nima.2003.11.124

[3] O. Arcizet, P.-F. Cohadon, T. Briant, M. Pinard, and A. Heidmann, "Radiation-pressure cooling and optomechanical instability of a micromirror," Nature, vol. 444, p. 71, 2006. [Online]. Available: http://dx.doi.org/10.1038/nature05244

[4] T. Corbitt, Y. Chen, E. Innerhofer, H. Mller-Ebhardt, D. Ottaway, H. Rehbein, D. Sigg, S. Whitcomb, C. Wipf, and N. Mavalvala, "An all-optical trap for a gram-scale mirror," Phys. Rev. Lett., vol. 98, p. 150802, 2007. [Online]. Available: http://link.aps.org/doi/10.1103/PhysRevLett.98.150802

[5] C. L. Degen, M. Poggio, H. J. Mamin, C. T. Rettner, and D. Rugar, "Nanoscale magnetic resonance imaging," Proceedings of the National Academy of Sciences, vol. 106, p. 1313, 2009. [Online]. Available: dx.doi.org/10.1073/pnas.0812068106

[6] S. Groblacher, J. B. Hertzberg, M. R. Vanner, G. D. Cole, S. Gigan, K. C. Schwab, and M. Aspelmeyer, "Demonstration of an ultracold micro-optomechanical oscillator in a cryogenic cavity," Nat. Phys., vol. 5, p. 485, 2009. [Online]. Available: http://dx.doi.org/10.1038/nphys1301

[7] D. G. Blair, E. N. Ivanov, M. E. Tobar, P. J. Turner, F. van Kann, and I. S. Heng, "High sensitivity gravitational wave antenna with parametric transducer readout," Phys. Rev. Lett., vol. 74, p. 1908, 1995. [Online]. Available: http://link.aps.org/doi/10.1103/PhysRevLett.74.1908

[8] K. R. Brown, J. Britton, R. J. Epstein, J. Chiaverini, D. Leibfried, and D. J. Wineland, "Passive cooling of a micromechanical oscillator with a resonant electric circuit," Phys. Rev. Lett., vol. 99, p. 137205, 2007. [Online]. Available: http://link.aps.org/doi/10.1103/PhysRevLett.99.137205

[9] L. Gottardi, A. de Waard, O. Usenko, G. Frossati, M. Podt, J. Flokstra, M. Bassan, V. Fafone, Y. Minenkov, and A. Rocchi, "Sensitivity of the spherical gravitational wave detector MiniGRAIL operating at 5 K," Phys. Rev. D, vol. 76, p. 102005, 2007. [Online]. Available: http://link.aps.org/doi/10.1103/PhysRevD.76.102005

[10] C. A. Regal, J. D. Teufel, and K. W. Lehnert, "Measuring nanomechanical motion with a microwave cavity interferometer," Nat. Phys., vol. 4, p. 555, 2008. [Online]. Available: http://dx.doi.org/10.1038/nphys974

[11] A. Vinante, M. Bignotto, M. Bonaldi, M. Cerdonio, L. Conti, P. Falferi, N. Liguori, S. Longo, R. Mezzena, A. Ortolan, G. A. Prodi, F. Salemi, L. Taffarello, G. Vedovato, S. Vitale, and J.-P. Zendri, "Feedback cooling of the normal modes of a massive electromechanical system to submillikelvin temperature," Phys. Rev. Lett., vol. 101, p. 033601, 2008. [Online]. Available: http://link.aps.org/doi/10.1103/PhysRevLett.101.033601

[12] T. Rocheleau, T. Ndukum, C. Macklin, J. B. Hertzberg, A. A. Clerk, and K. C. Schwab, "Preparation and detection of a mechanical resonator near the ground state of motion," Nature, vol. 463, p. 72, 2010. [Online]. Available: http://dx.doi.org/10.1038/nature08681

[13] A. D. O'Connell, M. Hofheinz, M. Ansmann, R. C. Bialczak, M. Lenander, E. Lucero, M. Neeley, D. Sank, H. Wang, M. Weides, J. Wenner, J. M. Martinis, and A. N. Cleland, "Quantum ground state and single-phonon control of a mechanical resonator," Nature, vol. 464, p. 697, 2010. [Online]. Available: http://dx.doi.org/10.1038/nature08967

[14] F. Massel, T. T. Heikkilä, J.-M. Pirkkalainen, S. U. Cho, H. Saloniemi, P. J. Hakonen, and M. A. Sillanpää, "Microwave amplification with nanomechanical resonators," Nature, vol. 480, p. 351, 2011. [Online]. Available: http://dx.doi.org/10.1038/nature10628

[15] J. D. Teufel, D. Li, M. S. Allman, K. Cicak, A. J. Sirois, J. D. Whittaker, and R. W. Simmonds, "Circuit cavity electromechanics in the strong-coupling regime," Nature, vol. 471, p. 204, 2011. [Online]. Available: http://dx.doi.org/10.1038/nature09898

[16] J. Suh, M. D. Shaw, H. G. LeDuc, A. J. Weinstein, and K. C. Schwab, "Thermally induced parametric instability in a back-action evading measurement of a micromechanical quadrature near the zero-point level," Nano Lett., vol. 12, p. 6260, 2012. [Online]. Available: http://dx.doi.org/10.1021/nl303353r

[17] H. Rokhsari, T. Kippenberg, T. Carmon, and K. Vahala, "Radiation-pressure-driven micro-mechanical oscillator," Opt. Express, vol. 13, p. 5293, 2005. [Online]. Available: http://dx.doi.org/10.1364/OPEX.13.005293

[18] V. Fiore, Y. Yang, M. C. Kuzyk, R. Barbour, L. Tian, and H. Wang, "Storing optical information as a mechanical excitation in a silica optomechanical resonator," Phys. Rev. Lett., vol. 107, p. 133601, 2011. [Online]. Available: http://link.aps.org/doi/10.1103/PhysRevLett.107.133601

[19] J. D. Thompson, B. M. Zwickl, A. M. Jayich, F. Marquardt, S. M. Girvin, and J. G. E. Harris, "Strong dispersive coupling of a high-finesse cavity to a micromechanical membrane," Nature, vol. 452, p. 72, 2008. [Online]. Available: http://dx.doi.org/10.1038/nature06715

[20] K. Hammerer, M. Wallquist, C. Genes, M. Ludwig, F. Marquardt, P. Treutlein, P. Zoller, J. Ye, and H. J. Kimble, "Strong coupling of a mechanical oscillator and a single atom," Phys. Rev. Lett., vol. 103, p. 063005, 2009. [Online]. Available: http://link.aps.org/doi/10.1103/PhysRevLett.103.063005

[21] T. P. Purdy, R. W. Peterson, P.-L. Yu, and C. A. Regal, "Cavity optomechanics with Si_3N_4 membranes at cryogenic temperatures," New J. Phys., vol. 14, p. 115021, 2012. [Online]. Available: http://dx.doi.org/10.1088/1367-2630/14/11/115021

[22] J. Gieseler, B. Deutsch, R. Quidant, and L. Novotny, "Subkelvin parametric feedback cooling of a laser-trapped nanoparticle," Phys. Rev. Lett., vol. 109, p. 103603, 2012. [Online]. Available: http://link.aps.org/doi/10.1103/PhysRevLett.109.103603

[23] T. P. Purdy, D. W. C. Brooks, T. Botter, N. Brahms, Z.-Y. Ma, and D. M. Stamper-Kurn, "Tunable cavity optomechanics with ultracold atoms," Phys. Rev. Lett., vol. 105, p. 133602, 2010. [Online]. Available: http://link.aps.org/doi/10.1103/PhysRevLett.105.133602

[24] K. Hammerer, K. Stannigel, C. Genes, P. Zoller, P. Treutlein, S. Camerer, D. Hunger, and T. W. Hänsch, "Optical lattices with micromechanical mirrors," Phys. Rev. A, vol. 82, p. 021803, 2010. [Online]. Available: http://link.aps.org/doi/10.1103/PhysRevA.82.021803

[25] M. H. Schleier-Smith, I. D. Leroux, H. Zhang, M. A. Van Camp, and V. Vuletić, "Optomechanical cavity cooling of an atomic ensemble," Phys. Rev. Lett., vol. 107, p. 143005, 2011. [Online]. Available: http://link.aps.org/doi/10.1103/PhysRevLett.107.143005

[26] M. Eichenfield, R. Camacho, J. Chan, K. J. Vahala, and O. Painter, "A picogram- and nanometre-scale photonic-crystal optomechanical cavity," Nature, vol. 459, p. 550, 2009. [Online]. Available: http://dx.doi.org/10.1038/nature08061

[27] H. Cavendish, "Experiments to determine the density of the earth (1798)." in Scientific Memoirs Vol. 9: The Laws of Gravitation, A. McKenzie, Ed. American Book Co., 1900, p. 62. [Online]. Available: http://books.google.com/books?id=zrkEAAAAMAAJ&pg=PA62#v=onepage&q&f=false

[28] Bettmann/Corbis / AP images. (1960, May 26) Henry Cabot Lodge pointing to seal, AP image 6005261265. Associated Press. [Online]. Available: http://www.apimages.com/Search.aspx?st=k&remem=x&entity=&kw=6005261265&intv=None&shgroup=-10&sh=10

[29] H. K. Melton, The Ultimate Spy Book. Dorling Kindersley, 1996.

[30] K. Murray. The great seal bug story. Murray Associates. [Online]. Available: http://www.spybusters.com/Great_Seal_Bug.html

[31] V. Braginsky and V. Rudenko, "Gravitational waves and the detection of gravitational radiation," Physics Reports, vol. 46, p. 165, 1978. [Online]. Available: http://dx.doi.org/10.1016/0370-1573(78)90192-8

[32] G. White. LIGO Hanford (LHO) Aerial 1. LIGO Laboratory. [Online]. Available: http://www.ligo.caltech.edu/LIGO_web/PR/scripts/photos.html

[33] J. Phillips. How to marry a microscope. JILA, CU Boulder and NIST. [Online]. Available: http://jila.colorado.edu/content/how-marry-microscope

[34] H. J. Mamin and D. Rugar, "Sub-attonewton force detection at millikelvin temperatures," Appl. Phys. Lett., vol. 79, p. 3358, 2001. [Online]. Available: http://dx.doi.org/10.1063/1.1418256

[35] M. J. Biercuk, H. Uys, J. W. Britton, A. P. VanDevender, and J. J. Bollinger, "Ultrasensitive detection of force and displacement using trapped ions," Nat. Nanotechnol., vol. 5, p. 646, 2010. [Online]. Available: http://dx.doi.org/10.1038/nnano.2010.165

[36] R. Maiwald, D. Leibfried, J. Britton, J. C. Bergquist, G. Leuchs, and D. J. Wineland, "Stylus ion trap for enhanced access and sensing," Nat. Phys., vol. 5, p. 551, 2009. [Online]. Available: http://dx.doi.org/10.1038/nphys1311

[37] W. Liller (International Halley Watch Large Scale Phenomena Network). (1986, March) Comet P/Halley. NASA, NSSDC. [Online]. Available: http://nssdc.gsfc.nasa.gov/photo_gallery/photogallery-comets.html

[38] Japan Aerospace Exploration Agency (JAXA). (2010, June) IKAROS (state of the solar electricity sail development that isolated camera imaged), image P100005965. JAXA digital archives. [Online]. Available: http://jda.jaxa.jp/result.php?lang=e&id=c08e77ea3af2606bac2c679c962a6672

[39] M. Köhler, T. Minato, H. Kimura, and I. Mann, "Radiation pressure force acting on cometary aggregates," Advances in Space Research, vol. 40, p. 266, 2007. [Online]. Available: http://dx.doi.org/10.1016/j.asr.2007.05.044

[40] A. Mann, "Solar sails pick up speed," Nature News, vol. 3 February 2011. [Online]. Available: http://dx.doi.org/10.1038/news.2011.68

[41] N. Meyer-Vernet, Basics of the solar wind. Cambridge University Press, 2007.

[42] E. F. Nichols and G. F. Hull, "A preliminary communication on the pressure of heat and light radiation," Phys. Rev. (Series I), vol. 13, p. 307, 1901. [Online]. Available: http://link.aps.org/doi/10.1103/PhysRevSeriesI.13.307

[43] D. J. Wineland, R. E. Drullinger, and F. L. Walls, "Radiation-pressure cooling of bound resonant absorbers," Phys. Rev. Lett., vol. 40, p. 1639, 1978. [Online]. Available: http://link.aps.org/doi/10.1103/PhysRevLett.40.1639

[44] C. Monroe, D. M. Meekhof, B. E. King, S. R. Jefferts, W. M. Itano, D. J. Wineland, and P. Gould, "Resolved-sideband Raman cooling of a bound atom to the 3D zero-point energy," Phys. Rev. Lett., vol. 75, p. 4011, 1995. [Online]. Available: http://link.aps.org/doi/10.1103/PhysRevLett.75.4011

[45] J. D. Teufel, J. W. Harlow, C. A. Regal, and K. W. Lehnert, "Dynamical backaction of microwave fields on a nanomechanical oscillator," Phys. Rev. Lett., vol. 101, p. 197203, 2008. [Online]. Available: http://link.aps.org/doi/10.1103/PhysRevLett.101.197203

[46] B. Abbott, et al. (LIGO Scientific Collaboration), "Observation of a kilogram-scale oscillator near its quantum ground state," New J. Phys., vol. 11, p. 073032, 2009. [Online]. Available: http://dx.doi.org/10.1088/1367-2630/11/7/073032

[47] R. Rivière, S. Deléglise, S. Weis, E. Gavartin, O. Arcizet, A. Schliesser, and T. J. Kippenberg, "Optomechanical sideband cooling of a micromechanical oscillator close to the quantum ground state," Phys. Rev. A, vol. 83, p. 063835, 2011. [Online]. Available: http://link.aps.org/doi/10.1103/PhysRevA.83.063835

[48] J. D. Teufel, T. Donner, D. Li, J. W. Harlow, M. S. Allman, K. Cicak, A. J. Sirois, J. D. Whittaker, K. W. Lehnert, and R. W. Simmonds, "Sideband cooling of micromechanical motion to the quantum ground state," Nature, vol. 475, p. 359, 2011. [Online]. Available: http://dx.doi.org/10.1038/nature10261

[49] J. Chan, T. P. M. Alegre, A. H. Safavi-Naeini, J. T. Hill, A. Krause, S. Groblacher, M. Aspelmeyer, and O. Painter, "Laser cooling of a nanomechanical oscillator into its quantum ground state," Nature, vol. 478, p. 89, 2011. [Online]. Available: http://dx.doi.org/10.1038/nature10461

[50] V. Braginsky and F. Khalili, Quantum measurement, K. S. Thorne, Ed. Cambridge University Press, 1992.

[51] K. S. Thorne, R. W. P. Drever, C. M. Caves, M. Zimmermann, and V. D. Sandberg, "Quantum nondemolition measurements of harmonic oscillators," Phys. Rev. Lett., vol. 40, p. 667, 1978. [Online]. Available: http://link.aps.org/doi/10.1103/PhysRevLett.40.667

[52] V. B. Braginsky, Y. I. Vorontsov, and K. S. Thorne, "Quantum nondemolition measurements," Science, vol. 209, p. 547, 1980. [Online]. Available: http://dx.doi.org/10.1126/science.209.4456.547

[53] A. A. Clerk, F. Marquardt, and K. Jacobs, "Back-action evasion and squeezing of a mechanical resonator using a cavity detector," New J. Phys., vol. 10, p. 095010, 2008. [Online]. Available: http://dx.doi.org/10.1088/1367-2630/10/9/095010

[54] K. W. Murch, K. L. Moore, S. Gupta, and D. M. Stamper-Kurn, "Observation of quantum-measurement backaction with an ultracold atomic gas," Nat. Phys., vol. 4, p. 561, 2008. [Online]. Available: http://dx.doi.org/10.1038/nphys965

[55] T. P. Purdy, R. W. Peterson, and C. A. Regal, "Observation of radiation pressure shot noise on a macroscopic object," Science, vol. 339, p. 801, 2013. [Online]. Available: http://dx.doi.org/10.1126/science.1231282

[56] A. H. Safavi-Naeini, S. Groeblacher, J. T. Hill, J. Chan, M. Aspelmeyer, and O. Painter, "Squeezing of light via reflection from a silicon micromechanical resonator," arXiv:1302.6179, 2013. [Online]. Available: http://arxiv.org/abs/1302.6179

[57] D. W. C. Brooks, T. Botter, S. Schreppler, T. P. Purdy, N. Brahms, and D. M. Stamper-Kurn, "Non-classical light generated by quantum-noise-driven cavity optomechanics," Nature, vol. 488, p. 476, 2012. [Online]. Available: http://dx.doi.org/10.1038/nature11325

[58] G.M. Harry (LIGO Scientific Collaboration), "Advanced LIGO: the next generation of gravitational wave detectors," Classical and Quantum Gravity, vol. 27, p. 084006, 2010. [Online]. Available: http://dx.doi.org/10.1088/0264-9381/27/8/084006

[59] W. Neuhauser, M. Hohenstatt, P. Toschek, and H. Dehmelt, "Optical-sideband cooling of visible atom cloud confined in parabolic well," Phys. Rev. Lett., vol. 41, p. 233, 1978. [Online]. Available: http://link.aps.org/doi/10.1103/PhysRevLett.41.233

[60] D. J. Wineland, W. M. Itano, J. C. Bergquist, and R. G. Hulet, "Laser-cooling limits and single-ion spectroscopy," Phys. Rev. A, vol. 36, p. 2220, 1987. [Online]. Available: http://link.aps.org/doi/10.1103/PhysRevA.36.2220

[61] F. Diedrich, J. C. Bergquist, W. M. Itano, and D. J. Wineland, "Laser cooling to the zero-point energy of motion," Phys. Rev. Lett., vol. 62, p. 403, 1989. [Online]. Available: http://link.aps.org/doi/10.1103/PhysRevLett.62.403

[62] A. H. Safavi-Naeini, J. Chan, J. T. Hill, T. P. M. Alegre, A. Krause, and O. Painter, "Observation of quantum motion of a nanomechanical resonator," Phys. Rev. Lett., vol. 108, p. 033602, 2012. [Online]. Available: http://link.aps.org/doi/10.1103/PhysRevLett.108.033602

[63] D. Wineland, C. Monroe, W. Itano, D. Leibfried, B. King, and D. Meekhof, "Experimental issues in coherent quantum-state manipulation of trapped atomic ions," J. Res. Natl. Inst. Stand. Technol., vol. 103, p. 259, 1998. [Online]. Available: http://nistdigitalarchives.contentdm.oclc.org/cdm/ref/collection/p13011coll6/id/38341

[64] D. Wineland and D. Leibfried, "Quantum information processing and metrology with trapped ions," Laser Phys. Lett., vol. 8, p. 175, 2011. [Online]. Available: http://dx.doi.org/10.1002/lapl.201010125

[65] E. Verhagen, S. Deleglise, S. Weis, A. Schliesser, and T. J. Kippenberg, "Quantum-coherent coupling of a mechanical oscillator to an optical cavity mode," Nature, vol. 482, p. 63, 2012. [Online]. Available: http://dx.doi.org/10.1038/nature10787

[66] T. A. Palomaki, J. W. Harlow, J. D. Teufel, R. W. Simmonds, and K. W. Lehnert, "Coherent state transfer between itinerant microwave fields and a mechanical oscillator," Nature, vol. 495, p. 210, 2013. [Online]. Available: http://dx.doi.org/10.1038/nature11915

[67] C. A. Regal and K. W. Lehnert, "From cavity electromechanics to cavity optomechanics," Journal of Physics: Conference Series, vol. 264, p. 012025, 2011. [Online]. Available: http://dx.doi.org/10.1088/1742-6596/264/1/012025

[68] J. M. Taylor, A. S. Sørensen, C. M. Marcus, and E. S. Polzik, "Laser cooling and optical detection of excitations in a LC electrical circuit," Phys. Rev. Lett., vol. 107, p. 273601, 2011. [Online]. Available: http://link.aps.org/doi/10.1103/PhysRevLett.107.273601

[69] J. D. Jost, J. P. Home, J. M. Amini, D. Hanneke, R. Ozeri, C. Langer, J. J. Bollinger, D. Leibfried, and D. J. Wineland, "Entangled mechanical oscillators," Nature, vol. 459, p. 683, 2009. [Online]. Available: http://dx.doi.org/10.1038/nature08006

[70] W. Marshall, C. Simon, R. Penrose, and D. Bouwmeester, "Towards quantum superpositions of a mirror," Phys. Rev. Lett., vol. 91, p. 130401, 2003. [Online]. Available: http://link.aps.org/doi/10.1103/PhysRevLett.91.130401

[71] M. Arndt, M. Aspelmeyer, and A. Zeilinger, "How to extend quantum experiments," Fortschr. Phys., vol. 57, p. 1153, 2009. [Online]. Available: http://dx.doi.org/10.1002/prop.200900104

[72] O. Romero-Isart, M. L. Juan, R. Quidant, and J. I. Cirac, "Toward quantum superposition of living organisms," New J. Phys., vol. 12, p. 033015, 2010. [Online]. Available: http://dx.doi.org/10.1088/1367-2630/12/3/033015

[73] I. Pikovski, M. R. Vanner, M. Aspelmeyer, M. S. Kim, and C. Brukner, "Probing planck-scale physics with quantum optics," Nat. Phys., vol. 8, p. 393, 2012. [Online]. Available: http://dx.doi.org/10.1038/nphys2262

[74] G. J. Grabovskij, L. J. Swenson, O. Buisson, C. Hoffmann, A. Monfardini, and J.-C. Villégier, "In situ measurement of the permittivity of helium using microwave NbN resonators," Appl. Phys. Lett., vol. 93, p. 134102, 2008. [Online]. Available: http://dx.doi.org/10.1063/1.2996263

[75] F. Marquardt, J. P. Chen, A. A. Clerk, and S. M. Girvin, "Quantum theory of cavity-assisted sideband cooling of mechanical motion," Phys. Rev. Lett., vol. 99, p. 093902, 2007. [Online]. Available: http://link.aps.org/doi/10.1103/PhysRevLett.99.093902

[76] J. Teufel, T. Donner, M. A. Castellanos-Beltran, J. Harlow, and K. W. Lehnert, "Nanomechanical motion measured with an imprecision below that at the standard quantum limit," Nat. Nanotechnol., vol. 4, p. 820, 2009. [Online]. Available: http://dx.doi.org/10.1038/nnano.2009.343

[77] D. M. Pozar, Microwave Engineering, 2nd ed. John Wiley & Sons, Inc., 1998.

[78] D. F. Walls and G. J. Milburn, Quantum Optics. Springer-Verlag, 1994.

[79] K. J. Åström and R. M. Murray, Feedback Systems: An Introduction for Scientists and Engineers. Princeton University Press, 2008.

[80] A. Schliesser, O. Arcizet, R. Riviere, G. Anetsberger, and T. J. Kippenberg, "Resolved-sideband cooling and position measurement of a micromechanical oscillator close to the heisenberg uncertainty limit," Nat Phys, vol. 5, p. 509, 2009. [Online]. Available: http://dx.doi.org/10.1038/nphys1304

[81] F. Y. Khalili, H. Miao, H. Yang, A. H. Safavi-Naeini, O. Painter, and Y. Chen, "Quantum back-action in measurements of zero-point mechanical oscillations," Phys. Rev. A, vol. 86, p. 033840, 2012. [Online]. Available: http://link.aps.org/doi/10.1103/PhysRevA.86.033840

[82] A. S. Parkins and H. J. Kimble, "Quantum state transfer between motion and light," Journal of Optics B: Quantum and Semiclassical Optics, vol. 1, p. 496, 1999. [Online]. Available: http://dx.doi.org/10.1088/1464-4266/1/4/323

[83] D. F. Phillips, A. Fleischhauer, A. Mair, R. L. Walsworth, and M. D. Lukin, "Storage of light in atomic vapor," Phys. Rev. Lett., vol. 86, p. 783, 2001. [Online]. Available: http://link.aps.org/doi/10.1103/PhysRevLett.86.783

[84] J. Zhang, K. Peng, and S. L. Braunstein, "Quantum-state transfer from light to macroscopic oscillators," Phys. Rev. A, vol. 68, p. 013808, 2003. [Online]. Available: http://link.aps.org/doi/10.1103/PhysRevA.68.013808

[85] J. Nunn, I. A. Walmsley, M. G. Raymer, K. Surmacz, F. C. Waldermann, Z. Wang, and D. Jaksch, "Mapping broadband single-photon wave packets into an atomic memory," Phys. Rev. A, vol. 75, p. 011401, 2007. [Online]. Available: http://link.aps.org/doi/10.1103/PhysRevA.75.011401

[86] A. V. Gorshkov, A. André, M. Fleischhauer, A. S. Sørensen, and M. D. Lukin, "Universal approach to optimal photon storage in atomic media," Phys. Rev. Lett., vol. 98, p. 123601, 2007. [Online]. Available: http://link.aps.org/doi/10.1103/PhysRevLett.98.123601

[87] I. Novikova, A. V. Gorshkov, D. F. Phillips, A. S. Sørensen, M. D. Lukin, and R. L. Walsworth, "Optimal control of light pulse storage and retrieval," Phys. Rev. Lett., vol. 98, p. 243602, 2007. [Online]. Available: http://link.aps.org/doi/10.1103/PhysRevLett.98.243602

[88] A. H. Safavi-Naeini and O. Painter, "Proposal for an optomechanical traveling wave phonon-photon translator," New J. Phys., vol. 13, p. 013017, 2011. [Online]. Available: http://dx.doi.org/10.1088/1367-2630/13/1/013017

[89] Y.-D. Wang and A. A. Clerk, "Using interference for high fidelity quantum state transfer in optomechanics," Phys. Rev. Lett., vol. 108, p. 153603, 2012. [Online]. Available: http://link.aps.org/doi/10.1103/PhysRevLett.108.153603

[90] ——, "Using dark modes for high-fidelity optomechanical quantum state transfer," New Journal of Physics, vol. 14, p. 105010, 2012. [Online]. Available: http://dx.doi.org/10.1088/1367-2630/14/10/105010

[91] S. A. McGee, "Using mechanical oscillators for transduction and memory of quantum states," Ph.D. dissertation, University of Colorado, 2012. [Online]. Available: http://jila.colorado.edu/thesis

[92] S. A. Gardiner, "Quantum measurement, quantum chaos, and Bose-Einstein condensates," Ph.D. dissertation, Leopold-Franzens-Universitat Innsbruck, 2000. [Online]. Available: http://massey.dur.ac.uk/sag/dthesis.html

[93] A. Nunnenkamp, K. Børkje, and S. M. Girvin, "Single-photon optomechanics," Phys. Rev. Lett., vol. 107, p. 063602, 2011. [Online]. Available: http://link.aps.org/doi/10.1103/PhysRevLett.107.063602

[94] A. N. Cleland, Foundations of Nanomechanics.   Springer-Verlag, 2003.

[95] S. C. Jun, X. M. H. Huang, M. Manolidis, C. A. Zorman, M. Mehregany, and J. Hone, "Electrothermal tuning of Al-SiC nanomechanical resonators," Nanotechnology, vol. 17, p. 1506, 2006. [Online]. Available: http://dx.doi.org/10.1088/0957-4484/17/5/057

[96] F. Pobell, Matter and Methods at low Temperatures, 2nd ed.   Springer, 1996.

[97] J. D. Teufel, C. A. Regal, and K. W. Lehnert, "Prospects for cooling nanomechanical motion by coupling to a superconducting microwave resonator," New J. Phys., vol. 10, p. 095002, 2008. [Online]. Available: http://dx.doi.org/10.1088/1367-2630/10/9/095002

[98] Q. P. Unterreithmeier, T. Faust, and J. P. Kotthaus, "Damping of nanomechanical resonators," Phys. Rev. Lett., vol. 105, p. 027205, 2010. [Online]. Available: http://link.aps.org/doi/10.1103/PhysRevLett.105.027205

[99] K. C. Gupta, R. Garg, I. Bahl, and P. Bhartia, <u>Microstrip Lines and Slotlines</u>. Boston: Artech House, 1996.

[100] EllipticK. [Online]. Available: http://reference.wolfram.com/mathematica/ref/EllipticK. html

[101] EllipticF. [Online]. Available: http://reference.wolfram.com/mathematica/ref/EllipticF.html

[102] Complete elliptic integral of the first kind. [Online]. Available: http://mathworld.wolfram. com/CompleteEllipticIntegraloftheFirstKind.html

[103] Elliptic integral of the first kind. [Online]. Available: http://mathworld.wolfram.com/ EllipticIntegraloftheFirstKind.html

[104] K. Cicak, D. Li, J. A. Strong, M. S. Allman, F. Altomare, A. J. Sirois, J. D. Whittaker, J. D. Teufel, and R. W. Simmonds, "Low-loss superconducting resonant circuits using vacuum-gap-based microwave components," <u>Appl. Phys. Lett.</u>, vol. 96, p. 093502, 2010. [Online]. Available: http://dx.doi.org/10.1063/1.3304168

[105] J. B. Hertzberg, T. Rocheleau, T. Ndukum, M. Savva, A. A. Clerk, and K. C. Schwab, "Back-action-evading measurements of nanomechanical motion," <u>Nat. Phys.</u>, vol. 6, p. 213, 2010. [Online]. Available: http://dx.doi.org/10.1038/nphys1479

[106] S. G. Hofer, W. Wieczorek, M. Aspelmeyer, and K. Hammerer, "Quantum entanglement and teleportation in pulsed cavity optomechanics," <u>Phys. Rev. A</u>, vol. 84, p. 052327, 2011. [Online]. Available: http://link.aps.org/doi/10.1103/PhysRevA.84.052327

[107] M. A. Castellanos-Beltran, "Development of a Josephson parametric amplifier for the preparation and detection of nonclassical states of microwave fields," Ph.D. dissertation, University of Colorado, 2010. [Online]. Available: http://jila.colorado.edu/thesis

[108] B. Yurke and E. Buks, "Performance of cavity-parametric amplifiers, employing Kerr nonlinearites, in the presence of two-photon loss," <u>J. Lightwave Technol.</u>, vol. 24, p. 5054, 2006. [Online]. Available: http://dx.doi.org/10.1109/JLT.2006.884490

[109] 2 edge coupled striplines (EM quasi-static): S2CLIN. [Online]. Available: https: //awrcorp.com/download/faq/english/docs/Elements/S2CLIN.htm

[110] M. B. Baždar, A. R. Djordjević, R. F. Harrington, and T. K. Sarkar, "Evaluation of quasi-static matrix parameters for multiconductor transmission lines using Galerkin's method," <u>Microwave Theory and Techniques, IEEE Transactions on</u>, vol. 42, p. 1223, 1994. [Online]. Available: http://dx.doi.org/10.1109/22.299760

[111] Two-layer stripline substrate definition: SSUBL. [Online]. Available: https://awrcorp.com/ download/faq/english/docs/Elements/ssubl.htm

Appendix A

Symbol definitions

$j = -\sqrt{-1} = -i$	imaginary constant
$\delta_{i,j}$	Kronecker delta function
$\delta[t - t']$	Dirac delta function
$S_{xy}[\omega]$	power spectral density, $\int_{-\infty}^{\infty} e^{-j\omega t} \left\langle \hat{x}^\dagger[0]\hat{y}[t] \right\rangle dt$
$\overline{\omega}_{\mathrm{c}}$	cavity resonance frequency
κ_i	cavity loss rate to port $i = \{\mathrm{l}, \mathrm{r}, 0\}$
$\kappa = \sum_i \kappa_i$	total cavity loss rate
N_i	complex coefficient for port $i = \{1, 2\}$
$\hat{a}, \hat{a}_{\mathrm{in}}, \hat{a}_{\mathrm{out}}$	annihilation operators for cavity and itinerant photons
$n_{\mathrm{l}}^{\mathrm{th}}, n_{\mathrm{r}}^{\mathrm{th}}, n_{0}^{\mathrm{th}}, n_{\mathrm{c}}^{\mathrm{th}}$	left, right, internal, and total thermal cavity photon numbers
n_{d}	number of cavity photons due to coherent drive
m	mechanical oscillator mass

$\Gamma_{\mathrm{m}}, \Gamma_{\mathrm{opt}}, \Gamma_{\mathrm{tot}}$	intrinsic, optomechanically induced, total mechanical linewidths
$\Omega_{\mathrm{m}}, \Omega_{\mathrm{opt}}, \Omega_{\mathrm{tot}}$	intrinsic, optomechanically induced, total mechanical frequencies
$\hat{b}$	phonon annihilation operator
$\hat{x} = x_{\mathrm{zp}}(\hat{b} + \hat{b}^{\dagger})$	mechanical position operator
$x_{\mathrm{zp}} = \sqrt{\hbar/(2m\Omega_{\mathrm{m}})}$	zero point mechanical motion
$n_{\mathrm{m}}^{\mathrm{th}}, n_{\mathrm{m}}^{\mathrm{f}}, n_{\mathrm{m}}^{\mathrm{imp}}, n_{\mathrm{m}}^{\mathrm{ba}}$	thermal, final, imprecision, and backaction phonon numbers
$\hat{\xi}_i$	noise operator for bath $i = \{\mathrm{l}, \mathrm{r}, 0, \mathrm{m}\}$
$G = d\omega_{\mathrm{c}}/dx$	cavity frequency coupling to mechanical displacement
$g_0 = Gx_{\mathrm{zp}}$	single photon optomechanical coupling
$g = g_0\sqrt{n_{\mathrm{d}}}$	total optomechanical coupling
ω_{d}	cavity drive frequency
ω_{p}	probe frequency in response measurements
Γ_{T}	state transfer rate in pulsed experiments
Γ_{p}	preparation state rise rate in pulsed experiments
η	interferometer efficiency
$\chi_{\mathrm{c}}[\omega]$	cavity susceptibility, $[\kappa/2 + j(\omega - \omega_{\mathrm{c}})]^{-1}$
$\chi_{\mathrm{m}}[\omega]$	bare mechanical susceptibility, $[\Gamma_{\mathrm{m}}/2 + j(\omega - \Omega_{\mathrm{m}})]^{-1}$
$\chi_{\mathrm{m,eff}}[\omega]$	effective mechanical susceptibility, $[\Gamma_{\mathrm{tot}}/2 + j(\omega - \Omega_{\mathrm{tot}})]^{-1}$

Appendix B

Conventions

B.1   Fourier transform conventions

Most of the time, I use the following Fourier Transform conventions:

$$f[\omega] = \int_{-\infty}^{\infty} e^{-j\omega t} f[t] dt \tag{B.1}$$

$$f[t] = \frac{1}{2\pi} \int_{-\infty}^{\infty} e^{j\omega t} f[\omega] d\omega \tag{B.2}$$

$$f^{\dagger}[\omega] = \int_{-\infty}^{\infty} e^{-j\omega t} f^{\dagger}[t] dt. \tag{B.3}$$

Here, I use $j = -\sqrt{-1} = -i$. Many physicists use the definitions with $-i$ substituted for j. It does not matter so long as the definition is consistent throughout a calculation. However, the above convention for imaginary numbers is already chosen for us when we use circuit notation for impedances (say, of an inductor): $Z_{\text{inductor}} = j\omega L$. This is because the impedance notation comes directly from the Fourier transform of the time-dependent circuit equation relating the voltage $V[t]$ to the current $I[t]$:

$$V[t] = L\frac{dI[t]}{dt} \tag{B.4}$$

$$V[\omega] = \int_{-\infty}^{\infty} e^{-j\omega t} V[t] dt = L \int_{-\infty}^{\infty} e^{-j\omega t} \frac{dI[t]}{dt} dt \tag{B.5}$$

$$= L\left[\left(e^{-j\omega t} I[t]\right)\big|_{-\infty}^{\infty} + j\omega \int_{-\infty}^{\infty} e^{-j\omega t} I[t] dt \right] = (j\omega L)I[\omega] \tag{B.6}$$

I will use the above Fourier transform definitions for all cases except when calculating spectral densities and operator expectation values. While it is still possible to use regular Fourier transforms

for spectral densities (the math will still work out), the expressions are less physically intuitive because they involve carrying around Dirac delta functions and canceling them at the end. Instead, I use the more physical windowed Fourier transforms:

$$f[\omega] = \lim_{T \to \infty} \frac{1}{\sqrt{T}} \int_{-T/2}^{T/2} e^{-j\omega t} f[t] dt \tag{B.7}$$

$$f[t] = \lim_{T \to \infty} \frac{\sqrt{T}}{2\pi} \int_{-T/2}^{T/2} e^{j\omega t} f[\omega] d\omega \tag{B.8}$$

$$f^\dagger[\omega] = \lim_{T \to \infty} \frac{1}{\sqrt{T}} \int_{-T/2}^{T/2} e^{-j\omega t} f^\dagger[t] dt \tag{B.9}$$

B.2   Operator expectation values and spectral densities

I have defined all of the noise operators to have the following expectation values:

$$\left\langle \hat{\xi}_i^\dagger[t_2]\hat{\xi}_j[t_1] \right\rangle = n_i^{\text{th}}\delta_{i,j}\delta[t_2 - t_1] \tag{B.10}$$

$$\left\langle \hat{\xi}_i[t_2]\hat{\xi}_j^\dagger[t_1] \right\rangle = \left(n_i^{\text{th}} + 1\right)\delta_{i,j}\delta[t_2 - t_1] \tag{B.11}$$

where the deltas with subscripts are Kronecker deltas and those with square brackets are Dirac deltas.

B.2.1   Regular Fourier transforms

As I said in the previous section, it is more natural here to use windowed Fourier transforms. However, here I'll present the way to use regular Fourier transforms so that the differences are clear. Note that this is not what I use throughout my dissertation. The expectation values in the frequency domain using regular Fourier transforms are then:

$$\left\langle \hat{\xi}_i^\dagger[\omega_2]\hat{\xi}_j[\omega_1] \right\rangle = \int_{-\infty}^{\infty} \int_{-\infty}^{\infty} e^{-j\omega_2 t_2} e^{-j\omega_1 t_1} \left\langle \hat{\xi}_i^\dagger[t_2]\hat{\xi}_j[t_1] \right\rangle dt_2 dt_1 \tag{B.12}$$

$$= \int_{-\infty}^{\infty} \int_{-\infty}^{\infty} e^{-j\omega_2 t_2} e^{-j\omega_1 t_1} n_i^{\text{th}}\delta_{ij}\delta[t_2 - t_1] dt_2 dt_1 \tag{B.13}$$

$$= n_i^{\text{th}}\delta_{ij} \int_{-\infty}^{\infty} e^{-j(\omega_1 + \omega_2)t_2} dt_2 \tag{B.14}$$

$$= 2\pi n_i^{\text{th}}\delta_{i,j}\delta[\omega_1 + \omega_2] \tag{B.15}$$

$$\left\langle \hat{\xi}_i[\omega_2]\hat{\xi}_j^\dagger[\omega_1] \right\rangle = 2\pi(n_i^{\text{th}} + 1)\delta_{i,j}\delta[\omega_1 + \omega_2] \tag{B.16}$$

Very similarly, the expectation values of the mechanical and output operators reveal expressions for their respective spectral densities:

$$\left\langle \hat{b}^\dagger[\omega_2]\hat{b}[\omega_1]\right\rangle = \int_{-\infty}^{\infty}\int_{-\infty}^{\infty} e^{-j\omega_2 t_2}e^{-j\omega_1 t_1}\left\langle \hat{b}^\dagger[t_2]\hat{b}[t_1]\right\rangle dt_2 dt_1 \tag{B.17}$$

$$= \int_{-\infty}^{\infty}\int_{-\infty}^{\infty} e^{-j\omega_2 t_2}e^{-j\omega_1(t_2+\tau)}\left\langle \hat{b}^\dagger[t_2]\hat{b}[t_2+\tau]\right\rangle dt_2 d\tau \tag{B.18}$$

$$= \int_{-\infty}^{\infty}\int_{-\infty}^{\infty} e^{-j\omega_2 t_2}e^{-j\omega_1(t_2+\tau)}\left\langle \hat{b}^\dagger[0]\hat{b}[\tau]\right\rangle dt_2 d\tau \tag{B.19}$$

$$= \int_{-\infty}^{\infty} e^{-j(\omega_1+\omega_2)t_2}dt_2 \int_{-\infty}^{\infty} e^{-j\omega_1\tau}\left\langle \hat{b}^\dagger[0]\hat{b}[\tau]\right\rangle d\tau \tag{B.20}$$

$$= 2\pi\delta[\omega_1+\omega_2]S_{bb}[\omega_1] \tag{B.21}$$

$$S_{bb}[\omega] = \frac{1}{2\pi\delta[0]}\left\langle \hat{b}^\dagger[-\omega]\hat{b}[\omega]\right\rangle \tag{B.22}$$

$$S_{a_{\text{out}}a_{\text{out}}}[\omega] = \frac{1}{2\pi\delta[0]}\left\langle \hat{a}_{\text{out}}^\dagger[-\omega]\hat{a}_{\text{out}}[\omega]\right\rangle. \tag{B.23}$$

In the third step, I used the fact that the autocorrelation function $G_{xy}[\tau] = \left\langle \hat{x}^\dagger[t_2]\hat{y}[t_2+\tau]\right\rangle$ is invariant to time-translation of t_2. I also used the definition of the spectral density:

$$S_{xx}[\omega] = \int_{-\infty}^{\infty} e^{-j\omega t}G_{xx}[t]dt = \int_{-\infty}^{\infty} e^{-j\omega t}\left\langle \hat{x}^\dagger[0]\hat{x}[t]\right\rangle dt \tag{B.24}$$

As stated previously, the expressions derived in this section will work (the operator expectation values will have Dirac deltas of 0 to cancel the ones in the denominators); however, using windowed Fourier transforms leads to much cleaner and more physical expressions for the spectral densities.

B.2.2 Windowed Fourier transforms

Windowed Fourier transforms can be used to calculate the expectation values and give nearly identical results to regular Fourier transforms. The one benefit is that the pesky Dirac delta

functions found with regular Fourier transforms end up as Kronecker delta functions here:

$$\left\langle \hat{\xi}_i^\dagger[\omega_2]\hat{\xi}_j[\omega_1] \right\rangle = \lim_{T\to\infty} \frac{1}{T} \int_{-T/2}^{T/2} \int_{-T/2}^{T/2} e^{-j\omega_2 t_2} e^{-j\omega_1 t_1} \left\langle \hat{\xi}_i^\dagger[t_2]\hat{\xi}_j[t_1] \right\rangle dt_2 dt_1 \tag{B.25}$$

$$= \lim_{T\to\infty} \frac{1}{T} \int_{-T/2}^{T/2} \int_{-T/2}^{T/2} e^{-j\omega_2 t_2} e^{-j\omega_1 t_1} n_i^{\text{th}} \delta_{i,j} \delta[t_2 - t_1] dt_2 dt_1 \tag{B.26}$$

$$= n_i^{\text{th}} \delta_{i,j} \lim_{T\to\infty} \frac{1}{T} \int_{-T/2}^{T/2} e^{-j(\omega_1+\omega_2)t_2} dt_2 \tag{B.27}$$

$$= n_i^{\text{th}} \delta_{i,j} \delta_{\omega_2,-\omega_1} \tag{B.28}$$

$$\left\langle \hat{\xi}_i[\omega_2]\hat{\xi}_j^\dagger[\omega_1] \right\rangle = (n_i^{\text{th}} + 1)\delta_{i,j}\delta_{\omega_2,-\omega_1} \tag{B.29}$$

$$\left\langle \hat{b}^\dagger[\omega_2]\hat{b}[\omega_1] \right\rangle = \lim_{T\to\infty} \frac{1}{T} \int_{-T/2}^{T/2} \int_{-T/2}^{T/2} e^{-j\omega_2 t_2} e^{-j\omega_1 t_1} \left\langle \hat{b}^\dagger[t_2]\hat{b}[t_1] \right\rangle dt_2 dt_1 \tag{B.30}$$

$$= \lim_{T\to\infty} \frac{1}{T} \int_{-T/2}^{T/2} \int_{-T/2-t_2}^{T/2-t_2} e^{-j\omega_2 t_2} e^{-j\omega_1 (t_2+\tau)} \left\langle \hat{b}^\dagger[t_2]\hat{b}[t_2 + \tau] \right\rangle dt_2 d\tau \tag{B.31}$$

$$= \lim_{T\to\infty} \frac{1}{T} \int_{-T/2}^{T/2} \int_{-\infty}^{\infty} e^{-j\omega_2 t_2} e^{-j\omega_1 (t_2+\tau)} \left\langle \hat{b}^\dagger[0]\hat{b}[\tau] \right\rangle dt_2 d\tau \tag{B.32}$$

$$= \lim_{T\to\infty} \frac{1}{T} \int_{-T/2}^{T/2} e^{-j(\omega_1+\omega_2)t_2} dt_2 \int_{-\infty}^{\infty} e^{-j\omega_1 \tau} \left\langle \hat{b}^\dagger[0]\hat{b}[\tau] \right\rangle d\tau \tag{B.33}$$

$$= \delta_{\omega_2,-\omega_1} S_{bb}[\omega_1] \tag{B.34}$$

$$S_{bb}[\omega] = \left\langle \hat{b}^\dagger[-\omega]\hat{b}[\omega] \right\rangle \tag{B.35}$$

$$S_{a_{\text{out}}a_{\text{out}}}[\omega] = \left\langle \hat{a}_{\text{out}}^\dagger[-\omega]\hat{a}_{\text{out}}[\omega] \right\rangle. \tag{B.36}$$

Using windowed Fourier transforms instead of the regular versions will not change the final outcome of a calculation in any way (assuming one or the other is used consistently). However, getting rid of the canceling Dirac deltas makes using windowed Fourier transforms a bit more physical.

B.3   Convolutions

The definition of a convolution is

$$f[\omega] * g[\omega] \equiv \frac{1}{2\pi} \int_{-\infty}^{\infty} f[\omega']g[\omega - \omega']d\omega'. \tag{B.37}$$

Thus, the product of two functions in the time domain is the convolution of those two functions in the frequency domain:

$$
\begin{aligned}
\int_{-\infty}^{\infty} f[t]g[t]e^{-j\omega t}dt &= \int_{-\infty}^{\infty} \left(\frac{1}{2\pi} \int_{-\infty}^{\infty} f[\omega']e^{j\omega' t}d\omega' \right) \left(\frac{1}{2\pi} \int_{-\infty}^{\infty} g[\omega'']e^{j\omega'' t}d\omega'' \right) e^{-j\omega t}dt & \text{(B.38)} \\
&= \frac{1}{(2\pi)^2} \int_{-\infty}^{\infty} d\omega' \int_{-\infty}^{\infty} f[\omega']g[\omega'']d\omega'' \int_{-\infty}^{\infty} e^{j(\omega'+\omega''-\omega)t}dt & \text{(B.39)} \\
&= \frac{1}{2\pi} \int_{-\infty}^{\infty} d\omega' \int_{-\infty}^{\infty} f[\omega']g[\omega'']\delta[\omega' + \omega'' - \omega]d\omega'' & \text{(B.40)} \\
&= \frac{1}{2\pi} \int_{-\infty}^{\infty} f[\omega']g[\omega - \omega']d\omega' & \text{(B.41)} \\
&= f[\omega] * g[\omega] & \text{(B.42)}
\end{aligned}
$$

If one of those functions is a complex conjugate, we get

$$
\int_{-\infty}^{\infty} f[t]g^*[t]e^{-j\omega t}dt = f[\omega] * g^*[-\omega]. \tag{B.43}
$$

Appendix C

Discussion of different Fano resonance models

Different strategies have been employed to understand response data that displays a Fano resonance attributed to wire bonds. One, presented in [74], attempts to extract the resonant frequency and linewidth of the cavity that would have been found had there not been reactive components in the feed line. This is a sensible strategy if the goal is to characterize the bare resonator - for instance if you wanted to study many resonators as a function of some fabrication parameter, such as dielectric thickness. The other strategy, the one that I develop in Section 2.1.3, attempts to find the resonant frequency and linewidth of the cavity that now characterize its behavior. I want to be able to infer the state of a mechanical oscillator from the cavity readout, so it is important that I know the cavity parameters that the mechanical oscillator 'sees'. Thus, I want the extracted parameters to correspond to the response of the voltage $\tilde{V}$ across the capacitor C, and I do not really care what the cavity parameters would have been had there not been reactive components in the feed line.

If I re-write the cavity response calculated in reference [74] in my own variables (and set the reactances in different ports equal), I find:

$$S_{21} = \frac{1}{1 + jB} - \frac{\kappa_{\text{ext}}/2}{\kappa/2 + j\left(\omega - \omega_0 + \kappa_{\text{ext}}B/2\right)}. \tag{C.1}$$

This is identical to Equation 2.39, but with ω_0 called the resonance frequency rather than ω_{c}. If I use both equations to fit the Fano resonance shown in Figure C(a), I get the exact same fit line and parameters other than resonance frequency; however, Equation 2.39 results in a resonance frequency of 5.22058 GHz, while Equation C.1 results in a resonance frequency of 5.22072 GHz.
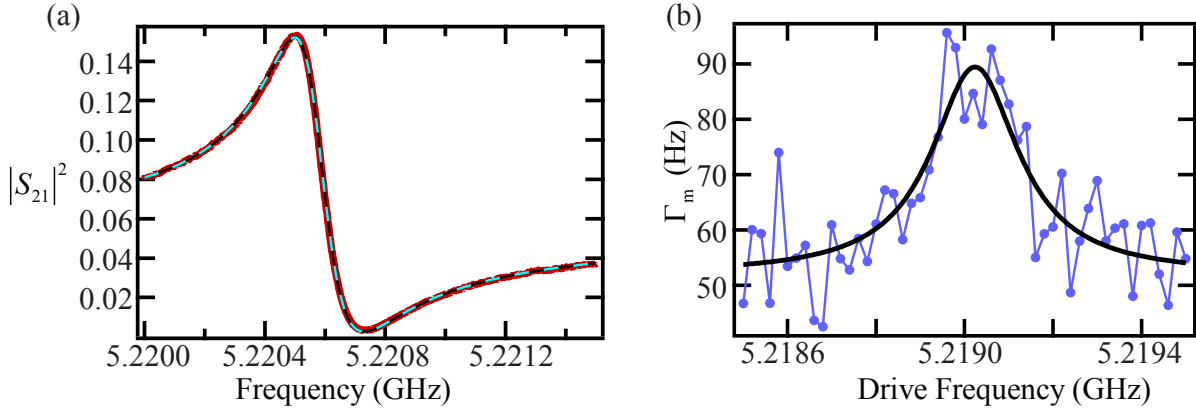
Figure C.1: Fano resonance fits. (a) Response and fits from a resonant circuit in the transmission geometry, displaying a Fano response. The data (red) is fit using Equation C.1 (black) and Equation 2.39 (teal, dashed). (b) Mechanical linewidth as a function of microwave drive frequency, along with a fit to Equation C.2

.

To see which resonance frequency interacts with the mechanics, I show data of the mechanical linewidth as a function of red-detuned microwave drive frequency, measured on the same device at a similar power (Figure C(b)). What we see is a Lorentzian lineshape, demonstrating that the mechanical oscillator 'sees' a Lorentzian voltage response, even if the cavity response is Fano. The mechanical resonance frequency for this device is 1.5249 MHz, putting it in the resolved sideband limit. Thus, the theoretical expression for the mechanical linewidth with an approximately red-detuned drive is

$$\Gamma_{\text{tot}} = \Gamma_{\text{m}} + \frac{4g^2\kappa}{\kappa^2 + 4(\omega_{\text{d}} - \omega_{\text{c}} + \Omega_{\text{m}})^2}. \tag{C.2}$$

From this I can extract a cavity frequency of 5.22055 GHz, consistent with the value extracted from fitting the cavity response with Equation 2.39.

Appendix D

Component responses for interferometric detection

D.1   Beam splitters and photodetectors as linear detectors

In Chapter 4, I discuss heterodyne and homodyne interferometric detection. I model these measurement schemes in the optical domain, as beam splitters and photodetector are easily modeled and understood. However, the physics behind interferometric detection is identical in the optical and microwave regimes, so all the results obtained are directly relevant to our experiments. In this section, I introduce the beam splitter and photodetector transformations and show how these elements can be combined to make either a single or two-quadrature linear detector.

A simple beam splitter (Figure D.1(a)) creates two output fields, $\hat{c}$ and $\hat{d}$, that are linear combinations of the input fields $\hat{a}$ and $\hat{b}$. For a beam splitter with transmission coefficient η, the fields are related by

$$\hat{c}[t] \;=\; \sqrt{\eta}\hat{b}[t] + j\sqrt{1-\eta}\hat{a}[t], \tag{D.1}$$

$$\hat{d}[t] \;=\; \sqrt{\eta}\hat{a}[t] + j\sqrt{1-\eta}\hat{b}[t]. \tag{D.2}$$

A simple photodetector (Figure D.1(b)) measures the intensity $\hat{I}$ due to the incoming field
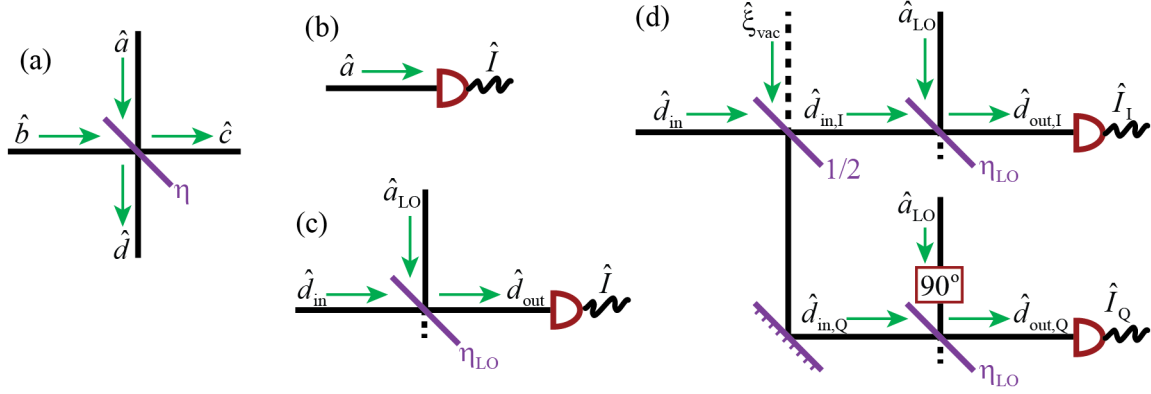
Figure D.1: Measurement models in the optical regime. (a) A beam splitter with transmission η transforms two input signals $\hat{a}$ and $\hat{b}$ into two linear combinations $\hat{c}$ and $\hat{d}$. (b) An optical photodetector detects the intensity $\hat{I}$ of an incident field $\hat{a}$. (c) Single quadrature linear field detector. A linear measurement of field $\hat{d}_{\text{in}}$ can be made by combining it with a strong coherent local oscillator $\hat{d}_{\text{LO}}$ and detecting the intensity $\hat{I}$ of the output field $\hat{d}_{\text{out}}$. (d) Two quadrature linear field detector. Both quadratures of the input field can be detected by first splitting the signal in half and then performing a linear measurement of each piece. The quadrature component is found by using a local oscillator that is ninety degrees out of phase. Additional noise $\hat{\xi}_{\text{vac}}$ must be added in this process through the vacuum port of the initial beam splitter.

$\hat{a}$: $\hat{I}[t] = \hat{a}^\dagger[t]\hat{a}[t]$. The average value of this intensity is

$$
\left\langle \hat{I}[t] \right\rangle = \left\langle \hat{a}^\dagger[t]\hat{a}[t] \right\rangle = \int_{-\infty}^{\infty} \left\langle \hat{a}^\dagger[t]\hat{a}[t+\tau] \right\rangle \delta[\tau] d\tau \tag{D.3}
$$

$$
= \int_{-\infty}^{\infty} \left\langle \hat{a}^\dagger[0]\hat{a}[\tau] \right\rangle \left(\frac{1}{2\pi} \int_{-\infty}^{\infty} e^{-j\omega\tau} d\omega \right) d\tau \tag{D.4}
$$

$$
= \frac{1}{2\pi} \int_{-\infty}^{\infty} \left(\int_{-\infty}^{\infty} e^{-j\omega\tau} \left\langle \hat{a}^\dagger[0]\hat{a}[\tau] \right\rangle d\tau \right) d\omega = \frac{1}{2\pi} \int_{-\infty}^{\infty} S_{aa}[\omega] d\omega, \tag{D.5}
$$

where, as in Appendix B, I have used the fact that the autocorrelation function $\left\langle \hat{x}^\dagger[t_2]\hat{y}[t_2+\tau] \right\rangle$ is invariant to time-translation of t_2. The result of these equations is that the average value of the intensity is the integral of the number spectral density, which is just the total photon number incident on the detector, as expected.

A linear measurement of a signal of interest $\hat{d}_{\text{in}}[t]$ can be performed by combining that signal on a beam splitter of transmission η_{LO} with a local oscillator $\hat{d}_{\text{LO}}[t] = A_{\text{LO}} e^{j\phi_{\text{LO}}} e^{j\omega_{\text{LO}}t} + \hat{\xi}_{\text{LO}}[t]$ (see Figure D.1(c)) and then detecting the output on a photodetector. The field incident on the

photodetector will be

$$\hat{d}_{\text{out}}[t] = \sqrt{\eta_{\text{LO}}}\hat{d}_{\text{in}}[t] + j\sqrt{1-\eta_{\text{LO}}}(A_{\text{LO}}e^{j\phi_{\text{LO}}}e^{j\omega_{\text{LO}}t} + \hat{\xi}_{\text{LO}}[t]). \tag{D.6}$$

Any noise $\hat{\xi}_{\text{LO}}[t]$ accompanying the strong coherent LO field will add to the signal of interest unless $\eta_{\text{LO}} \gg 1 - \eta_{\text{LO}}$. Making this assumption, and the assumption that the local oscillator power is much larger than the signal power $(A_{\text{LO}}^2(1-\eta_{\text{LO}}) \gg \langle \hat{d}_{\text{in}}^\dagger[t]\hat{d}_{\text{in}}[t] \rangle \eta_{\text{LO}})$, the detected intensity is

$$\hat{I}[t] = \hat{d}_{\text{out}}^\dagger[t]\hat{d}_{\text{out}}[t] \tag{D.7}$$

$$\approx A_{\text{LO}}^2(1-\eta_{\text{LO}}) + jA_{\text{LO}}\sqrt{\eta_{\text{LO}}(1-\eta_{\text{LO}})}\left(e^{j\phi_{\text{LO}}}e^{j\omega_{\text{LO}}t}\hat{d}_{\text{in}}^\dagger[t] - e^{-j\phi_{\text{LO}}}e^{-j\omega_{\text{LO}}t}\hat{d}_{\text{in}}[t]\right) \tag{D.8}$$

$$\hat{I}[\omega] = A_{\text{LO}}^2(1-\eta_{\text{LO}})2\pi\delta[\omega] \tag{D.9}$$

$$+jA_{\text{LO}}\sqrt{\eta_{\text{LO}}(1-\eta_{\text{LO}})}\left(e^{j\phi_{\text{LO}}}\hat{d}_{\text{in}}^\dagger[\omega - \omega_{\text{LO}}] - e^{-j\phi_{\text{LO}}}\hat{d}_{\text{in}}[\omega + \omega_{\text{LO}}]\right).$$

The average value of the intensity is $\langle \hat{I}[t] \rangle = A_{\text{LO}}^2(1-\eta_{\text{LO}})$, which is just the number of coherent photons. The AC part of the intensity can be re-written in terms of two orthogonal field quadratures, $\hat{X}$ and $\hat{Y}$:

$$\hat{X}[\omega] = \hat{X}^\dagger[\omega] = \hat{d}[\omega + \omega_{\text{LO}}] + \hat{d}^\dagger[\omega - \omega_{\text{LO}}], \tag{D.10}$$

$$\hat{Y}[\omega] = \hat{Y}^\dagger[\omega] = -j(\hat{d}[\omega + \omega_{\text{LO}}] - \hat{d}^\dagger[\omega - \omega_{\text{LO}}]), \tag{D.11}$$

$$\hat{I}[\omega] = \hat{I}^\dagger[\omega] = A_{\text{LO}}\sqrt{\eta_{\text{LO}}(1-\eta_{\text{LO}})}\left(-\sin[\phi_{\text{LO}}]\hat{X}[\omega] + \cos[\phi_{\text{LO}}]\hat{Y}[\omega]\right). \tag{D.12}$$

This expression illustrates that this detection scheme can only detect a single quadrature at a time. Which quadrature it detects is determined by the local oscillator phase.

Returning to the intensity in terms of fields, the spectral density of the intensity (ignoring the part at DC and referencing back to the input state to put the spectrum in photon units) is:

$$S_{II}^{\text{photon}}[\omega] = \frac{S_{II}[\omega]}{2A_{\text{LO}}^2\eta_{\text{LO}}(1-\eta_{\text{LO}})} = \frac{\langle \hat{I}^\dagger[-\omega]\hat{I}[\omega] \rangle}{2A_{\text{LO}}^2\eta_{\text{LO}}(1-\eta_{\text{LO}})} \tag{D.13}$$

$$= \frac{1}{2}\left\{\langle \hat{d}_{\text{in}}[-\omega + \omega_{\text{LO}}]\hat{d}_{\text{in}}^\dagger[\omega - \omega_{\text{LO}}] \rangle + \langle \hat{d}_{\text{in}}^\dagger[-\omega - \omega_{\text{LO}}]\hat{d}_{\text{in}}[\omega + \omega_{\text{LO}}] \rangle\right. \tag{D.14}$$

$$\left. -e^{2j\phi_{\text{LO}}}\langle \hat{d}_{\text{in}}^\dagger[-\omega - \omega_{\text{LO}}]\hat{d}_{\text{in}}^\dagger[\omega - \omega_{\text{LO}}] \rangle - e^{-2j\phi_{\text{LO}}}\langle \hat{d}_{\text{in}}[-\omega + \omega_{\text{LO}}]\hat{d}_{\text{in}}[\omega + \omega_{\text{LO}}] \rangle\right\}$$

$$= \frac{1}{2} + \frac{1}{2}\left(S_{d_{\text{in}}d_{\text{in}}}[\omega_{\text{LO}} - \omega] + S_{d_{\text{in}}d_{\text{in}}}[\omega_{\text{LO}} + \omega]\right) \tag{D.15}$$

$$-\frac{1}{2}\left(e^{2j\phi_{\text{LO}}}\langle \hat{d}_{\text{in}}^\dagger[-\omega - \omega_{\text{LO}}]\hat{d}_{\text{in}}^\dagger[\omega - \omega_{\text{LO}}] \rangle + e^{-2j\phi_{\text{LO}}}\langle \hat{d}_{\text{in}}[-\omega + \omega_{\text{LO}}]\hat{d}_{\text{in}}[\omega + \omega_{\text{LO}}] \rangle\right)$$

There is half a quanta of overall added noise, two spectral terms now converted to low frequencies and folded on top of each other, and two extra terms which for certain conditions may be nonzero and cause interference.

As I showed above, the detection scheme in Figure D.1(c) only measures one quadrature of the field of interest. In order to measure both quadratures, the signal can be split in half on a beam splitter and then each half can be sent to a single-quadrature linear detector, one of which has a local oscillator ninety degrees out of phase from the other (Figure D.1(d)). This allows detection of both the in-phase and quadrature components of the field; however, it comes at the cost of additional added noise that comes in through the vacuum port of the first beam splitter. This extra noise is in fact required of any measurement of both quadratures of the field due to the non-commutativity of the field quadratures. The intensities measured for each quadrature of the two-quadrature measurement are

$$
\hat{I}_{\mathrm{I}}[\omega] = j\frac{A_{\mathrm{LO}}}{\sqrt{2}}\sqrt{\eta_{\mathrm{LO}}(1-\eta_{\mathrm{LO}})}\left\{ e^{j\phi_{\mathrm{LO}}}\left(\hat{d}_{\mathrm{in}}^{\dagger}[\omega-\omega_{\mathrm{LO}}]-j\hat{\xi}_{\mathrm{vac}}^{\dagger}[\omega-\omega_{\mathrm{LO}}]\right) \right. \tag{D.16}
$$
$$
\left. -e^{-j\phi_{\mathrm{LO}}}\left(\hat{d}_{\mathrm{in}}[\omega+\omega_{\mathrm{LO}}]+j\hat{\xi}_{\mathrm{vac}}[\omega+\omega_{\mathrm{LO}}]\right)\right\}
$$
$$
= \frac{A_{\mathrm{LO}}}{\sqrt{2}}\sqrt{\eta_{\mathrm{LO}}(1-\eta_{\mathrm{LO}})}\left(\sin[\phi_{\mathrm{LO}}](-\hat{X}[\omega]+\hat{Y}_{\xi}[\omega])+\cos[\phi_{\mathrm{LO}}](\hat{Y}[\omega]+\hat{X}_{\xi}[\omega])\right), \tag{D.17}
$$
$$
\hat{I}_{\mathrm{Q}}[\omega] = \frac{A_{\mathrm{LO}}}{\sqrt{2}}\sqrt{\eta_{\mathrm{LO}}(1-\eta_{\mathrm{LO}})}\left\{ e^{j\phi_{\mathrm{LO}}}\left(\hat{d}_{\mathrm{in}}^{\dagger}[\omega-\omega_{\mathrm{LO}}]+j\hat{\xi}_{\mathrm{vac}}^{\dagger}[\omega-\omega_{\mathrm{LO}}]\right) \right. \tag{D.18}
$$
$$
\left. +e^{-j\phi_{\mathrm{LO}}}\left(\hat{d}_{\mathrm{in}}[\omega+\omega_{\mathrm{LO}}]-j\hat{\xi}_{\mathrm{vac}}[\omega+\omega_{\mathrm{LO}}]\right)\right\}
$$
$$
= \frac{A_{\mathrm{LO}}}{\sqrt{2}}\sqrt{\eta_{\mathrm{LO}}(1-\eta_{\mathrm{LO}})}\left(\sin[\phi_{\mathrm{LO}}](\hat{Y}[\omega]-\hat{X}_{\xi}[\omega])+\cos[\phi_{\mathrm{LO}}](\hat{X}[\omega]+\hat{Y}_{\xi}[\omega])\right). \tag{D.19}
$$

Here, $\hat{X}_{\xi}$ and $\hat{Y}_{\xi}$ are quadratures of the vacuum noise field. Ignoring the noise terms, the in-phase detector measures $(-\sin[\phi_{\mathrm{LO}}]\hat{X}[\omega]+\cos[\phi_{\mathrm{LO}}]\hat{Y}[\omega])$, the same field quadrature as the single-quadrature detector above. The quadrature detector measures the orthogonal combination, $(\sin[\phi_{\mathrm{LO}}]\hat{Y}[\omega]+\cos[\phi_{\mathrm{LO}}]\hat{X}[\omega])$. The intensity spectral densities from two-quadrature measurement (returning to

field notation) are

$$
S^{\text{photon}}_{I(Q)I(Q)}[\omega] \;=\; \frac{\left\langle \hat{I}^\dagger_{\text{I(Q)}}[-\omega]\hat{I}_{\text{I(Q)}}[\omega]\right\rangle}{A^2_{\text{LO}}\eta_{\text{LO}}(1-\eta_{\text{LO}})} \tag{D.20}
$$

$$
=\; 1 + \frac{1}{2}\left(S_{d_{\text{in}}d_{\text{in}}}[\omega_{\text{LO}}-\omega] + S_{d_{\text{in}}d_{\text{in}}}[\omega_{\text{LO}}+\omega]\right) \tag{D.21}
$$

$$
\mp\frac{1}{2}\left(e^{2j\phi_{\text{LO}}}\left\langle \hat{d}^\dagger_{\text{in}}[-\omega-\omega_{\text{LO}}]\hat{d}^\dagger_{\text{in}}[\omega-\omega_{\text{LO}}]\right\rangle\right.
$$

$$
\left.+e^{-2j\phi_{\text{LO}}}\left\langle \hat{d}_{\text{in}}[-\omega+\omega_{\text{LO}}]\hat{d}_{\text{in}}[\omega+\omega_{\text{LO}}]\right\rangle\right).
$$

The negative sign is for the in-phase intensity, while the positive sign is for the quadrature intensity. The in-phase part is identical to what I found for the single-quadrature measurement, except that there is now an extra half quantum of added noise. For some cases, the last two terms will be nonzero and can interfere maximally and oppositely for the two quadratures. However, for cases where these terms are zero, the information is split equally between the two quadratures. In this case, it is optimal to measure the spectral density of a combination of the in-phase and quadrature intensities: $\hat{I}_\theta = \left(e^{j\theta}\hat{I}_\text{I} + e^{-j\theta}\hat{I}_\text{Q}\right)/\sqrt{2}$. The spectral density in this case is

$$
S^{\text{photon}}_{I_\theta I_\theta}[\omega] \;=\; \frac{\left\langle \hat{I}^\dagger_\theta[-\omega]\hat{I}_\theta[\omega]\right\rangle}{A^2_{\text{LO}}\eta_{\text{LO}}(1-\eta_{\text{LO}})} \tag{D.22}
$$

$$
=\; 1 + \frac{1-\sin[2\theta]}{2}S_{d_{\text{in}}d_{\text{in}}}[\omega_{\text{LO}}-\omega] + \frac{1+\sin[2\theta]}{2}S_{d_{\text{in}}d_{\text{in}}}[\omega_{\text{LO}}+\omega]. \tag{D.23}
$$

A choice of θ essentially filters away frequencies above or below the local oscillator.

D.2 Linear, phase-insensitive amplifiers

In this section, I look at the kind of linear amplifiers most frequently employed in microwave experiments - those whose amplification is not sensitive to the phase of the signal being amplified. The most state-of-the-art phase insensitive microwave amplifiers are High Electron Mobility Transistor (HEMT) amplifiers. I will show that a phase insensitive amplifier must necessarily add noise to the signal it is amplifying. A very similar but more extensive discussion can be found in [107, Chapter 2.4].

A phase insensitive amplifier must amplify all quadratures of the microwave field by the same amount. However, the output fields $\hat{c}_{\text{out}}$ cannot simply be an amplified version of the input fields

$\hat{c}_{\text{in}}$. If they were, the field commutation rules would be violated:

$$\left[\hat{c}_{\text{out}}[\omega_1], \hat{c}_{\text{out}}^{\dagger}[\omega_2]\right] = \delta_{\omega_1, -\omega_2}, \tag{D.24}$$

$$\left[\sqrt{G}\hat{c}_{\text{in}}[\omega_1], \sqrt{G}\hat{c}_{\text{in}}^{\dagger}[\omega_2]\right] = G\delta_{\omega_1, -\omega_2}, \tag{D.25}$$

$$\hat{c}_{\text{out}}[\omega] \neq \sqrt{G}\hat{c}_{\text{in}}[\omega]. \tag{D.26}$$

In order for the commutation relations to be preserved, noise due to the internal modes of the amplifier must be added to the amplified input field:

$$\hat{c}_{\text{out}}[\omega] = \sqrt{G}\hat{c}_{\text{in}}[\omega] + j\sqrt{G-1}\hat{\xi}_{\text{amp}}^{\dagger}[\omega], \tag{D.27}$$

$$\left[\hat{c}_{\text{out}}[\omega], \hat{c}_{\text{out}}^{\dagger}[\omega]\right] = \left[\sqrt{G}\hat{c}_{\text{in}}[\omega] + j\sqrt{G-1}\hat{\xi}_{\text{amp}}^{\dagger}[\omega], \sqrt{G}\hat{c}_{\text{in}}^{\dagger}[\omega] - j\sqrt{G-1}\hat{\xi}_{\text{amp}}[\omega]\right] \tag{D.28}$$

$$= G\left[\hat{c}_{\text{in}}[\omega], \hat{c}_{\text{in}}^{\dagger}[\omega]\right] + (G-1)\left[\hat{\xi}_{\text{amp}}^{\dagger}[\omega], \hat{\xi}_{\text{amp}}[\omega]\right] \tag{D.29}$$

$$= G - (G-1) = 1. \tag{D.30}$$

The effective output signal (normalized by the gain G) is

$$\hat{c}_{\text{out,eff}}[\omega] = \hat{c}_{\text{in}}[\omega] + j\sqrt{1 - G^{-1}}\hat{\xi}_{\text{amp}}^{\dagger}[\omega], \tag{D.31}$$

$$\left[\hat{c}_{\text{out,eff}}[\omega], \hat{c}_{\text{out,eff}}^{\dagger}[\omega]\right] = \frac{1}{G}. \tag{D.32}$$

For sufficiently large gain, the commutation of the effective microwave fields will be zero, indicating that the fields can be thought of classically.

D.3   Josephson parametric amplifiers (linear, phase-sensitive amplifiers)

In this section, I solve the equations of motion for the Josephson Parametric Amplifier (JPA) and arrive at the transformation between incident signal fields and their amplified outgoing counterparts. Much of this analysis follows [108] (but retains my definitions of Fourier transforms and stays in the lab frame).

D.3.1   Equation of motion and solution for the JPA

I model the JPA as a cavity resonator with a Kerr nonlinearity, coupled to a single input/output port with coupling rate γ_{ext} (see figure D.2). The total linear cavity dissipation rate is
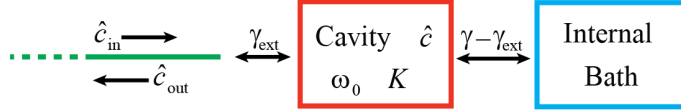
Figure D.2: Model of the Josephson Parametric Amplifier. A nonlinear resonant cavity with resonant frequency ω_0 and Kerr constant K is coupled via rate γ_{ext} to a single input/output port. The total linear loss rate for the cavity is γ. The operators for internal, input, and output modes are $\hat{c}$, $\hat{c}_{\text{in}}$, and $\hat{c}_{\text{out}}$, respectively.

γ. I am only interested in the response of the system, so I will ignore all noise sources. The system Hamiltonian is

$$\hat{\mathcal{H}}_{\text{system}}[t] = \hbar\omega_0 \hat{c}^\dagger[t]\hat{c}[t] + \frac{\hbar}{2}K\hat{c}^\dagger[t]\hat{c}^\dagger[t]\hat{c}[t]\hat{c}[t], \tag{D.33}$$

where ω_0 is the bare cavity resonance frequency, K is the Kerr constant, and $\hat{c}^\dagger(\hat{c})$ is the creation (annihilation) operator for the cavity. Including the input field $\hat{c}_{\text{in}}$, I arrive at the Heisenberg-Langevin equation of motion:

$$\dot{\hat{c}}[t] = \frac{j}{\hbar}\left[\hat{c}[t], \hat{\mathcal{H}}_{\text{system}}[t]\right] + \sqrt{\gamma_{\text{ext}}}\hat{c}_{\text{in}}[t] - \frac{\gamma}{2}\hat{c}[t] \tag{D.34}$$

$$= -\left(\frac{\gamma}{2} - j\omega_0\right)\hat{c}[t] + jK\hat{c}^\dagger[t]\hat{c}[t]\hat{c}[t] + \sqrt{\gamma_{\text{ext}}}\hat{c}_{\text{in}}[t]. \tag{D.35}$$

I assume that the fields incident on the JPA are a large coherent pump field at frequency ω_{p} with amplitude $c_{\text{in},0}$ and a relatively smaller signal field with amplitude $\hat{c}_{\text{in},1}$. I can thus write these fields in the following form:

$$\hat{c}_{\text{in}}[t] = c_{\text{in},0}e^{j\omega_{\text{p}}t} + \hat{c}_{\text{in},1}[t], \tag{D.36}$$

$$\hat{c}[t] = c_0 e^{j\phi_{\text{p}}}e^{j\omega_{\text{p}}t} + \hat{c}_1[t], \tag{D.37}$$

$$\hat{c}^\dagger[t] = c_0 e^{-j\phi_{\text{p}}}e^{-j\omega_{\text{p}}t} + \hat{c}_1^\dagger[t]. \tag{D.38}$$

Here, the coherent amplitude $c_{\text{in},0}$ is generally complex, but c_0 is defined to be real with ϕ_{p} accounting for phase. The number of pump photons n_{p} in the cavity is c_0^2. The zeroth order (coherent) solution to the equation of motion ($\hat{c}_{\text{in},1} = \hat{c}_1 = 0$) is

$$c_{\text{in},0} = c_0 e^{j\phi_{\text{p}}}\frac{\gamma + 2j(Kc_0^2 - z)}{2\sqrt{\gamma_{\text{ext}}}}, \tag{D.39}$$

where $z = \omega_0 - \omega_p + 2Kc_0^2$. Linearizing the Heisenberg-Langevin equations of motion about the zeroth order solution gives

$$\dot{\hat{c}}_1[t] = -\left(\frac{\gamma}{2} - j(\omega_p + z)\right)\hat{c}_1[t] + je^{2j(\omega_p t + \phi_p)}Kc_0^2\hat{c}_1^\dagger[t] + \sqrt{\gamma_{ext}}\hat{c}_{in,1}[t], \qquad (D.40)$$

$$\dot{\hat{c}}_1[t] + (W - j\omega_p)\hat{c}_1[t] + e^{2j\omega_p t}V\hat{c}_1^\dagger[t] = \sqrt{\gamma_{ext}}\hat{c}_{in,1}[t]. \qquad (D.41)$$

Here, $W = \gamma/2 - jz$ and $V = -je^{2j\phi_p}Kc_0^2$. Equation D.41 is equivalent to the one before it, but is arranged with the inter-cavity fields on the left of the equation and the input field on the right. Making a transformation to take $x = $ Equation D.41 to $\dot{x} + (W^* - j\omega_p)x - e^{2j\omega_p t}Vx^\dagger$ gives a new equation

$$\ddot{\hat{c}}_1[t] + (W + W^* - 2j\omega_p)\dot{\hat{c}}_1[t] + ((W - j\omega_p)(W^* - j\omega_p) - |V|^2)\hat{c}_1[t] \qquad (D.42)$$

$$= \sqrt{\gamma_{ext}}\left(\dot{\hat{c}}_{in,1}[t] + (W^* - j\omega_p)\hat{c}_{in,1}[t] - e^{2j\omega_p t}V\hat{c}_{in,1}^\dagger[t]\right).$$

The reason for re-writing the equation of motion this way is that it is now in terms of only the cavity annihilation operator - the creation operator has been eliminated. Fourier transforming into the frequency domain now easily results in a solution for $\hat{c}_1$, and thus the output field, in terms of the input fields:

$$\hat{c}_1[\omega]\left((W + j(\omega - \omega_p))(W^* + j(\omega - \omega_p)) - |V|^2\right) \qquad (D.43)$$

$$= \sqrt{\gamma_{ext}}\left((W^* + j(\omega - \omega_p))\hat{c}_{in,1}[\omega] - V\hat{c}_{in,1}^\dagger[\omega - 2\omega_p]\right),$$

$$\hat{c}_1[\omega] = \sqrt{\gamma_{ext}}\frac{(W^* + j(\omega - \omega_p))\hat{c}_{in,1}[\omega] - V\hat{c}_{in,1}^\dagger[\omega - 2\omega_p]}{(W + j(\omega - \omega_p))(W^* + j(\omega - \omega_p)) - |V|^2}, \qquad (D.44)$$

$$\hat{c}_{out,1}[\omega] = \hat{c}_{in,1}[\omega] - \sqrt{\gamma_{ext}}\hat{c}_1[\omega] = L[\omega]\hat{c}_{in,1}[\omega] + M[\omega]\hat{c}_{in,1}^\dagger[\omega - 2\omega_p], \qquad (D.45)$$

$$\hat{c}_{out,1}^\dagger[\omega] = \; = L^*[-\omega]\hat{c}_{in,1}^\dagger[\omega] + M^*[-\omega]\hat{c}_{in,1}[\omega + 2\omega_p]. \qquad (D.46)$$

Here, $L[\omega]$ is the direct (amplitude) gain and $M[\omega]$ is the intermodulation (amplitude) gain.

D.3.2   JPA direct and intermodulation gains

The direct gain of the JPA is

$$
\begin{aligned}
L[\omega] &= \frac{(W - \gamma_{\text{ext}} + j(\omega - \omega_{\text{p}}))(W^* + j(\omega - \omega_{\text{p}})) - |V|^2}{(W + j(\omega - \omega_{\text{p}}))(W^* + j(\omega - \omega_{\text{p}})) - |V|^2} \tag{D.47} \\
&= \frac{(\gamma/2 - \gamma_{\text{ext}} + j(\omega - \omega_{\text{p}} - z))(\gamma/2 + j(\omega - \omega_{\text{p}} + z)) - K^2 n_{\text{p}}^2}{(\gamma/2 + j(\omega - \omega_{\text{p}} - z))(\gamma/2 + j(\omega - \omega_{\text{p}} - z)) - K^2 n_{\text{p}}^2}, \tag{D.48}
\end{aligned}
$$

where I have written the expression in terms of number of photons $n_{\text{p}} = c_0^2$. As a function of frequency, the maximum gain should be achieved at $\omega = \omega_{\text{p}}$. The optimal pump frequency can then be found by maximizing the direct gain $|L[\omega]|^2$ with respect to z. This occurs at $z = 0$, indicating that the pump frequency and photon number should be chosen such that $\omega_{\text{p}} = \omega_0 + 2K n_{\text{p}}$ to optimize gain. From now on, I assume that $z = 0$. The direct gain on resonance ($\omega = \omega_{\text{p}}$) is then

$$
L[\omega_{\text{p}}] = L_0 = \frac{4K^2 n_{\text{p}}^2 - \gamma(\gamma - 2\gamma_{\text{ext}})}{4K^2 n_{\text{p}}^2 - \gamma^2} \tag{D.49}
$$

. Rewriting the frequency dependent direct gain in terms of L_0 rather than the number of pump photons gives

$$
L[\omega] = \frac{L_0 \gamma \gamma_{\text{ext}} - 2j(\omega - \omega_{\text{p}})(L_0 - 1)(\gamma - \gamma_{\text{ext}} + j(\omega - \omega_{\text{p}}))}{\gamma \gamma_{\text{ext}} - 2j(\omega - \omega_{\text{p}})(L_0 - 1)(\gamma + j(\omega - \omega_{\text{p}}))}. \tag{D.50}
$$

If I make the substitutions $\omega_{\text{p}} = \omega_{\text{J}}$, $\gamma_{\text{ext}} = L_0 \kappa_{\text{J}}$ and $\gamma = L_0 \tilde{\kappa}_{\text{J}}$ and then expand to linear order in $1/L_0$ (large gain approximation), I find

$$
L[\omega] \approx \frac{L_0 \kappa_{\text{J}}}{\kappa_{\text{J}} - 2j(\omega - \omega_{\text{J}})}. \tag{D.51}
$$

This is a Lorentzian response with linewidth κ_{J} and resonant frequency ω_{J}. The amplifier bandwidth $\kappa_{\text{J}} = \gamma_{\text{ext}}/L_0$ decreases with increasing on-resonant gain (or photon number). This expression makes clear the fact that the gain-bandwidth product $L_0 \kappa_{\text{J}} = \gamma_{\text{ext}}$ is always constant (since γ_{ext} is a fixed function of cavity geometry).

The intermodulation gain of the JPA is

$$
\begin{aligned}
M[\omega] &= \frac{-\sqrt{\gamma_{\text{ext}}} V}{(W + j(\omega - \omega_{\text{p}}))(W^* + j(\omega - \omega_{\text{p}})) - |V|^2} \tag{D.52} \\
&= je^{2j\phi_{\text{p}}} \frac{\gamma \gamma_{\text{ext}} \sqrt{(L_0 - 1)(L_0 - 1 + 2\gamma_{\text{ext}}/\gamma)}}{\gamma \gamma_{\text{ext}} - 2j(\omega - \omega_{\text{p}})(L_0 - 1)(\gamma + j(\omega - \omega_{\text{p}}))}. \tag{D.53}
\end{aligned}
$$

If I make the substitutions $\omega_p = \omega_J$ and $\gamma = \gamma_{ext} = L_0 \kappa_J$ and then expand to linear order in $1/L_0$ (large gain approximation), I find

$$M[\omega] \approx je^{2j\phi_p} \frac{L_0 \kappa_J}{\kappa_J - 2j(\omega - \omega_p)} \approx je^{2j\phi_p} L[\omega]. \tag{D.54}$$

D.3.3   JPA quadrature amplification

I have so far found how the incident and reflected creation and annihilation operators are affected by the JPA. However, the transformations performed on orthogonal quadrature representations of the input and output fields is more interesting. Two orthogonal field quadratures can be defined by

$$X_{in(out)}^J[\omega] = e^{-j\phi}\hat{c}_{in(out),1}[\omega] + e^{j\phi}\hat{c}_{in(out),1}^\dagger[\omega - 2\omega_J], \tag{D.55}$$

$$Y_{in(out)}^J[\omega] = -je^{-j\phi}\hat{c}_{in(out),1}[\omega] + je^{j\phi}\hat{c}_{in(out),1}^\dagger[\omega - 2\omega_J]. \tag{D.56}$$

Choosing the quadrature phase to be $\phi = \phi_p + \pi/4$, the JPA transformations to these quadratures are

$$X_{out}^J[\omega] = (L[\omega] - je^{-2j\phi_p}M[\omega])X_{in}^J[\omega] \approx 2L[\omega]X_{in}^J[\omega], \tag{D.57}$$

$$Y_{out}^J[\omega] = (L[\omega] + je^{-2j\phi_p}M[\omega])Y_{in}^J[\omega] \approx \frac{Y_{in}^J[\omega]}{2L^*[\omega]}. \tag{D.58}$$

To get these results, I have used the equivalences $L^*[-\omega + 2\omega_J] = L[\omega]$ and $M^*[-\omega + 2\omega_J] = -e^{-4j\phi_p}M[\omega]$. To get the approximate expressions, I plugged in the full expressions for L and M, expanded to lowest order in $1/L_0$, and then re-wrote the result in terms of L. These expressions make it clear that the Y^J quadrature is deamplified by the same amount that the X^J quadrature is amplified, such that the product of their power gains is always unity. This means that no added noise is required in order to preserve commutation relations between input and output fields. Because the JPA amplifies the two quadratures by different amounts, it is a phase-sensitive amplifier.

If I had instead used the approximate expressions for the direct and intermodulation gains, I would have found the same result for X_{out}^J but I would have found $Y_{out}^J = 0$. In practice, the Y quadrature will be deamplified below the noise floor, so these are fine approximations to make for

calculating measured quantities, even though they do not preserve the product of the quadrature power gains.

Appendix E

Effective mass

When calculating the force sensitivity of an optomechanical system, we are often most interested in its sensitivity to a force at the mechanical oscillator's point of maximum displacement (at this point, a force will result in the largest change of motion and thus the most sensitive detection of that force). For a wire's fundamental mode, this means a force at its midpoint. For a circular membrane's fundamental mode, this means a force at the center. For other modes, the position of optimal force sensitivity might be located at some other point.

In order to determine the sensitivity to a force near the mechanical resonance frequency at a mechanical wire's midpoint, $z = l/2$, I want to model that wire as an effective point mass m_{eff} on a spring, where the mass' displacement $\tilde{u}$ is the displacement at the center of the wire $u[l/2]$ (see Figure E.1). The total energy of the mass on a spring will then be $m_{\text{eff}} \Omega_{\text{m}}^2 \tilde{u}^2$, while the energy of
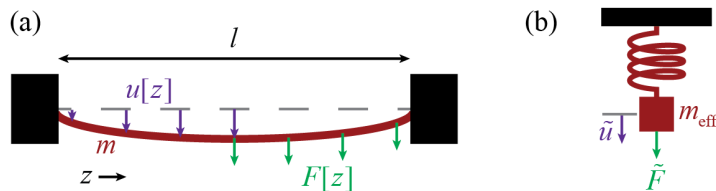
Figure E.1: Equivalent effective mechanical oscillator. (a) Illustration of a mechanical wire of length l, mass m, and displacement $u[z]$, where z points along the wire. The wire is acted on by a force $F[z]$. (b) Illustration of a point mass on a spring of mass m_{eff}, displacement $\tilde{u}$, and force $\tilde{F}$. The spring constant can be chosen such that both oscillators have the same resonant frequency Ω_{m}.

the wire is $\int_0^l (m/l)\Omega_m^2 u[z]^2 dz$. Equating the energies of the two systems, I find

$$m_{\text{eff}} = \boxed{\frac{m \int_0^l u[z]^2 dz}{l u[l/2]^2}}. \tag{E.1}$$

For a wire under high tension, the displacement of the first eigenmode is $u[z] = A\sin[\pi z/l]$. For a wire under low tension, the displacement of the first mode is given in reference [94, pg. 235]: $u[z] = a(\cos[\beta z] - \cosh[\beta z]) + b(\sin[\beta z] - \sinh[\beta z])$, where $\beta l = 4.73$ and $a = -1.0178b$ for the first mechanical mode. Integrating these distributions, I find the effective masses in the two cases:

$$\boxed{m_{\text{eff}} = m/2 \qquad \text{wire with tension}} \tag{E.2}$$

$$\boxed{m_{\text{eff}} = 0.396m \qquad \text{wire without tension}} \tag{E.3}$$

The effective force that will be detected given a force anywhere on the wire can be found by setting the work done in these two pictures equal. The work done on the mass on a spring by a force $\tilde{F}$ is $\tilde{F}\tilde{u}$. The work done on the wire by any force along its length is $\int_0^l (F[z]/l)u[z]dz$. Setting these equal would give a measured force

$$\tilde{F} = \frac{\int_0^l F[z]u[z]dz}{l u[l/2]}. \tag{E.4}$$

Thus, if the wire were acted on by a force constant along the wire's length, $F[z] = F$, the force measured would be $\tilde{F} = 2F/\pi$ for a tensioned wire. However, we are more interested in the case when the force is just a point force at the center of the wire $F[z]/l = F\delta[z - l/2]$. Then the measured force is the actual force $\tilde{F} = F$.

A similar analysis can be done for a circular tensioned membrane of radius R. Here, the radially-symmetric modes are Bessel functions of the first kind of order zero, $u[r, \theta] = J_0[\alpha_i r/R]$, where α_i is the ith root of the Bessel function. The energy of the lowest order mode is

$$\Omega_m^2 \int_0^{2\pi} d\theta \int_0^R r(m/(\pi R^2))u[r, \theta]^2 dr = m\Omega_m^2 J_1[\alpha_1]^2. \tag{E.5}$$

Equating this with the energy of the mass on a spring at the center of the membrane, $m_{\text{eff}}\Omega_m^2$, and plugging in $\alpha_1 = 2.4048$, I find

$$m_{\text{eff}} = m J_1[\alpha_1]^2 = \boxed{0.27m \qquad \text{circular membrane with tension}}. \tag{E.6}$$

Appendix F

Microwave office simulations of wire capacitance

In this appendix, I will describe how I used Microwave Office to simulate the capacitance of a mechanical wire of dimensions $l \times w \times t$, spaced by distance s from a ground plane. I simulated both wires similar to those in references [10, 45, 76] (Section F.1) as well as short wires similar to the one in reference [14] (Section F.2).

For all simulations, I modeled the wire and ground plane as two coupled striplines using Microwave Office's built-in schematic element for 2 Edge Coupled Striplines [109]: "S2CLIN'. It is possible for Microwave Office to model this system as a schematic because it is a problem described by a set of integral equations which can be numerically solved [110]. S2CLIN takes separate widths $W1$ and $W2$ for each conductor, the gap spacing S, the length L, and a substrate definition (see Figure F.1). The substrate definition I used is a Two-Layer Stripline Substrate Definition [111]:
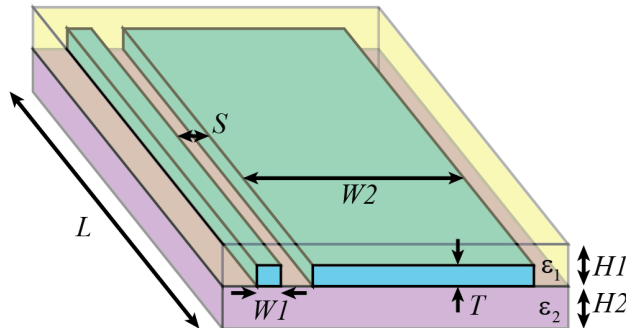
Figure F.1: Geometry for Microwave Office simulations. This is the layout of the S2CLIN schematic built in to Microwave Office.

"SSUBL". It takes a relative dielectric constant ϵ_r and thickness H for dielectrics above and below the conductors, and a conductor thickness T. To model our geometry, I made $W2$ and the H's much larger than the other dimensions and set $\epsilon_\mathrm{r} = 1$ to have vacuum as the dielectrics. In the schematic, I grounded the infinite conductor and connected a 50 Ohm port to the other conductor (the wire). The capacitance between the conductors was found by measuring the admittance Y_{11} at some frequency and then dividing by that frequency: $C = \mathrm{Im}[Y_{11}]/\omega$.

F.1 Microwave Office simulations for long wires

The fabrication dimensions for the best wire devices I made are

$$(t_0, l_0, w_0) = (130\mathrm{nm}, 150\mu\mathrm{m}, 150\mathrm{nm}), \qquad\qquad s \geq 350\mathrm{nm}. \qquad\qquad (\mathrm{F.1})$$

I therefore took sweeps of $50\mathrm{nm} < s < 1\mu\mathrm{m}$ as a function of either l, w, or t with the other two variables fixed to these reference values. The dependencies on each of these variables individually is discussed in the following subsections and a full formula including all variables is found at the end of this section. As I fit to non-integer power laws in the following sections, it is important to know that all variables in the equations are in SI units.

F.1.1 Width dependence for long wires

In Figure F.2(a), the simulated wire capacitance is plotted as a function of spacing from the ground plane for several values of the width w with $t = t_0$ and $l = l_0$ fixed. The simulation for (t_0, l_0, w_0) is in black in all plots. In this plot, the analytic result for the zero thickness coplanar stripline model with $t = t_0$, $l = l_0$, and $w = w_0$ (long black dashes) estimates less capacitance than the simulation and agrees less and less well for small spacings. The parallel wire model (short black dashes) also estimates less capacitance, but seems to have a similar spacing dependence. The coplanar stripline model with thickness (dash-dotted black line) agrees well for large spacings and becomes invalid for small spacings. Looking at the simulations for different widths, there is not much width-dependence. These simulations can be fit to power laws $C_\mathrm{wire} = y_0 + A[w]s^{p[w]}$.
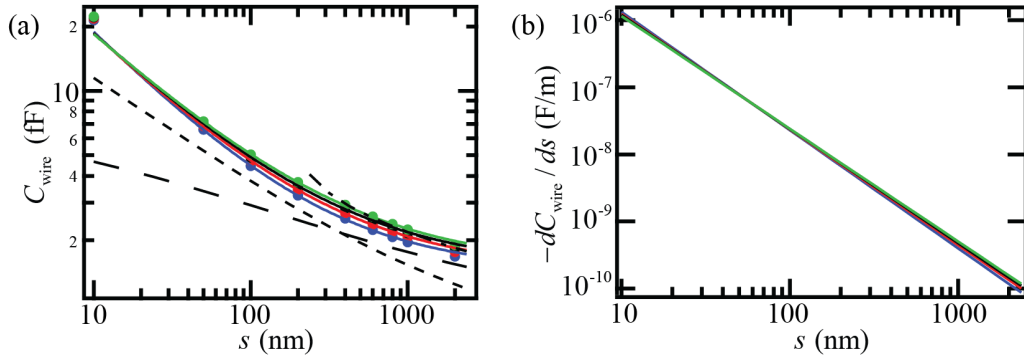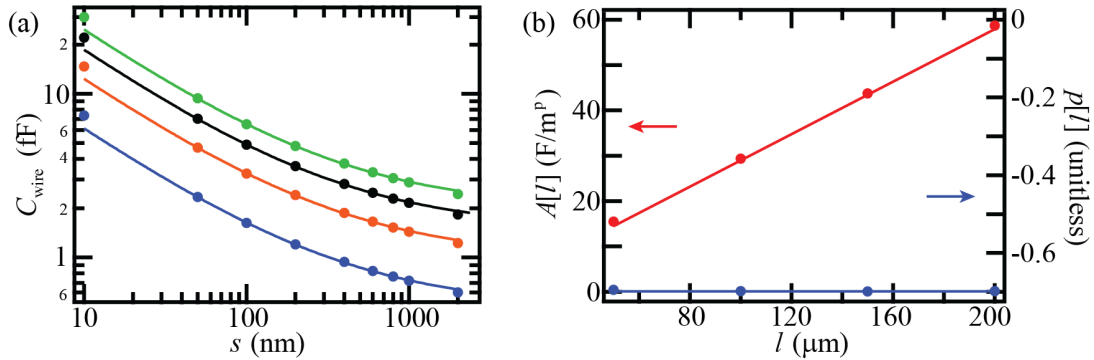
Figure F.2: Width dependence for long wires. (a) Wire capacitance as a function of spacing. The dots are simulations for $t = 130$ nm, $l = 150$ μm, and four values of width: $w = 50$ nm (blue), $w = 100$ nm (red), $w = 150$ nm (black), and $w = 200$ nm (green). The colored lines are power law fits to the data with spacing larger than 50 nm. The black lines are the analytical models presented in Section 5.2.1.3: the parallel wire model (long dashes), the zero thickness coplanar stripline model (short dashes), and the coplanar stripline model with thickness (dash-dotted line). (b) Derivative of wire capacitance with spacing. The derivative (and hence the coupling) is independent of width. The colors are the same as in (a).

Figure F.3: Length dependence for long wires. (a) Wire capacitance as a function of spacing. The dots are simulations for $t = t_0$, $w = w_0$, and four values of length: $l = 50$ μm (blue), $l = 100$ μm (orange), $l = 150$ μm (black), and $l = 200$ μm (green). The colored lines are power law fits to the data with spacing larger than 50 nm. (b) Power law coefficients A (red, left axis) and p (blue, right axis) as a function of length. The power p is essentially independent of length, while the coefficient A is essentially linear in length.

The derivative of capacitance with spacing is then $-dC_{\text{wire}}/ds = A[w]p[w]s^{p[w]-1}$ (shown in figure F.2(b)). This figure makes it clear that dC_{wire}/ds is essentially independent of width.

F.1.2   Length dependence for long wires

In figure F.3(a), the simulated wire capacitance is plotted as a function of spacing from the ground plane for several values of the width l with $w = w_0$ and $t = t_0$. I once again fit this data to power laws $C_{\text{wire}} = y_0 + A[l]s^{p[l]}$. I find that $p[l]$ is essentially the same for the different lengths (figure F.3(b)). The coefficient $A[l]$ is essentially linear in l, so the total capacitance, and therefore also dC_{wire}/ds, is linear in length.

F.1.3   Thickness dependence for long wires

In figure F.4(a), the simulated wire capacitance is plotted as a function of spacing from the ground plane for several values of the thickness t with $w = w_0$ and $l = l_0$. I once again fit this data to power laws $C_{\text{wire}} = y_0 + A[t]s^{p[t]}$. However, C_{wire} is neither independent nor linear in t (unlike for for w or l). In figure F.4(b), I plot the derivative of capacitance $-dC_{\text{wire}}/ds = A[t]p[t]s^{p[t]-1}$ as a function of thickness for several values of spacing. This dependence is essentially linear in t with an offset: $-dC_{\text{wire}}/ds = \alpha[s] + \beta[s]t$. In figure F.4(c), I plot $\alpha[s]$ and $\beta[s]$ as a function of spacing and fit to a power law. This gives me an expression for dC_{wire}/ds:

$$\frac{-dC_{\text{wire}}}{ds} = 1.97 \times 10^{-15} s^{-0.9} + 3.12 \times 10^{-14} s^{-1.8} t = \frac{1.97 \times 10^{-15}}{s^{1.8}} \left(s^{0.9} + 16t\right). \qquad \text{(F.2)}$$

F.1.4   Final formula for long wires

The coupling for long wires appears to be independent of w and proportional to l, at least for cross sections along (l_0, t_0, w) and (l, t_0, w_0), respectively. Assuming these dependences are true for the whole parameter space, the final formula for $-dC_{\text{wire}}/ds$ is

$$\frac{-dC_{\text{wire}}}{ds} = \frac{l}{150 \times 10^{-6}} \frac{1.97 \times 10^{-15}}{s^{1.8}} \left(s^{0.9} + 16t\right) \qquad \text{(F.3)}$$

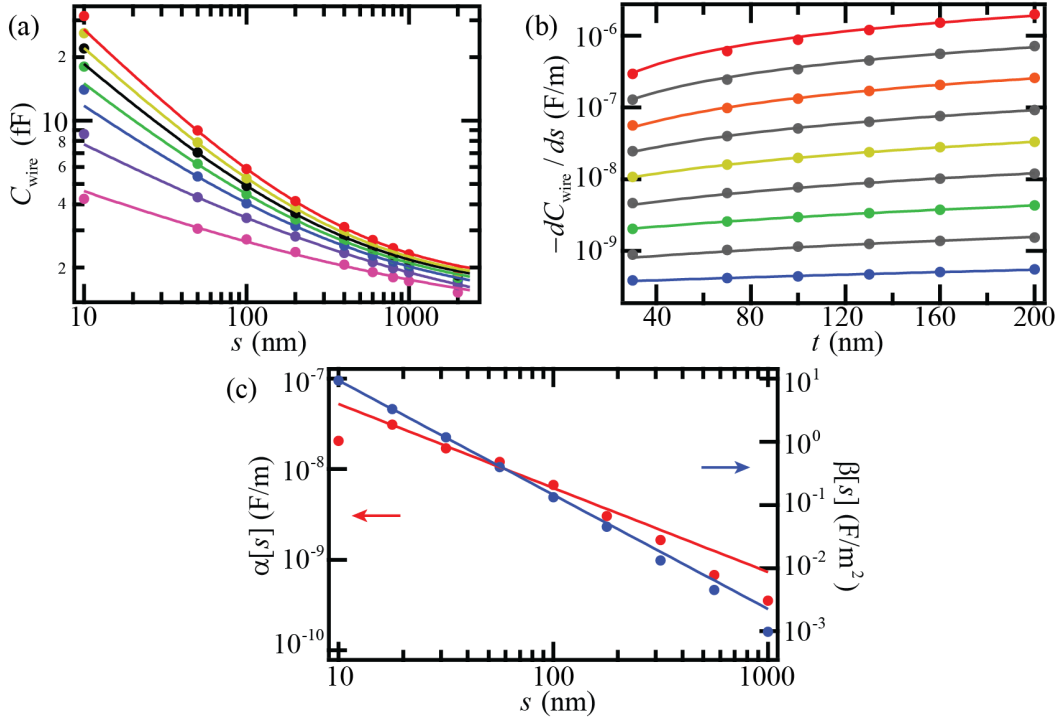$$= \boxed{\frac{1.31 \times 10^{-11}}{s^{1.8}} \left(s^{0.9} + 16t\right) l}. \qquad \text{(F.4)}$$

Figure F.4: Thickness dependence for long wires. (a) Wire capacitance as a function of spacing. The dots are simulations for $l = l_0$, $w = w_0$, and seven values of thickness: $t = 0$ nm (pink), $t = 30$ nm (purple), $t = 70$ nm (blue), $t = 100$ nm (green), $t = 130$ nm (black), $t = 160$ nm (yellow), and $t = 200$ nm (red). The colored lines are power law fits to the data with spacing larger than 50 nm. (b) Derivative of capacitance with respect to spacing, plotted as a function of thickness. Several logarithmically spaced values of the spacing from $s = 10$ nm (red) to $s = 1000$ nm (blue) are plotted. The lines are linear fits. (c) Plot of linear fit coefficients $\alpha[s]$ (red, left axis) and $\beta[s]$ (blue, right axis) as a function of spacing. The lines are power law fits with no offset.

F.2   Microwave Office simulations for short wires

The approximate fabrication dimensions for short wire devices are:

$$(t_0, l_0, w_0) = (130\text{nm}, 5\mu\text{m}, 150\text{nm}), \qquad\qquad s \sim 18\text{nm}. \qquad\qquad \text{(F.5)}$$

I therefore took sweeps of $4\text{nm} < s < 100\text{nm}$ as a function of each of l, w, and t, with the other two variables fixed to the reference values. The dependencies on each of these variables individually is discussed in the following subsections and a full formula including all variables is found at the end of this section.
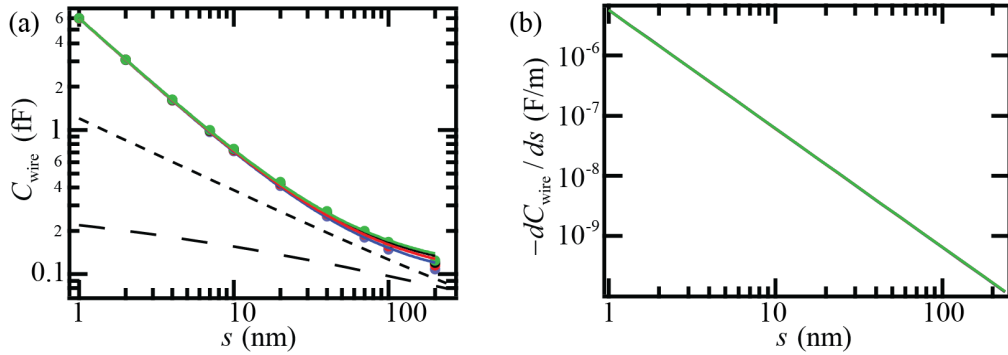
Figure F.5: Width dependence for short wires. (a) Wire capacitance as a function of spacing. The dots are simulations for $t = t_0$, $l = l_0$, and four values of width: $w = 50$ nm (purple), $w = 100$ nm (red), $w = 150$ nm (black), and $w = 200$ nm (green). The colored lines are power law fits to the data. The black lines are the analytical models presented in Section 5.2.1.3: the parallel wire model (long dashes) and the zero thickness coplanar stripline model (short dashes). (b) Derivative of wire capacitance with spacing. The derivative (and hence the coupling) is independent of width. The colors are the same as in (a).
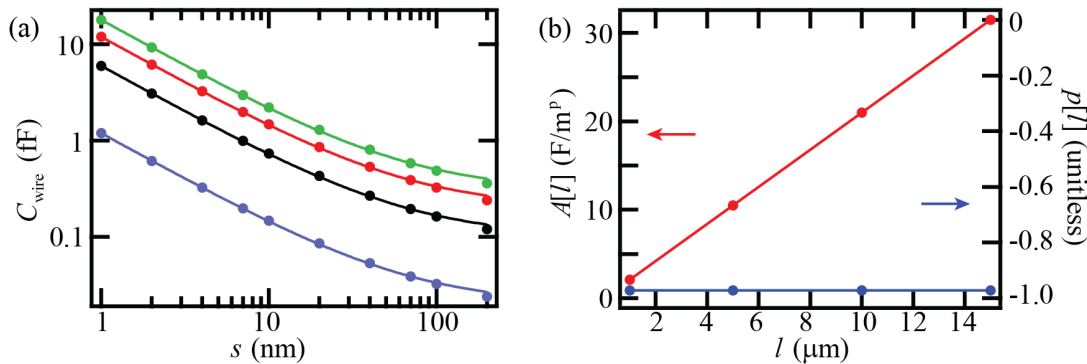

Figure F.6: Length dependence for short wires. (a) Wire capacitance as a function of spacing. The dots are simulations for $t = t_0$, $w = w_0$, and four values of length: $l = 1$ μm (purple), $l = 5$ μm (black), $l = 10$ μm (red), and $l = 15$ μm (green). The colored lines are power law fits to the data. (b) Power law coefficients A (red, left axis) and p (blue, right axis) as a function of length. The power p is essentially independent of length, while the coefficient A is essentially linear in length.

F.2.1   Width dependence for short wires

In figure F.5(a), the simulated wire capacitance is plotted as a function of spacing from the ground plane for several values of the width w. Once again, simulations for (t_0, l_0, w_0) are in black. Both the parallel wire model for $t = t_0$, $w = w_0$, and $l = l_0$ (short black dashes) and the zero thickness coplanar stripline model (long black dashes) estimate a lower capacitance than the simulation and agree less and less well for small spacings. The coplanar stripline model with thickness is not appropriate for these dimensions, so it is not plotted. The simulated data can be fit to power laws $C_{\text{wire}} = y_0 + A[w]s^{p[w]}$. The derivative of capacitance with spacing is then $-dC_{\text{wire}}/ds = A[w]p[w]s^{p[w]-1}$ (shown in figure F.5(b)). Just as for long wires, dC_{wire}/ds is essentially independent of width.

F.2.2   Length dependence for short wires

In figure F.6(a), the simulated wire capacitance is plotted as a function of spacing from the ground plane for several values of the width l with $t = t_0$ and $w = w_0$. I once again fit this data to power laws $C_{\text{wire}} = y_0 + A[l]s^{p[l]}$. As in the long wire case, I find that $p[l]$ is essentially the same for the different lengths (figure F.6(b)) and $A[l]$ is essentially linear in l. Thus, the total capacitance, and therefore also dC_{wire}/ds, is linear in length.

F.2.3   Thickness dependence for short wires

In figure F.7(a), the simulated wire capacitance is plotted as a function of spacing from the ground plane for several values of the thickness t with $l = l_0$ and $w = w_0$. I once again fit this data to power laws $C_{\text{wire}} = y_0 + A[t]s^{p[t]}$. In figure F.7(b), I plot the derivative of capacitance $-dC_{\text{wire}}/ds = A[t]p[t]s^{p[t]-1}$ as a function of thickness for several values of spacing. This dependence is once again essentially linear in t with an offset: $-dC_{\text{wire}}/ds = \alpha[s] + \beta[s]t$. In figure F.7(c), I plot $\alpha[s]$ and $\beta[s]$ as a function of spacing and fit to a power law. This gives me an expression for
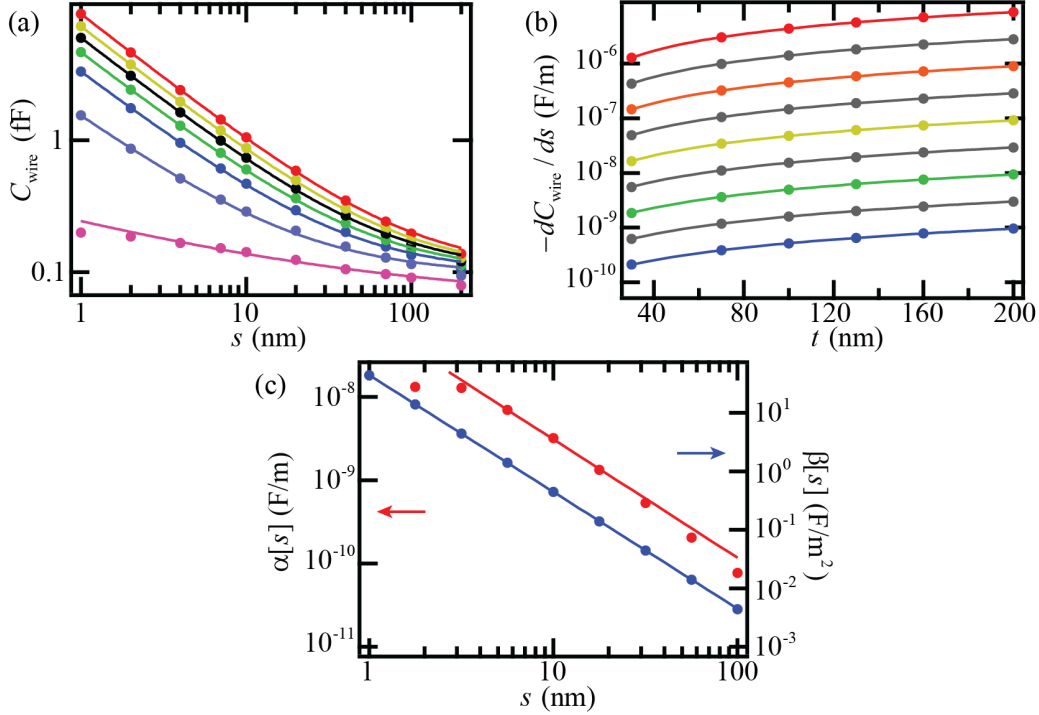
Figure F.7: Thickness dependence for short wires. (a) Wire capacitance as a function of spacing. The dots are simulations for $l = l_0$, $w = w_0$, and seven values of thickness: $t = 0$ nm (pink), $t = 30$ nm (purple), $t = 70$ nm (blue), $t = 100$ nm (green), $t = 130$ nm (black), $t = 160$ nm (yellow), and $t = 200$ nm (red). The colored lines are power law fits to the data. (b) Derivative of capacitance with respect to spacing, plotted as a function of thickness. Several logarithmically spaced values of the spacing from $s = 1$ nm (red) to $s = 100$ nm (blue) are plotted. The lines are linear fits. (c) Plot of linear fit coefficients $\alpha[s]$ (red, left axis) and $\beta[s]$ (blue, right axis) as a function of spacing. The lines are power law fits with no offset.

dC_{wire}/ds:

$$\frac{-dC_{\mathrm{wire}}}{ds} = 1.28 \times 10^{-20} s^{-1.4} + 4.65 \times 10^{-17} s^{-2} t = \frac{1.28 \times 10^{-20}}{s^2} \left(s^{0.6} + 3600t \right). \tag{F.6}$$

F.2.4 Final formula for short wires

The coupling for short wires appears to be independent of w and proportional to l, at least for cross sections along (l_0, t_0, w) and (l, t_0, w_0), respectively. Assuming these dependences are true for the whole parameter space, the final formula for $-dC_{\mathrm{wire}}/ds$ is

$$\frac{-dC_{\mathrm{wire}}}{ds} = \frac{l}{5 \times 10^{-6}} \frac{1.28 \times 10^{-20}}{s^2} \left(s^{0.6} + 3600t \right) = \boxed{\frac{2.56 \times 10^{-15}}{s^2} \left(s^{0.6} + 3600t \right) l}. \tag{F.7}$$
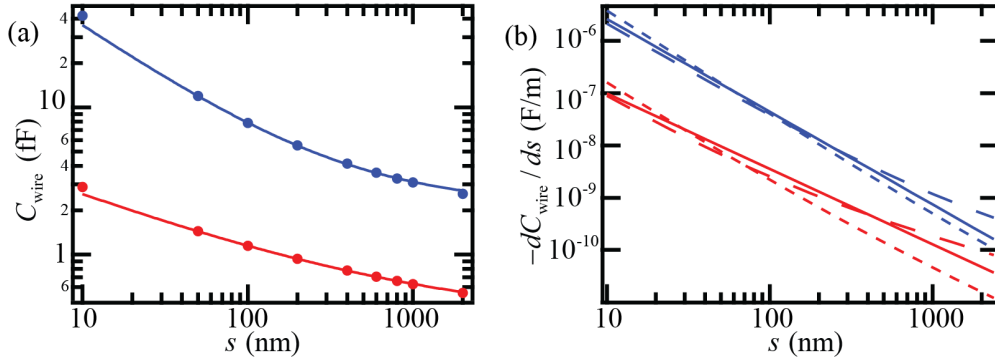
Figure F.8: Check of empirical simulation formula for long wires. The two wires shown are of dimensions $t = 30$ nm, $w = 150$ nm, $l = 50$ μm (red) and $t = 200$ nm, $w = 150$ nm, $l = 200$ μm (blue). (a) Wire capacitance as a function of spacing, with power law fits. (b) Derivative of capacitance with respect to spacing. The solid lines are the simulation. The long and short dashed lines are the predictions from the long and short wire formulas, respectively.

Figure F.9: Check of empirical simulation formulas for short wires. The two wires shown are of dimensions $t = 30$ nm, $w = 150$ nm, $l = 1$ μm (red) and $t = 200$ nm, $w = 150$ nm, $l = 15$ μm (blue). (a) Wire capacitance as a function of spacing, with power law fits. (b) Derivative of capacitance with respect to spacing. The solid lines are the simulation. The long and short dashed lines are the predictions from the long and short wire formulas, respectively.
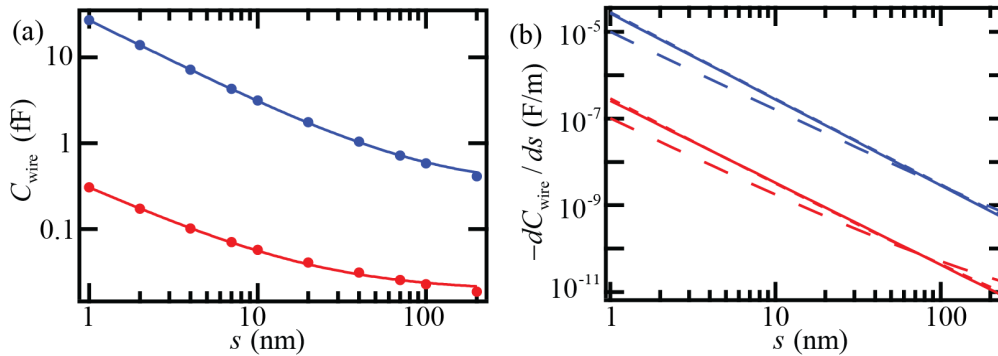
F.3   Check of simulation formulas

I can check the formulas for the long and short wires and see how they differ by applying them to simulated wires at the edges of short and long wire parameter space. The simulated wires and the long and short formulas expectations are shown in figures F.8 and F.9. Surprisingly, both the long and short wire formulas provide reasonably good agreement with the simulations for both

long and short wires. I will therefore only use the long wire formula as the empirical simulation form of coupling in Chapter 5.

Appendix G

Wire device fabrication recipe

Chips used:

- High resistivity wafer with 150 nm thermal oxide, cut into 1 cm squares

Chemicals/resists used:

- ACE (acetone), IPA (isopropanol), DI (deionized water), N2 (nitrogen gas)

- S1813 photoresist (Shipley)

- RD6 photoresist developer (Futurrex)

- Buffer-HF Improved: Ammonium Fluoride, Hydrofluoric Acid, DI (Transene)

- 950 PMMA A7 in anisole (MicroChem)

- 1:3 MIBK/IPA (MicroChem)

General comments:

- Vent RIE 3x after SF_6 etch and clean using O_2 ash (50 sccm, 500 W, 5 min)

- Always place chip on quartz wafer in RIE

- Always agitate chip slightly while developing/etching

- Always spin resist at 4000 rpm, max acceleration, 45 sec

- S1813 resist (4000 rpm): $\sim$ 12000 to 14000 Å

- PMMA (4000 rpm): $\sim$ 4000 Å

- NPGS patterns: $\sim$ 15 nC/cm dose, $\sim$ 25 Å spacing for lines, $\sim$ 425 μC/cm^2, $\sim$ 150 Å for areas

- Evaporating faster gives compressive stress (floppier mechanical elements)

Recipe:

(1) Clean chip

- Blow of dust, soak in ACE w/ sonication, IPA, N2 dry

(2) Alignment mark pattern

- Bake 100°C, 1 min, cool 1 min

- Spin S1813 (5 drops)

- Edge bead removal with ACE, N2 dry

- Bake 100°C, 90 sec

- Align to mask and expose 6 sec

- Develop 35 sec in 15 mL RD6, 10 sec DI, 10 sec fresh DI, N2 dry

(3) Evaporate alignment marks

- O2 ash 50 sccm, 250 W, 30 sec

- Evaporate 5 nm Ti, density 4.5, $\sim$ 5 Å/s, $\sim$ 100 mA

- Evaporate 40 nm Au, density 19.3, $\sim$ 5 Å/s, $\sim$ 85 mA

- Liftoff in ACE > 1 hr, squirt with ACE, sonicate in ACE, IPA, N2 dry

(4) SiO$_2$ holes

- Bake 100°C, 1 min, cool 1 min

- Spin S1813 (5 drops)

- Edge bead removal with ACE, N2 dry

- Bake 100°C, 90 sec

- Align to mask and expose 6 sec

- Develop 35 sec in 15 mL RD6, 10 sec DI, 10 sec fresh DI, N2 dry

- Hard Bake 115°C, 2 min, cool 1 min

- HF 1 min 35 sec, 10 sec DI, 10 sec fresh DI, N2 dry

- Sonicate in ACE, IPA, N2 dry

(5) Double layer resist

- Bake 180°C, 1 min, cool 1 min

- Spin PMMA (2 drops)

- Edge bead removal with ACE, N2 dry

- Bake 180°C, 5 min, cool 1 min

- Spin S1813 (5 drops)

- Edge bead removal with ACE, N2 dry

- Bake 50°C, 90 sec (higher temp can ruin PMMA)

- Align to mask and expose 4 sec

- Develop 30 sec in 15 mL RD6, 5 sec fresh RD6, 10 sec DI, 10 sec fresh DI, N2 dry

- If you screw up:

  * Flood expose 4 sec

  * Develop 40 sec in RD6, 10 sec DI, 10 sec fresh DI, N2 dry

  * Bake PMMA 180°C, 30 sec, cool 45 sec

∗ Spin S1813 (5 drops) and continue as above

(6) Transfer resist pattern to PMMA

- O2 ash 50 sccm, 400 W, 240 sec plus more time until smooth surface is visible in all ashed areas

- Flood expose 4 sec

- Develop 40 sec in 15 mL RD6, 10 sec DI, 10 sec fresh DI, N2 dry

(7) E-beam write

- Write at 35kV, 8mm, probe current 14, current 10 pA

- Write all wires, focusing between each write

- Develop 90 sec in 15 mL 1:3 MIBK/IPA, 20 sec IPA, 20 sec fresh IPA, N2 dry

(8) Evaporate aluminum

- DO NOT DO AN O2 ASH!!

- Evaporate Al, density 2.7, ~ 5 Å/s, ~ 35 mA

- Liftoff in ACE, squirt with ACE, sonicate in ACE, IPA, N2 dry

(9) Cut chip

- Spin S1813 (5 drops)

- Mount chip, sharpen blade, cut using saw speed 2, remove chip

- DI, ACE, IPA, N2 dry

(10) Anneal

- Bake in oven at 340°C for 30 min

- Let cool > 15 min

(11) Suspend wires

- SF6 etch 18 sccm, 450 W, start with $\sim$ 120 sec

- Look in SEM at 28kV, 15mm, to see if mechanics is suspended. If not, repeat.

(12) Mount on sample mount

- Attach chip to board with small dot of rubber cement and allow to dry > 5 min

- Wire bond

Appendix H

Calibration details for two-drive experiments

Measurements of sideband occupation in the two-drive scheme (such as those presented in Chapter 9) rely sensitively on the values used for the number of photons in the cavity due to the red and blue drives (or equivalently, the values of the calibration parameter $\lambda[\omega_r]$ and $\lambda[\omega_b]$). In the following sections, I discuss the methods I use to calibrate these photon numbers, including example data sets.

H.1   Calibration of red drive voltage to photon unit conversion

The number of red drive photons can be found by fitting the magnitude squared of the dressed response of the cavity in the presence of a strong red-detuned drive:

$$|S_{21,\text{meas}}[\omega]|^2 \;=\; G\left|N_2 - \frac{\kappa_1\chi_c[\omega]}{1 + g_r^2\chi_c[\omega]\chi_m[\omega - \omega_r]}\right|^2 + \frac{P_{\text{noise}}}{P_{\text{in}}}. \tag{H.1}$$

Here, G is some gain coefficient and $P_{\text{noise}}/P_{\text{in}}$ is a separately determined background[1] due to the noise of the measurement. This background is usually negligible compared to the signals of interest but could be important as features of the dressed response (especially in the two drive scheme) can approach zero transmission. It is not a free parameter of the fits. The value of $\lambda[\omega_r]$ can be easily

---

[1] If the voltage measured at the output of the experiment has average and fluctuating contributions, $V = \overline{V} + \delta V$, then the measured output power is $P = \overline{V}^2 + 2\overline{V}\delta V + (\delta V)^2$. The average power, assuming that the voltage fluctuations have mean zero, is $\langle P \rangle = \overline{V}^2 + \langle(\delta V)^2\rangle = P_{\text{out}} + P_{\text{noise}}$ and the system response is $|S_{21}|^2 = P_{\text{out}}/P_{\text{in}} + P_{\text{noise}}/P_{\text{in}}$. The variation of the power, averaged over N_{avg} measurements, is $\sigma_P^2 = (\langle P^2 \rangle - \langle P \rangle^2)/N_{\text{avg}} = 4\overline{V}^2\langle(\delta V)^2\rangle/N_{\text{avg}} = 4P_{\text{out}}P_{\text{noise}}/N_{\text{avg}}$. The noise floor of a measurement of $|S_{21}|^2$ is then $P_{\text{noise}}/P_{\text{in}} = N_{\text{avg}}\sigma_{|S_{21}|^2}^2/(4|S_{21}|^2)$. This quantity can be determined experimentally by looking at the value and standard deviation of response data off resonance, where it is constant as a function of frequency.

calculated from the extracted coupling g_r, the bare cavity response parameters, and the measured output drive power:

$$\frac{\lambda[\omega_r]}{g_0^2} = \frac{2\kappa_l Z_0 P_r}{g_r^2 |N_2/\chi_c[\omega_r] - \kappa_l|^2}. \tag{H.2}$$

In addition to determining g_r, a measurement of the dressed response magnitude reveals the bare cavity response parameters, $\overline{\omega}_c$, κ, κ_l, and $N_2 = 1/(1+jB)$, as well as the effective mechanical parameters, Ω_{tot} and Γ_{tot}. Figure H.1 shows measurements of the dressed response and the raw voltage spectrum in the presence of a range of red-detuned drive strengths, along with fits to the theoretical expressions. Figure H.1(a) shows the dressed response over a frequency range where the bare response of the cavity is visible. At the lowest drive power, no mechanical feature is present, while at the highest drive power, the cavity and mechanical modes have begun to hybridize. Figures H.1(b-d) show zoom-ins on the mechanical features from the same data. These figures show that the observed cavity and mechanical features are well described by the theoretical function for the dressed response. Figures H.1(e-f) show the raw voltage spectral densities measured with the same red-detuned drives. Even without a full calibration into optomechanical units, these spectra reveal the total mechanical resonance frequency and linewidth.

Figure H.2 shows the parameters extracted from the data in Figure H.1. Figures H.2(a) and (b) show the cavity resonance frequency and linewidths as a function of generator power. The parameters extracted using the full dressed response fit expression are shown as circles, while those extracted using only a bare cavity fit are shown as crosses. These parameters agree well for all except the highest powers, where the cavity and mechanical modes begin to hybridize and the notion of bare cavity parameters breaks down. Figures H.2(c) and (d) show the extracted mechanical parameters from both the dressed response (black solid circles) and the raw spectral data (red open circles). The spectral data is more reliable at low powers, where the response feature is small, while the response data is more reliable at high powers, where the spectral data is small and squashing must be taken into account. However, the parameters extracted from the two
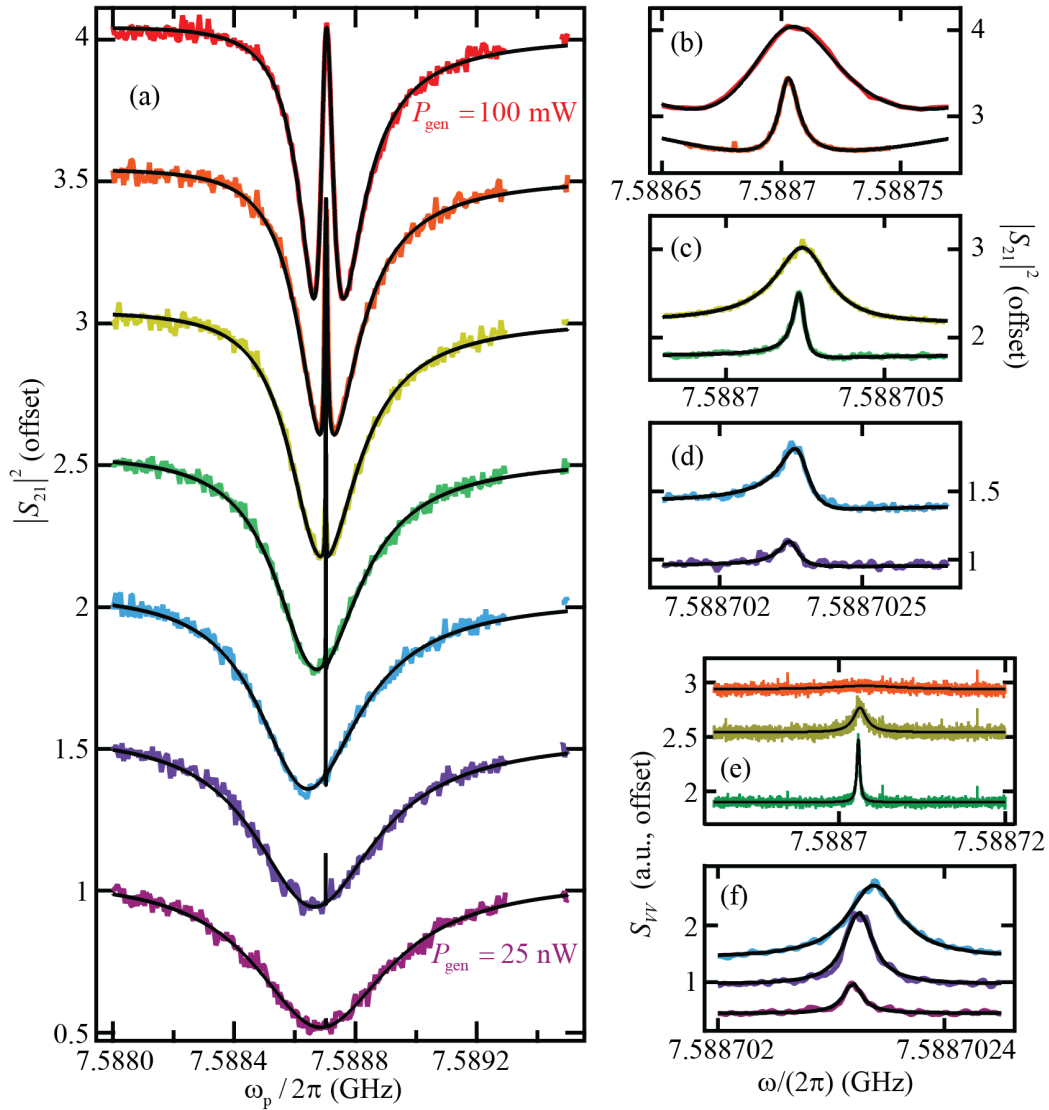
Figure H.1: Dressed response and spectra with a red-detuned drive only. The y-axes of all plots have been offset by 0.5 for each trace to enable clearer examination. All data for a given power is shown in the same color. (a) Dressed response measured for red-detuned generator drive powers in 6 dB steps from 25 nW (magenta) to 100 mW (red). (b-d) Zoom in on the upper red sideband features from (a). (e-f) Raw voltage spectral densities of the mechanical sideband for the same drive frequencies and powers as in the color-corresponding response data.
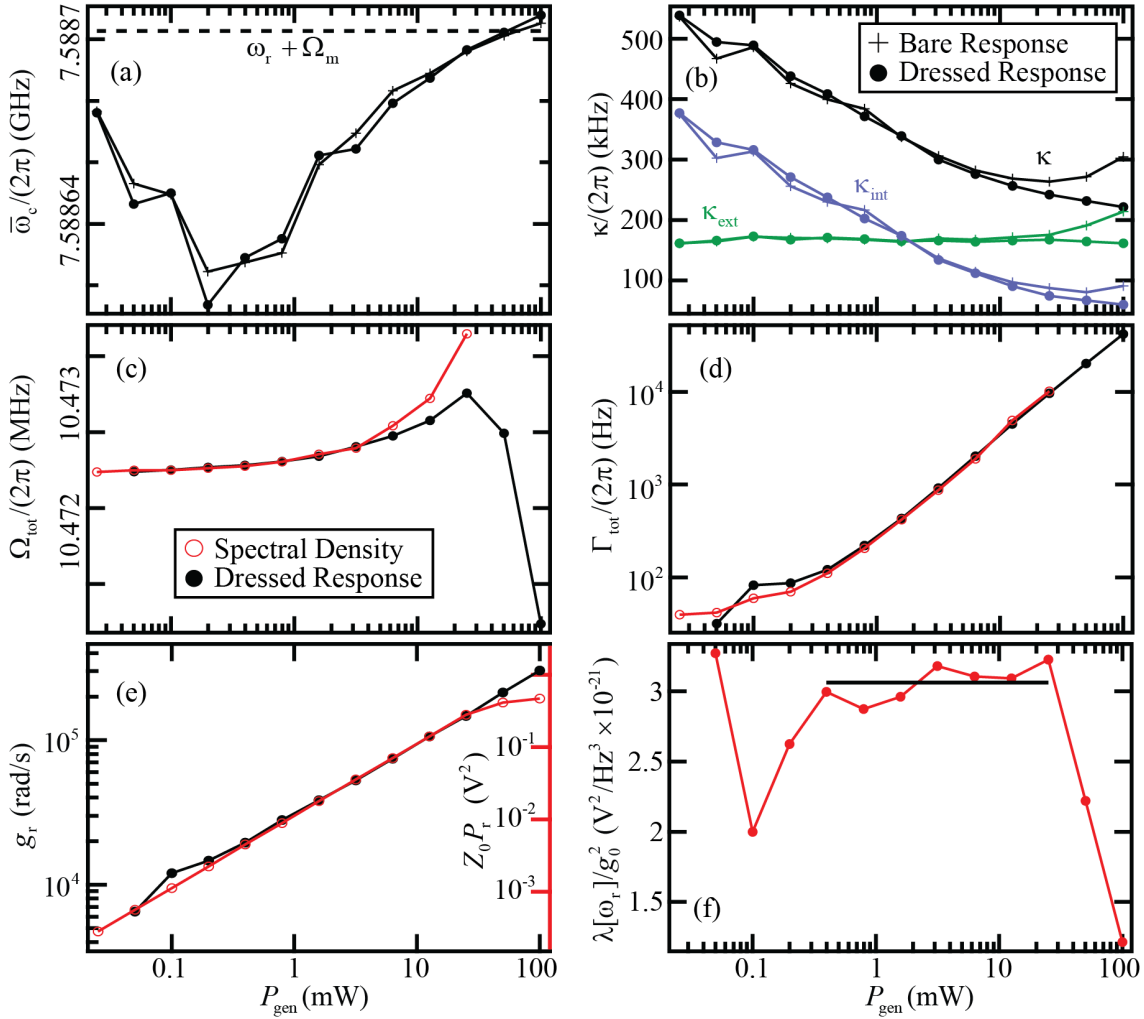
Figure H.2: Extracted parameters from dressed response and spectral data in the presence of a single red-detuned drive. (a) Cavity resonance frequency extracted from both bare (crosses) and dressed (circles) cavity fits. The upper red sideband frequency is shown as a dashed line, indicating that the drive stays approximately red-detuned (compared to the cavity linewidth) for all powers. (b) Cavity linewidths extracted from both bare (crosses) and dressed (circles) cavity fits. The internal (and thus total) linewidth changes drastically with power. (c-d) Effective mechanical resonance frequency and linewidth extracted form dressed response (black solid circles) and raw voltage spectral density (red, open circles) data. (e) Optomechanical coupling $g_r = g_0\sqrt{n_r}$ (black solid circles, left axis) and measured output drive power $Z_0 P_r$ (blue open circles, right axis). (e) Calculated voltage to photon unit conversion factor $\lambda[\omega_r]$. The average over the mid-power section of data is shown as a black line.

types of data agree, especially over the mid-range of powers. Figure H.2(e) shows the extracted values of g_r at each power (black solid circles, left y-axis) as well as the measured output drive power (red open circles, right y-axis). As expected, the output power follows an approximately linear dependence on generator power, while $g_r = g_0\sqrt{n_r}$ follows a square root dependence. Figure H.2(f) shows the calculated values for the parameter $\lambda[\omega_r]$. Ignoring the lowest three values (where the measurement of g_r is less consistent) and the highest two values (where the system begins to hybridize), the average value (black line) is $\lambda[\omega_r]/g_0^2 = 3.0617 \times 10^{-21}$.

H.2   Calibration of blue drive voltage to photon unit conversion

Determining the number of photons in the cavity due to the blue-detuned drive (or equivalently determining $\lambda[\omega_b]$) has proved to be substantially more difficult than determining the number from the red-detuned drive. This section discusses three potential methods I have investigated for doing this calibration: using the dressed response to directly extract g_b, using spectral data with two nearly equal drives to make a relative measurement of g_b/g_r, and using the onset of mechanical parametric oscillation to determine the point where $g_r = g_b$. I will find that the dressed response is often inconsistent with either the expectations found in Section 3.2 or with spectral data taken with the same input fields. These discrepancies likely indicate that our model of the system is incomplete. I avoid these difficulties by measuring spectral data at high occupancy (where any asymmetry should be negligible) and assuming that $n_{m,r}^f = n_{m,b}^f$, allowing me to determine the relative value g_b/g_r. This seems to be the best method for determining the value of $\lambda[\omega_b]$. I also use the onset of mechanical parametric oscillation to try to determine the point where $g_r = g_b$. I find that this method seems to result in a less reproducible calibration than using high occupancy spectral data.

H.2.1   Direct calibration of blue photon number from the dressed cavity response

The number of photons in the cavity due to a blue-detuned drive can theoretically be extracted directly from a measurement of the two-drive dressed response (the dressed response cannot

be measured with only a blue drive at the powers of interest because the mechanical oscillator would self-oscillate). However, I often find that two-drive dressed response measurements do not match the theoretical expectations from my model. One reason for the discrepancy could be dynamic effects from the power dependence of the internal cavity loss, similar to the dynamic photo-thermo-refractive frequency shift described in the supplemental information of reference [65]. This effect is a likely candidate because the internal loss decreases with increasing drive photon number, presumably due to saturation of two-level fluctuators. If this saturation and accompanying decrease in loss are instantaneous, the cavity resonance frequency will decrease ninety degrees in phase later. This will change the number of photons in the cavity, potentially leading to a feedback effect on the cavity resonance frequency.

Additionally, I sometimes see that the mechanical parameters extracted from response and spectral data do not agree. Two examples of this are shown in Figure H.3. These points are the lowest and highest temperature points of a temperature sweep with $g_b \sim g_r \sim 4 \times 10^4$ ($\mathcal{C}_r \sim \mathcal{C}_b \sim 15$). In both figures, the red upper sideband feature in the dressed response is shown in orange (left y-axis) and the red upper spectral sideband is shown in purple (right y-axis). They have been plotted so as to match the backgrounds and peaks of these features, enabling easy comparison of the linewidths and resonance frequencies. In Figure H.3(a), the spectral feature is 40% wider than
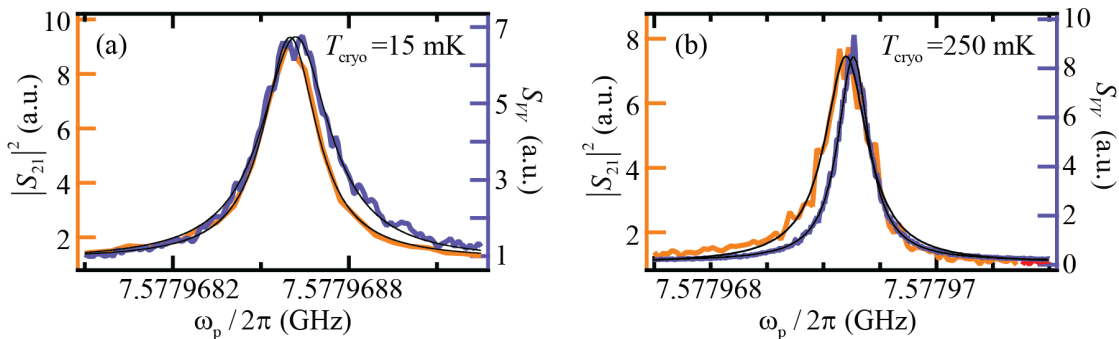

Figure H.3: Examples of inconsistent response (orange) and spectral (purple) features. Sometimes the mechanical resonance frequencies and linewidths extracted from response and spectral data do not agree. Even without fitting to a model, this discrepancy is clear from a visual comparison of the sideband features.

the response feature, while in Figure H.3(b), the response feature is 25% wider. The resonance frequencies also seem slightly different. These discrepancies make it difficult to rely on the two-drive dressed response as a means for calibrating the number of drive photons in the cavity. I also sometimes see discrepancies between the cavity resonance frequency and linewidth extracted from response data (bare or dressed) and the frequency and linewidth of the thermal cavity photon peak in the spectral data.

Despite these difficulties, I have found some drive situations for which two-drive dressed response measurements do seem to be described by my model. Figure H.4 shows a set of measurements for which this is the case. The red and blue drive powers were chosen to be approximately the same, so as to enhance both sideband features, but with the red drive slightly larger than the blue drive, so as to avoid self-oscillation of the mechanical oscillator. The different traces are labeled by point number because both drive powers change between points, as listed in Table H.1. These generator powers correspond to approximate values of cooperativity $0.1 < \mathcal{C} < 600$.

Figure H.4(a) shows a wide view of the dressed response for the even numbered points, along with fits to the two drive dressed response model. The highest powers (points 0 and 2) display the onset of normal mode splitting while the lowest power (point 14) shows no mechanical sideband features. Zoom-ins of the the intermediate power sideband features are shown in Figures H.4(b) and (c). The model agrees well with both the cavity and mechanical features.

Figure H.5 shows the parameters extracted from the two-drive dressed response in Figure H.4 as well as from raw voltage spectral data. Even without calibration of the y-axis, the raw voltage spectral data at high occupancy allows us to extract the mechanical parameters Ω_{tot} and Γ_{tot}, as well as the ratio of red to blue photon numbers (described in more detail in the next section). Figures H.5(a) and (b) show the mechanical parameters extracted from both the response (purple circles) and spectrum (green triangles). These parameters agree well, unlike for the data presented in Figure H.3. Figure H.5(c) shows the voltage to photon unit conversion parameter $\lambda[\omega]$ at the two drive frequencies, calculated using the measured output drive power and the photon numbers extracted from the two-drive dressed response. The parameter extracted at the red drive frequency,

Point	0	1	2	3	4	5	6	7	8	9	10	11	12	13	14
$P_{\text{gen,r}}$ (dBm)	17	14	11	8	5	2	-1	-4	-7	-7	-10	-13	-16	-19	-22
$P_{\text{gen,b}}$ (dBm)	19	17	14	11	8	5	2	-1	-1	-2	-5	-8	-11	-14	-17

Table H.1: Red and blue drive generator powers used in the blue calibration example. The powers were adjusted to keep the number of photons in the cavity due to the two drives approximately balanced.
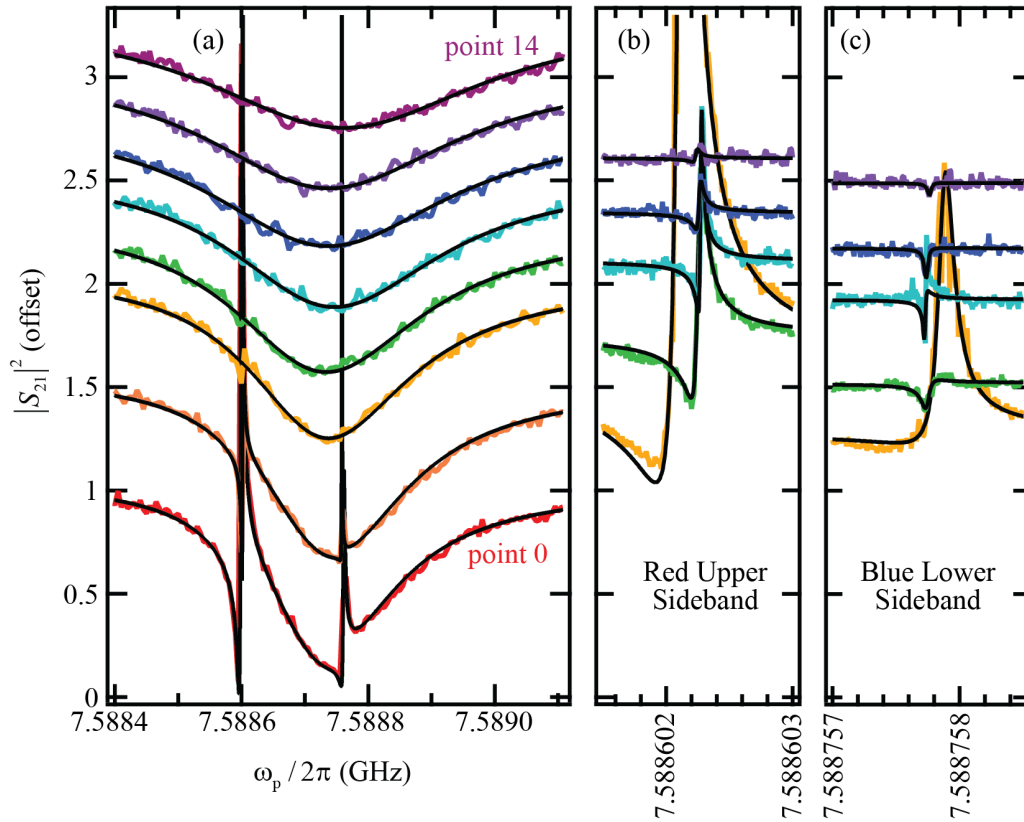

Figure H.4: Dressed cavity response in the presence of two drives, one red-detuned and one blue-detuned, for the even numbered points in Table H.1 (colored consistently in all parts). Each dressed response is offset by 0.25 for clarity of display, except those for points 2 and 4, which are offset by 0.5. (a) Wide view of the dressed response. (b,c) Narrow views of the data in (a) showing the red upper and blue lower sideband features.
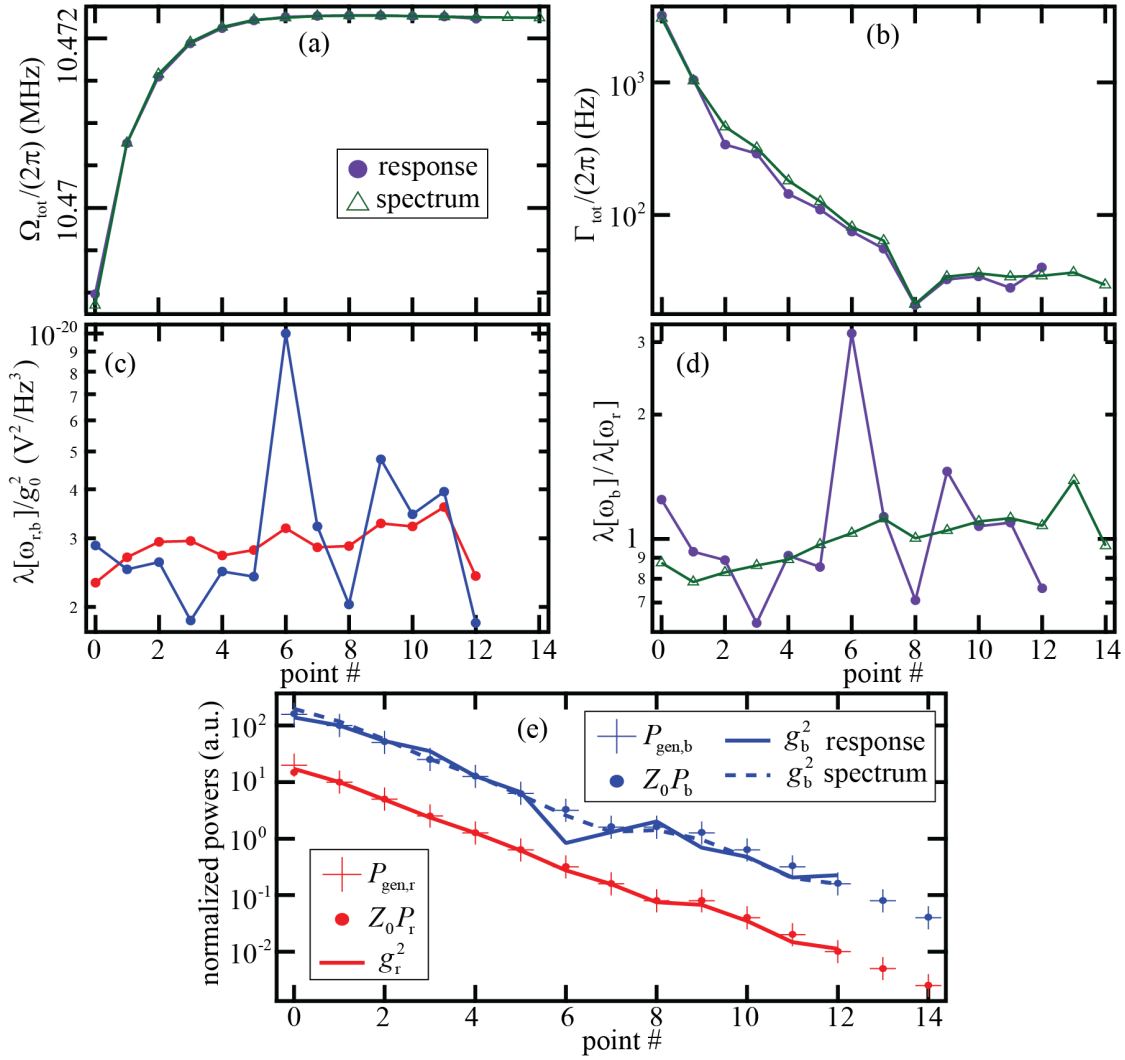
Figure H.5: Summary of parameters extracted from two-drive dressed response and spectral measurements. (a,b) Mechanical resonance frequency and linewidth extracted from the two-drive dressed response and the raw voltage spectral density. (c) Extracted λ at the red and blue drive frequencies from the dressed response. (d) Ratio of λ's at the two drive frequencies extracted both from the dressed response and spectral data. (e) Normalized quantities that should be proportional to the generator power for both drives. The number of blue photons (or g_b^2) extracted from the dressed response is less consistent than the blue photon number extracted from spectral data.

$\lambda[\omega_r]$, is far more consistent from point to point than the parameter at the blue drive frequency, $\lambda[\omega_b]$. In Figure H.5(d), the ratio of these parameters, $\lambda[\omega_b]/\lambda[\omega_r]$ is shown. The purple circles come directly from the data in Figure H.5(c), while the green triangles are calculated using g_b/g_r from the spectral data. This ratio calculated with the spectral data seems far more consistent point

to point than that from the dressed response. The accuracy of the values for g_{b} extracted from the two types of data can be seen another way, looking at Figure H.5(e). In this figure, the various measures of power (generator power, measured power, and photon number) have been normalized by arbitrary factors to permit comparison. The number of red photons clearly follows both the red generator and measured red drive powers. The measured blue power also follows the blue generator power, but the number of blue photons extracted from the dressed response (solid blue line) has several noticeable deviations away from this dependence. The number of blue photons inferred from the number of red photons and the spectral photon ratio (dashed blue line) follows the generator and measured powers much more faithfully.

I conclude that fitting the two-drive dressed response does not provide an adequate determination of the number of blue drive photons in the cavity, as this measurement does not always agree with my model of the system, does not always agree with spectral measurements, and is less reproducible than calibrating with high-occupancy spectral measurements. The insufficiency of my model to explain the data can likely be attributed to dynamic effects due to the highly power-dependent nature of the internal cavity loss.

H.2.2   Relative photon number calibrations using high-occupancy spectra or mechanical parametric oscillation

Rather than measuring the number of cavity photons due to the blue-detuned drive directly, we can calibrate it by making a relative measure of the number of red and blue photons and then using the red-drive calibration above to find the number of blue photons (or equivalently $\lambda[\omega_{\mathrm{b}}]$). One way to do this is to measure the voltage spectral density of the upper red and lower blue mechanical sidebands when the mechanical occupancy is large. In this case, both the asymmetry and any thermal photon occupancy contributions to the sidebands should be negligible and we can make the assumption that $n_{\mathrm{m,r}}^{\mathrm{f}} = n_{\mathrm{m,b}}^{\mathrm{f}} = n_{\mathrm{m}}^{\mathrm{f}}$. Assuming that the sidebands are separated by many

mechanical linewidths, the spectral density takes the limiting form

$$S_{a_{\text{out}} a_{\text{out}}}[\omega] \;\; = \;\; \kappa \kappa_{\text{l}} n_{\text{c}}^{\text{th}} \, |\chi_{\text{c}}[\omega]|^2 + \kappa_{\text{l}} g_{\text{r}}^2 \Gamma_{\text{tot}} n_{\text{m}}^{\text{f}} \, |\chi_{\text{c}}[\omega]|^2 \, |\chi_{\text{m,eff}}[\omega - \omega_{\text{r}}]|^2 \tag{H.3}$$

$$+ \kappa_{\text{l}} g_{\text{b}}^2 \Gamma_{\text{tot}} n_{\text{m}}^{\text{f}} \, |\chi_{\text{c}}[\omega]|^2 \, |\chi_{\text{m,eff}}[\omega_{\text{b}} - \omega]|^2 \, .$$

The ratio of the red to blue sideband amplitudes in this case is $g_{\text{r}}^2/g_{\text{b}}^2$. Thus, even without converting the (high mechanical occupancy) measured voltage spectrum into photon or displacement units, the ratio of red to blue photon numbers can be found by fitting the spectrum with the form

$$S_{VV}[\omega] \;\; = \;\; A_0 + |\chi_{\text{c}}[\omega]|^2 \left(A_{\text{cav}} + A_{\text{r}} \, |\chi_{\text{m,eff}}[\omega - \omega_{\text{r}}]|^2 + A_{\text{b}} \, |\chi_{\text{m,eff}}[\omega_{\text{b}} - \omega]|^2 \right), \tag{H.4}$$

where the A's are some amplitude coefficients. The ratios of photon numbers and λ's are then

$$\frac{g_{\text{b}}}{g_{\text{r}}} = \sqrt{\frac{A_{\text{b}}}{A_{\text{r}}}} \qquad \text{and} \qquad \frac{\lambda[\omega_{\text{b}}]}{\lambda[\omega_{\text{r}}]} = \frac{g_{\text{r}}^2 P_{\text{b}} \, |N_2/\chi_{\text{c}}[\omega_{\text{r}}] - \kappa_{\text{l}}|^2}{g_{\text{b}}^2 P_{\text{r}} \, |N_2/\chi_{\text{c}}[\omega_{\text{b}}] - \kappa_{\text{l}}|^2}. \tag{H.5}$$

Another calibration method that I tried was to use the parametric oscillation of the mechanical oscillator to determine the point where the red and blue photon numbers were the same. At high power, the mechanical linewidth is given by

$$\Gamma_{\text{tot}} = \Gamma_{\text{m}} + \frac{4 g_{\text{r}}^2}{\kappa} - \frac{4 g_{\text{b}}^2}{\kappa} \approx \frac{4(g_{\text{r}}^2 - g_{\text{b}}^2)}{\kappa}. \tag{H.6}$$

Therefore, the linewidth reaches zero and the mechanical oscillator parametrically oscillates at approximately the point where the two drive photon number are equal. I found this point by fixing the blue drive power and decreasing the red drive power until parametric oscillation was observed. I then returned the red drive to the lowest power for which the mechanical oscillator did not parametrically oscillate and measured the output drive powers and bare cavity response. This calibration method is appealing over the high-occupancy spectral calibration, as it does not require spectral measurements (each of which includes measurements of the spectrum with the JPA on, the spectrum with the JPA off, and the JPA response) and can therefore be performed much more quickly.

In order to determine the calibration parameters $\lambda[\omega_{\text{r}}]$ and $\lambda[\omega_{\text{b}}]$ (which we assume could change day-to-day) for a data set of interest, I make several (usually four) identical calibration

measurements before the data set and several (usually four) more after the data set. Averaging over these extracted values, I then assume the calibration parameters are constant throughout the data set. Figure H.6 shows the results obtained from the calibrations associated with the example red calibration above, the example blue calibration above, the temperature sweep used in Chapter 9, and twelve sweeps of the red drive power in an attempt to observe asymmetry similar to the theoretical plot shown in Figure 4.3(c). I call these sweeps asymmetry sweeps 3-14. The frequencies used for each data set are shown in Figure H.6(a), where the upper red and lower blue sideband frequencies are shown relative to the cavity response, which changes from the solid to dashed line throughout the data set. Figure H.6(b) shows the calibration factor $\lambda[\omega_\mathrm{r}]$ extracted from the each measurement of the red-drive-only dressed response (colored markers). The average for each data set is shown as a colored horizontal line. The calibrated values usually seem consistent across a single data set (with the exception of those from data set 13, where the first four points are noticeably different than the last four, indicating that the gain probably changed during the data set). The results presented in this plot confirm my assumptions that the calibration is relatively constant throughout a data set, but can change substantially from day to day.

Figure H.6(c) shows the relative calibration parameters $\lambda[\omega_\mathrm{b}]/\lambda[\omega_\mathrm{r}]$ extracted from each calibration measurement as the colored open markers (ignore the black dots for now). No data is shown for the red calibration example above, as no data was taken with the blue drive on. The values shown for the blue calibration example are those extracted from the high-occupancy spectral data. The temperature sweep and asymmetry sweeps 2-8 were also calibrated using the high-occupancy spectral method, while asymmetry sweeps 9-14 were calibrated using the parametric oscillation method. Once again, the averages of the measured values associated with each data set are shown as horizontal lines. The first conclusion I make from this data is that the values extracted from the high-occupancy spectral calibration method exhibit far less scatter than those extracted from the parametric oscillation method. They are also more closely grouped about one (as we might expect because λ should only be weakly frequency dependent). In an effort to check whether these calibrations were valid, I also analyzed any high-occupancy points (points with $n_\mathrm{m}^\mathrm{f} > 20$) from the

asymmetry sweeps as if they were calibrations and plotted them as the black dots in the figure (remember that some of the calibration points were measured before the asymmetry sweep and some were measured after, so these points were actually taken in between the designated calibrations). Not surprisingly, the black dots for the data sets calibrated using the high-occupancy spectral method are very consistent with the calibration (as there is essentially no difference between the
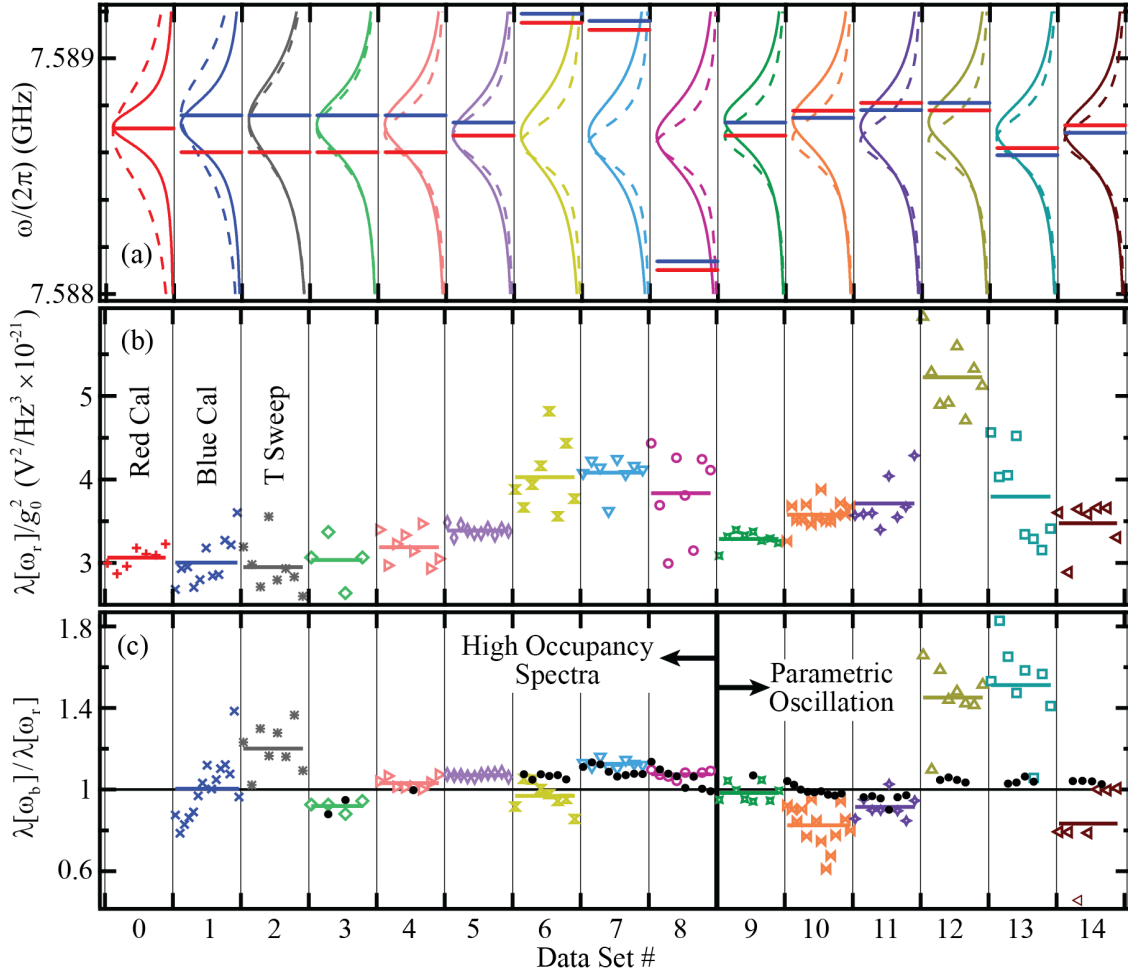

Figure H.6: Summary of parameters extracted from many different relative calibration measurements. For each data set, I plot (a) the cavity lineshape and the upper red and lower blue sideband frequencies, (b) the red-drive calibration parameter $\lambda[\omega_r]$, and (c) the relative calibration parameter $\lambda[\omega_b]/\lambda[\omega_r]$. Values from each individual calibration are shown as colored symbols, with the averages (which were the employed calibration values) for each data set indicated as lines. The black dots in (c) are extracted from high-occupancy points in the actual asymmetry sweep.

two types of data). However, there are substantial differences between the black dots and the calibrated values found using the parametric oscillation method. The last thing to notice about Figure H.6(c) is that all of the relative calibration parameters extracted using the high-occupancy spectral calibration method (either as intentional calibration points or as the black dots) are grouped about one, but can vary by about 10% (a frequency dependence that seems reasonable for the HEMT gain over 20 MHz). I therefore conclude that using mechanical parametric oscillation to find the point of equal red and blue photon numbers is both less repeatable and less reliable than the high-occupancy spectral method.

Unfortunately (in retrospect), some of the best asymmetry sweeps are data sets 9-14. This is not because of the calibration choice made (as the actual power sweep does not depend on this choice), but is instead a consequence of the input drive choices made for each sweep. Asymmetry sweeps 3 and 4 are different from all of the other sweeps because the sidebands of interest (see Figure H.6(a)) are further apart in frequency. In theory, this should not affect the asymmetry. However, in practice the asymmetry may be degraded, as it will be far more sensitive to errors in the cavity resonance frequency, linewidth, and thermal occupancy, as well as the JPA gain frequency dependence. Keep in mind that errors in the extracted cavity parameters might not be surprising, as I am using the cavity response function derived in the theory chapters to fit the bare cavity response, which likely does not not fully describe the system. In particular, we sometimes observe discrepancies between the bare cavity response and the thermal cavity spectral shape, making it unclear which values are relevant for converting between different quantities. Asymmetry sweep 5 exhibits similar asymmetry to that seen in data sets 9-14, but required a lot of point-specific analysis to remove non-ideal effects like JPA gain drift. The other asymmetry sweeps calibrated with the high occupancy spectral method (sweeps 6-8) are so far detuned that the power required to produce a significant asymmetry saturates the JPA (although the fact that no asymmetry is observed for these sweeps confirms our expectations). In Chapter 9, I therefore present asymmetry sweep 11, where the sidebands of interest are detuned by about $\kappa/3$ from the cavity resonance, and asymmetry sweep 14, where the sidebands are nearly on-resonance. To rectify the poor calibration

of these data sets, I scale the extracted blue occupancies by a common factor (one for each set) such that the highest occupancy point has equal red and blue occupancies. This method of calibration is clearly not very rigorous, as it uses data points in the data set to calibrate the data set. However, doing this does allow us to understand what the asymmetry would look like if we did have a valid independent calibration.